NASA CR 152029

LOW SPEED AERODYNAMIC CHARACTERISTICS OF A VECTORED THRUST V/STOL TRANSPORT WITH TWO LIFT/CRUISE FANS

BY DIRK J. RENSELAER

JULY 1977

Prepared under contract NAS2-9003 by

LOS ANGELES AIRCRAFT DIVISION
ROCKWELL INTERNATIONAL CORPORATION
Los Angeles, California

for

NASA

AMES RESEARCH CENTER
NATIONAL AERONAUTICS AND SPACE ADMINISTRATION

NASA CR 152,029

LOW SPEED AERODYNAMIC CHARACTERISTICS OF A VECTORED THRUST V/STOL TRANSPORT WITH TWO LIFT/CRUISE FANS

By Dirk J. Renselaer

July 1977

Prepared under contract NAS2-9003 by
LOS ANGELES AIRCRAFT DIVISION
ROCKWELL INTERNATIONAL CORPORATION
Los Angeles, California
for
AMES RESEARCH CENTER
NATIONAL AERONAUTICS AND SPACE ADMINISTRATION

1. Report No.	2. Government Accession No.	3. Recipient's Catalog No.
NASA CR 152,029		

4. Title and Subtitle	5. Report Date
Low Speed Aerodynamic Characteristics of a Vectored Thrust V/STOL Transport with Two Lift/Cruise Fans	August 1977
	6. Performing Organization Code
7. Author(s)	8. Performing Organization Report No.
Dirk J. Renselaer	
	10. Work Unit No.
9. Performing Organization Name and Address	
Rockwell International Corporation Los Angeles, California	11. Contract or Grant No. NAS2-9003
	13. Type of Report and Period Covered
12. Sponsoring Agency Name and Address	Contractor Report
National Aeronautics and Space Administration Washington, D. C. 20546	14. Sponsoring Agency Code

15. Supplementary Notes

16. Abstract

A wind tunnel test was conducted to obtain power-on low-speed characteristics of a twin fan vectored thrust V/STOL transport aircraft. Longitudinal as well as some lateral-directional data were analyzed. Hover, STOL, and conventional flight modes were investigated.

The scope of the investigation included the determination of STOL characteristics in and out of ground effect, hover characteristics with and without bank angle, roll control effectiveness as affected by ground proximity and aircraft attitude. The study also included various means to improve the lifting capability of the aircraft such as by application of fuselage strakes, exhaust vanes capable of shifting the thrust vector aft, and external flap blowing for STOL performance.

A number of theoretical equations for longitudinal and lateral-directional characteristics were derived and results compared with test data.

17. Key Words (Suggested by Author(s))	18. Distribution Statement
V/STOL Lift Fan Wind Tunnel Test	

19. Security Classif. (of this report)	20. Security Classif. (of this page)	21. No. of Pages	22. Price*
Unclassified	Unclassified	188	-

*For sale by the National Technical Information Service, Springfield, Virginia 22161

LOW SPEED AERODYNAMIC CHARACTERISTICS OF A VECTORED THRUST V/STOL TRANSPORT WITH TWO LIFT/CRUISE FANS

By Dirk J. Renselaer

SUMMARY

A wind tunnel test was conducted to obtain low speed characteristics in and out of ground effect of a twin fan vectored thrust V/STOL transport. Hover, STOL and conventional flight modes were investigated using a 10% scale model with thrust nozzles vectored to various angles. Primarily longitudinal data were obtained, as well as some lateral-directional data.

In hover, only minor interference lift losses were encountered in ground effect with wings level. Larger losses were encountered in a banked condition both with and without roll control application.

Lift characteristics at forward speed were found to be essentially those of the power-off characteristics plus the direct thrust contribution with only minor negative interference. The negative interference was found to be much less than that of a previously tested VTOL model with twin exhausts (ref. 4).

Various means to improve the lift were investigated. In hover, simple exhaust nozzle wall extensions, strakes, and a strake box proved beneficial. At forward speed strakes were also beneficial, and rotating the nozzles fully aft for flap blowing may be advantageous below $C_T = 2$. However, a hybrid configuration with half the nozzles deflected downward and half deflected aft was not promising to improve lift.

INTRODUCTION

Considerable interest exists in the design of a small transport aircraft with V/STOL capability for application in the 1980's. A viable propulsion concept for such an aircraft consists of using two lift fans the exhaust of which can be vectored aft for cruise, and downward for VTOL and STOL operation. Such a concept is proposed in reference 1.

The design of such an aircraft requires detailed knowledge of propulsion induced aerodynamic interference effects in hover and in the low speed regime in and out of ground effect. The nature of the interference is such that heavy reliance on empirical data is required.

The present report includes test data for hover and transition of a ten percent scale wind tunnel model. Primarily longitudinal data were acquired, but some lateral and directional data were also obtained with emphasis on obtaining power effects. The tests were conducted in the V/STOL tunnel of the Langley Research Center of the National Aeronautics and Space Administration.

CONTENTS

LIST OF ILLUSTRATIONS

SYMBOLS

A	Total nozzle exit area
A_1	Nozzle exit area of one fan (i.e., exit area of two swivel nozzles)
AC	Aerodynamic Center
a_N	Distance from center of fan inlet to the c.g. (of each fan), see figure 75a
AR	Aspect ratio
a_R	Moment arm of ram drag with respect to c.g., in pitch, $\alpha = 0$ (fig. 49a)
a_T	Moment arm of thrust vector with respect to c.g. in pitch (fig. 49a)
b	Wing span
$\bar{c}$	MAC of wing
$\bar{c}_H$	MAC of horizontal tail
$\bar{c}_V$	MAC of vertical tail
C_D	Drag coefficient, D/qS
$C_{D_{aero}}$	Coefficient of aerodynamic forces in drag
c.g.	Center of gravity (assumed to be located at 25% $\bar{c}$)
$C_{D_{TOT}}$	Coefficient of total drag, identical to C_D
C_L	Lift coefficient, L/qS
$C_{L_{aero}}$	Lift coefficient of circulation lift
$C_{L_{TOT}}$	Coefficient of total lift, identical to C_L
C_ℓ	Rolling moment coefficient, M_R/qSb
C_m	Pitching moment coefficient (about 25% $\bar{c}$), M/qSb
$C_{m_{aero}}$	Coefficient of aerodynamic portion of pitching moment
C_{m_R}	Pitching moment due to ram drag
$C_{m_{TOT}}$	Total pitching moment coefficient, identical to C_m
C_n	Yawing moment coefficient. N/qSb
C_T	Thrust coefficient, T/qS
C_Y	Side force coefficient, Y/qS
D	Drag force
ΔD_{int}	Interference drag, i.e. aerodynamic drag with power, minus aerodynamic drag without power
d_e	Diameter of equivalent circular exhaust area of one fan
D_R	Inlet momentum drag
EBF	Externally blown flaps
f	Ratio of inlet mass flow/exhaust mass flow
FRP	Fuselage reference plane
F_x	Force in x-direction in body axis system
F_z	Force in z-direction in body axis system
g	Gravitational constant, 9.81 m/sec^2 (32.2 ft/sec^2)

h	Distance between ground and center of exhaust plane of nozzles when $\delta_N = 90°$. At other nozzle angles the nozzle height is defined as if the nozzles were at 90°. In banked conditions h is the average between left and right hand fan nozzles.
i_H	Horizontal tail incidence with respect to FRP; positive trailing edge down
IGE	In ground effect
L	Total lift (stability axis system)
LE	Leading edge
ΔL_{int}	Interference lift due to power
ℓ	Longitudinal distance between nacelle inlets and moment reference point
ℓ_1	Lateral moment arm of left hand ram drag with respect to c.g. (fig. 75a)
ℓ_2	Lateral moment arm of right hand ram drag with respect to c.g. (fig. 75a)
ℓ_y	Same distance as ℓ_1 or ℓ_2, except that $\beta = 0$
ℓ_z	Vertical distance of ram drag vector above c.g. (fig. 49a)
M	Pitching moment
MAC	Mean aerodynamic chord
M_R	Rolling moment (fig. 1)
$\dot{m}$	Inlet mass flow per second
N	Yawing moment
NS	Nacelle station. (Stations are called out in inches)
OGE	Out of ground effect
OH	Overhang of flap shroud
op	Subscript denoting zero power
p	Subscript denoting a total effect due to power
P_T	Total pressure
$P_{T_{f_e}}$	P_T at location of fan exit (figure 4)
P_o	Free stream static pressure
q	Free stream dynamic pressure
RPM	Revolutions per minute
r	Longitudinal displacement of nozzle thrust with respect to nozzle center (fig. 49a)
S	Wing area of reference wing
STOL	Short takeoff and landing
T	Total nozzle exhaust thrust (both fans)
T_1	Nozzle exhaust thrust of one fan. Also nozzle exhaust thrust of left fan
T_2	Nozzle exhaust thrust of right fan

v	Free stream velocity
v_j	Exhaust velocity
v_{TIP}	Fan tip velocity based on radius 7.63 cm (3.0 in)
VTOL	Vertical takeoff and landing
$(v/v_j)_e$	Effective velocity ratio
w	Width of swivel nozzle exhaust
w_i	Vertical downwash velocity in stability axis system
WCP	Wing chord plane
WRP	Wing reference plane
WS	Wing station, lateral distance from plane of symmetry (called out in inches)
x	Forward direction in body axis system (fig. 1)
x_o	Fuselage station, positive aft (called out in inches from fuselage nose)
Y	Side force (fig. 1)
y	Lateral dimensions in body axis system
Δy	Lateral distance between the centers of the exits of the two nozzles of one nacelle (fig. 6b)
z	Upward direction in body axis system (fig. 1). Also distance downstream behind nozzle exit
z_o	Vertical distance above FRP (called out in inches)
α	Angle of attack of FRP
β	Sideslip angle (fig. 1)
γ	Angle of inclination of nozzle side wall (fig. 6b)
δ	Ratio of atmospheric pressure/pressure at sea level standard day
δ_F	Flap angle
δ_N	Nozzle angle (0° full aft, 90° full down in body axis system)
ϵ	Downwash angle with respect to free stream direction
θ	Ratio of absolute temperatures at actual atmospheric condition/sea level standard condition. Also pitch angle, positive nose up
θ_j	Exhaust flow angle with respect to FRP
ρ	Atmospheric density
ρ_j	Density of jet exhaust
ϕ	Bank angle (fig. 1)
$\dot{\omega}$	Inlet weight flow per second
μ	Tip speed ratio, v_{TIP}/v
η	Turning efficiency (see sketch on page 10)
χ	Angle, defined in fig. 75a

MODEL AND APPARATUS

The model represents a 10% scaling of a twin lift/cruise fan aircraft with fans located in wing nacelles. Photographs of the model are presented in figure 2 and a three-view is given in figure 3.

Each of the two model nacelles carries a tip turbine powered TD-457 fan from the Tech Development Company as shown in figure 4. The exit diameter of the fan including the tip turbine exhaust is 15.25 cm (6.0 in). The drive air is supplied internally. The fan axis of rotation is drooped 5.5° with respect to the fuselage reference plane.

Each nacelle carries two independently rotatable exhaust nozzles (fig.5). The nozzles can be rotated from a full aft cruise position to a forward position for braking. The axis of rotation of the nozzles is inclined with a double angle. Viewed along the fan axis, the axis of rotation is laterally inclined 21° from horizontal, lying in plane A-A of figure 6a and within the plane A-A the axis of rotation is rotated aft by 19°.

In order to locate the nozzle exhaust with respect to the model more conveniently, the nozzle angles were measured in front and side view, and the locations of the exhaust centers were measured longitudinally, vertically, and laterally using the definitions given in figure 6b. Results are:

Nominal Nozzle Angle, δ_N (Deg)	Actual Nozzle Angle in Side View (With Respect to FRP*, Deg)	Inclination of Outer Nozzle Wall in Front View, γ (With Respect to Plane of Symmetry**, Deg)
0 (full aft)	0.2	Not measured (approx. 0)
23	22.6	Not measured (approx. 0)
62	61.8	+9.3
80	80.5	+3.7
90 (full down)	90.1	+0.2
103	103.5	-5.5
120 (braking)	119.9	-15.7

*measured from photographs, positive with exhaust directed downward.
**measured from photographs, positive where flow is directed inward towards the nacelle plane of symmetry.

Nominal Nozzle Angle, δ_N (Deg)	Fuselage Station x_o	Vertical Station z_o	Distance Δy Between the two Nozzle Centers of one Nacelle	
			(cm)	(in)
0	(27.7)	(+0.40)	15.75	(6.20)
23	(27.4)	(-0.80)	14.15	(5.57)
62	(26.0)	(-2.29)	14.35	(5.65)
80	(24.9)	(-2.66)	16.10	(6.34)
90	(24.5)	(-2.67)	16.57	(6.52)
103	(24.0)	(-2.57)	18.24	(7.18)
120	(23.6)	(-2.50)	18.72	(7.37)

The exhaust shape of each nozzle is rectangular (fig.5). The width is 6.22 cm (2.45 in), height 12.45 cm (4.9 in), and the exhaust area is 77.4 cm^2 (12.0 in^2). The upper and lower walls of each nozzle are parallel. The side walls have a converging angle of 88.33° as indicated in figure 7.

The figure also illustrates the internal duct shape of the nacelles. Fillets are used to eliminate sharp corners. The duct opening at the plane of rotation is circular and has a diameter of 12.45 cm (4.9 in).

The reference wing planform is trapezoidal (fig. 3). The reference wing has an area of 0.387 m^2 (4.17 ft^2) and a mean aerodynamic chord of 22.75 cm (8.96 in). The true wing planform includes an unswept portion with a constant chord between the fuselage and the nacelle, up to 32% semispan. The chord length of this section is 35.1 cm (13.82 in) and the airfoil is a NACA 64A412 section extending from the true leading edge to the true trailing edge. Outboard of the nacelles, from 43.3% to 97.5% semispan, a 17% thick supercritical airfoil is used with a camber of 3.15% and a leading-edge radius of 4.5% chord. Between the 32% and 43.3% semispan stations a transition exists between the conventional inboard wing panel and the supercritical outboard panel. The transition is made using straight lines between points of equal percent chord station.

The incidence of the airfoil reference line on the inboard panel with respect to the fuselage is 5.3°, constant up to a lateral wing station of 43.3% semispan. The outboard wing panel has a twist and thickness such that all constant percent chord stations fall laterally on a straight line. The incidence at 97.5% is 2.4°. The incidence is obtained by rotating the airfoil at the 97.5% semispan station about its 50% chord station; no dihedral is used at this chord station. Due to the twist, the quarter chord element lies below the wing reference plane and has a slight negative dihedral.

The model has a double slotted flap over 70% of the wing span. The flap chord inboard of 43.3% semispan is constant in absolute value, whereas a constant percentage wing chord is used between 43.3 and 70.0% semispan. Outboard of the 43.3% semispan station the detail flap dimensions are as shown in figure 8. A photograph of the flap near the nacelle afterbody is presented in figure 9.

Drooped and extended ailerons, from 70% to about 100% semispan, are used for one run. Geometric details are given in figure 10. The upper surface inclination of the extension is 20° with respect to the airfoil chord.

Slotted Krueger flaps are installed inboard of the nacelles with chordwise dimensions as given in figure 11. The span is 9.9 cm (3.9 in) for each. No lateral gap exists between the flaps and the fuselage sidewall, however a gap exists between the flap and the sidewall of the nacelle because of the curved wing-nacelle fairings. The flap deflection is 60 degrees with respect to the wing chord.

Plain Krueger flaps are attached to the wing leading edge outboard of the nacelle fairings, figure 11. Flap chord is 15% of the wing chord, and the average deflection is 65 degrees with respect to the wing chord.

Nacelle strakes for the outboard sides of the nacelles are located as shown in figure 12. They were used on only a few test runs.

A few runs were made with exhaust vanes installed at the nozzle exits. A geometric description is given in figure 13.

Fuselage lower surface strakes are shown in figure 14a. The fuselage strakes consist of two walls parallel to the fuselage center line, and, in case of the "strake box", a laterally connecting wall in the front and rear of the two parallel walls.

Nozzle exhaust fences, consisting of an extension of the side wall of the nozzle so as to shield the nacelles from the exhaust flow, are shown in figure 14b.

Landing gear geometry is presented in figure 15. No associated gear doors were simulated.

Fan inlet covers (plugs) are illustrated in figure 16. Their shape is such that the forward portion of the nacelle represents a smooth streamline body.

External exhaust rake geometries and their location with respect to the left hand nacelle are presented in figure 17.

Each nacelle contains a built-in internal total pressure rake just aft of the fan stator (fig. 4). Six total pressure probes are manifolded together to produce one average total pressure for each nacelle. Two static pressure orificies are located in the nacelle wall in the same plane as the leading edge of the total pressure probes. The two static pressures were also manifolded together to produce one average static pressure for each nacelle.

Unless specifically noted otherwise, the configuration tested was equipped with slotted inboard and plain outboard Krueger flaps, but had no aileron droop or extensions, no fences or strakes, no landing gear, no inlet covers, and no external pressure rakes installed.

A boundary layer trip was applied 3.2 cm (1.25 in) behind the wing and tail leading edges and behind the fuselage and nacelle nose. Number 60 grit was applied 1.6 mm (1/16 in) wide.

The model was tested in the V/STOL facility of the National Aeronautics and Space Administration's Langley Research Center (tests 148, 149, and 152). Wall corrections were applied to all data at forward speed out of ground effect, based on H. Heyson's methods. In ground effect no wall corrections were applied because they were very small.

Calibration tests were made in the wind tunnel as well as in the adjacent static test facility to determine static thrust by model force measurements. Most of the calibration tests were made with the nacelles and the fuselage shielded against the exhaust flow (reference 2). Shielding is necessary so that the forces of the model to be measured are ideally only those of the exhaust thrust. Without shields, entrainment flow and the exhaust plume generate interference forces on the model.

The shielding used is schematically shown in figure 18a. The wing and other surfaces were deleted or substituted for by minimum structure to minimize forces on the model from interference. The fans were not operated simultaneously to avoid the generation of a "fountain" flow. Also, some calibration tests were made with the nacelle shields removed, but with the fuselage still shielded; see figure 18b. Additional details of the calibration setup are found in reference 2.

The inlet flow rate was calibrated under static conditions. For this calibration, the model inlet was removed and a bellmouth inlet was attached to the front of the fan. Total pressure in front of the bellmouth entrance (equal to room ambient pressure) and the static pressure in the bellmouth throat were measured.

CALIBRATION RESULTS

The thrust of each of the two nozzles of each nacelle has a component in the axial and normal direction, as well as a small component in the lateral direction because of the inclinations of the axes of rotation of the nozzles (fig. 6a). The calibrated thrust of the exhaust nozzles, however, is defined as being only the resultant force in the X-Z plane (parallel to plane of symmetry), leaving out any lateral components that may exist at each swivel nozzle position in this definition; see fig. 6b. The calibrated thrust so defined is presented as the sum of the thrusts of both nozzles per fan.

The calibrated thrust of the right hand fan, corrected for temperature and pressure, is presented in figure 19. The data are presented versus the square of RPM. Such a presentation facilitates detection of deviations from a first order linear theory that treats the fan as if it were a propeller. The figure pertains to conditions out of ground effect. Similar data are given in figure 20 in ground effect, with and without bank angle. Results show that the fan thrust decreases somewhat with closer proximity to the ground. Maximum scatter at high RPM values is in the order of 8N (approximately 2 lbs.).

The calibrated thrust of the left hand fan is similar except that the ground effect is not as pronounced. Thrust data for this fan are presented in reference 2.

Comparison of the data with shields (as in figure 18a) and without shields (as in figure 18b) yields the exhaust interference on the nacelle. Results are given in figure 21. It is seen that, out of ground effect, the nacelle generates a "suck down" of about 5% at a nozzle angle of 90°. In ground effect this loss is increased to about 10%

Exhaust flow turning angles are shown in figure 22 a and b for the fans with calibration shields. It is seen that the turning angles almost coincide with the nozzle rotation angles. Average turning angles of the right and left hand fan together are listed in the following table:

Nozzle angle, δ_N	(deg)	0	23	62	80	90	103	120
Jet deflection angle, θ_j	(deg)	3.0	26.8	62.5	81.9	91.5	105.1	122.7

An assessment of the location of the exhaust thrust vector is made using moment data from the fans with calibration shields. Pitching moment data about $\bar{c}/4$ are plotted in figure 23 for various RPM's in and out of ground effect. Computed moments of thrust times moment arm to the geometric center of the exhaust are also indicated for comparison. The measured moments out of ground effect show more negative values except at $\delta_N = 120°$, indicating that the thrust is generally located behind the center line. The average distance r behind the center is for the left and right hand fan:

δ_N	80°	90°	103°	120°
$r/\bar{c}$	0.0828	0.0727	0.0247	-0.0388

In ground effect the measured moments are more negative, indicating that the center of thrust is located further behind the geometric nozzle center.

Lateral flow angularities are measured from rake surveys of the outboard nozzle of the left hand fan at distances of 0.40 d_e and 1.12 d_e downstream of the nozzle. On one occasion measurements were also taken at 0.03 d_e distance from the outboard nozzle of the right hand fan. Data are presented in figure 24, indicating only a slight lateral inclination of the exhaust flow.

Additional exit flow characteristics are given in figure 25 where the pressure ratio at the fan exit is given as a function of thrust. The pressures are based on averages of six total pressure rakes and two static orifices, each manifolded together. The data are given only for nozzle angles of 90 and 103 degrees; at other angles oil was suspected to have accumulated in the pressure lines. Results are used in an assessment of the thrust increase with forward speed during the discussion of transition characteristics.

Inlet flow data are presented in figure 26 with correction factors for temperature, θ, and pressure, δ, which are unity for standard atmosphere. By first approximation, the inlet flow follows a linear variation with the square root of the thrust. Theoretically this is seen as follows. Assuming a uniform distribution of the flow across the fan exit area:

$$(\rho_j A_1 v_j) v_j = T_1$$

$$(\rho_j A_1 v_j)^2 = (\rho_j A_1) T_1$$

Herein, the mass flow leaving the fan is equal to $(\rho_j A_1 v_j)$ and consists of the inlet mass flow and the mass added to the system by the fan turbine supply air. A factor f is now defined to exclude the supply air, so that the inlet mass flow of one fan is

$$\dot{m}_1 = f \cdot (\rho_j A_1 v_j) = \frac{\dot{\omega}_1}{g}$$

and thus the weight flow per fan becomes

$$\dot{\omega}_1 = (fg\sqrt{\rho_j A_1})\sqrt{T_1}$$

In the present case, figure 26 yields

$$\frac{\dot{\omega}_1}{\sqrt{T_1}} = \left(fg\sqrt{\rho_j A_1}\right) \approx 1.11 \frac{N/sec}{\sqrt{N}} \left(=0.524 \frac{lb/sec}{\sqrt{lb}}\right)$$

and thus

$$f = \frac{\left(fg\sqrt{\rho_j A_1}\right)}{g\sqrt{\rho A_1 \frac{\rho_j}{\rho}}} = 0.815\sqrt{\frac{\rho}{\rho_j}}$$

HOVER DATA AND STATIC TURNING CHARACTERISTICS

Tail-off longitudinal forces and moments in hover are shown in figure 27a for various distances of the model above the ground. The distance, h, is the height of the exit center of the nozzle if it were deflected to an angle of 90° even though the actual nozzle angle may be different. The quantity d_e is the diameter of an equivalent circular exhaust area equal to the exhaust areas of the two swivel nozzles fed by one fan. The graphs cover a range of h/d_e values up to 6. Numerical values for out of ground effect, where $h/d_e = \infty$, are included in the upper right hand corner of each graph.

The lift characteristics are given in this figure in terms of the lift/thrust ratio, L/T, where T is the total calibrated exhaust thrust of both fans. A high RPM case (100%T) and a lower RPM case (80%T) are shown. The lift loss due to aerodynamic interference is 5 to 6.7% out of ground effect and 10 to 14% in ground effect. The larger lift loss pertains to the lower RPM case. An almost identical lift loss for high RPM was found in figure 21 for the nacelle alone which suggests, at this nozzle angle, that the nacelle is primarily responsible for most of the lift loss for the whole model.

Similar data are given in figure 27b at various nozzle angles, δ_N, but all at high RPM. The data show that L/T decreases from 0.98 to 0.88 in going from $\delta_N = 80°$ to $\delta_N = 100°$, out of ground effect, and that ground effect decreases L/T further by approximately 6% at $h/d_e = 1.0$. These are readings at zero pitch angle; in ground effect a decrease in L/T is found with increasing pitch angle (fig. 27c, 27d).

In an effort to reduce the lift loss due to ground effect, a strake box was tested on the bottom of the fuselage. The box consisted of sidewalls and a front and rear wall (see fig. 14a), and is designed to capture a "fountain" flow between the two fans. The box changed the ground effect by 17% from a lift loss to a lift gain at $h/d_e = 1.0$. The change was less at greater ground distances (fig. 28a).

Another sidewall which is formed by an extension of nozzle walls as illustrated in figure 14b, also helps reduce the loss due to ground effect by at least 5% throughout the range of h/d_e values (fig. 28b). This may be caused by moving the region of flow mixing between the exhaust and surrounding air further downstream, thereby reducing the velocity of entrained air at the lower surface of the nacelle which, in turn, decreases the suction forces at that surface. Application of these sidewalls reduces the lift loss due to interference to only 5% of the nozzle thrust at $h/d_e = 1.0$.

A summary of minimum values of L/T encountered at a nozzle angle of 90 degrees is included in the following table (in addition to asymmetric conditions which will be discussed further below):

	Minimum L/T at $\delta_N = 90°$, IGE			
	No control input			With control input
	No bank		10° bank	10° bank
	$T/T_{max}=1.0$	$T/T_{max}=0.8$	$T/T_{max}=0.8$	$T/T_{max}=0.8 \pm 0.2$
Without strakes	0.90	0.86	0.80	0.72
With strake box	0.92		0.84	0.78
With nozzle side-wall extension	0.95			

Pitching moment characteristics are also presented in the figures. The data show a pitch-up due to ground effect. Interference effects in ground proximity were analyzed in figure 27c, showing that the interference effects increase the stability in pitch. In this figure the computed curves without interference effects are based on $\theta_j = 90°$ and on a varying value of $r/\bar{c}$ as a function of nozzle attitude as derived from figure 23 for close ground proximity.

The effect of the horizontal tail on pitching moment in hover, in or out of ground effect, is negligible; see figure 29.

The discussion of the above hover data pertains to symmetric flow conditions. However, with the aircraft banked 10° (no strake box, 80% thrust setting) a minimum value of L/T = 0.80 is reached as compared to 0.86 without bank (see fig. 30a and 27a) indicating that the lift loss in bank is larger. It is believed that the fountain existing between the exhausts of the two fans is oblique; it escapes the fuselage bottom somewhat, thereby generating less positive pressure which, in turn, cannot overcome the suckdown, see sketch:

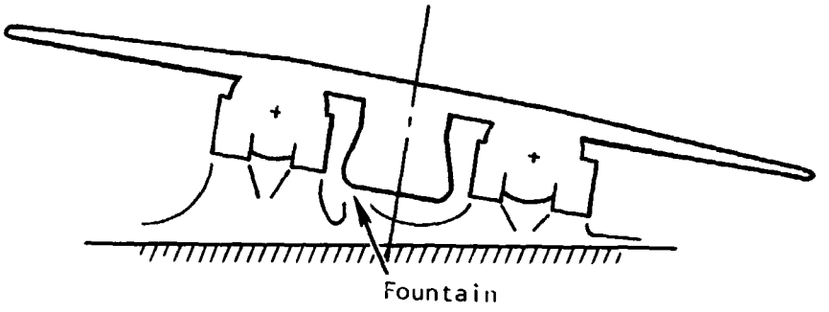

Using the strake box to capture the fountain increases the lift to L/T = 0.84 in the banked condition, as compared to 0.80 without strake box, see figure 30a.

Application of roll control in the banked condition, in the direction against the bank, reduces L/T to 0.72 at h/d_e = 1.0 without the strake box (fig. 30b). This may be due to an increased obliqueness of the fountain when control is applied. The amount of control is based on an approximate 20% fan thrust increase on one side and about 20% decrease on the other. The strake box limits the lift loss to L/T = 0.78 as shown in the same figure. Results are included in above table.

This trend of the above lift characteristics has also been shown in previous tests of a twin fan VTOL model, using water as a test medium rather than air (see ref. 3). Results of this previous test were used in selecting test runs for the present test.

Roll control characteristics are also affected by ground effect. Basic data for wings level, without strakes are given in figure 30c, and are analyzed in figure 30d. The control effectiveness is reduced to 81% at the critical distance of $h/d_e = 1.6$. This is with respect to the rolling moment computed from the thrust differential. Use of strakes changes the effectiveness to 72% as shown in the same figure. In the banked condition at a height of $h/d_e = 1.0$ the roll control moment remaining is about 61%, as compared to 81% wings level, and is roughly unaffected by the strake box (fig. 30b, d). The percentage improves rapidly with increasing ground distance.

The effect of the landing gear on hover characteristics is presented in figure 31. The effect is negligible.

Static turning characteristics are given in figure 32, based on data obtained at the highest RPM values tested, and pertain to conditions out of ground effect with the landing flap deflected and no strakes or nozzle wall extensions. The thrust efficiency and turning angle are defined in the following sketch, where F_X and F_Z are measured model forces with interference effects, and where T is the total calibrated fan thrust.

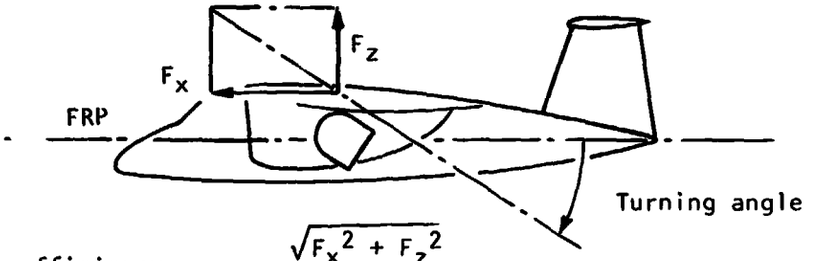

$$\text{Turning efficiency} = \eta = \frac{\sqrt{F_X^2 + F_Z^2}}{T}$$

The thrust efficiency decreases by 4% while increasing the nozzle angle from 90° to 123°, and increases 6% in going from 90° to 23°. The turning angles are essentially equal to those of the calibration data with shields installed (fig. 22), i.e., interference effects do not change the turning angles significantly.

Included in figure 32 is a case with zero nozzle deflection where the exhaust impinges on the flap (without EBF deflector). As expected, the thrust efficiency is considerably lower, and the turning angle significantly different from zero.

LONGITUDINAL POWER-OFF DATA

Power-off data were measured in conjunction with power-on data so that it is possible to isolate power effects. The power-off data are given in figures 33 and 34 for flaps up and down, with and without fan inlets covered, all without ground effect. The data are presented in the stability axis system.

Flaps up, without leading edge devices and with the landing gear retracted, a tail-off $C_{L_{MAX}}$ of 1.32 is obtained (fig. 33, fans windmilling). The increase in the maximum lift coefficient due to flap deflection and full span leading-edge devices is $\Delta C_{L_{MAX}} = 1.24$, bringing the $C_{L_{MAX}}$ to 2.56 (see summary in figure 35). The tunnel dynamic pressure in this condition was $q = 2769\ N/m^2$ (60 lb/ft^2).

Inlet covers produced, in all cases, a decrease of $C_{L_{MAX}}$ (fig. 34 and 35). In a number of runs, covers were used for drag investigations, showing a reduction in drag.

Flaps-up, the tail-off aerodynamic center for low positive angles of attack is located at 12% MAC, and tail-on at 49% (fig. 33a). The stall is stable with tail on and off, although a destabilizing trend exists at high angles of attack. Flaps-down, the tail-off aerodynamic center is located at about 14% MAC, and tail-on at 36% (fig. 33c). Addition of the flaps made the model stall unstable with and without tail.

Additional power-off characteristics, such as downwash and tail effectiveness are included in summary plots in the subsequent section.

LONGITUDINAL DATA FOR TRANSITION OUT OF GROUND EFFECT

In the present report, transition is defined as the speed regime between hover and conventional wing-borne flight.

Reference Thrust

Either the thrust coefficient $C_T = T/(qS)$, or its inverse qS/T, is used in the present report to describe the power effects. Herein, the static value of the thrust, T, is used and was computed from calibration data using measured RPM values and applying appropriate corrections for atmospheric temperature and pressure.

The static thrust, rather than the exhaust thrust existing at forward speed, is used because the change of this thrust with speed is small. An indication of the change with speed may be obtained from figure 36. The figure shows the increase of the pressure ratio at the fan exit when RPM is held constant while the tunnel dynamic pressure is increased. This pressure ratio increase can be compared with the static exhaust thrust increase with pressure ratio obtained during calibration, see figure 25. Such a comparison (not explicitly shown here) indicates that a speed increase between the static condition and $C_T = 2$ results in an exhaust thrust increase of approximately 2%.

Inlet Effects

Inlet effects are included in the power-on test data given. However, the ram drag portion of the inlet effects can be isolated using the inlet mass flow information given in figure 26 and using a procedure discussed in the drag section of this report. The remainder of the inlet effects are considered here as part of aerodynamic interference effects. Also the analysis plots include the ram drag effects unless it is specifically stated that they are excluded.

Lift

Test data for swivel nozzle deflections of 0°, 23°, 62°, 80°, 90°, 103°, and 120° are given in figures 37 through 44 for conditions out of ground effect.

A discussion of the maximum lift is given in the following. $C_{L_{MAX}}$ is defined as the lift coefficient where the first reversal in the lift curve slope occurs, even though a higher value in C_L may be reached at higher angles of attack.

Maximum lift information for zero nozzle angle is correlated in figures 45a and 45b, showing that the $C_{L_{MAX}}$ increment due to power in the flaps-up case consists primarily of the vertical component of the thrust vector. However, flaps-down, an additional maximum lift increment exists beyond this vector component because an externally blown flap (EBF) principle is involved, rather than a vectored thrust principle. With this principle the exhaust jet impinges on the flap and leaves the flap trailing edge similar to a jet sheet. This generates supercirculation analogous to a jet flap, and is responsible for the additional increase of $C_{L_{MAX}}$ with C_T.

The figure also shows the effect of leading-edge devices on the maximum lift at this nozzle angle. The increase in $C_{L_{MAX}}$ from these devices is only slightly affected by C_T.

Maximum lift information for other nozzle angles, flaps down, is summarized in figure 45c. A strong rise of the maximum lift coefficient with C_T is shown in all cases. For these larger nozzle angles this is primarily caused by the direct thrust contribution to lift.

A more detailed discussion of the lift characteristics now follows. First, the direct thrust contribution is subtracted to isolate the aerodynamic circulation lift, $C_{L_{aero}}$. This is carried out for various nozzle angles and as a function of angle of attack in figures 46a through 46g, using

$$C_{L_{aero}} = C_L - C_T \sin(\theta_j + \alpha)$$

Herein, C_L is the coefficient of the total measured and θ_j is the jet deflection angle.

Results show that $C_{L_{aero}}$ decreases as C_T increases when the angle of attack is low, except for $\delta_N = 0$ where the flap is externally blown. The difference between $C_T = 0$ (fans windmilling) and finite C_T values represents the interference effect of power on the circulation lift. Thus, except for $\delta_N = 0$, the interference lift coefficient is negative at low α's.

For a further discussion of the data it may be helpful to introduce a different form of presentation since the significance of the lift loss is not easy to assess immediately from above curves. For example, a large drop in C_L may be relatively insignificant when multiplied by a very low dynamic pressure. To obtain a proper assessment of a change in lift the actual lift value, rather than C_L, should be compared with a tangible quantity such as aircraft weight or nozzle thrust.

In the present report the static thrust is used for comparison, being always relatively high at low transition speeds:

$$\frac{\Delta L}{T} = \frac{\Delta C_L qS}{T} = \frac{\Delta C_L}{C_T}$$

The data are now also presented as a function of the inverse of C_T, i.e. qS/T, so that conditions for zero velocity can be shown graphically. A schematic of such a presentation is given in the following sketch for the total aircraft lift:

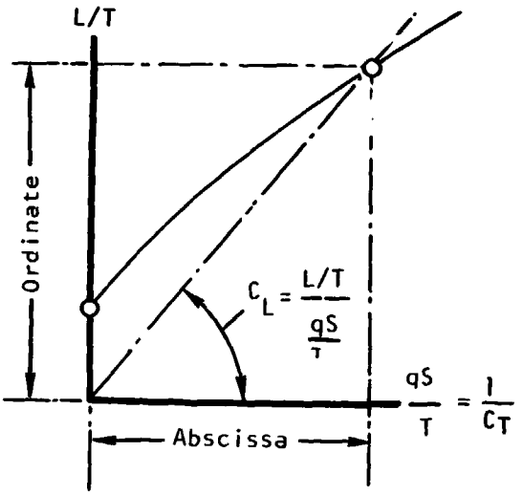

Graphs of this type give a clear visibility of the magnitude of lift change with speed during takeoff, a characteristic which cannot be found in presenting C_L versus C_T because of the large changes in C_L encountered when q is increased at low speed. For example, when speed is increased from zero the large associated drop in C_L does not even give an immediate impression as to whether L actually increases or decreases. However, when the data are expressed in terms of L/T a change in q gives a clear impression of the magnitude and sign of the lift change. Also, for a known thrust and given aircraft weight W = L, the dynamic pressure needed for flight equilibrium can immediately be determined in the latter format.

One reason for the selection of qS/T as the abscissa is to preserve a ready determination of conventional coefficients from these graphs based on the following equation:

$$C_L = \frac{L}{qS} = \frac{(L/T)}{(qS/T)}$$

For example, in a graph showing L/T versus qS/T, the C_L value can be determined by dividing the ordinate L/T by the abscissa qS/T as is illustrated in the above sketch (note also that $C_L = (L/T)C_T$).

Furthermore, the abscissa qS/T can easily be related to the often quoted physically important velocity ratio $(v/v_j)_e$. This is shown as follows: The thrust is

$$T = (v_j \rho_j A) v_j$$

where A is the total nozzle exhaust area when T is the total nozzle thrust. Thus

$$\frac{qS}{T} = \frac{\frac{1}{2}\rho v^2 S}{\rho_j v_j^2 A} = \frac{S}{2A}\left(\frac{\rho v^2}{\rho_j v_j^2}\right)$$

Defining

$$\frac{\rho v^2}{\rho_j v_j^2} = \left(\frac{v}{v_j}\right)_e^2$$

The desired relation becomes

$$\left(\frac{v}{v_j}\right)_e = \sqrt{\frac{qS}{T}}\sqrt{\frac{2A}{S}}$$

With the geometric property of A/S = 0.080 for the present model the relation reduces to

$$\left(\frac{v}{v_j}\right)_e = 0.40\sqrt{\frac{qS}{T}}$$

This yields the following numerical comparison between qS/T and $(v/v_j)_e$:

C_T	0	0.5	1	2	4	8	16	50	∞
qS/T	∞	2	1	0.5	0.25	0.125	0.0625	0.020	0
$(v/v_j)_e$	∞	0.565	0.400	0.283	0.200	0.1415	0.100	.0565	0

Applying the above relationships the increase in maximum lift in terms of L_{MAX}/T versus qS/T is presented in figure 47a, showing that with an increase in freestream dynamic pressure the maximum lift capability of the

present aircraft increases immediately while keeping the thrust constant. Also, the lift at low angle of attack increases immediately with increase in forward speed (fig. 47b). An angle of attack of four degrees was chosen because at a lesser angle of attack the lift decreases significantly at very low speeds (fig. 42b). The lift presented is the total lift which includes the aerodynamic lift as affected by power, and the direct lift component from the exhaust thrust.

The above form of presentation leads to a different analysis procedure than before. The lift is broken up into various components. The various components are illustrated in figure 47c, describing the case of $\delta_N = 90°$ from figure 47b. In general, the total lift consists of the following three contributions:

$$L = C_{Lop} qS + T \sin(\theta_j + \alpha) + \Delta L_{int}$$

or

$$\frac{L}{T} = C_{lop} \frac{qS}{T} + \sin(\theta_j + \alpha) + \frac{\Delta L_{int}}{T}$$

Herein, C_{Lop} is the lift coefficient at zero power. It is seen that, given a certain thrust, the power-off-lift/thrust ratio (first term on the right in the equation) is proportional to qS/T because of the dynamic pressure variation. The second term is a constant (assuming a constant angle of attack). In the figure the two terms together are represented as a straight line. An increase above this line indicates positive interference lift, ΔL_{int}, and a drop below this line represents a negative interference lift. In the case of figure 47c, the negative interference lift amounts to only about 7% of the thrust. The loss occurs at speeds where sufficient lift is generated to enable the aircraft to lift weights in excess of those at hover. In this figure, the power-off lift used was that for fans windmilling ($C_T = 0$, $\alpha = 4°$, $C_L = 2.00$, fig. 42a).

In figure 47d this interference lift is isolated and summarized for various nozzle angles and for various angles of attack.

The above results reveal that the interference lift loss of the present model is significantly less than a previously tested model with twin exhausts (ref. 4). In that test, losses in excess of 25% T were encountered for a nozzle location slightly forward of 25% MAC ($\delta_N = 90°$, flaps down). It is surmised that in the present test the nacelle afterbody shape is such that not as much flow separation exists behind the exhaust pipes at forward speeds.

Drag

Similarly to the lift, the drag can also be broken up into various components. The total drag is

$$C_{D_{tot}} = C_{D_{aero}} + C_{D_R} - C_T \cos(\alpha + \theta_j)$$

Herein, C_{D_R} is the ram drag, and the last term on the right hand side is the direct nozzle thrust component. In figures 48a through 48g the aerodynamic drag, $C_{D_{aero}}$, is presented by subtracting the ram drag and the thrust component from the total measured drag.

The ram drag was computed using

$$D_R = \frac{\dot{\omega} V}{g} = \frac{\dot{\omega}}{g}\sqrt{\frac{2q}{\rho}}$$

where, for two fans (see before):

$$\dot{\omega} = 2\left(fg\sqrt{\rho_j A_1}\right)\sqrt{T_1}$$

and where the subscript 1 denotes one fan. This yields for two fans:

$$D_R = 2\left(fg\sqrt{\rho_j A_1}\right)\sqrt{2T_1}\,\frac{\sqrt{q}}{g\sqrt{\rho}}$$

and because $2T_1 = T$:

$$\frac{D_R}{T} = \frac{2\left(fg\sqrt{\rho_j A_1}\right)}{g\sqrt{\rho S}}\sqrt{\frac{qS}{T}}$$

Note that conversions between the forms of presentation can be carried out using:

$$C_D = \frac{D}{qS} = \frac{D/T}{qS/T} = \left(\frac{D}{T}\right) C_T$$

so that

$$C_{D_R} = \frac{D_R}{qS} = \left(\frac{D_R}{T}\right) C_T = \frac{2\left(fg\sqrt{\rho_j A_1}\right)}{g\sqrt{\rho S}}\sqrt{C_T}$$

in which, from calibration results:

$$f_g \sqrt{\rho_j A_1} = 1.11 \frac{N/sec}{\sqrt{N}} \left(= 0.524 \frac{lb/sec}{\sqrt{lb}} \right)$$

The above figure 48 gives the aerodynamic drag for $C_T = 0$ (fan windmilling), as well as for finite C_T values. An aerodynamic interference drag, ΔD_{int}, is defined as the difference between the aerodynamic drag at $C_T = 0$ and $C_T > 0$ while the angle of attack is held constant. This drag, in terms of

$$\frac{\Delta D_{int}}{T} = \Delta C_{D_{int}} \frac{qS}{T}$$

is plotted separately in figure 48h. When this drag is combined with the direct thrust term the sum represents the total power effect:

$$\Delta D_p = \Delta D_{int} + T \cos (\alpha + \theta_j)$$

This quantity, non-dimensionalized by T, is presented in figure 48i, along with the associated lift change due to power, all for zero angle of attack. The data show the lift and drag increment due to power as being relatively constant with speed over a fairly large speed range (a fact that could not have been visible if the data were plotted in customary coefficient form since constants divided by qS show large variations).

Pitching Moment

The aerodynamic contribution in the tail-off pitching moment has been isolated according to equation

$$C_{m_{aero}} = C_{m_{tot}} - C_{m_R} - \frac{T}{qS} \frac{a_T}{\bar{c}}$$

Herein, a_T is the moment arm of the thrust with respect to the center of gravity as illustrated in figure 49a. The coefficient C_{m_R} is defined as the ram drag contribution to the pitching moment coefficient, i.e.

$$C_{m_R} = \frac{\ell_z \cdot D_R}{qS\bar{c}}$$

The distance ℓ_z is the height of the center of the inlet above the center of gravity, and is (see fig. 49a for the definition of a_T and ℓ):

$$\ell_z = \ell\alpha \quad a_R$$

Because

$$D_R = \frac{2\left(fg\sqrt{\rho_j A_1}\right)}{g\sqrt{\rho S}}\sqrt{\frac{qS}{T}} \cdot T$$

the pitching moment coefficient contribution from the ram drag becomes

$$C_{m_R} = \left(\frac{\ell}{\bar{c}}\alpha - \frac{a_R}{\bar{c}}\right)\frac{2\left(fg\sqrt{\rho_j A_1}\right)}{g\sqrt{\rho S}}\sqrt{\frac{T}{qS}}$$

Results of $C_{m_{aero}}$ are presented in figures 49b through d for various nozzle angles and C_T values.

Similar to the presentation of aerodynamic lift and drag, the difference between the values for $C_T = 0$ and $C_T > 0$ is due to the power effect on the aerodynamic moment, and is presented separately in figure 49f, non-dimensionalized, using the form

$$\frac{\Delta M_{aero}}{T\bar{c}} = \frac{\Delta C_{m_{aero}}\, qS\bar{c}}{T\bar{c}} = \frac{\Delta C_{m_{aero}}}{C_T}$$

In the numerical treatment, the following geometric quantities have been used:

$$\frac{\ell}{\bar{c}} = 1.32\ , \frac{a_R}{\bar{c}} = 0.39$$

δ_N	80	90	103	120
$\frac{a_T}{\bar{c}}$	0.227	0,157	0.077	-0.058

The values for $a_T/\bar{c}$ were determined using thrust inclinations θ_j (as opposed to δ_N) and using thrust displacements $r/\bar{c}$, both as tabulated in the calibration section.

Stability

Longitudinal tail-on stability characteristics as a function of the inverse of the thrust coefficient are presented in figure 50a, showing a forward shift of the aerodynamic center when speed is decreased (given a constant thrust level). For comparison, tail-off aerodynamic center locations are presented in figure 50b, revealing a much lesser AC shift. The tail contribution in stability is given in figure 51a showing a large decrease of its effectiveness which is responsible for the forward shift in the tail-on case.

In general the pitching moment curves are quite nonlinear. The nonlinearity is probably due to early local wing upper surface flow separations at positive angles of attack, and early wing lower surface flow separations at negative angles. This may be caused by large flow non-uniformity due to power effects and by low Reynolds numbers. In many instances it appeared impossible to read reliable slopes and corresponding points have been deleted from figure 50. Examples of cases where slopes have been read or where it was possible to isolate the tail contribution in stability are presented in figures 51b, c, and d. These figures cover nozzle angles of zero and 90 degrees, and C_T values of zero to about 8. The slopes were consistently read at $\alpha \geq 2$ degrees, and care was taken to exclude conditions where the tail was stalled.

Stability changes with power were also computed for comparison with test data. The computations were made for the tail-off case for selected nozzle angles, and results are included in figure 50b. The computation is based on the assumption that the AC shift is caused only by inlet momentum effects. The equations are derived as follows: From

$$C_{m_R} = \left(\frac{\ell}{\bar{c}}\alpha - \frac{a_R}{\bar{c}}\right) 2 \frac{\left(fg\sqrt{\rho_j A_1}\right)}{g\sqrt{\rho S}} \sqrt{\frac{T}{qS}} \frac{\ell}{\bar{c}}$$

it follows that

$$\Delta \frac{dC_m}{d\alpha} = 2 \frac{\left(fg\sqrt{\rho_j A_1}\right)}{g\sqrt{\rho S}} \sqrt{\frac{T}{qS}} \frac{\ell}{\bar{c}}$$

where T is the total exhaust thrust of two fans. The lift curve slope without interference is

$$\frac{dC_L}{d\alpha} = \frac{d\left[T \sin(\theta_j + \alpha) + C_{L_{op}} qS\right]}{qS \cdot d\alpha_{rad}} = C_{L_{\alpha_{op}}} + \frac{T}{qS} \cos(\theta_j + \alpha)$$

so that the aerodynamic center shift becomes (positive for a forward shift):

$$\Delta \frac{dC_m}{dC_L} = \frac{2\left(\frac{fg\sqrt{\rho_j A_1}}{g\sqrt{\rho S}}\right) \cdot \frac{\ell}{\bar{c}} \sqrt{\frac{T}{qS}}}{C_{L_{\alpha_{op}}} + \left(\frac{T}{qS}\right) \cos\left(\theta_j + \alpha\right)} = \frac{2\left(\frac{fg\sqrt{\rho_j A_1}}{g\sqrt{\rho S}}\right) \cdot \frac{\ell}{\bar{c}} \sqrt{\frac{qS}{T}}}{C_{L_{\alpha_{op}}} \frac{qS}{T} + \cos\left(\theta_j + \alpha\right)}$$

In figure 50b this shift was added to experimentally obtained power-off locations. (The power-off locations are indicated at $qS/T = \infty$).

The large difference between the above computed AC locations and the experimentally obtained locations shown in this figure for $\delta_N = 90°$ may result from a positive pressure field just ahead of the nozzle exhaust; see sketch below. However, no pressure measurements were made that could verify this.

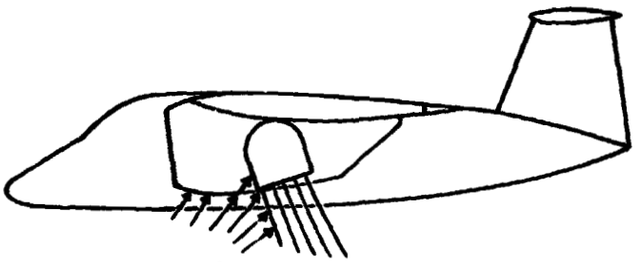

Positive pressures (+)

Note that moment characteristics presented in the form $M/(T\bar{c})$ can be converted to regular coefficient form using

$$C_m = \frac{M}{q S \bar{c}} = \frac{\left(\frac{M}{T\bar{c}}\right)}{\left(\frac{qS\bar{c}}{T\bar{c}}\right)} = \frac{\left(\frac{M}{T\bar{c}}\right)}{(qS/T)} = \left(\frac{M}{T\bar{c}}\right) \cdot C_T$$

$$C_{m_\alpha} = \frac{d\left(\frac{M}{T\bar{c}}\right)}{d\alpha} \cdot C_T$$

$$\frac{dC_m}{dC_L} = \frac{C_{m_\alpha}}{C_{L_\alpha}} = \frac{\frac{d\left(\frac{M}{T\bar{c}}\right)}{d\alpha} \cdot C_T}{\frac{d\left(\frac{L}{T}\right)}{d\alpha} \cdot C_T} = \frac{d\left(\frac{M}{T\bar{c}}\right)}{d\left(\frac{L}{T}\right)}$$

Downwash and Tail Effectiveness

A downwash correlation is presented in figure 52a for various nozzle angles and C_T values. They are generally obtained at intersections of tail-off and tail-on pitching moments to avoid inaccuracies due to interpolations of nonlinear data.

The theoretical downwash shown in this figure is based on a jet flap theory with full span blowing and with the downwash located at an infinite distance behind the wing. Calling w_i the vertical velocity at infinity of a stream tube with diameter b representing the virtual mass, the following is obtained:

$$w_i\left(\rho v \pi \frac{b^2}{4}\right) + T \sin \epsilon = L$$

or

$$\frac{w_i}{v}\left(\frac{1}{2}\rho v^2 \pi \frac{b^2}{S} \cdot S\right) + 2T \sin \epsilon = 2L$$

where ϵ is the downwash with respect to the free stream direction. Substituting for small angles:

$$\frac{w_i}{v} = \tan \epsilon \approx \epsilon$$

$$\sin \epsilon \approx \epsilon$$

the above relation becomes

$$\epsilon = \frac{2C_L}{\pi AR + 2C_T}$$

or, in non-conventional form:

$$\epsilon = \frac{2L/T}{\left(\frac{qS}{T}\right)\pi AR + 2}$$

Considerable scatter of experimental data points exists about this theoretical relation. However, the theory is a simplification and is not really applicable for vectored thrusts at discrete points along the span. Also, the average value of the downwash is somewhat larger than the theory indicates which may be due to the wing twist.

Perhaps a better correlation is obtained by removing the direct thrust contribution T.sin ($\delta_N + \alpha$) from the correlation, see figure 52b. This curve leads to a downwash due to circulation lift, plus a downwash increment $\Delta\epsilon$ due to interaction of the jet exhaust with the surrounding flow, figure 52c, i.e.

$$\epsilon = \left(\frac{d\epsilon}{dC_L}\right)_{aero} \cdot C_{L_{aero}} + \Delta\epsilon$$

Herein, the circulation lift $C_{L_{aero}}$ includes power effects on the circulation.

The tail effectiveness $\partial Cm/\partial i_H$ is given in figure 53 showing an increase with C_T as may be expected from an increased velocity due to entrainments into the exhaust flow.

Aircraft Modifications

Modifications to the basic vectored thrust aircraft configuration were tested as part of this investigation. These modifications were an externally blown flap (EBF) with flaps extended but with $\delta_N = 0$, a hybrid configuration (asymmetric nozzle deflections), a configuration using nozzle exhaust vanes, and a configuration having a fuselage strake box. The EBF and hybrid are illustrated in figure 54 along with the vectored thrust concept. Detail information of the vanes and the strake box are given in figures 13 and 14a respectively. Basic data are in figures 38a, 55, 56 and 57.

Test data pertaining to externally blown flaps (EBF) from figure 38a are analyzed in terms of the lifting capability L/T versus nozzle angle for conditions where a net forward thrust or zero thrust exists, see figure 58a. This is done to investigate only conditions of interest for takeoff. At low nozzle angles, the lift is limited by stall while $D/T < 0$. At high nozzle angles the lift is limited by $D/T = 0$. Results are plotted in figure 58b. At each point a different angle of attack exists. Without making a complete analysis it appears from figure 58b that at $C_T = 4$ the vectored thrust concept ($\delta_N > 20°$) yields better lifting capabilities, whereas at $C_T = 2$ the externally blown flap (EBF, $\delta_N < 20°$) shows promise (a complete analysis would require the application of flight safety margins not considered here). In selecting the points for zero or forward acceleration the ram drag was included in the drag.

Application of thrust deflectors for the EBF configuration did not increase the maximum lift (fig. 58c). The deflectors used were considered to be formed by double fold-out landing gear doors and may not have had the optimum shape, size, or location.

The hybrid configuration is defined as having half the nozzles deflected downward for lift and half deflected aft for external blowing and thrust. It yields an L/T value of 1.33 at $C_T = 3.19$ (D/T = 0), but does not have enough thrust at $C_T = 1.57$ to achieve D/T ≤ 0, see figure 55. Comparison with the EBF concept in figure 58b shows the hybrid configuration to be inferior.

The effect of exhaust vanes as compared to regular nozzles without vanes is presented in figure 59 for flow angles of about 60° and for flow angles of 90° to 100°. The data are obtained from figure 56. Only a negligible affect on C_L is shown for about 60°, but for about 100° a decrease in lift is shown with vanes at low μ, and an increase at high μ. However, the comparison is made at equal fan operating conditions using the speed ratio $\mu = v_T/v$ rather than on the basis of equal C_T values. This is done because it was not possible to calibrate the thrust with vanes because of their physical interference with calibration shields. In this way it is not necessary to know the accurate thrust for the presentation of the data.

Strake box effects are presented in figure 57, showing an increase in maximum lift, as well as an increase of lift at zero angle of attack. An increase in lift is even found for conditions of equal drag.

LONGITUDINAL DATA FOR TRANSITION IN GROUND EFFECT

Longitudinal forces and moments in ground effect and as a function of power are presented in figures 60 through 65 for nozzle angles of 0° through 103°. In addition, data for fuselage strakes are given in figure 66. All data pertain to wings level conditions.

Lift coefficients are presented in figures 67a, and b for $h/d_e = 1.0$ and $\alpha = 0$, and in figure 67c for $\alpha = 4°$. Comparison with figure 47b for $\alpha = 4°$ shows the lift in ground effect to be lower than out of ground effect.

The addition of parallel strakes shows an increase in lift in all cases tested (fig. 66a, b, and c). A larger increase in lift is obtained using the strake box in close proximity to the ground, as indicated in the same figure.

The tail-off aerodynamic enter for $\delta_N = 62°$ is shifted aft by the ground (fig. 68). At $\delta_N = 90°$ the effect is difficult to determine at low speeds because of the small lift change involved when the aircraft is rotated.

Downwash data are summarized in figure 69, showing that ϵ is reduced when the nozzle angle is increased from 0° to 90°. The quanties ΔM and ΔC_m in this figure pertain to the difference in pitching moment due to the tail.

LATERAL-DIRECTIONAL DATA AT FORWARD SPEEDS

Lateral-directional data were acquired on a limited basis using a relatively small range of sideslip angles. Larger sideslip angles required a different model support sting which was outside the scope of the present investigation. All data pertain to zero bank angle conditions.

Basic lateral-directional test data are presented in figure 70 for power-off conditions with zero nozzle angle, and in figure 71 with power and various nozzle angles (0°, 62°, and 90°). They pertain to tail on and off conditions, all out of ground effect. Figure 72, however, contains basic data with ground effect. All data are given in the stability axis system.

The data are given in the customary coefficient form for $C_T = 0$ to about 4, as well as in the form non-dimensionalized by T or Tb for $C_T = 2$ to about 50. Conversion between the two forms is readily accomplished by using:

$$C_n = \frac{\left(\frac{N}{Tb}\right)}{\left(\frac{qS}{T}\right)} = \left(\frac{N}{Tb}\right) C_T$$

$$C_l = \frac{\left(\frac{M_R}{Tb}\right)}{\left(\frac{qS}{T}\right)} = \left(\frac{M_R}{Tb}\right) C_T$$

$$C_y = \frac{\left(\frac{Y}{T}\right)}{\left(\frac{qS}{T}\right)} = \left(\frac{Y}{T}\right) C_T$$

Similarly, slopes with respect to sideslip angles are converted using

$$C_{n_\beta} = \frac{N_\beta}{Tb} \cdot C_T$$

$$C_{l_\beta} = \frac{dM_R/d_\beta}{Tb} \cdot C_T$$

$$C_{Y_\beta} = \frac{Y_\beta}{T} \cdot C_T$$

Analysis plots of directional stability, out of ground effect, are presented in figures 73 and 74. Tail-on as well as tail-off data are shown. In the case of the tail-off data both the horizontal and vertical tails are removed.

Generally, power decreases the directional stability when changing δ_N from 0° to 62°. At 62° even the tail-on aircraft becomes unstable. At this angle C_{n_β} can even become relatively large in the unstable direction when C_T is high (fig. 74a, top). However, this value is large not so much because of a large instability, but because of the low dynamic pressure used for reference at the high C_T values. To obtain a true impression of the magnitude of instability the value of C_{n_β} should be multiplied by a term containing that dynamic pressure:

$$N_\beta = \left(\frac{N_\beta}{qSb}\right) qSb$$

When non-dimensionalized by thrust (which is always high at low speed), this becomes:

$$\frac{N_\beta}{Tb} = \left(\frac{N_\beta}{qSb}\right)\frac{qSb}{Tb} = C_{n_\beta} \cdot \frac{q}{T/S}$$

It is seen in figure 74a, bottom, that at $C_T = 9$ the value of N_β is only about -0.0001 (Tb) per deg, which represents only a slight instability in this tail-on case.

Contrary to the above characteristics for $\delta_N = 62°$, at $\delta_N = 90°$ the aircraft is generally directionally stable, tail-on, and even stable at $C_T = 4$ with the tail off; see figure 74b. Tests were repeated and verified these characteristics. It is surmised that the model exhausts act, in this case, as a wall in front of which a positive pressure may build up. This build-up may be greater at the windward side than at the lee side, which then contributes to a positive stability; see sketch below. However, no pressure measurements were made in this area of the model, nor were flow visualizations attempted that may have substantiated this pattern.

When the exhaust flow is bent backwards due to higher free stream dynamic pressure, such as at $C_T = 2$, this phenomenon disappears. Similarly, when the flow is bent backwards due to ground proximity, this characteristic also disappears; see figure 74c.

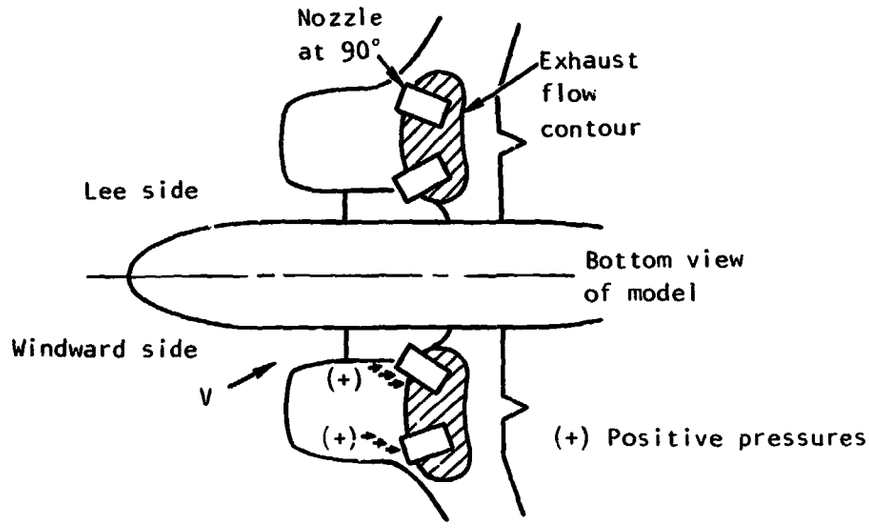

The above variation with C_T, out of ground effect, is relatively unaffected by the tail except for a general shift in stable direction. The tail contributions in directional stability are about the same for $\delta_N = 90°$ as for $\delta_N = 62°$. The tail effectiveness increases moderately with C_T; see figure 74d.

A component breakdown, tail-off, for directional stability with power is now given for $\delta_N = 62°$ for analysis purposes. The stability can be broken down into a power-off portion, inlet momentum effects, and interference effects. The power-off portion is obtained directly from test data for $C_T = 0$ (fans windmilling). Expressed in coefficient form it was found that

$$C_{n_{\beta_{op}}} = -0.0006 \text{ deg}^{-1}$$

Thus, for any given thrust, the actual power-off yawing moment increases with q according to

$$\frac{N_{\beta_{op}}}{Tb} = C_{n_{\beta_{op}}} \frac{q}{T/S} = -0.0006 \frac{q}{T/S}$$

The inlet momentum effect is derived theoretically. This is carried out as follows, using the geometric definitions of figure 75a.

The moment arm of the center of the inlet of the left fan engine is:

$$\ell_1 = a_N \cos(\chi + \beta)$$

Calling D_R the total inlet momentum drag of both fans, then the contribution of the left engine only is:

$$\Delta N_1 = -\frac{D_R}{2}\ell_1 = \frac{D_R}{2}\, a_N \cos(\chi+\beta)$$

Similarly, for the right hand fan:

$$\ell_2 = a_N \cos(\chi-\beta)$$

$$\Delta N_2 = -\frac{D_R}{2}\ell_2 = -\frac{D_R}{2}\, a_N \cos(\chi-\beta)$$

The total moment increment ΔN due to ram drag becomes:

$$\Delta N = \frac{D_R}{2}\, a_N \left[\cos(\chi+\beta) - \cos(\chi-\beta)\right]$$

so that (per radian):

$$\Delta N_\beta = \frac{d\Delta N}{d\beta} = \frac{D_R}{2}\, a_N \left[-\sin(\chi+\beta) - \sin(\chi-\beta)\right]$$

For $\beta = 0$, this yields

$$\Delta N_\beta = -D_R\, a_N \sin\chi = -D_R\,\ell$$

Substituting

$$D_R = \frac{2\left(fg\sqrt{\rho_j A_1}\right)}{g\sqrt{\rho S}}\sqrt{\frac{qS}{T}}\,T$$

the increment in stability due to inlet momentum effects becomes then

$$\frac{\Delta N_\beta}{Tb} = -2\,\frac{\left(fg\sqrt{\rho_j A_1}\right)}{g\sqrt{\rho S}}\,\frac{\ell}{b}\,\sqrt{\frac{q}{T/S}}\ \text{rad}^{-1}$$

Herein is to be used:

$$\left(fg\sqrt{\rho_j A_1}\right) \approx 1.11\ \frac{N/\sec}{\sqrt{N}}\ \left(= 0.524\ \frac{lb/\sec}{\sqrt{lb}}\right)$$

The power-off portion as well as the inlet momentum effect is plotted in figure 75b, both labeled "computed". Comparison of the sum of these

two portions with power-on test data shows that no significant difference exists between test and computation at that nozzle angle, indicating that interference effects on yawing moment are negligible in this tail-off case.

Similar analyses were made for the side force derivative with respect to β and for the dihedral effect. The side force characteristics are shown in figure 75c. It is seen that the total derivative is larger than the sum of the power-off portion and the computed inlet momentum effect. This indicates the existence of a power-on interference effect in side force.

Herein, the computation of the power-off portion is made using

$$\frac{Y_{\beta_{op}}}{T} = C_{y_\beta} \frac{qS}{T} = C_{y_{\beta_{op}}} \left(\frac{1}{C_T}\right) = -0.0092 \left(\frac{1}{C_T}\right)$$

and the inlet momentum effect is obtained using:

$$\Delta y = -D_R \cdot \beta$$

$$\frac{\Delta Y_\beta}{T} = \frac{\Delta dY/d\beta}{T} = -\frac{D_R}{T} = \frac{-2\left(fg\sqrt{\rho_j A_1}\right)}{g\sqrt{\rho S}} \sqrt{\frac{qS}{T}} \text{ rad}^{-1}$$

The dihedral effect is presented in figure 75d for zero nozzle angle, and in figure 75e for nozzle angles of 62° and 90°. It is seen that the ram drag contribution is relatively small, and that also the interference effects are small compared to the basic power-off dihedral effect. Herein, the power-off portion is computed from (assuming the thrust is finite and given)

$$\left(\frac{C_{R}/d\beta}{Tb}\right)_{op} = \frac{C_{\ell_{\beta_{op}}} qSb}{Tb} = C_{\ell_{\beta_{op}}} \left(\frac{1}{C_T}\right)$$

while the inlet momentum effect is based on

$$\frac{\Delta dM_R/d\beta}{Tb} = \frac{+\ell_z \Delta y_\beta}{Tb} = \frac{-\ell_z}{b}\left(\frac{D_R}{T}\right) = \frac{-\ell_z}{b} \frac{2\left(fg\sqrt{\rho_j A_1}\right)}{g\sqrt{\rho S}} \sqrt{\frac{qS}{T}} \text{ rad}^{-1}$$

Herein, ℓ_z is the location of the center of the inlets above the center of gravity. In the present case ℓ_z/b is equal to -0.0476 (at zero angle of attack).

CONCLUSIONS

A powered wind tunnel model of a V/STOL transport aircraft with two fans for vectored thrust was tested. The major conclusions of the data analysis are:

Interference lift losses in hover near the ground are about 10% of the nozzle thrust. This loss can be reduced to only 5% when the nozzle exhaust walls are extended somewhat so as to shield the nacelles from exhaust flow interference.

The lift losses increase when the aircraft is banked, as well as when roll control is applied (in the direction against the bank) by increasing the nozzle thrust on one side and decreasing it on the other.

In the transition speed range interference lift losses of only 7% of the nozzle thrust were encountered ($\delta_N = 90°$, $\alpha = 4°$, no strakes) which is significantly less than was found with a previously tested twin-jet VTOL model (ref. 4). The loss can be further reduced by employing a strake box.

The lift characteristics can be enhanced by rotating all nozzles fully aft for external flap blowing, provided that the speed is high enough so that C_T is less than approximately 2. However, a hybrid configuration with half the nozzles deflected downward and half deflected aft was not as promising.

Power effects decreased the directional stability at a nozzle angle of 62°, but showed an increase in directional stability at 90°.

The twin fan vectored thrust concept is a feasible concept for a V/STOL transport aircraft in terms of lift and pitching moment characteristics, provided that the lift losses in hover during momentary banked conditions can be accommodated.

The reduction of the lateral control effectiveness due to ground effect in hover is an important consideration; additional roll control tests with nozzle shields and using flow visualization are recommended to investigate the possibility of improving the roll control.

The adequacy of lateral-directional characteristics at forward speeds cannot be fully assessed from the data due to the limited sideslip angles imposed on the test. At low sideslip angles unknown flow phenomena were encountered at high nozzle angles, but the forces and moments were controllable.

Analytical methods for the determination of the inlet momentum effects on the longitudinal and directional stability appeared to adequately describe the whole power effect for tail-off conditions at low nozzle angles. At high nozzle angles, however, additional power effects exist.

REFERENCES

1. J. C. Ford: Three-Engine Two-Fan Navy Multimission V/STOL Aircraft Considerations. SAE 751104, November 1975.

2. J. P. Barrack: Static Thrust Calibration of a 13.98 cm (5.5 in) Tip Turbine Fan with Two Swiveling Nozzles for Thrust Vectoring. NASA TM 73,268.

3. D. J. Renselaer and R. J. Oberto: Jet Effects in Hover of a VTOL Aircraft Model Using Water as a Test Medium. Naval Air Systems Command Research and Technology Group, Procedings of a Workshop on Prediction Methods for Jet V/STOL Propulsion Aerodynamics. Vol. 1, pp. 194-213, Arlington, Va. July 28-31, 1975.

4. R. E. Mineck and M. F. Schwendemann: Aerodynamic Characteristics of a Vectored-Thrust V/STOL Fighter in the Transition-Speed Range. NASA TN D-7191, May 1973.

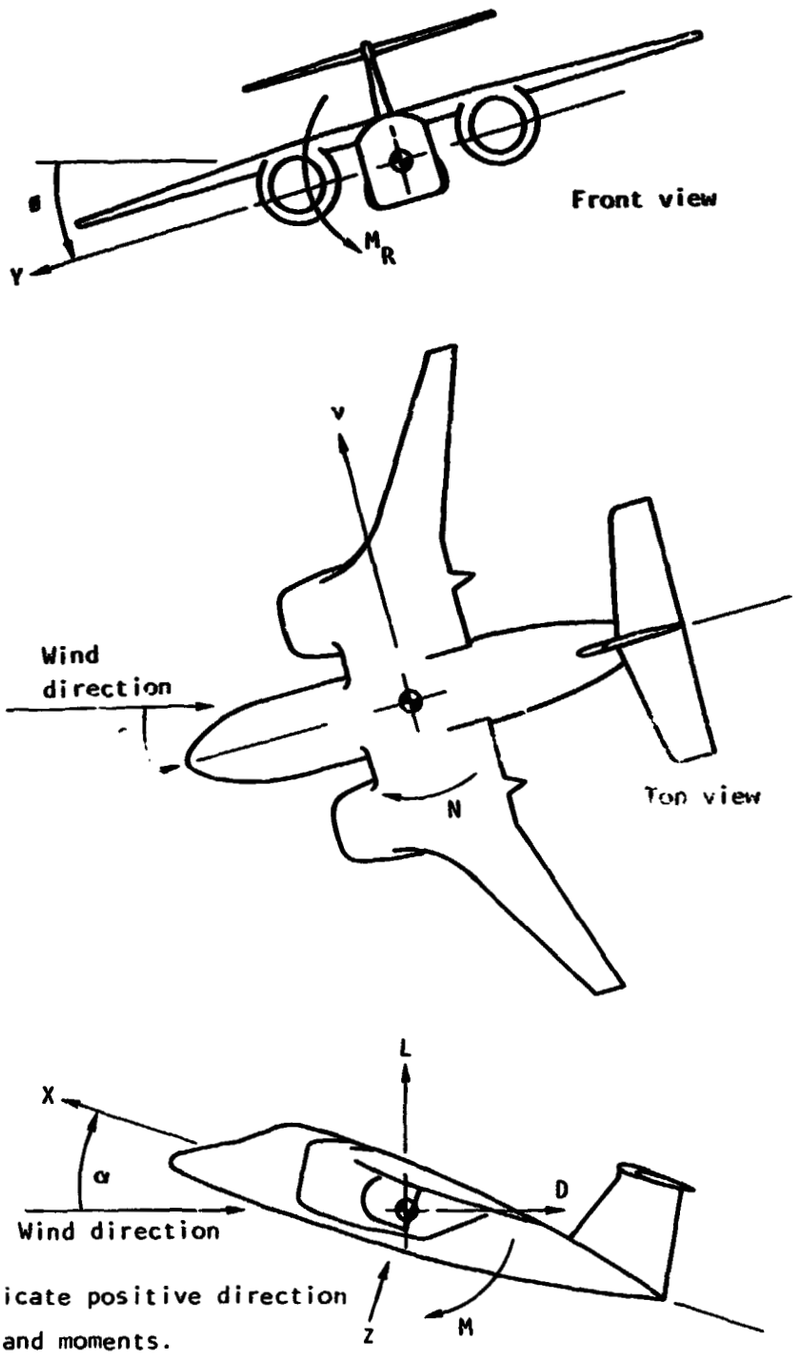

Figure 1. - Axis system.

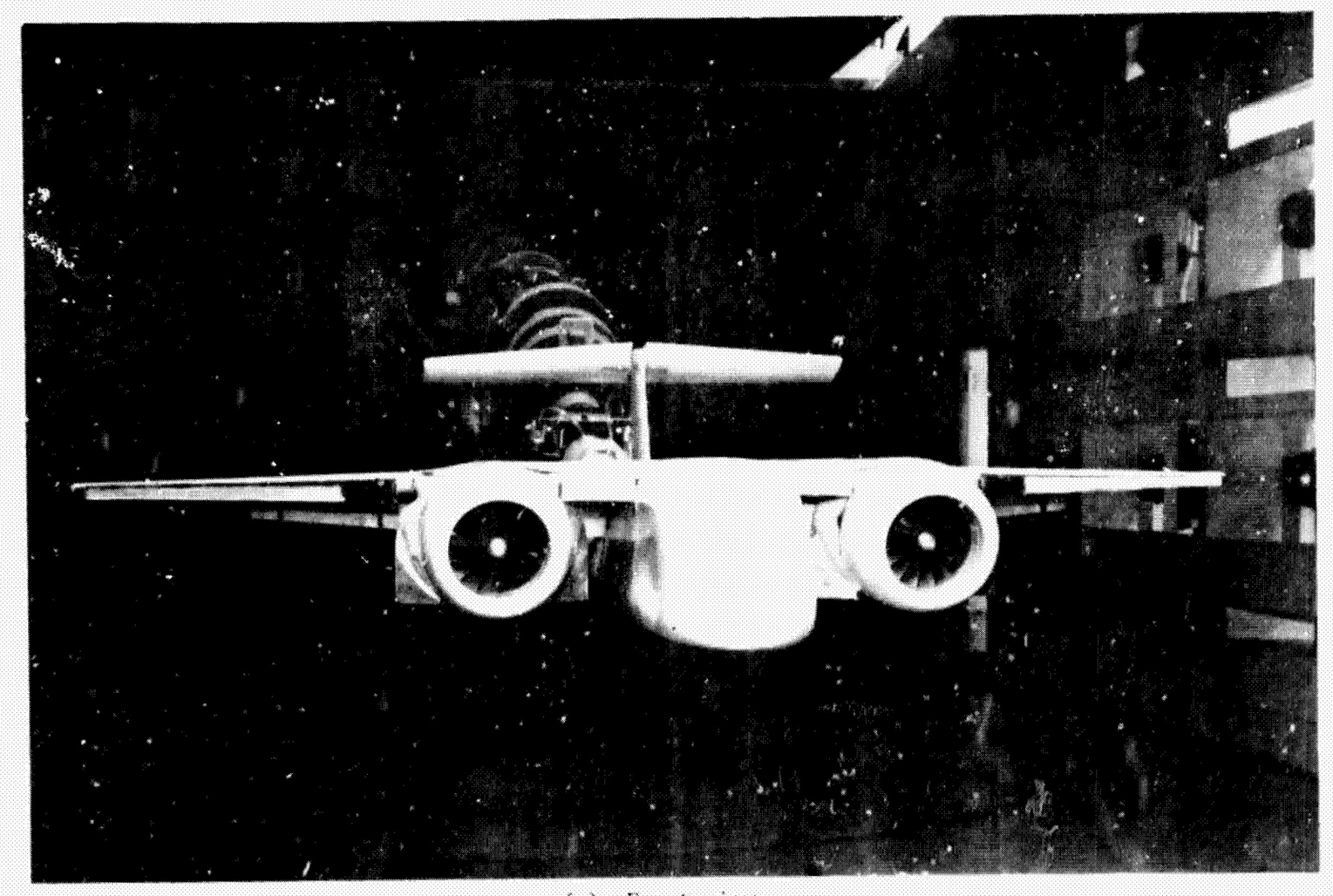

(a) Front view

Figure 2. - Photograph of model.

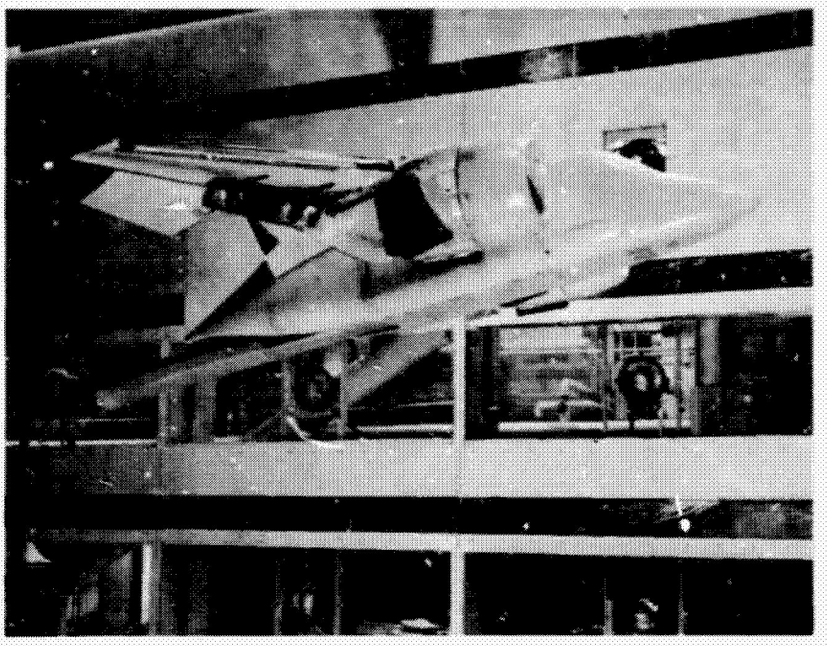

(b) Side view

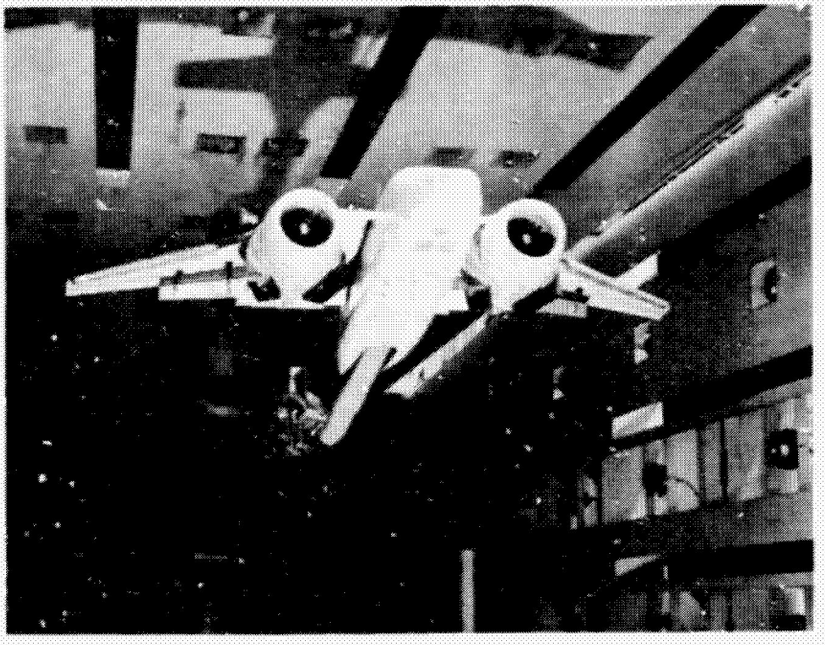

(c) One-fourth lower view

Figure 2. - concluded.

Wing:		
Area	0.3874 m^2	(4.170 ft^2)
Root chord (actual)	35.1 cm	(13.82 in.)
Tip chord at 97.5% span	9.58 cm	(3.769 in.)
$\bar{c}_W$	22.75 cm	(8.958 in.)
Span	186.73 cm	(73.514 in.)
Aspect ratio	9.0	
Root incidence	5.3 deg	
Tip incidence	2.4 deg	
Dihedral at 50% chord	0.0 deg	
Horizontal tail:		
Area	0.1147 m^2	(1.235 ft^2)
$\bar{c}_H$	15.68 cm	(6.173 in.)
Span	74.52 cm	(29.340 in.)
Aspect ratio	4.84	
Vertical tail:		
Area	0.074 m^2	(0.797 ft^2)
$\bar{c}_V$	24.90 cm	(9.805 in.)
Span	30.84 cm	(12.140 in.)
Aspect ratio	1.274	

Dimensions in sketches are in cm (inches)

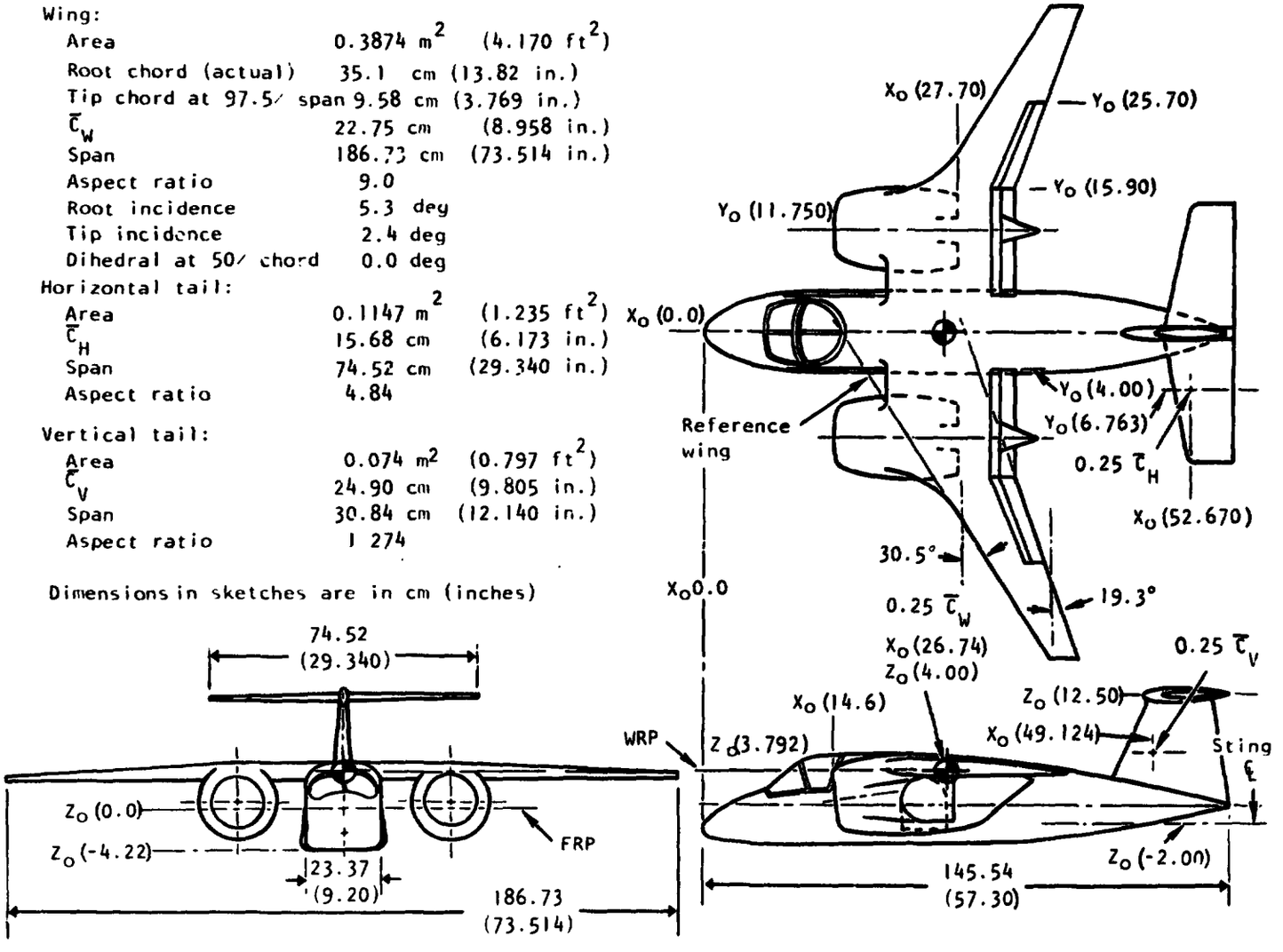

Figure 3. - Three-view of model.

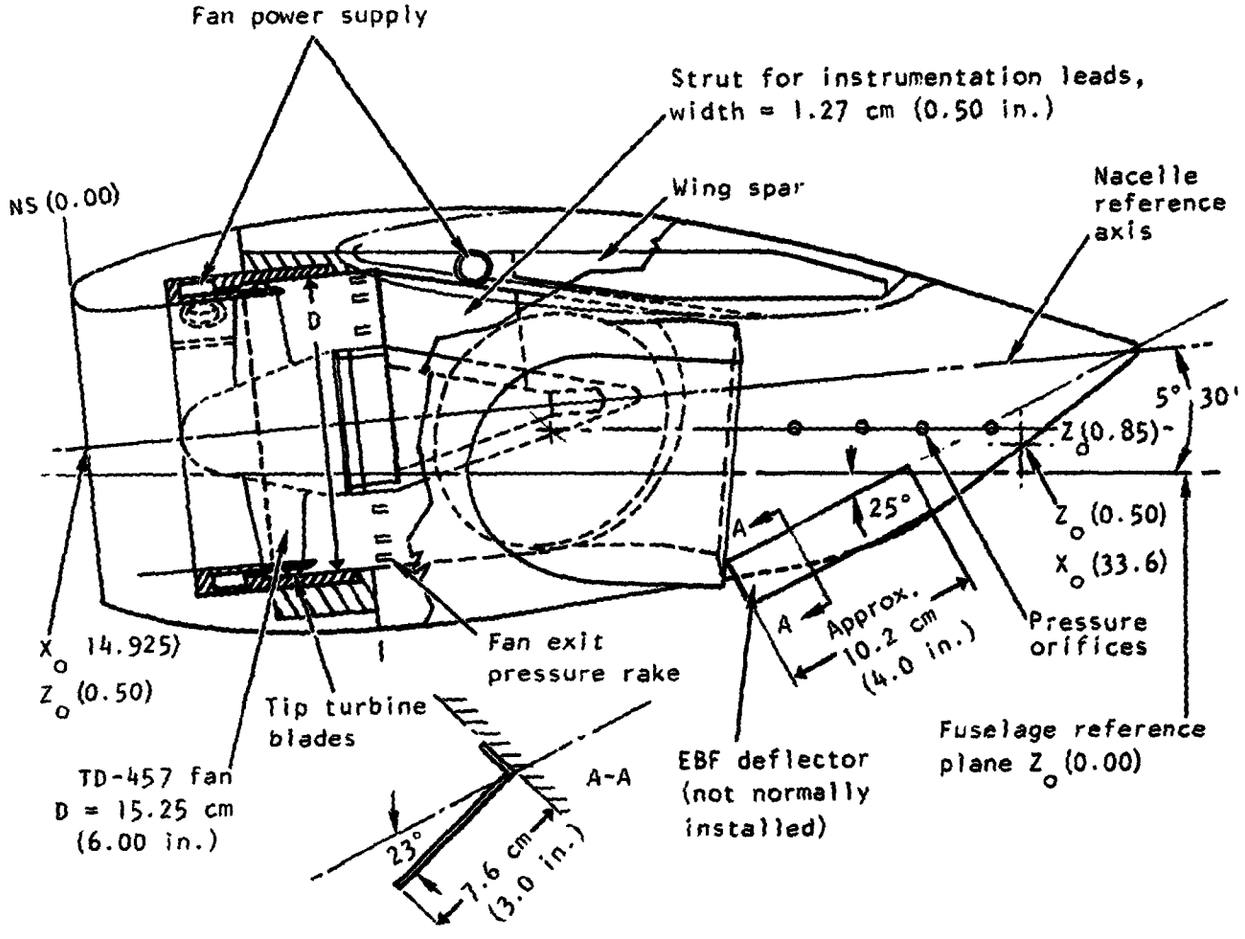

Figure 4. - Nacelle details in side view.

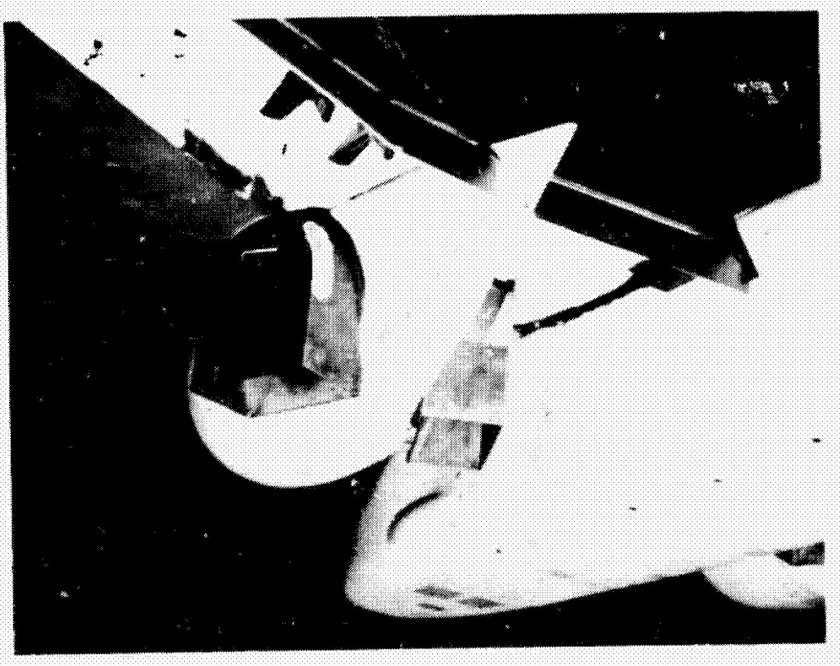

Figure 5. - Photograph of nacelle details.

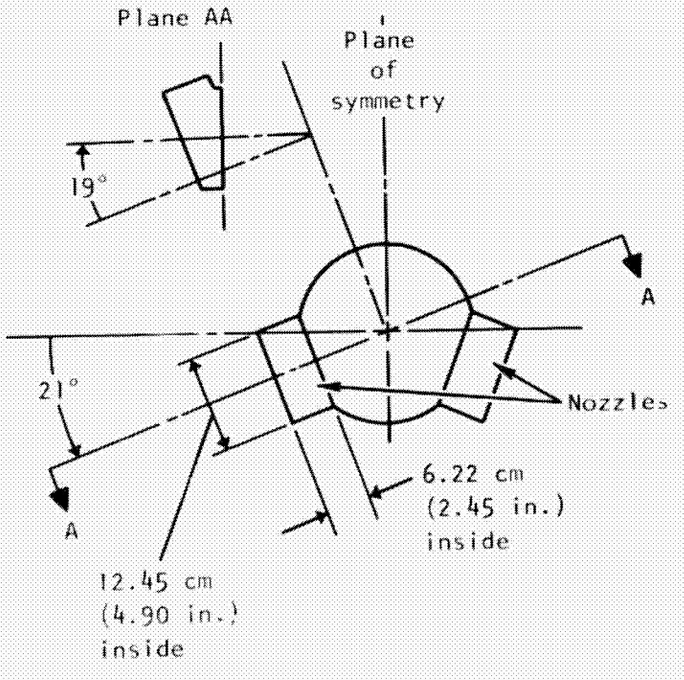

(a) Axes of rotation of nozzles.

Figure 6. - Nozzle angles and nozzle exit locations.

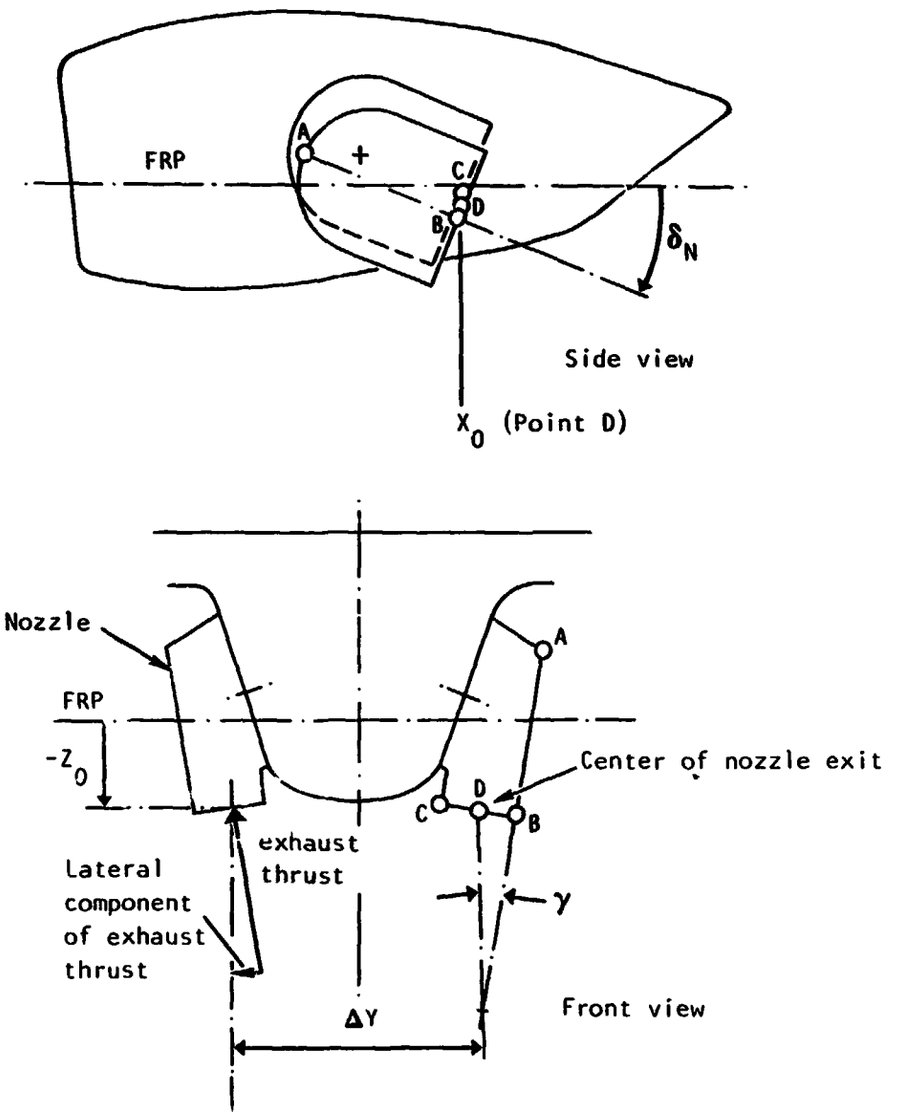

(b) Definition of measured nozzle distances and angles.

Figure 6. - Concluded.

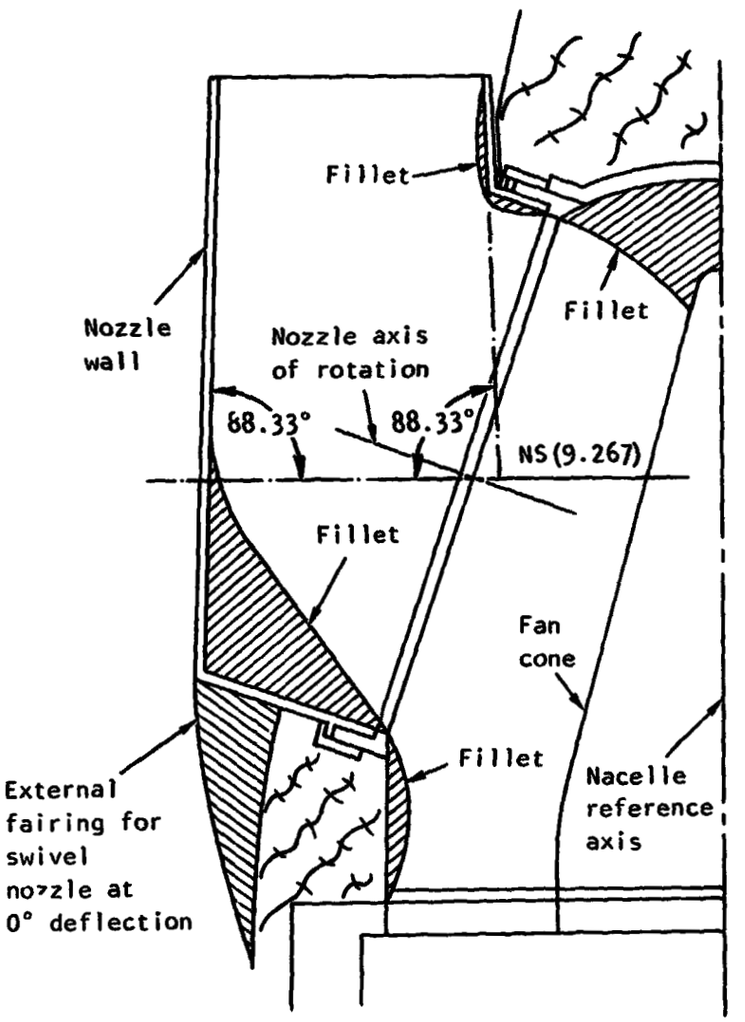

Figure 7. - Ducting details of nozzle.

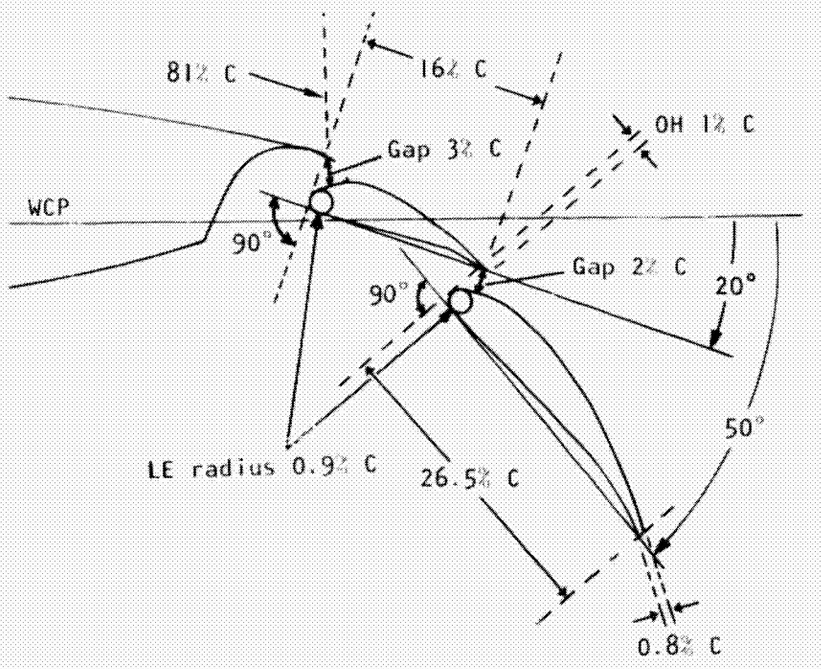

Figure 8. - Flap geometry

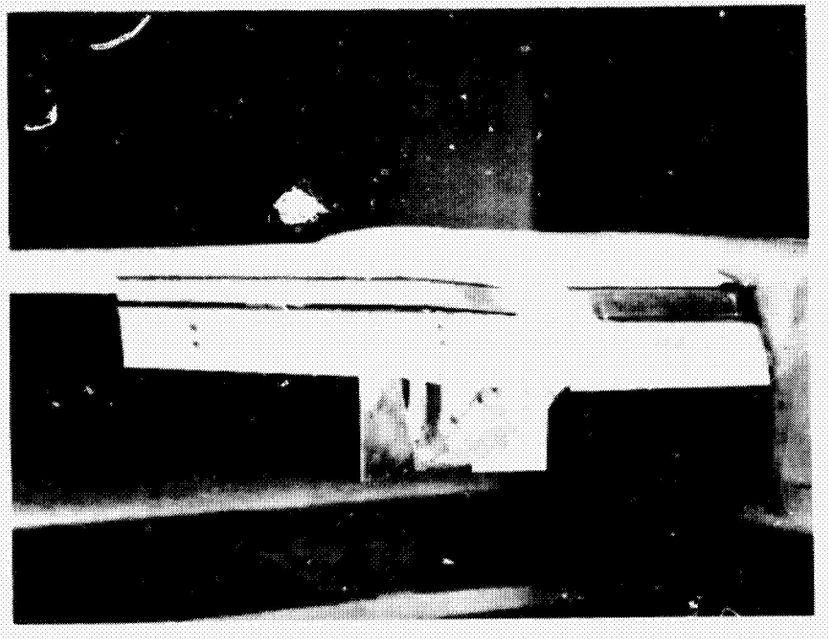

Figure 9. - Photograph of flaps.

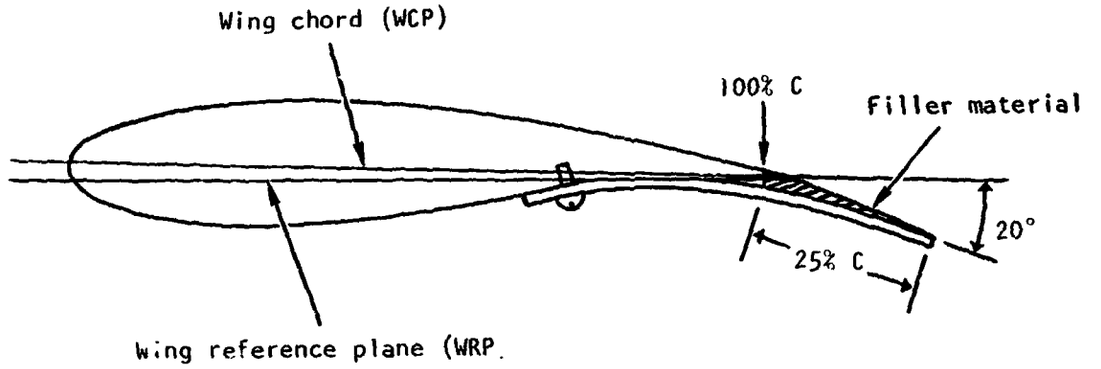

Figure 10. - Drooped and extended aileron.

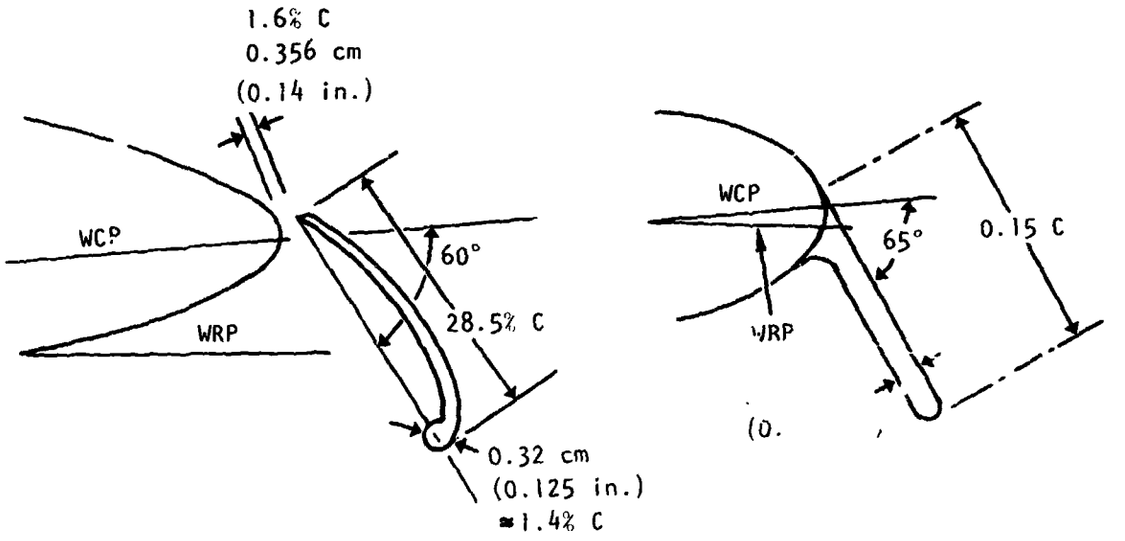

(a) Inboard.

(b) Outboard.

Figure 11. - Leading edge flaps.

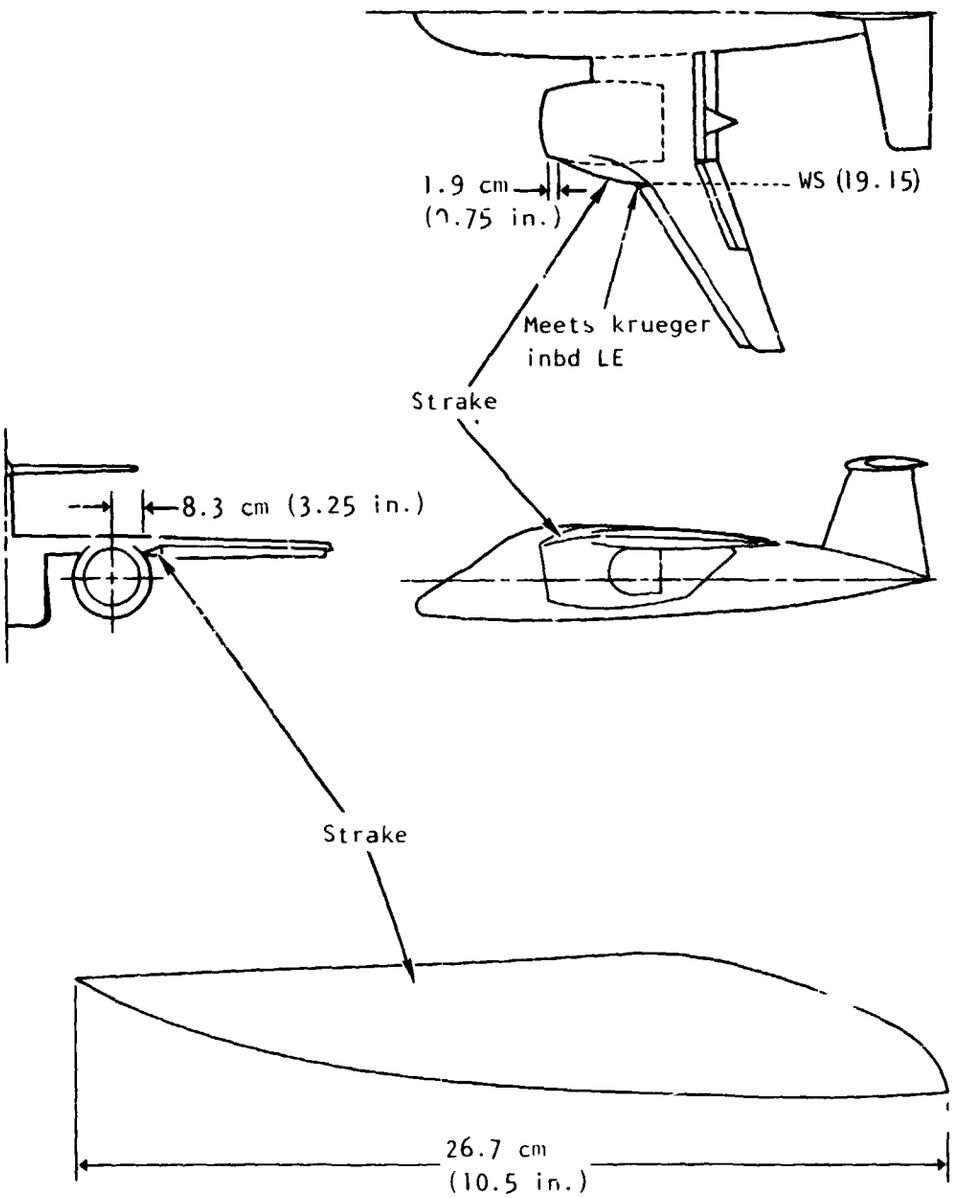

Figure 12. Details of nacelle strakes.

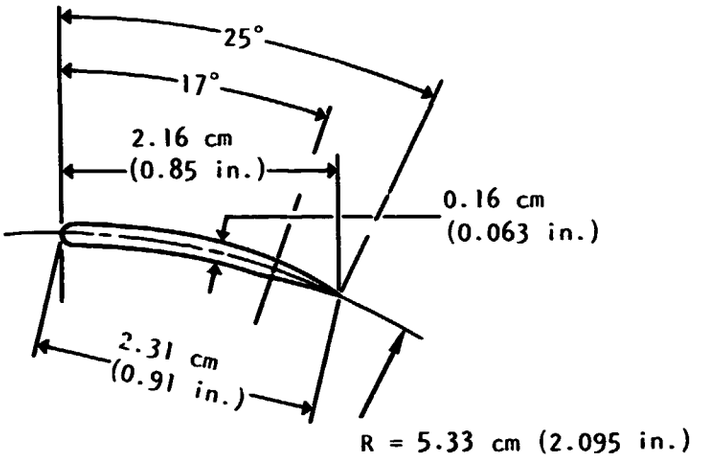

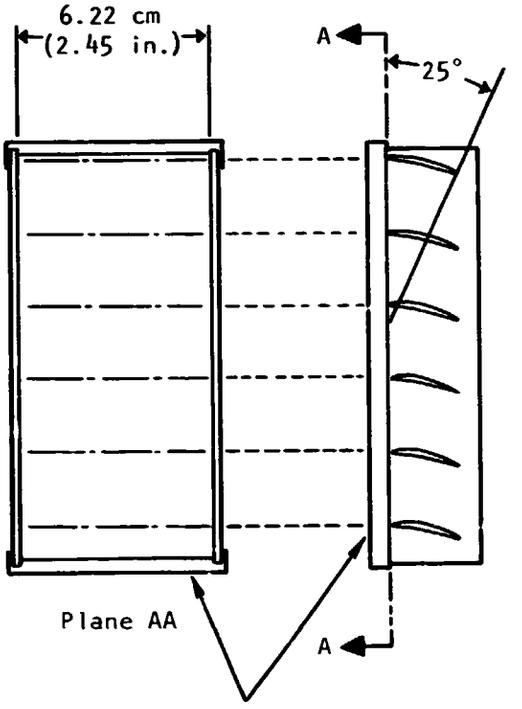

Collar fitting over nozzle walls

Figure 13. - Exhaust vane details.

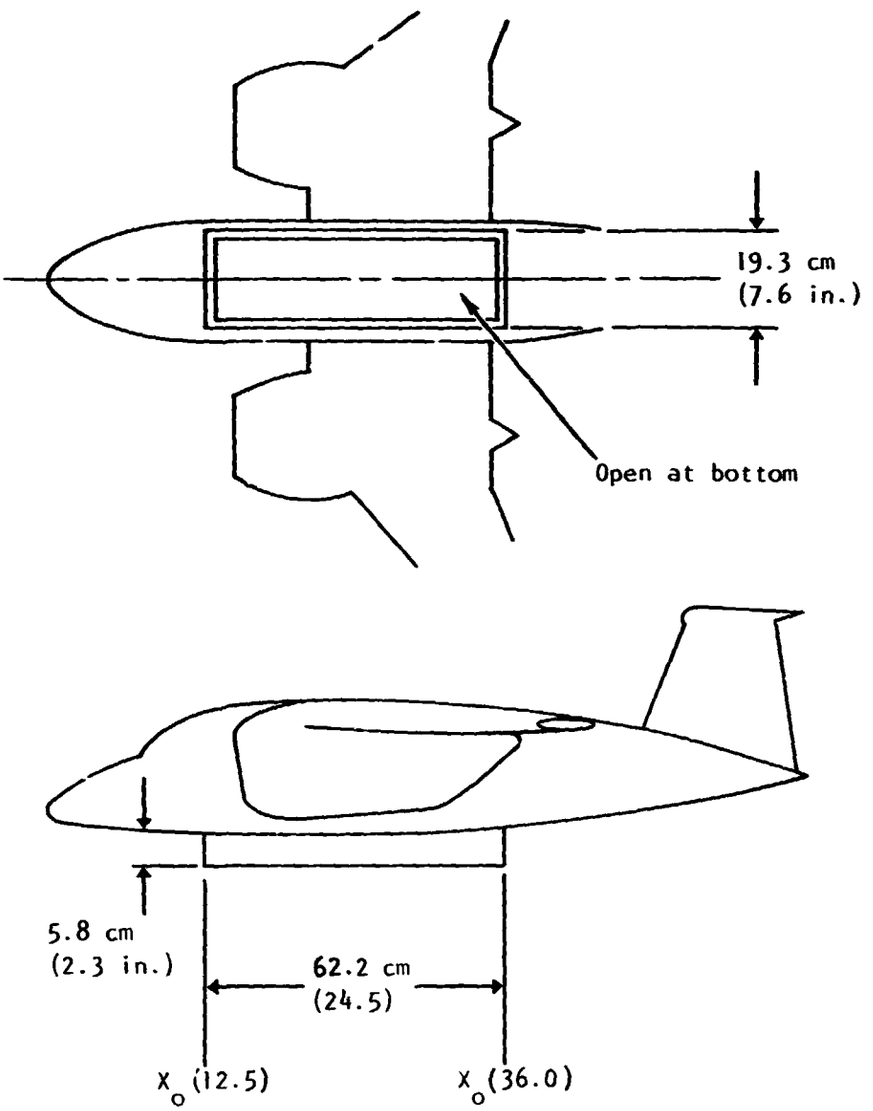

(a) Fuselage strakes.

Figure 14. - Fuselage strakes and exhaust fences.

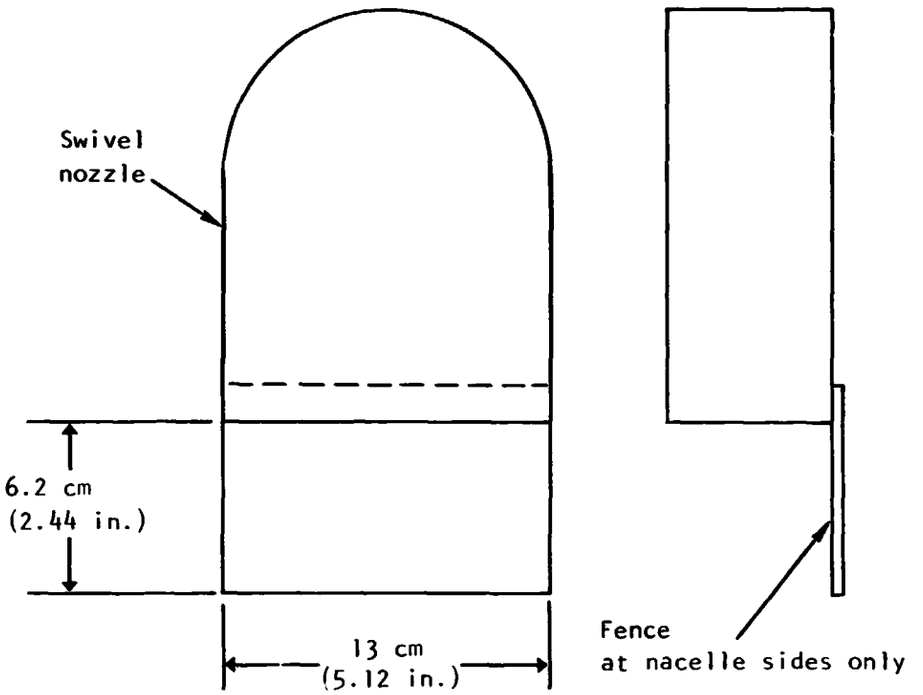

(b) Nozzle exhaust fences.

Figure 14. - Concluded.

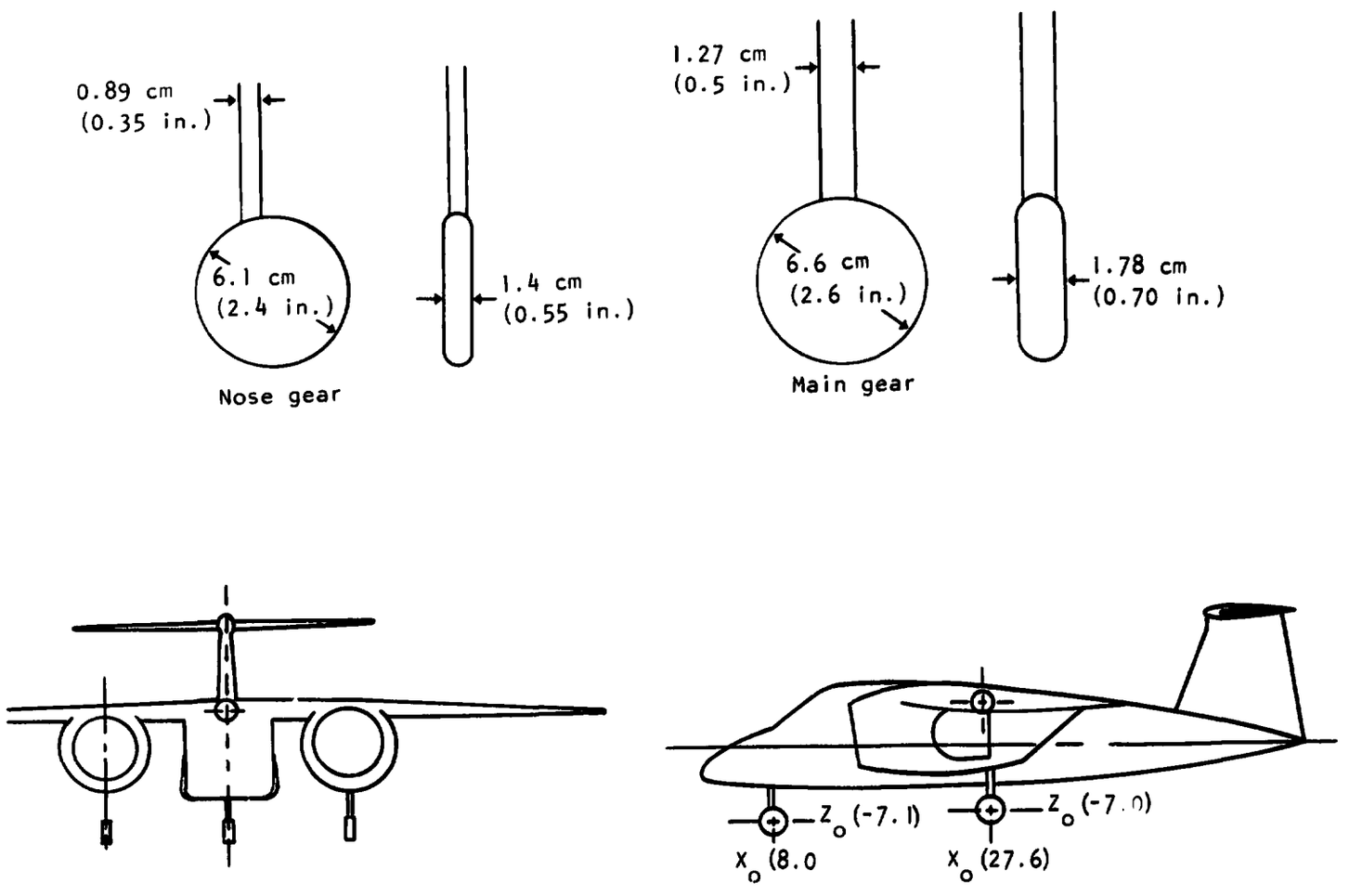

Figure 15. - Landing gear dimensions.

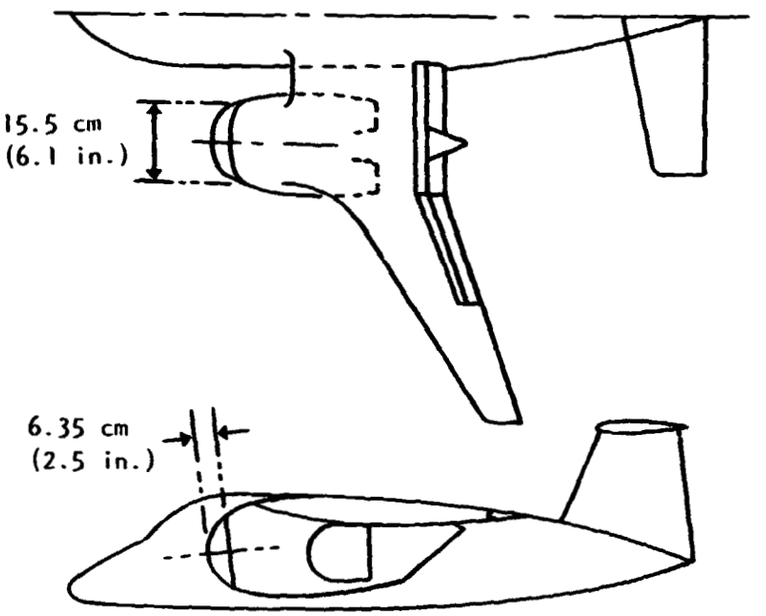

Figure 16. - Fan inlet covers.

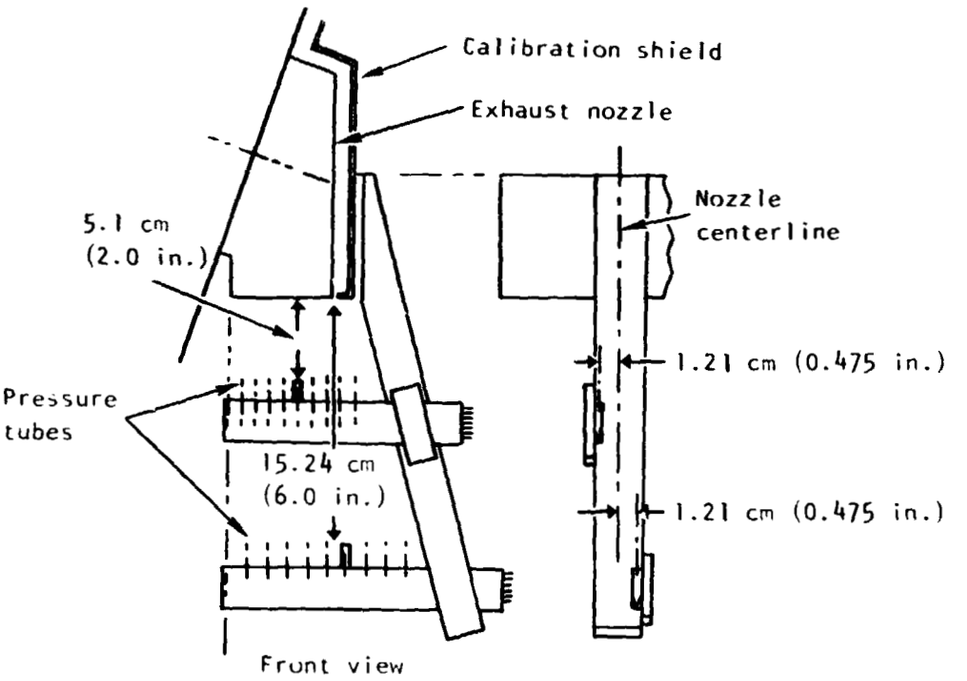

Figure 17. - Exhaust rakes.

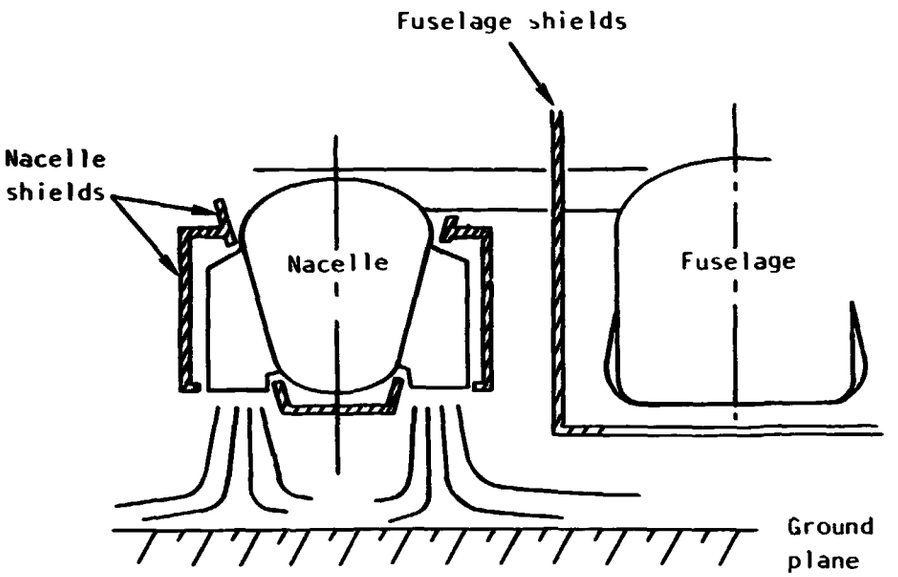

(a) Shields installed

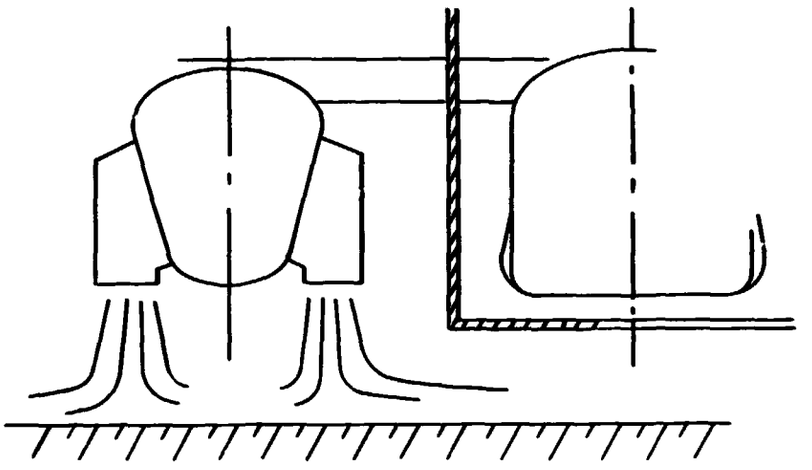

(b) Shields removed

Figure 18. - Schematic of calibration test setup (not to scale).

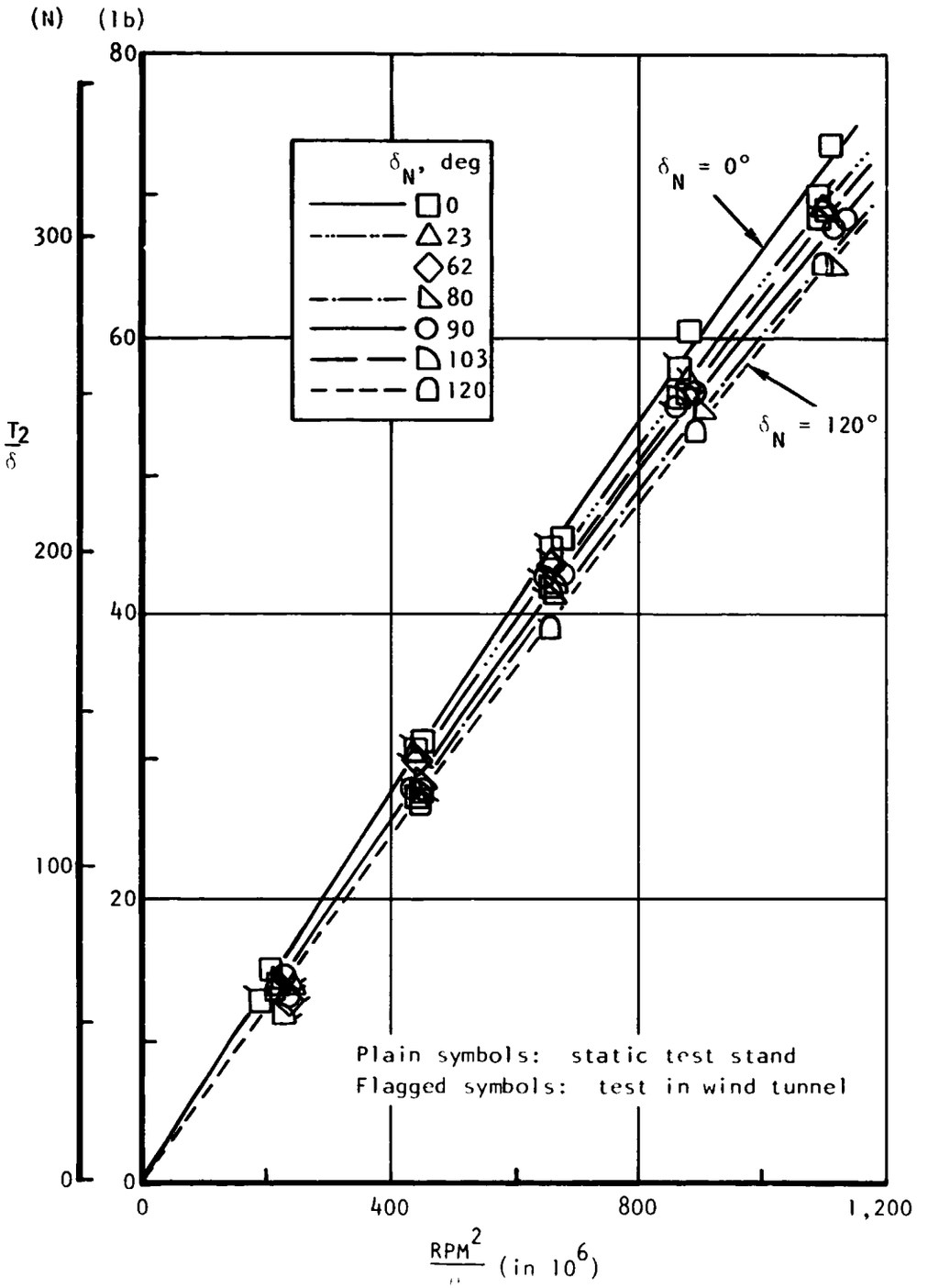

Figure 19. - Calibrated thrust of right-hand fan (starboard), OGE.

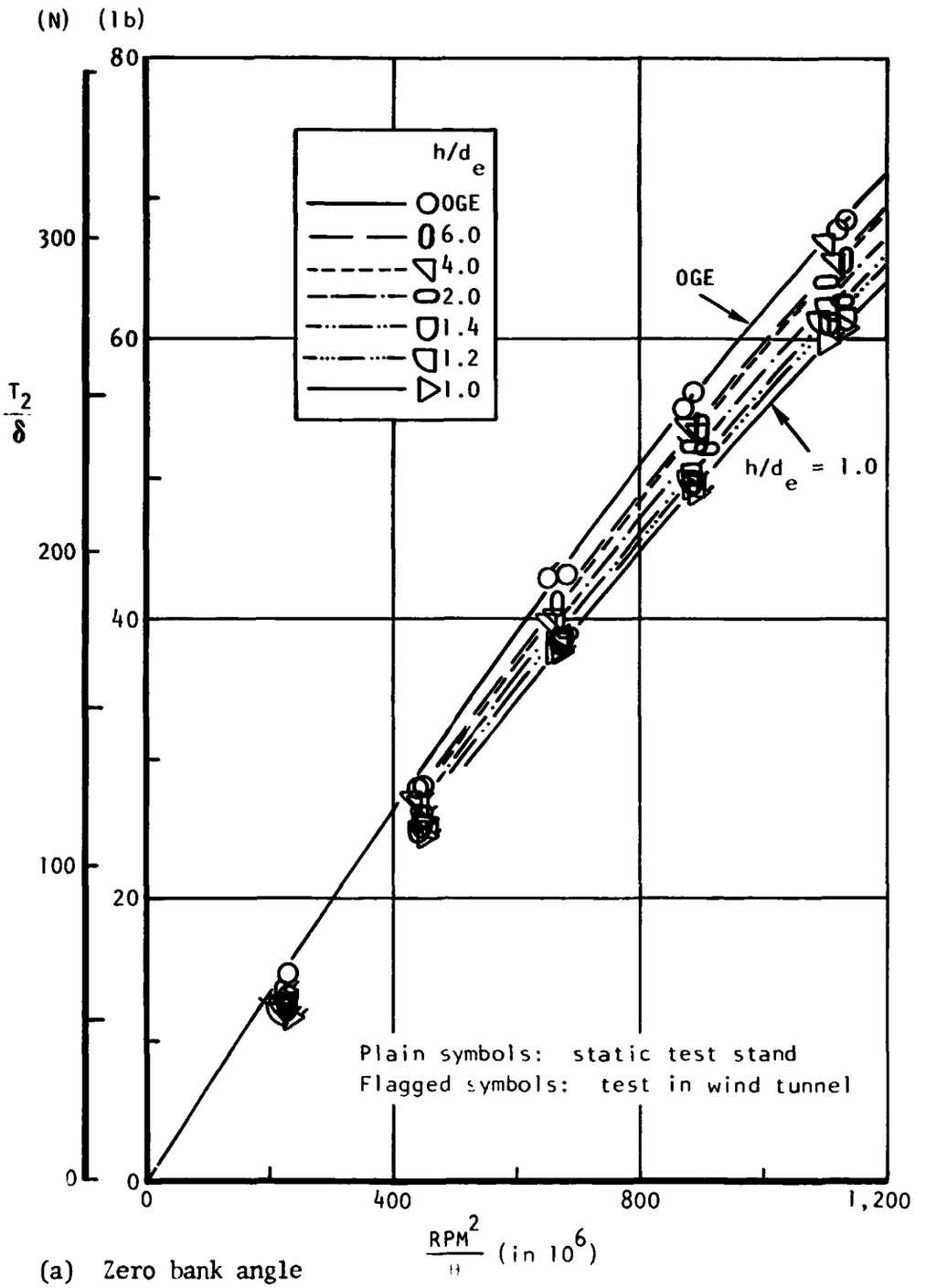

(a) Zero bank angle

Figure 20. - Calibrated thrust of right-hand fan in ground effect, $\delta_N = 90°$

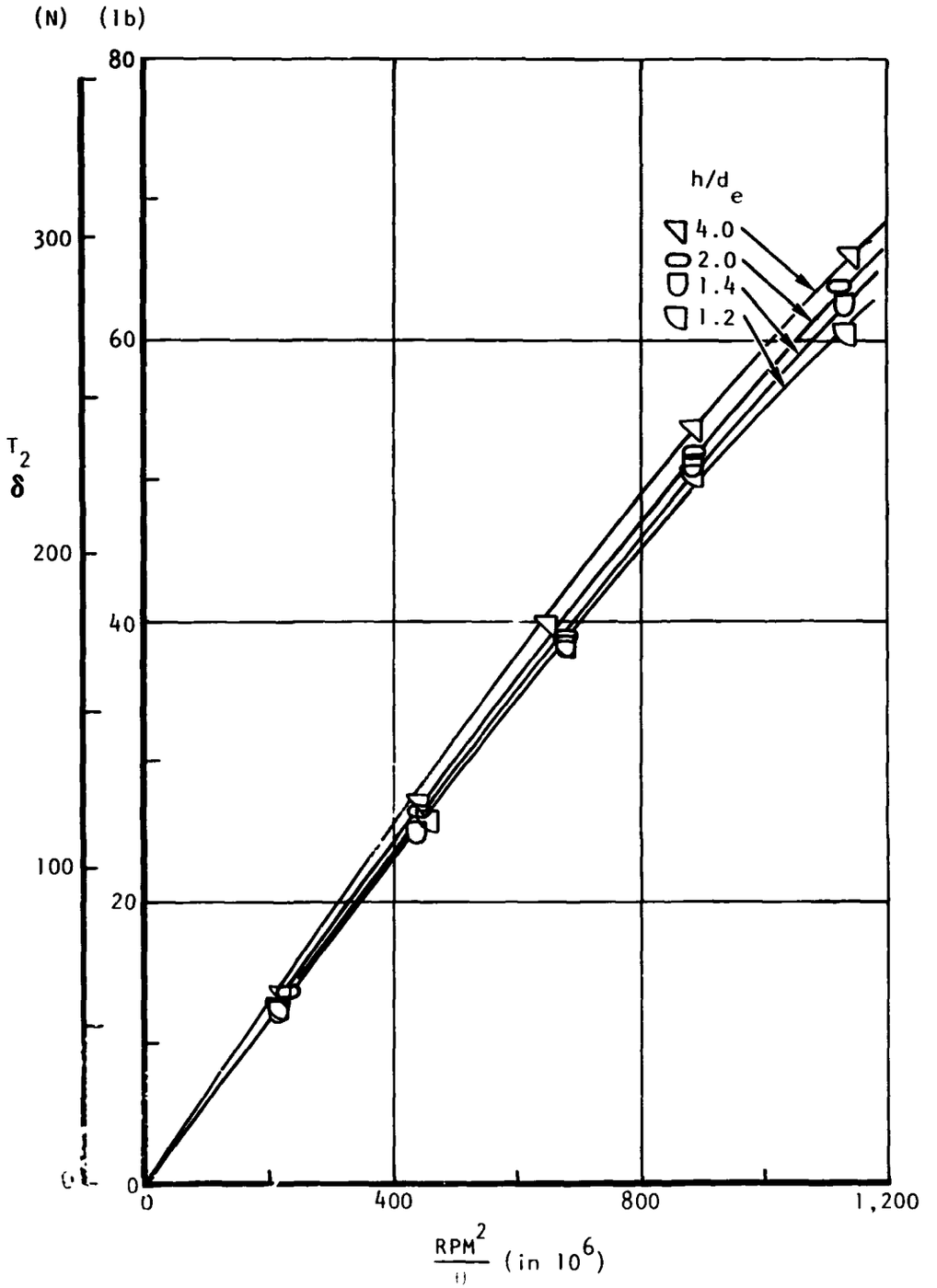

(b) Bank angle 10°

Figure 20. - Concluded.

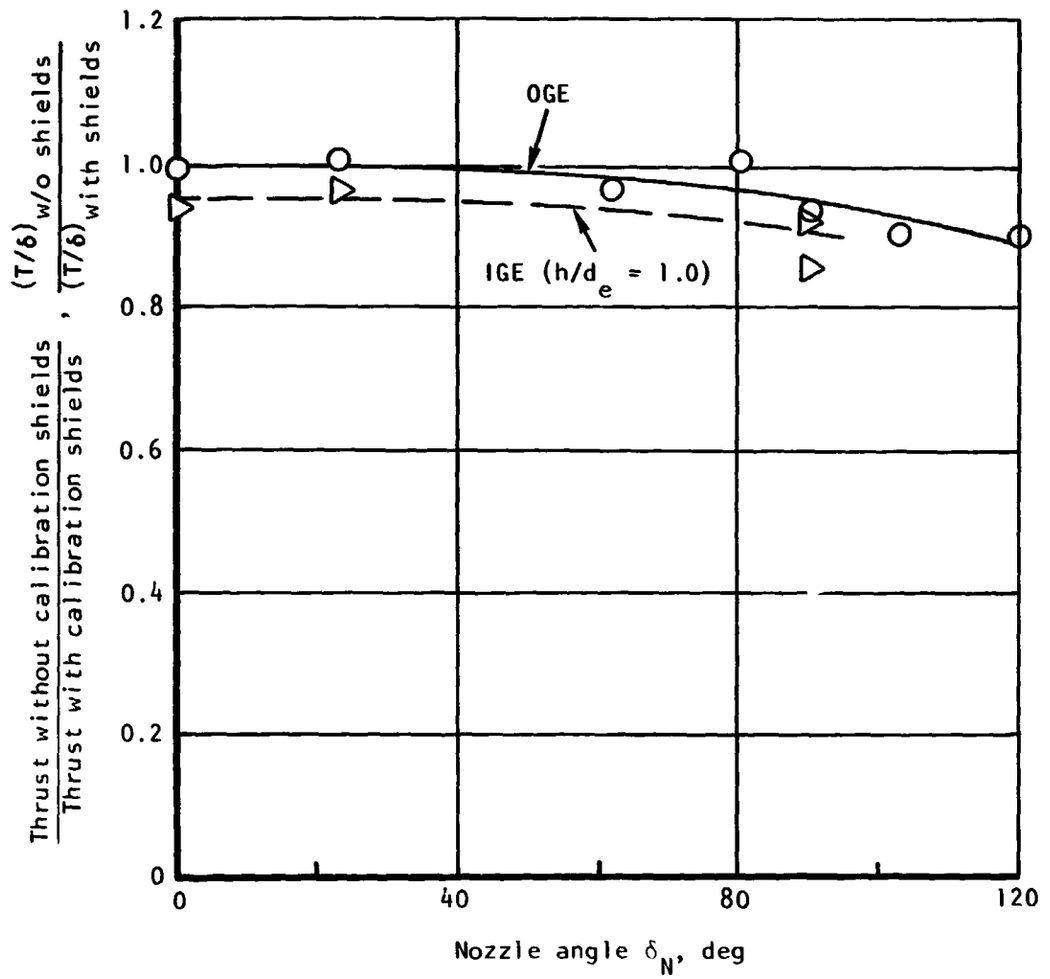

Figure 21. - Nacelle interference on static thrust of right-hand fan.

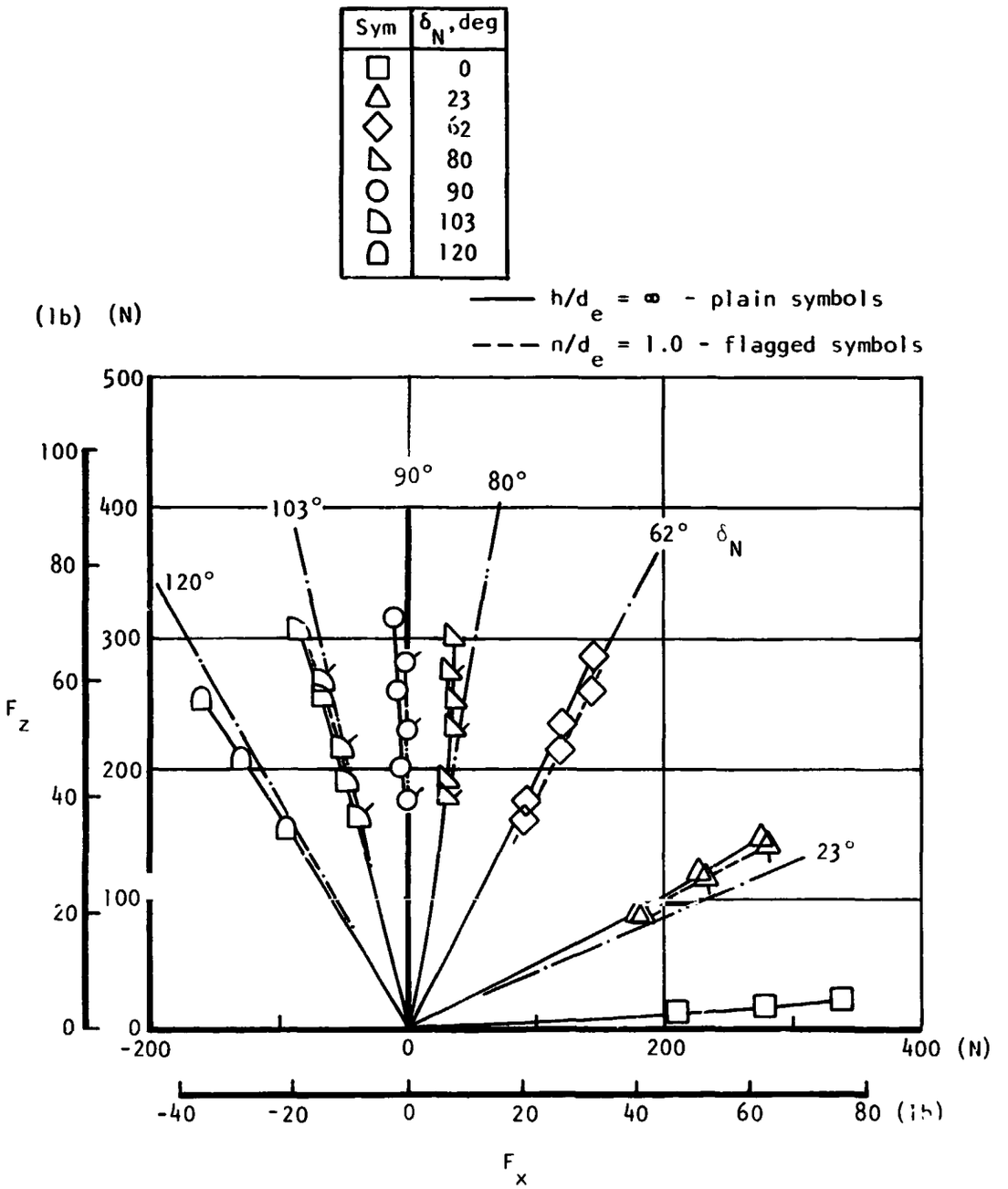

(a) Right-hand fan.

Figure 22. - Calibrated flow turning characteristics.

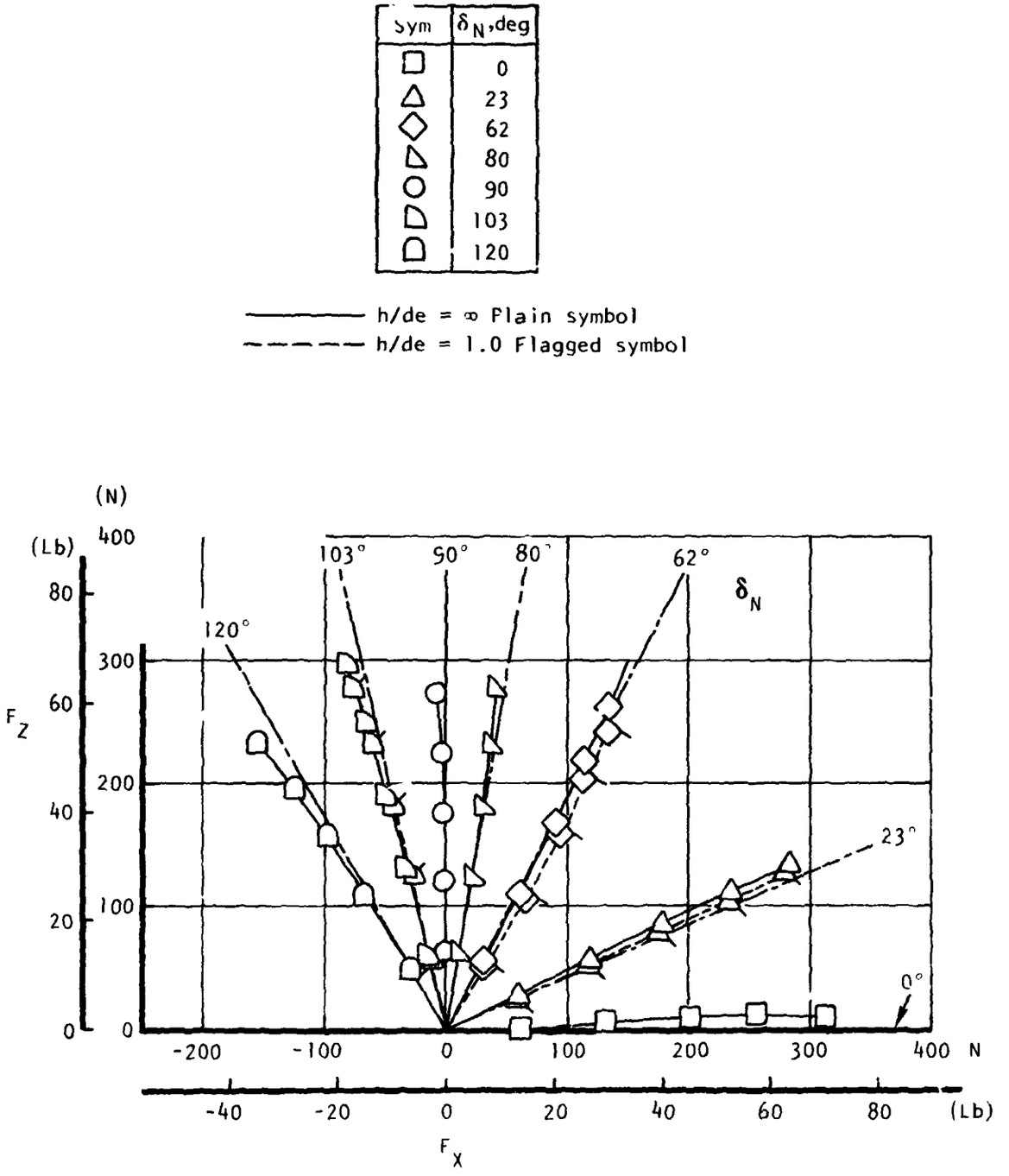

(b) Left-hand fan.

Figure 22. Concluded.

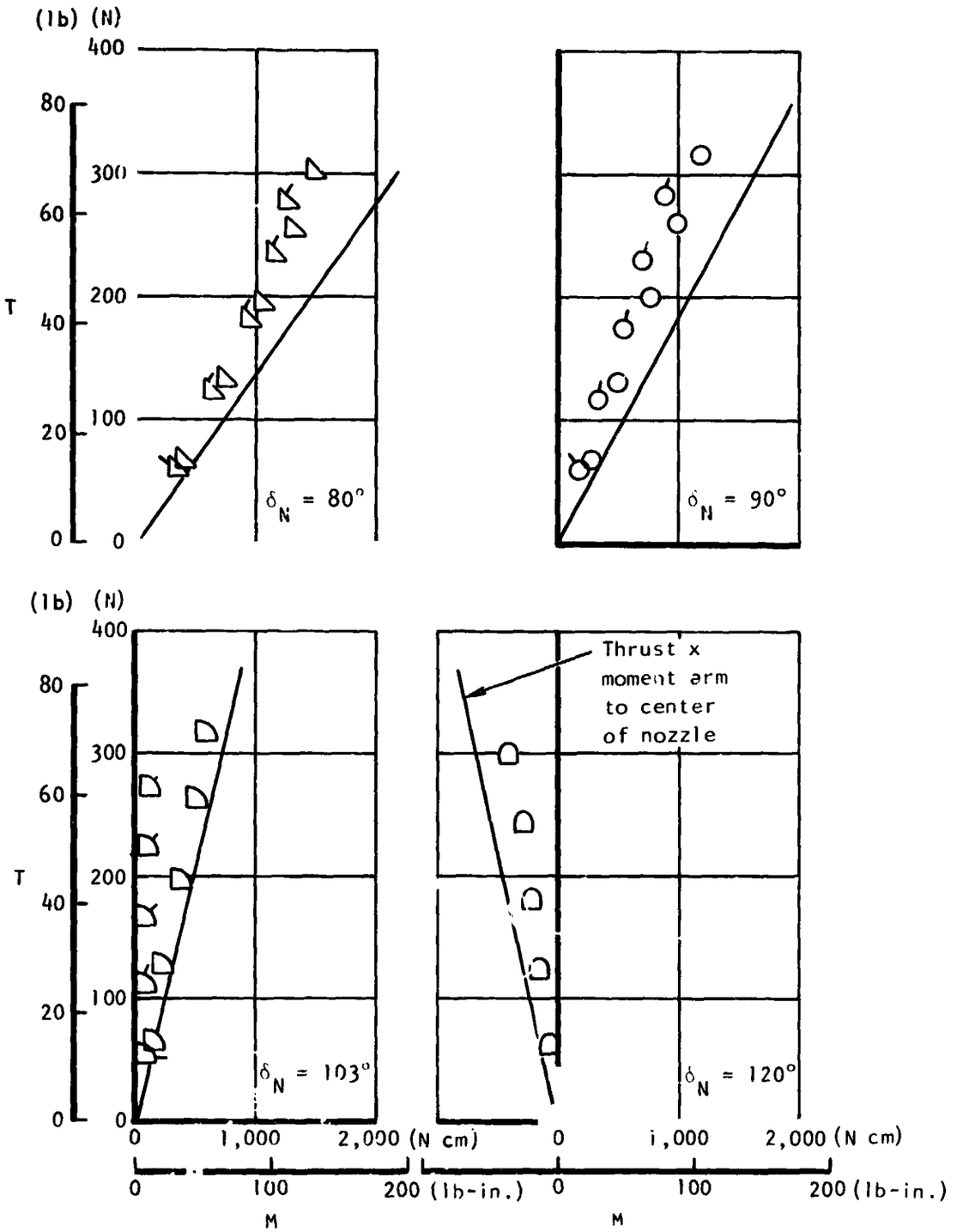

(a) Right-hand fan.

Figure 23.- Thrust versus pitching moment of fan during calibration.

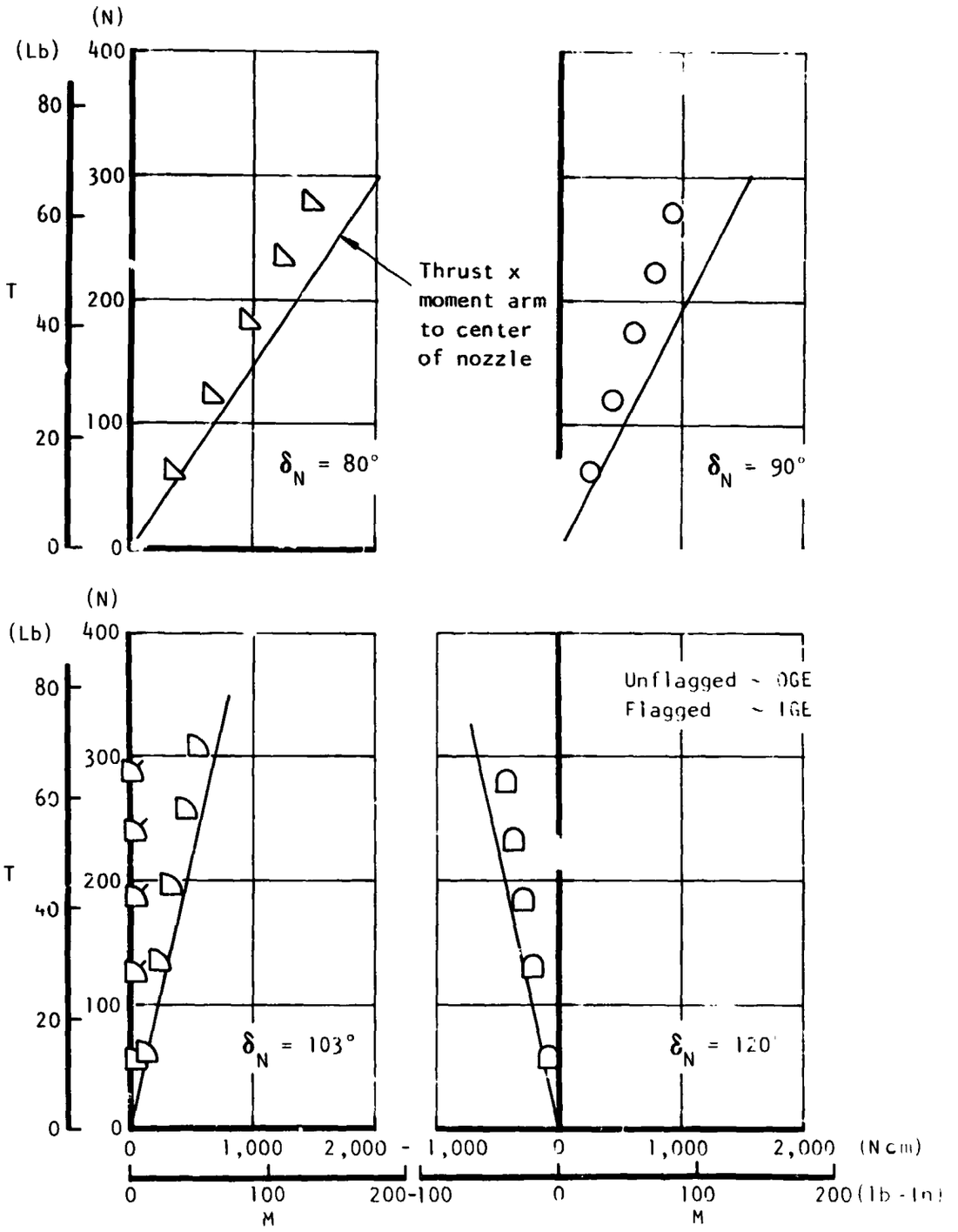

(b) Left-hand fan.

Figure 23. - Concluded.

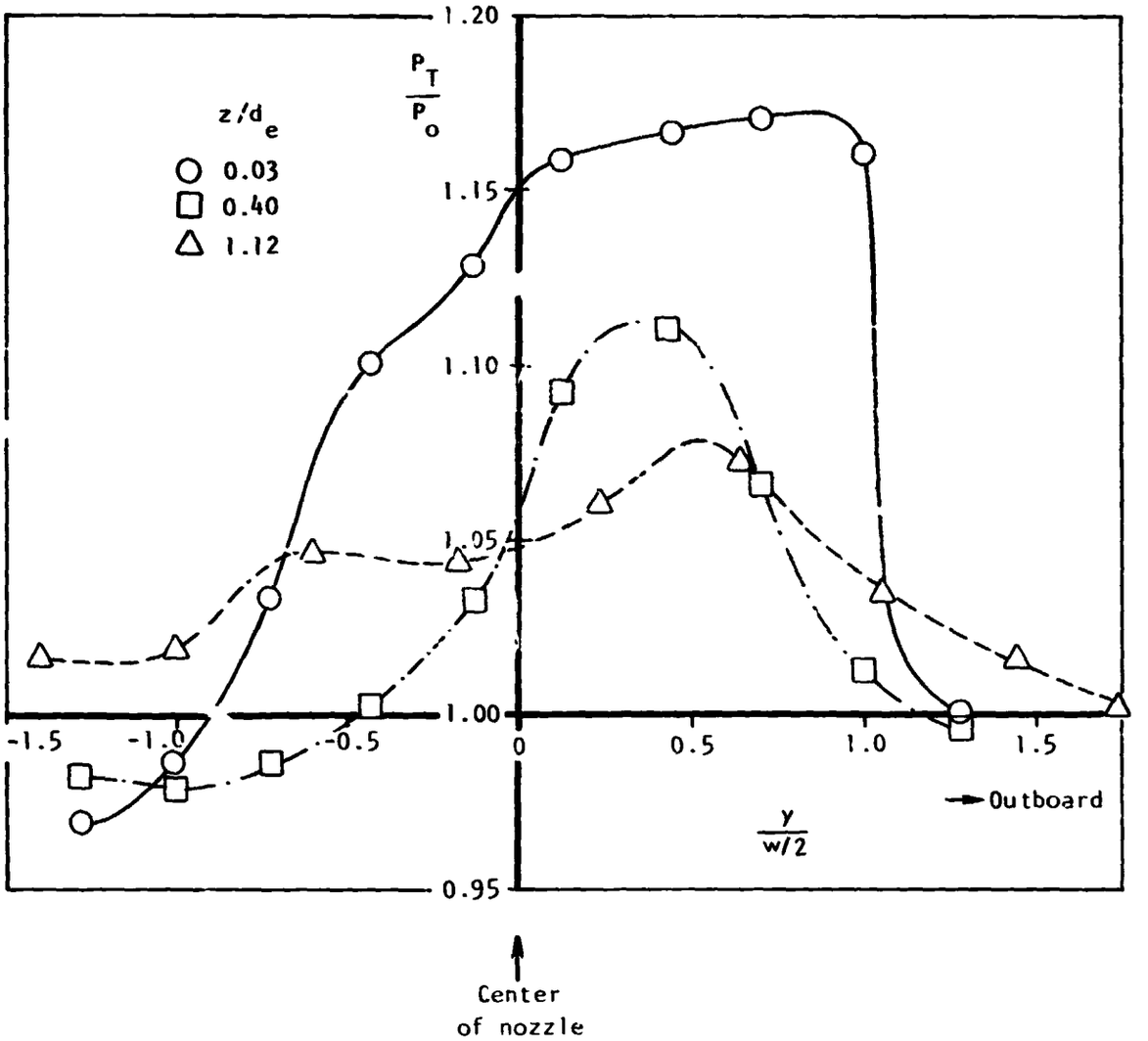

Figure 24. - Nozzle exit total pressure profile for $\delta_N = 90°$.

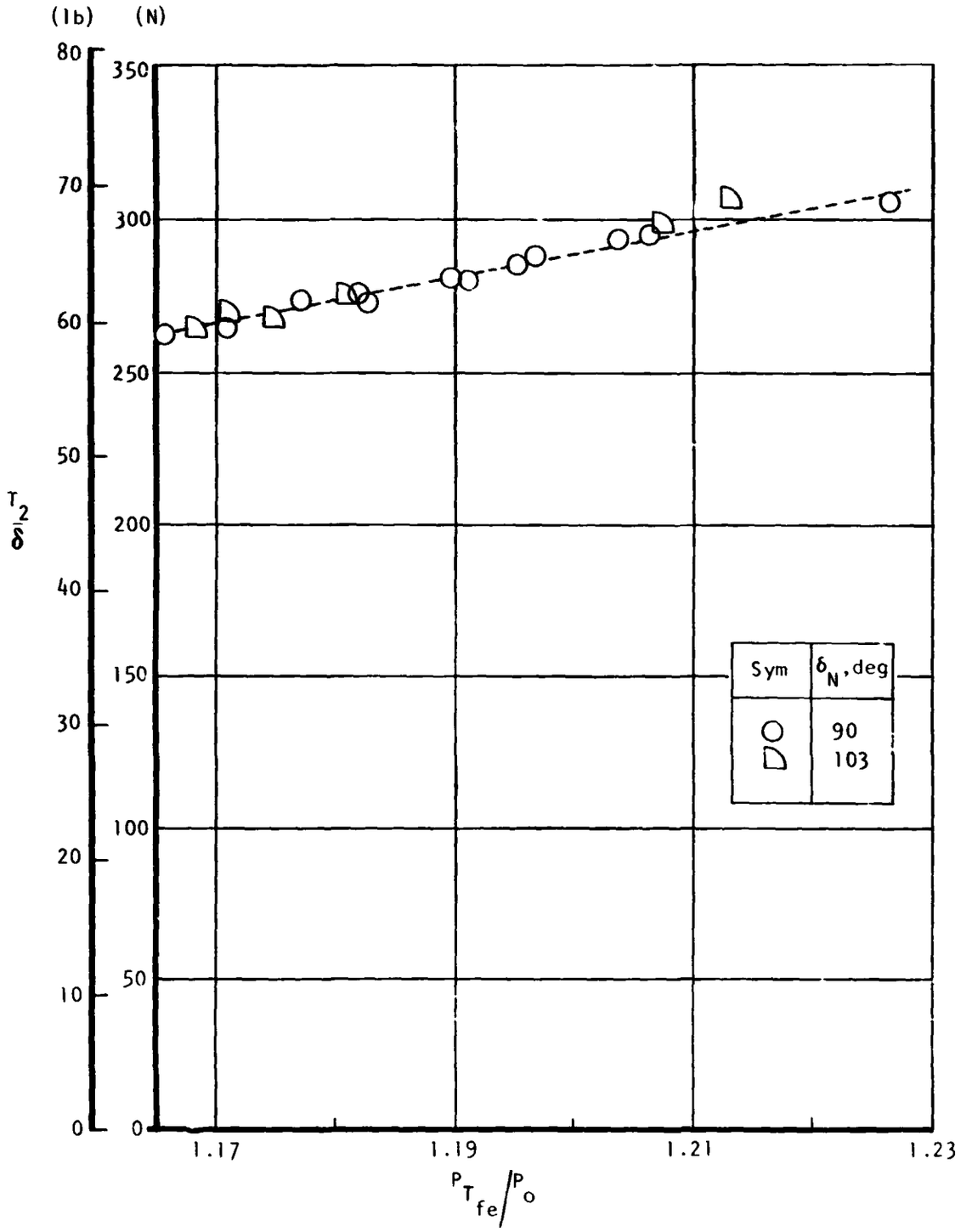

Figure 25. - Thrust of right-hand fan versus fan exit pressure ratio.

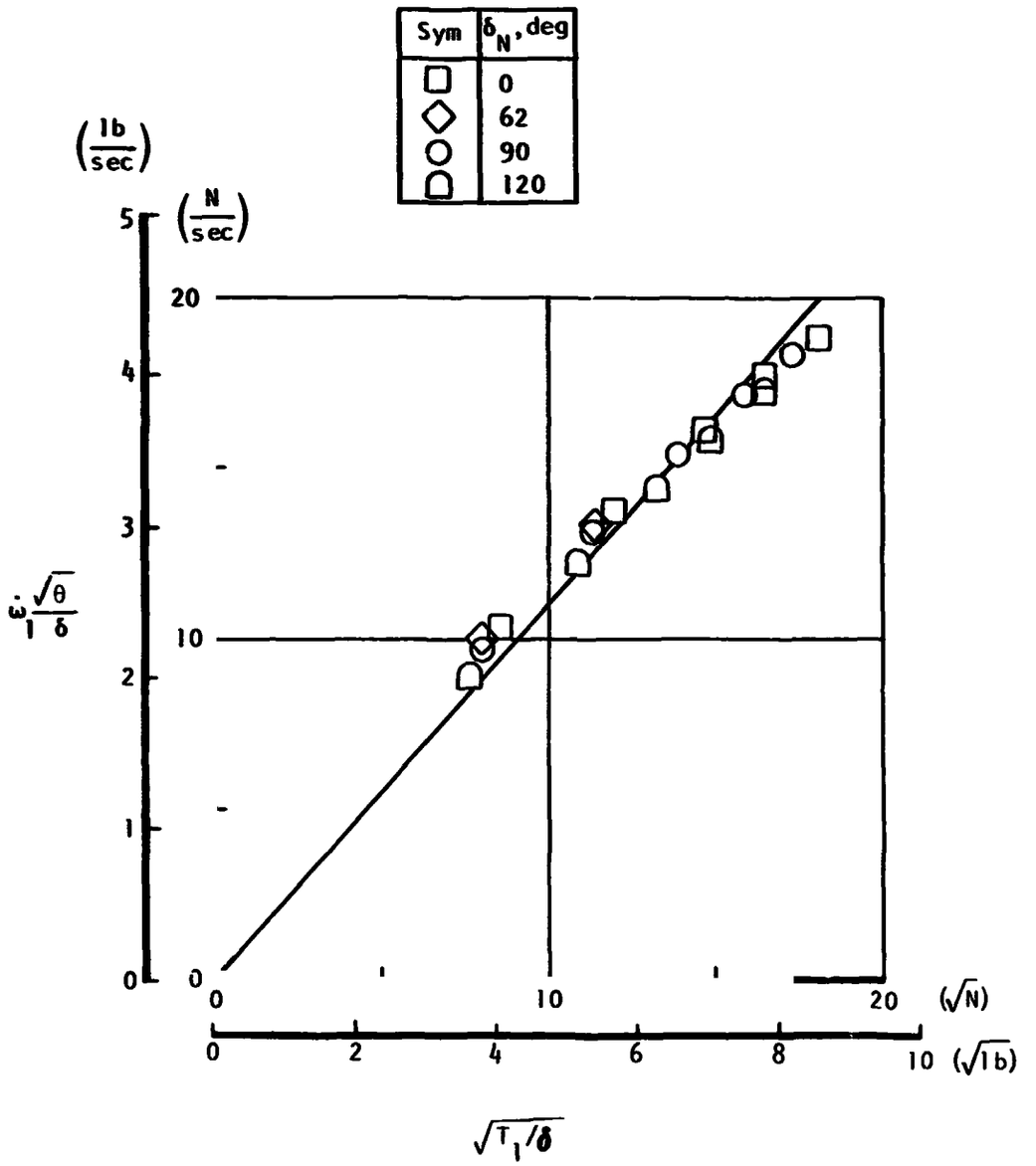

Figure 26. - Inlet flow rate of right-hand fan, out of ground effect.

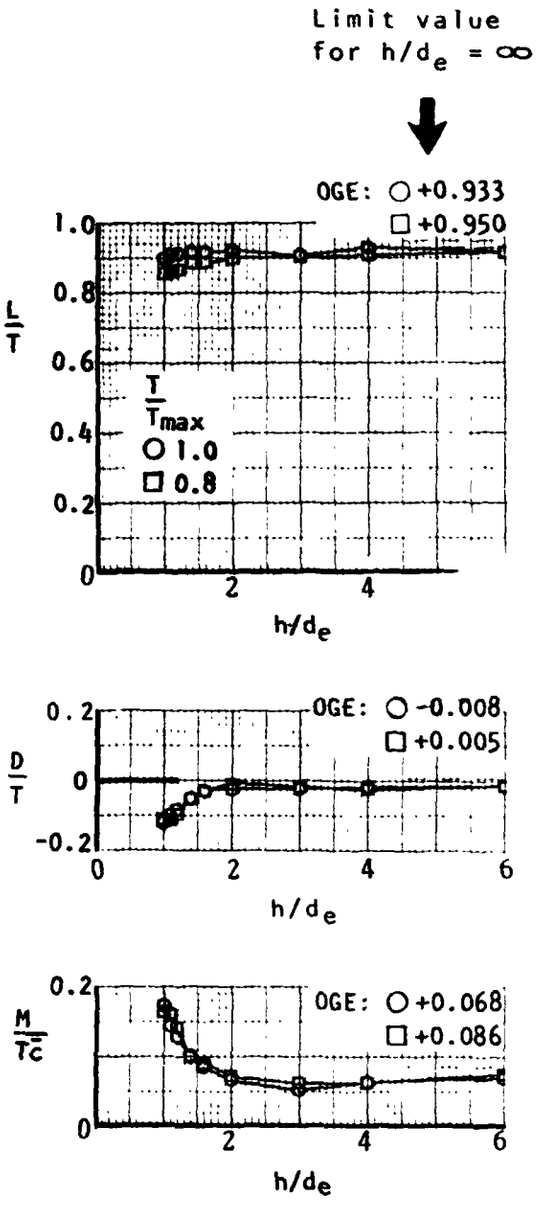

(a) Effect of thrust setting. Various ground distances, $\theta = 0$, $\delta_N = 90°$.

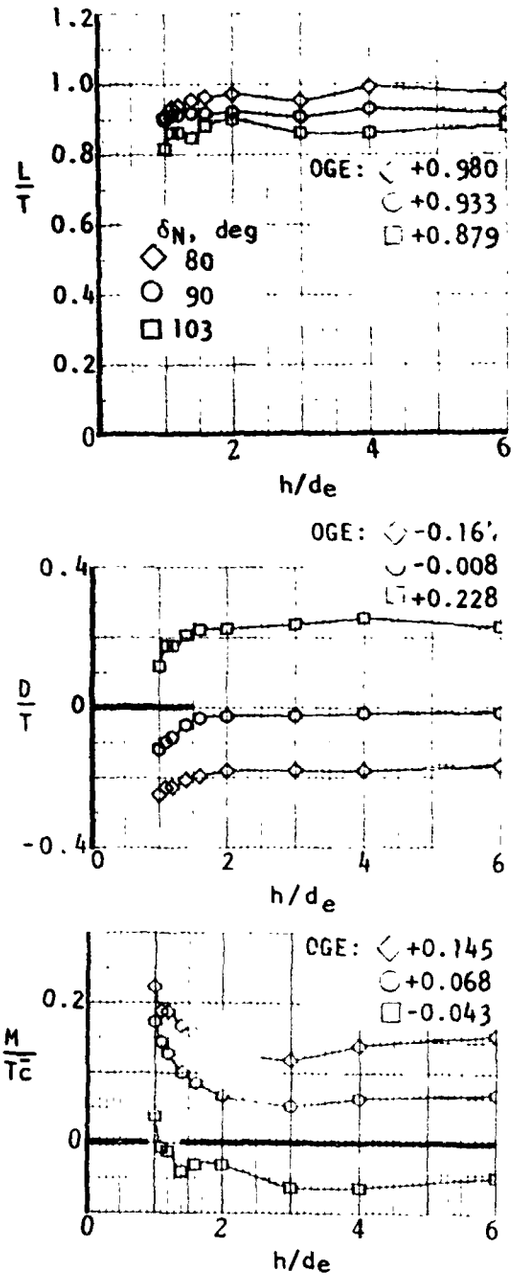

(b) Effect of ground height at various nozzle angles. $\theta = 0$, $T/T_{max} = 1.0$.

Figure 27.- Tail-off longitudinal forces and moments in hover.

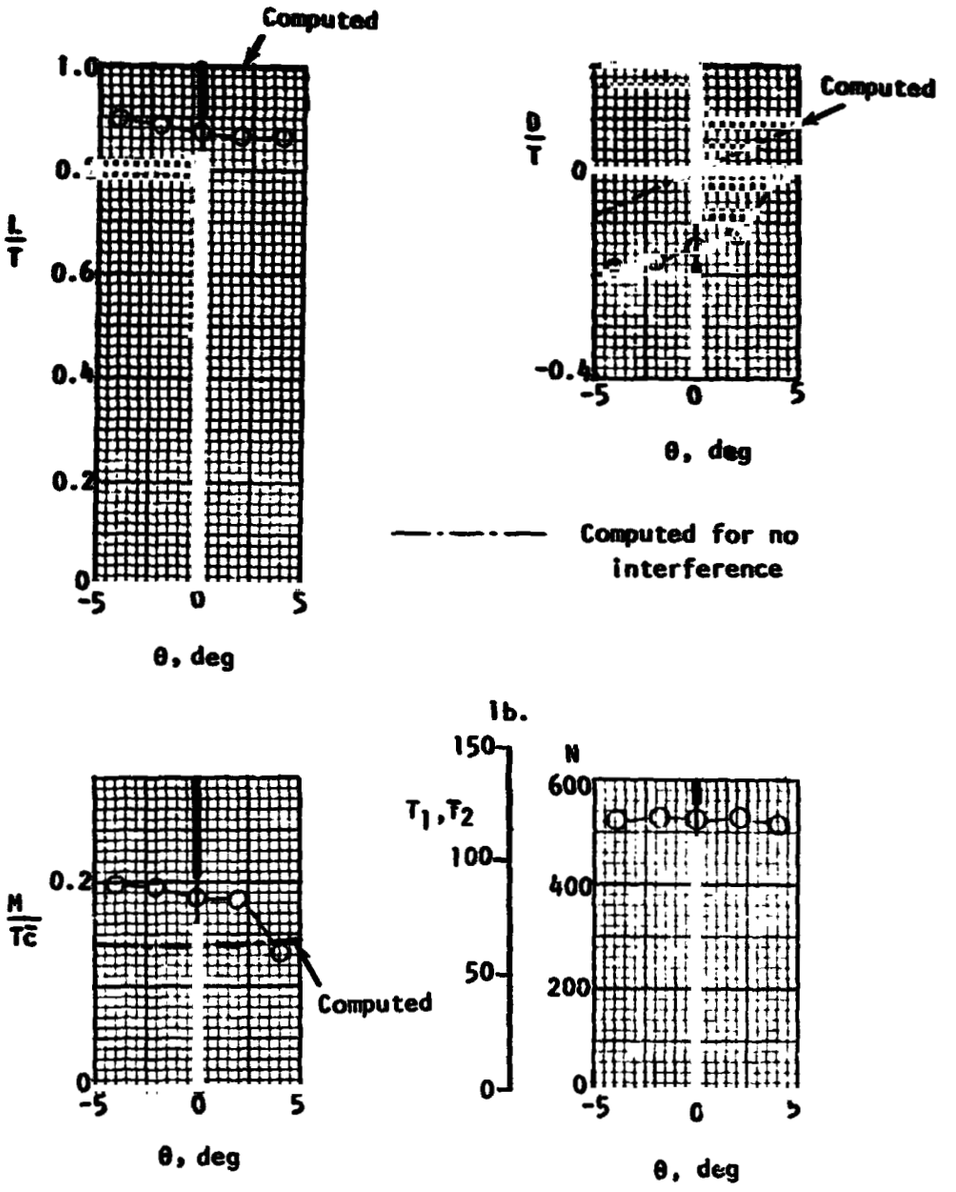

(c) Effect of pitch angle at $h/d_e = 1.0$. $\delta_N = 90°$.

Figure 27.- Continued.

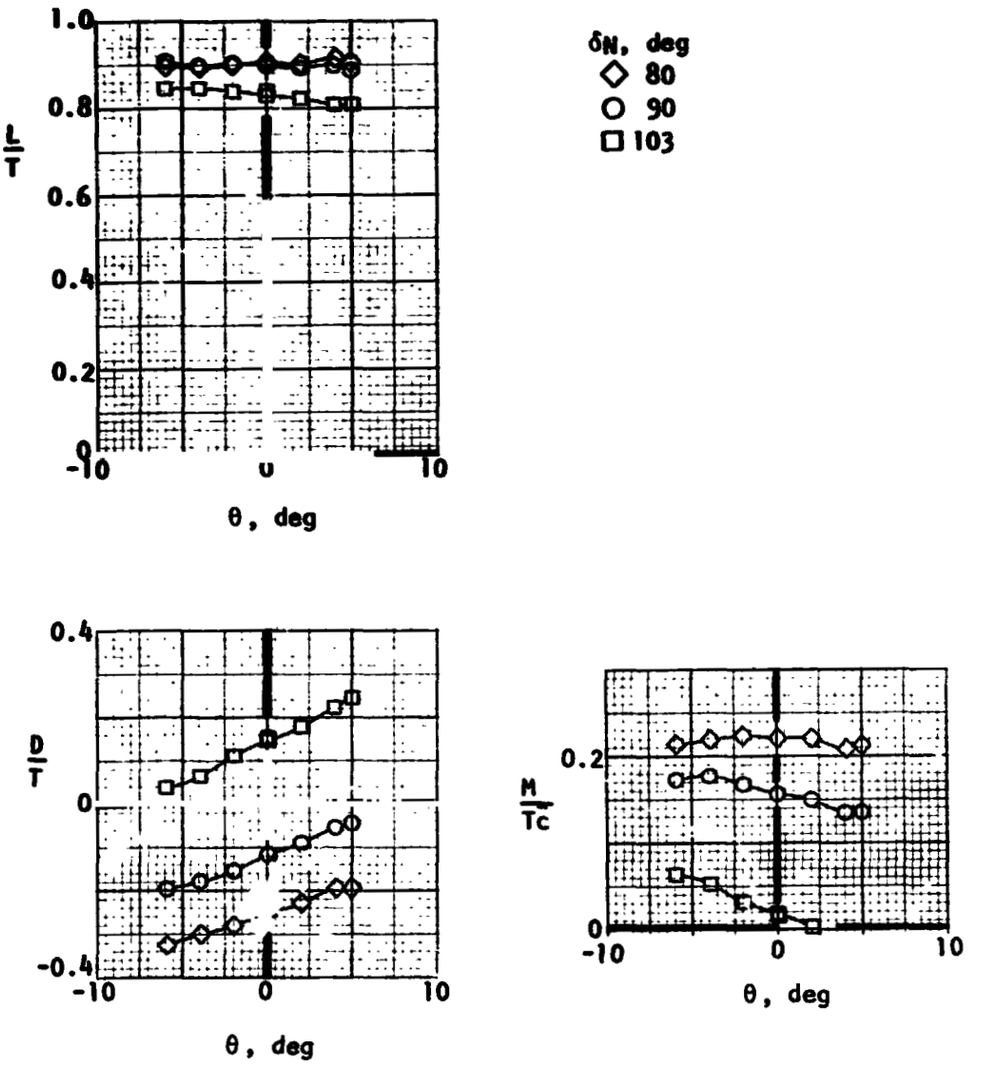

(d) Effect of pitch angle at $h/d_e = 1.2$. Various nozzle angles.

Figure 27.- Concluded.

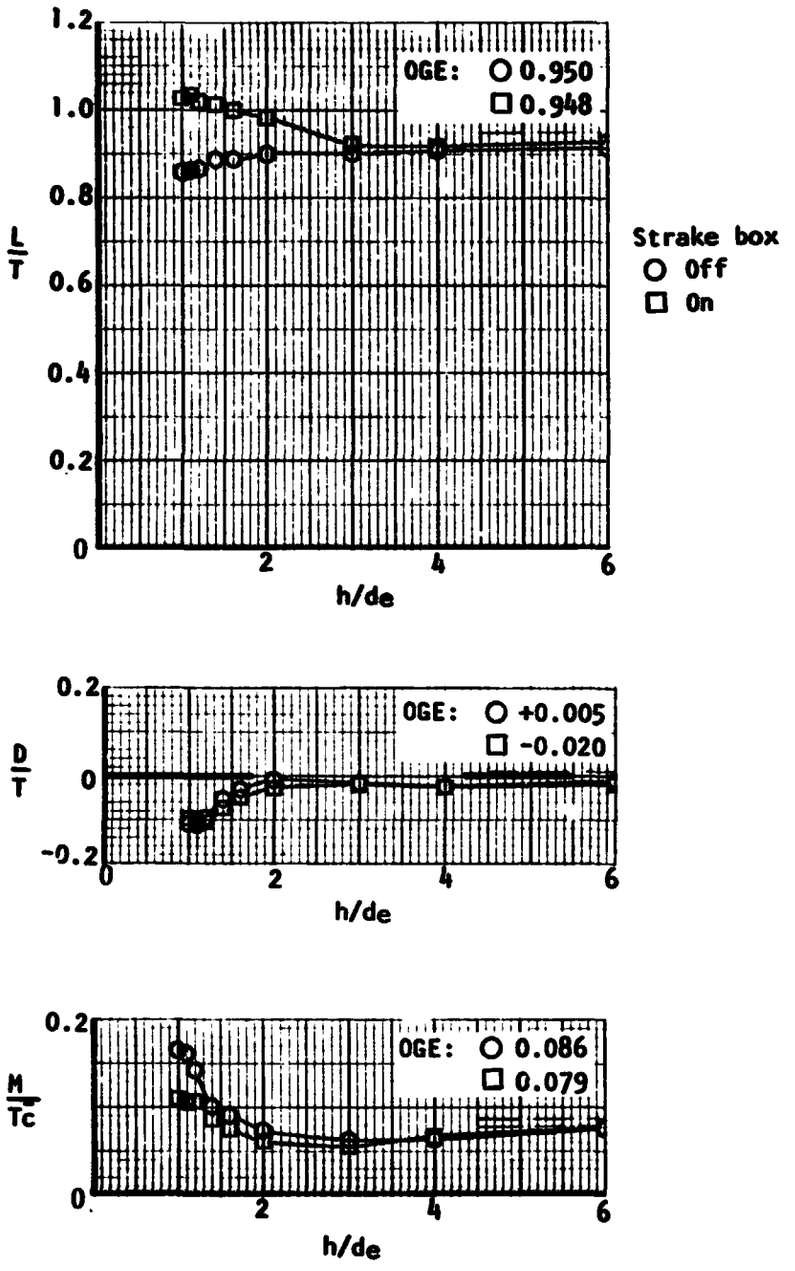

(a) Effect of strake box.

Figure 28.- Effect of shields on tail-off longitudinal forces and moments in hover. $\Theta = 0$, $\Phi = 0$, $\delta_N = 90°$.

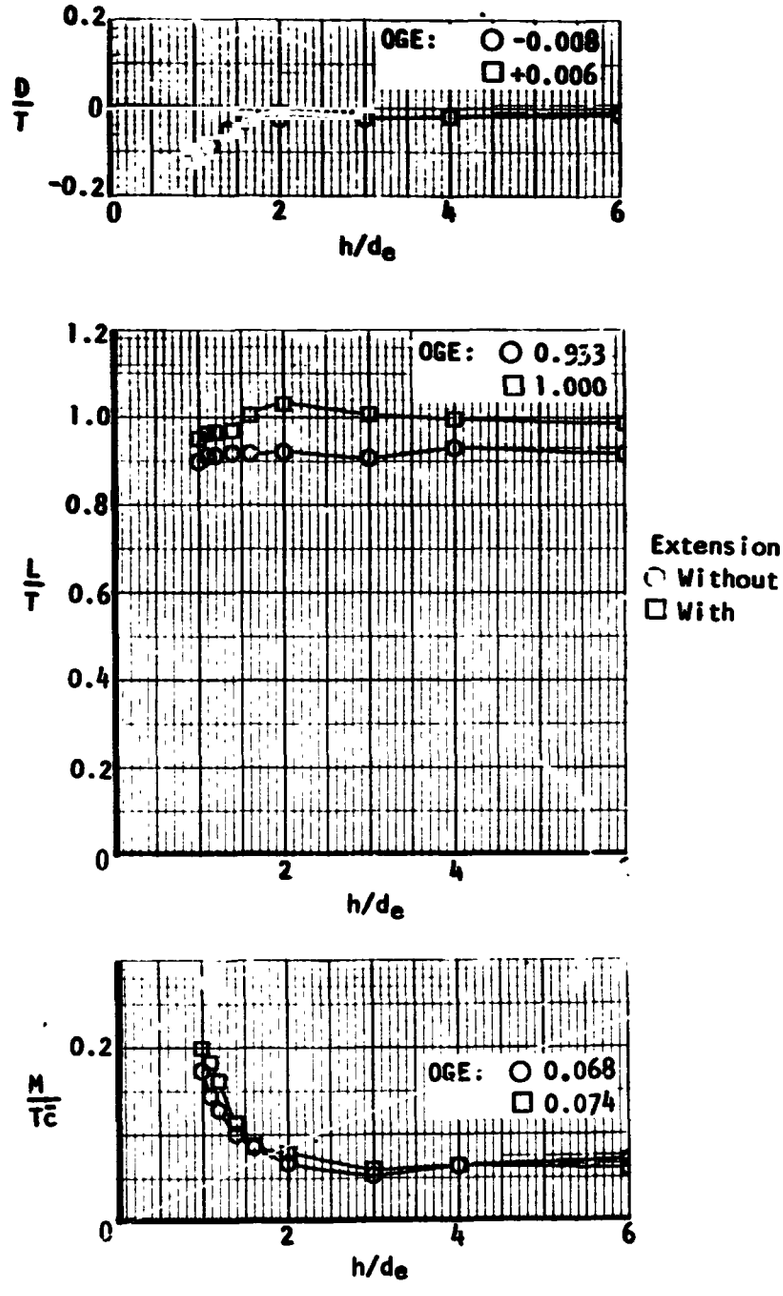

(b) Effect of nozzle wall extension.

Figure 28.- Concluded

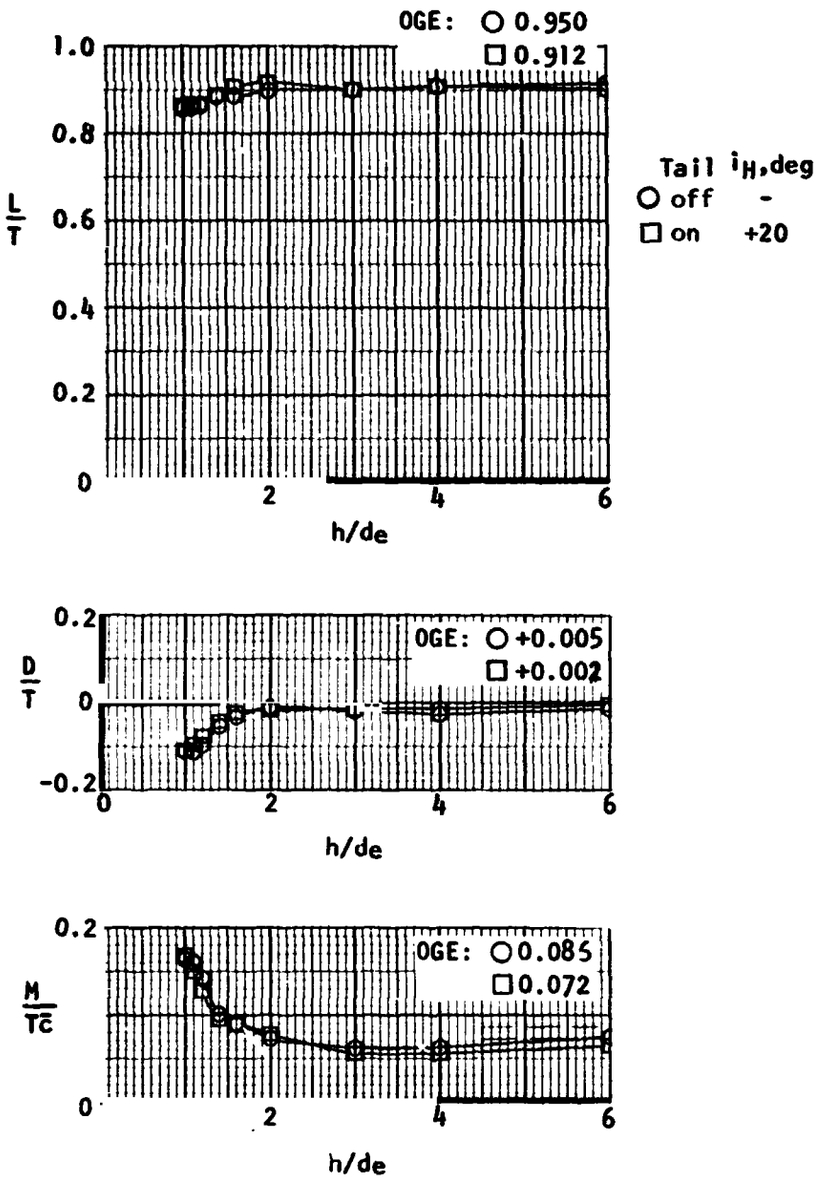

Figure 29.- Tail effect on longitudinal forces and moments in hover. $\theta = 0$, $\delta_N = 90°$.

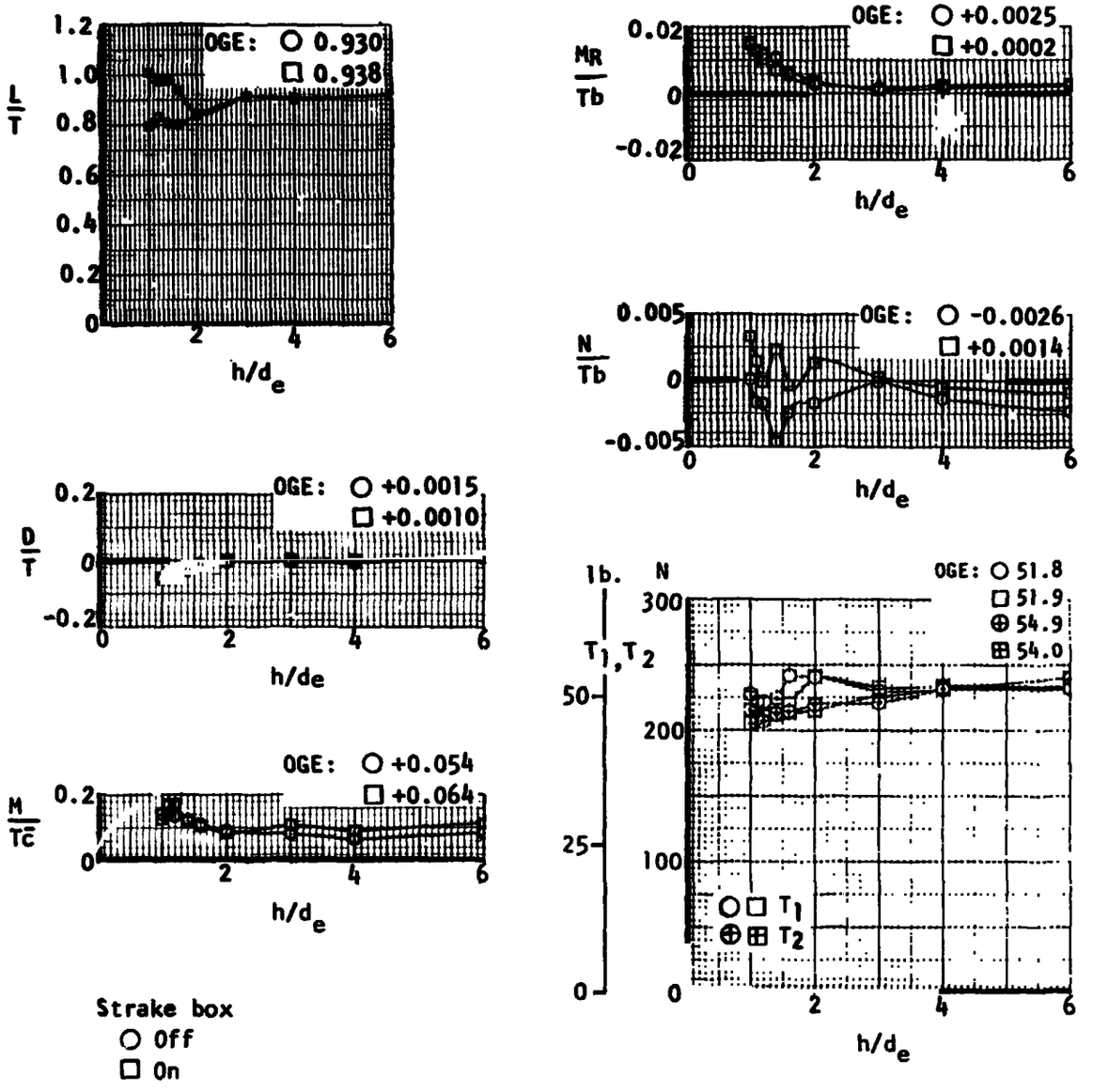

(a) Aircraft banked, no roll control input, 80% thrust setting, strake box on and off.

Figure 30.- Tail-off forces and moments in asymmetric hover condition. $\delta_N = 90°$, $\theta = 0$.

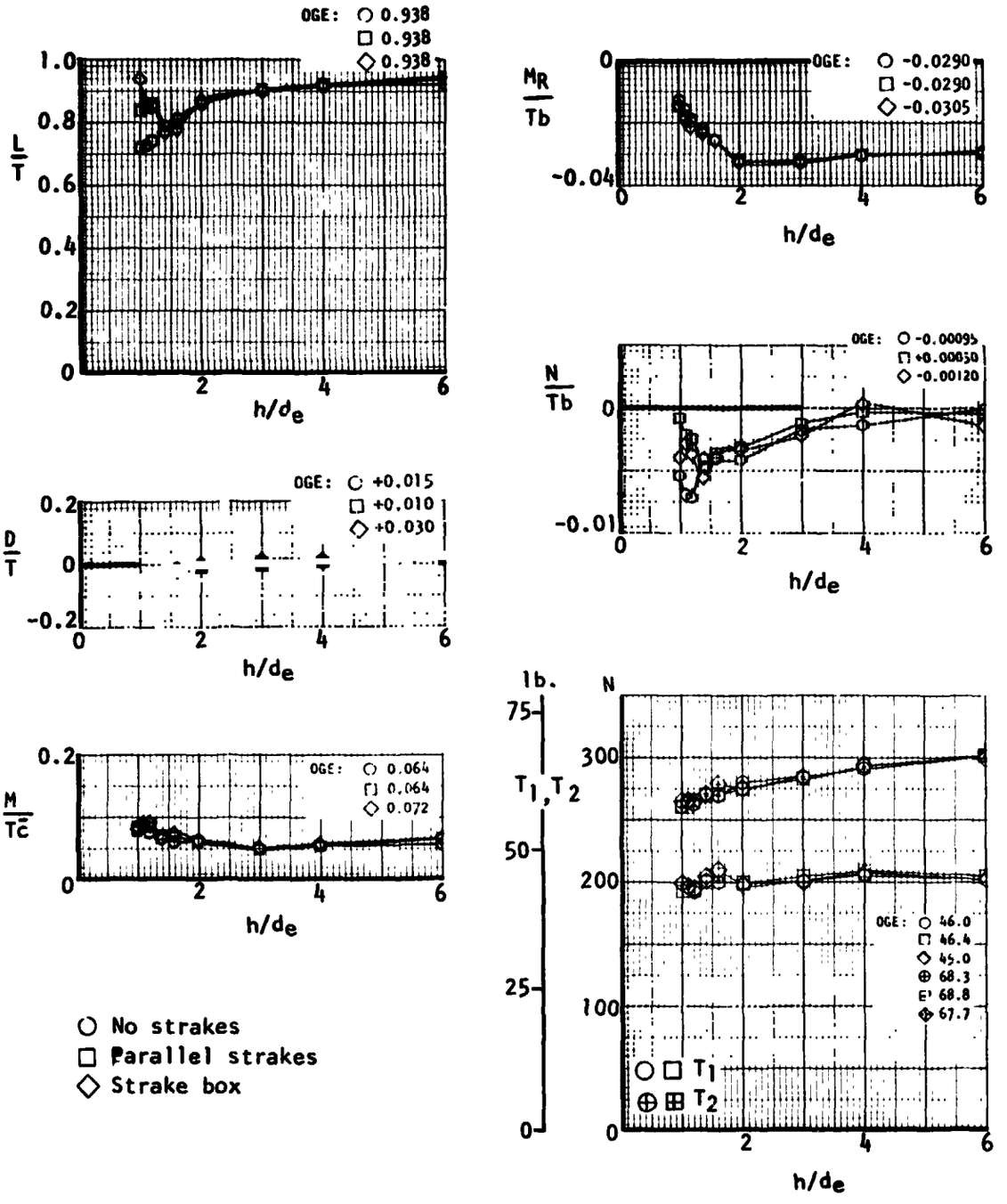

(b) Aircraft banked, with corrective roll control input. With and without strakes or strake box.

Figure 30.- Continued.

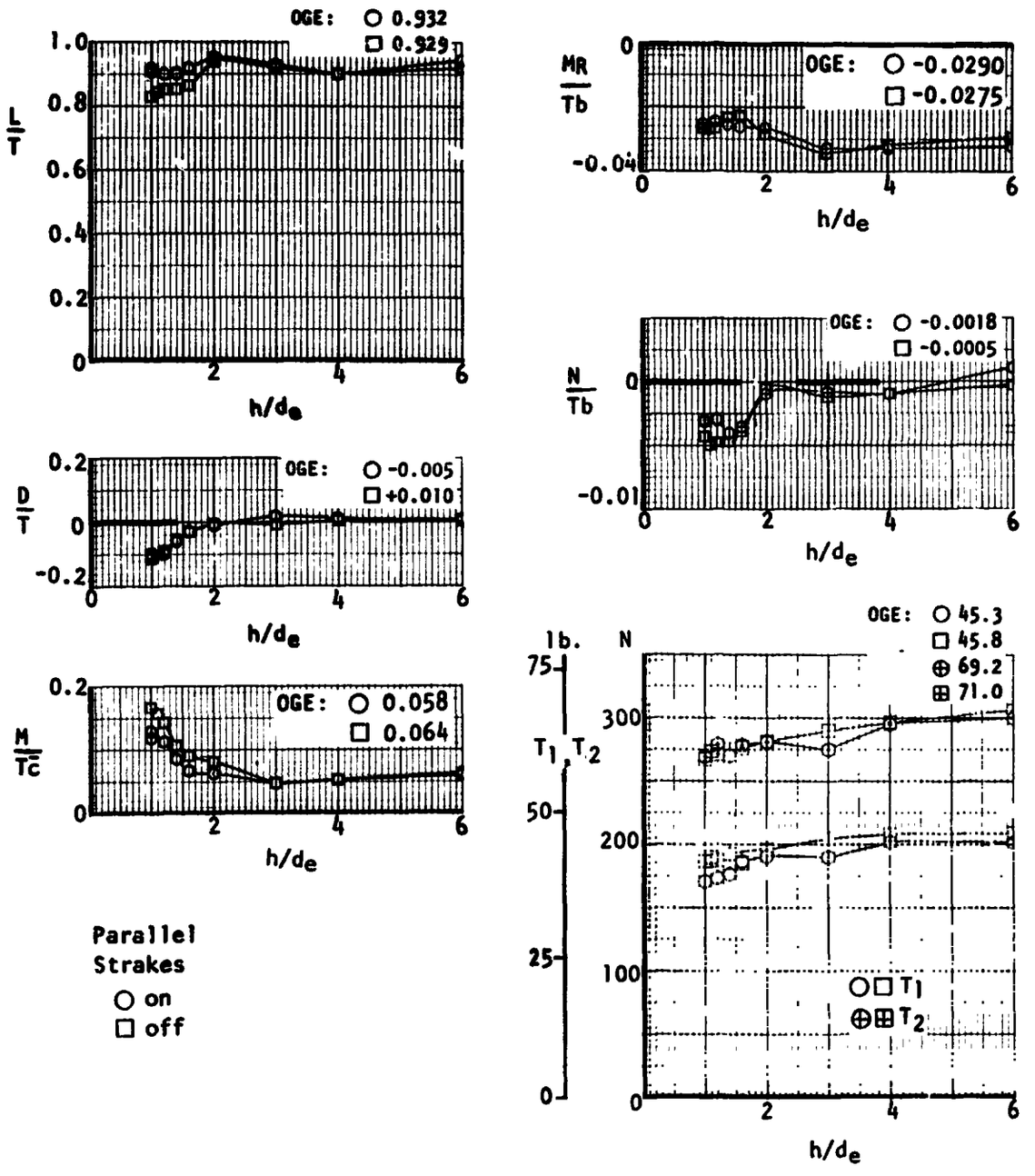

(c) Aircraft level, with roll control input.
With and without parallel strakes.

Figure 30.- Continued.

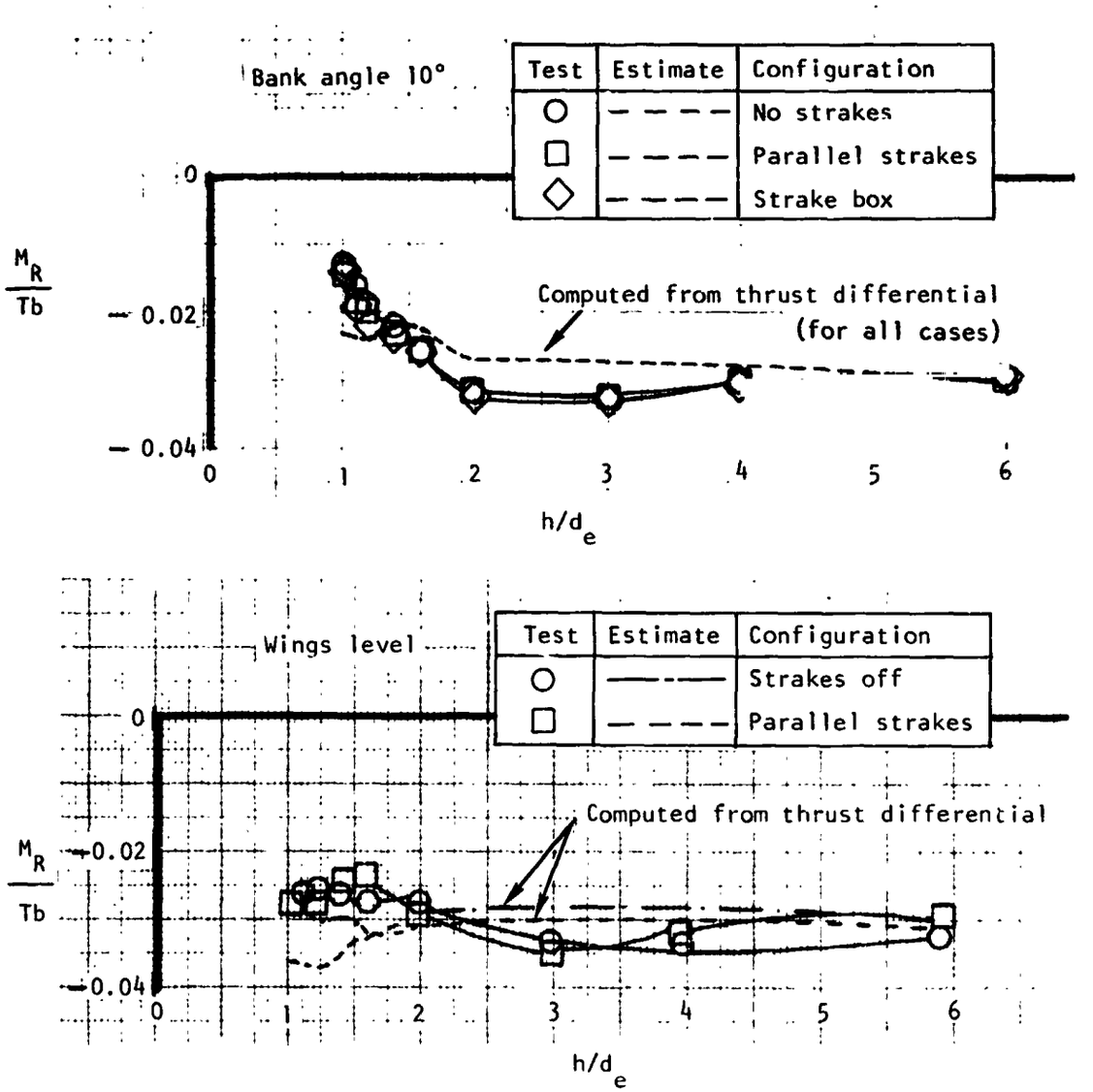

(d) Roll control effectiveness.

Figure 30. - Concluded.

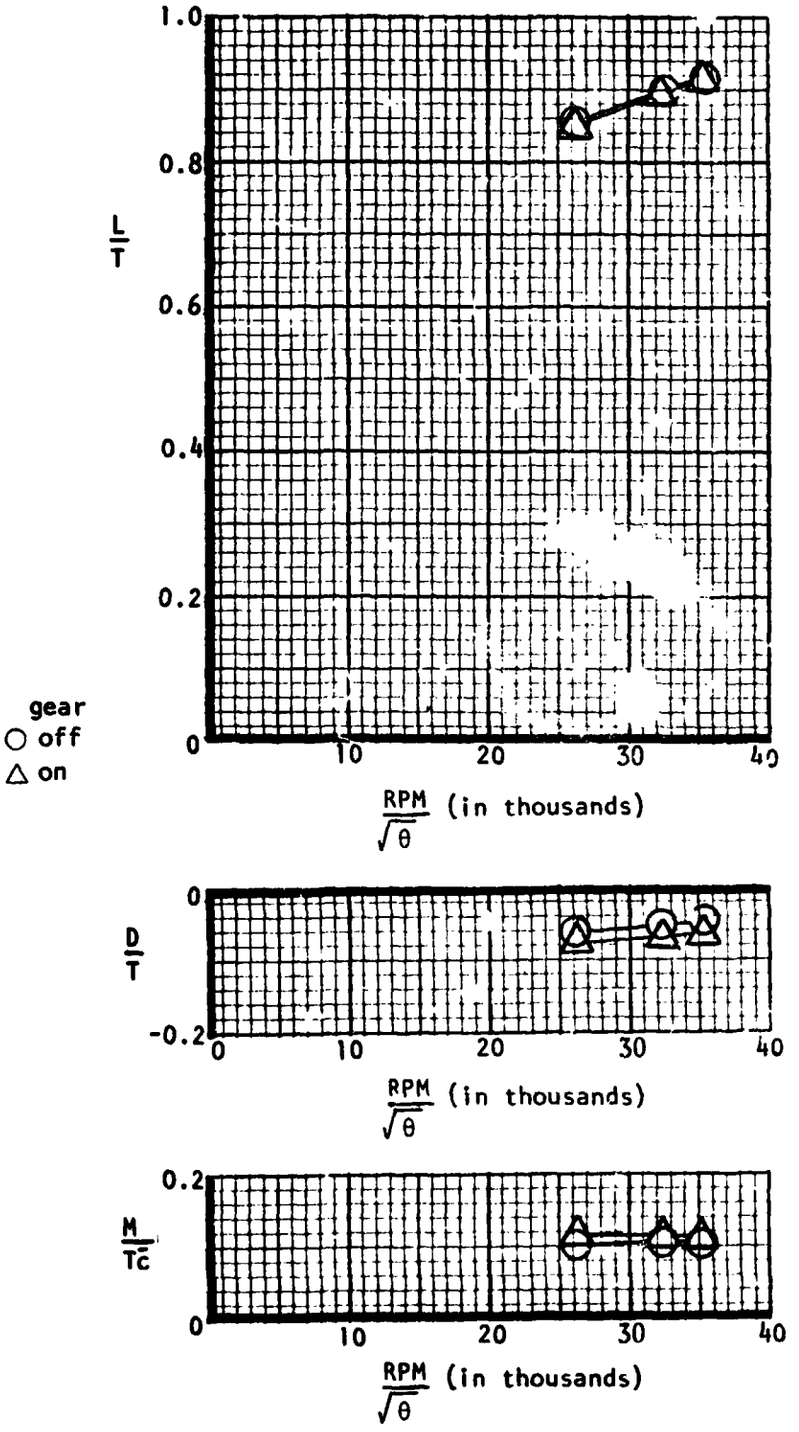

Figure 31.- Effect of landing gear in hover.
$\delta_N = 90°$, tail off, θ J, $\phi = 0$, $h/d_e = 1.2$.

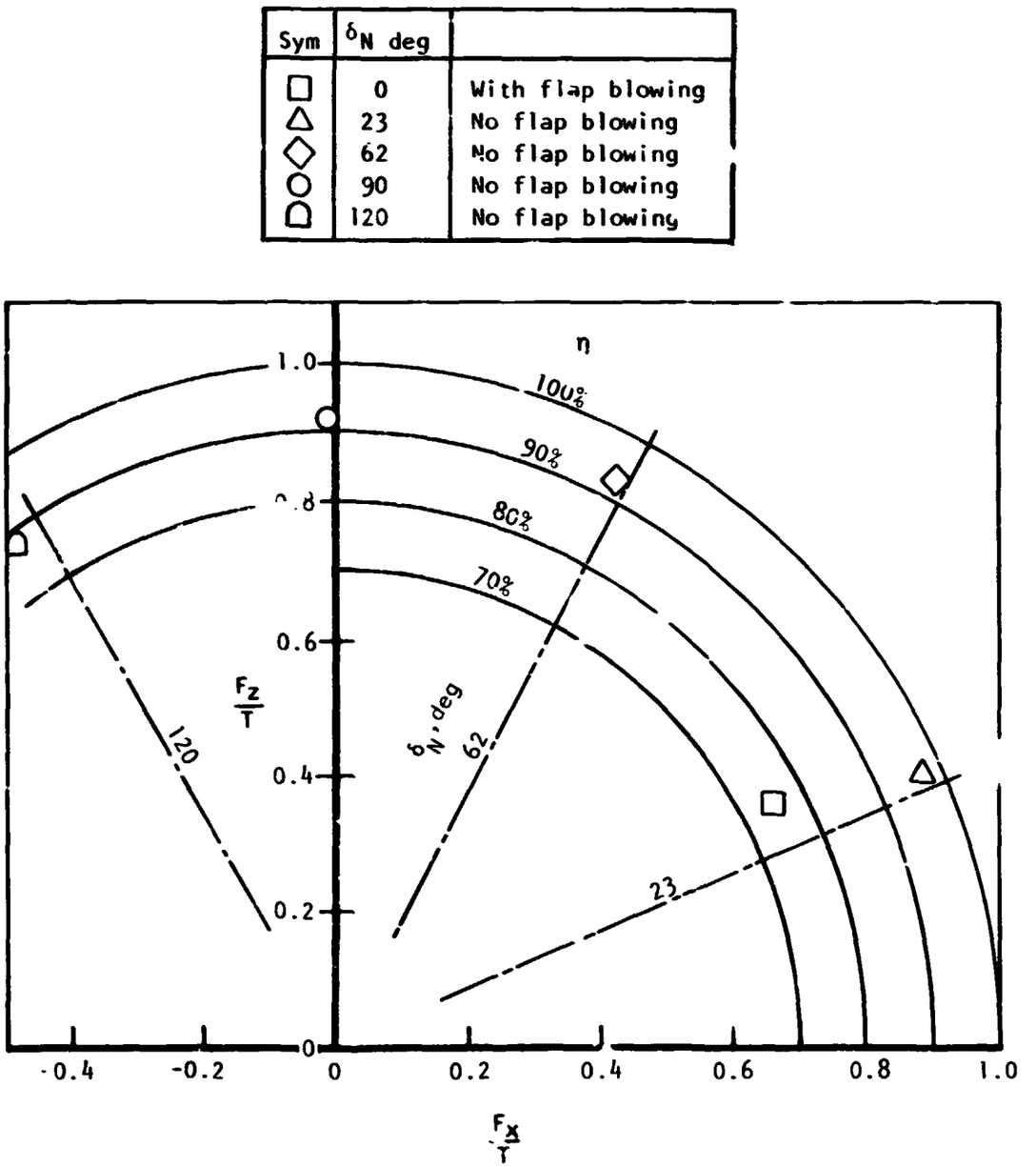

Figure 32. - Static turning characteristics OGE.

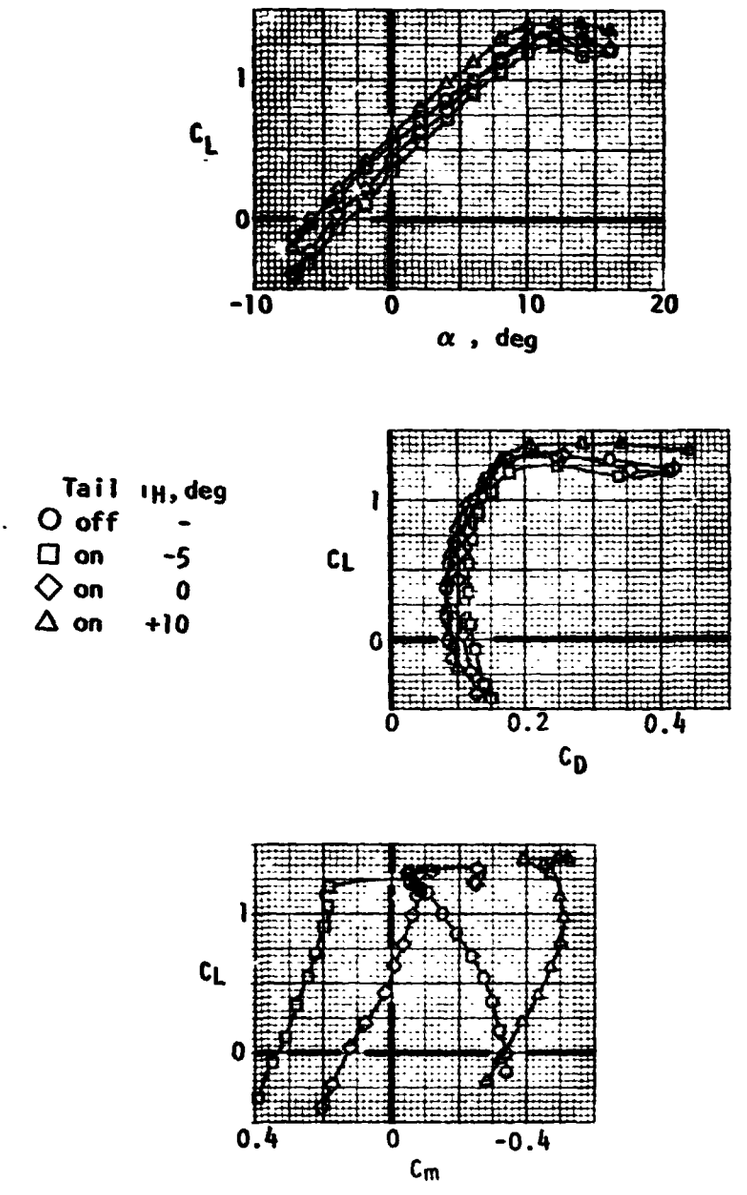

(a) Flaps up, tail on and off, fan inlets open.

Figure 33.- Longitudinal power-off forces and moments out of ground effect. $\delta_N = 0$.

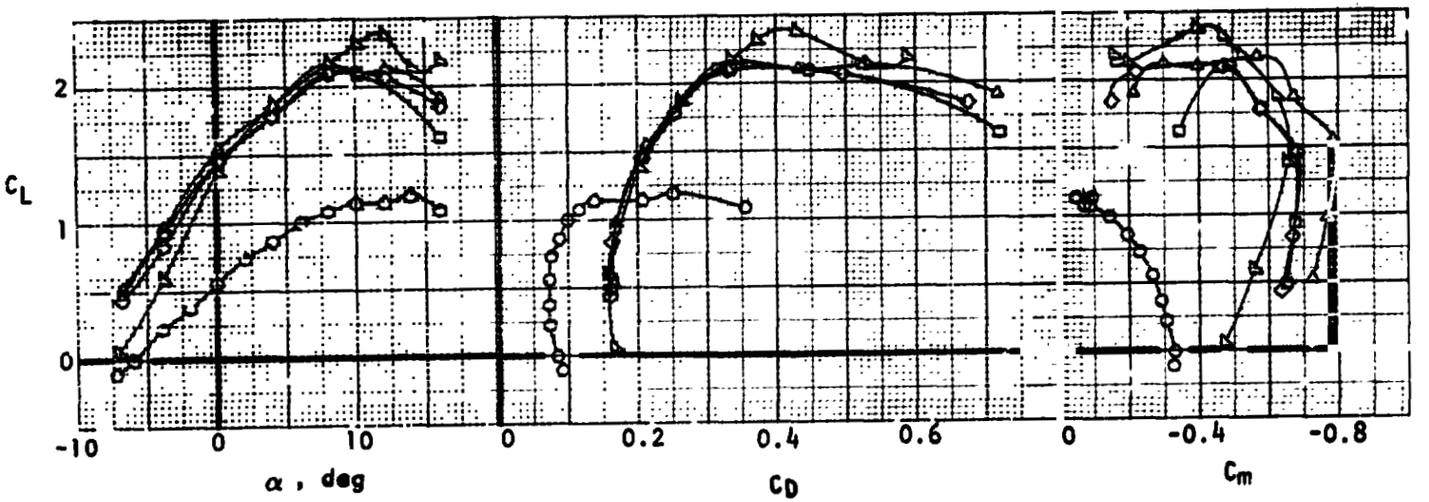

	Flaps	L.E. devices	Ailerons
○	up	none	0
□	dn	none	0
◇	dn	inb'd Krueger only	0
△	dn	inb'd Krueger only	drooped
◁	dn	full span Krueger	0

(b) High lift devices, tail off, inlets covered.

Figure 33.- Continued.

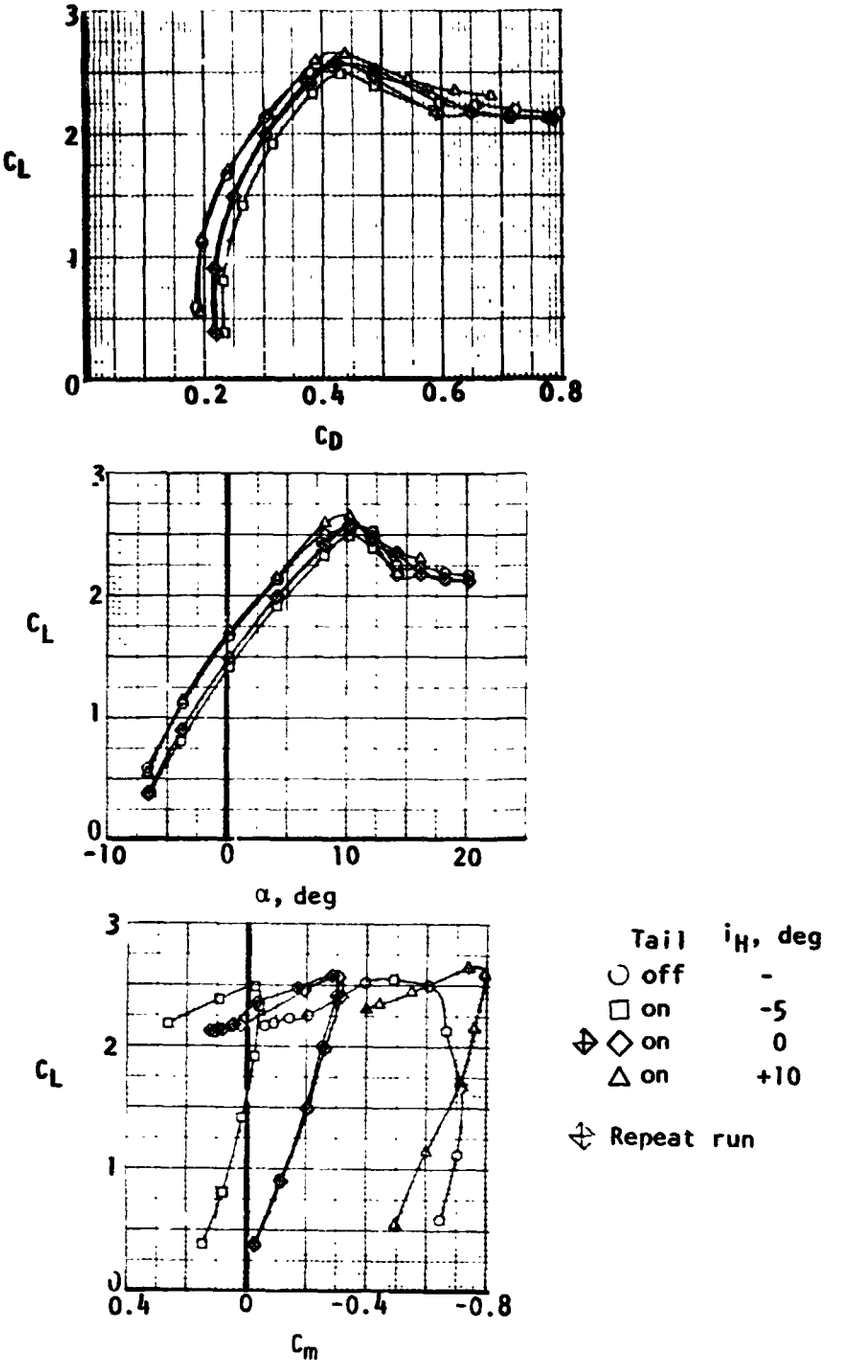

(c) Flaps down, tail on and off, fan inlets open.

Figure 33.- Concluded.

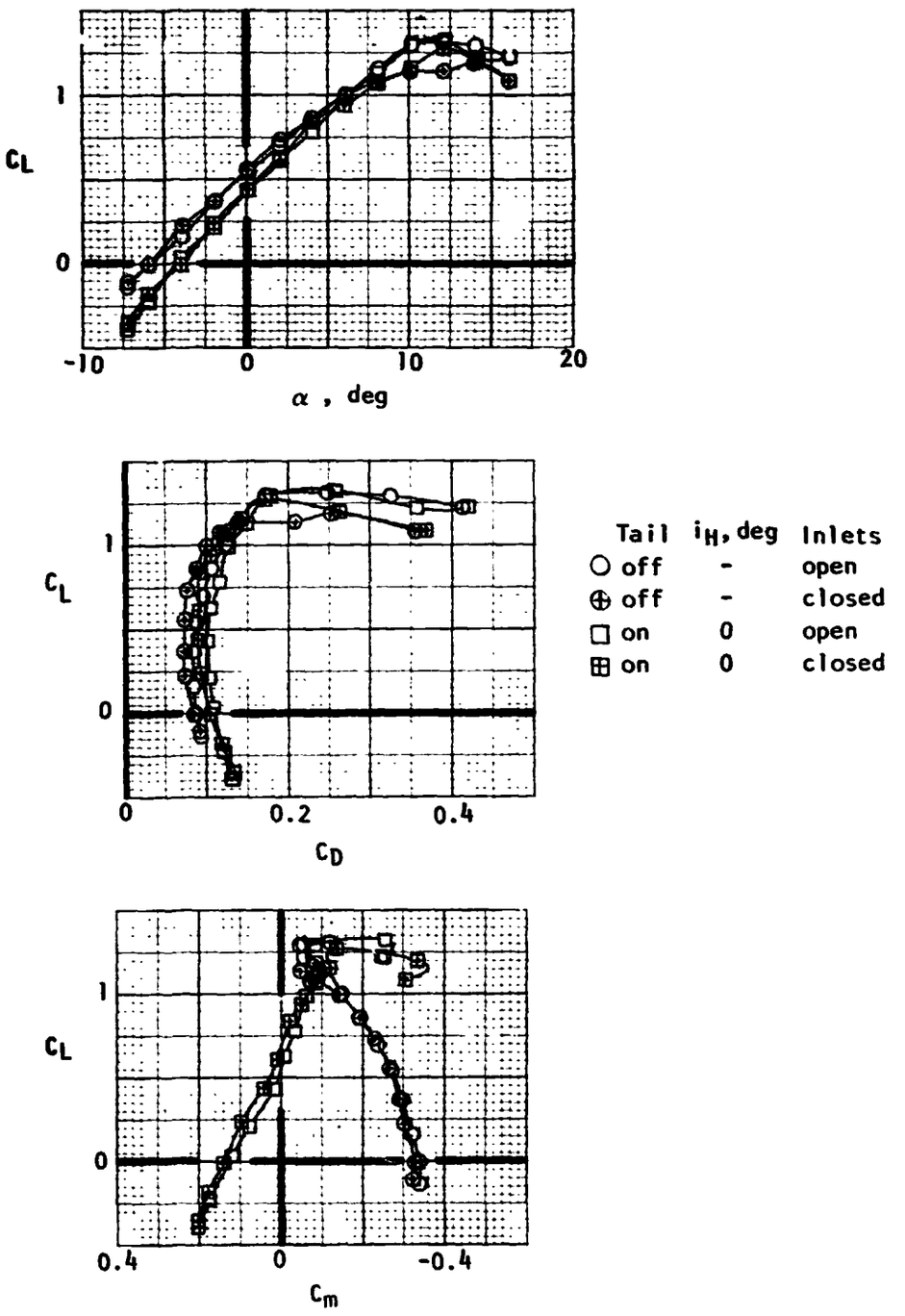

(a) Flaps up.

Figure 34.- Effect of fan inlet covers on power-off longitudinal forces and moments out of ground effect. δ_N = 0.

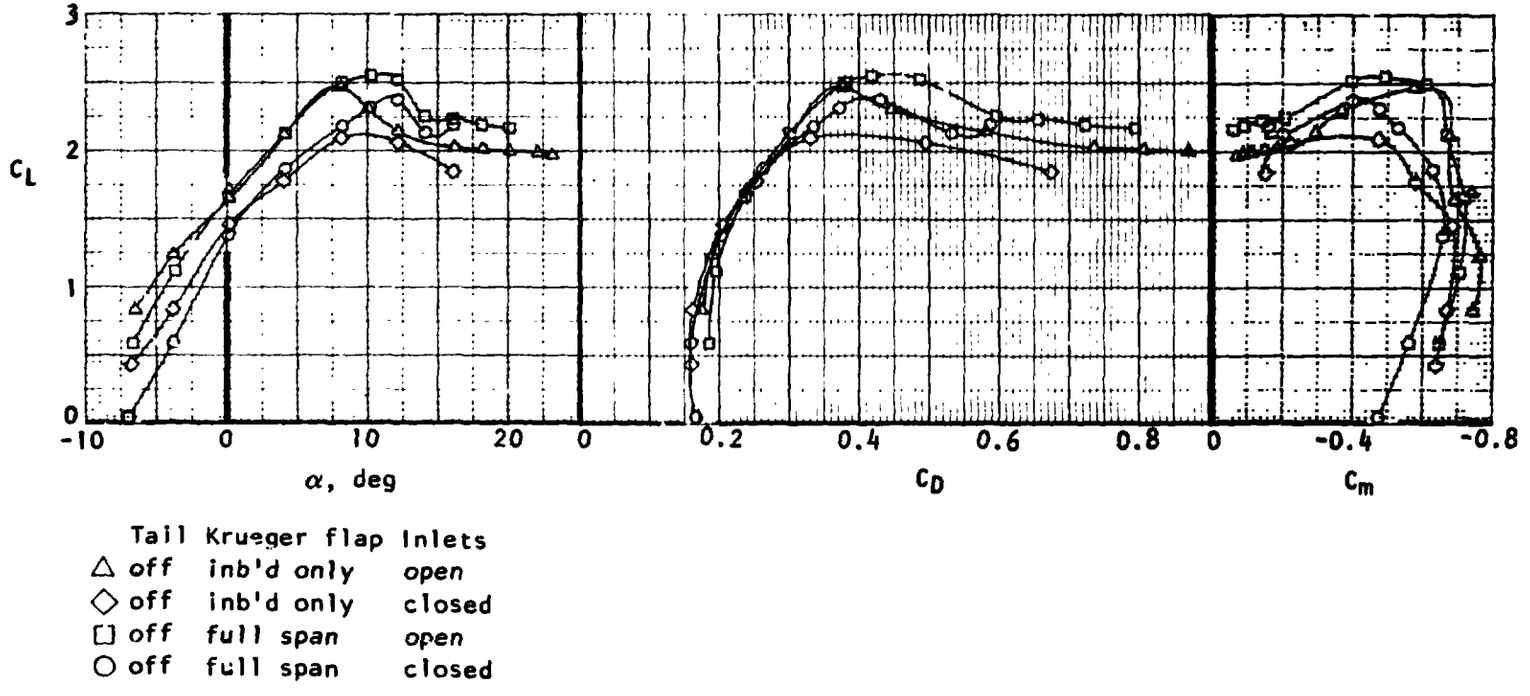

(b) Flaps down.

Figure 34.- Concluded.

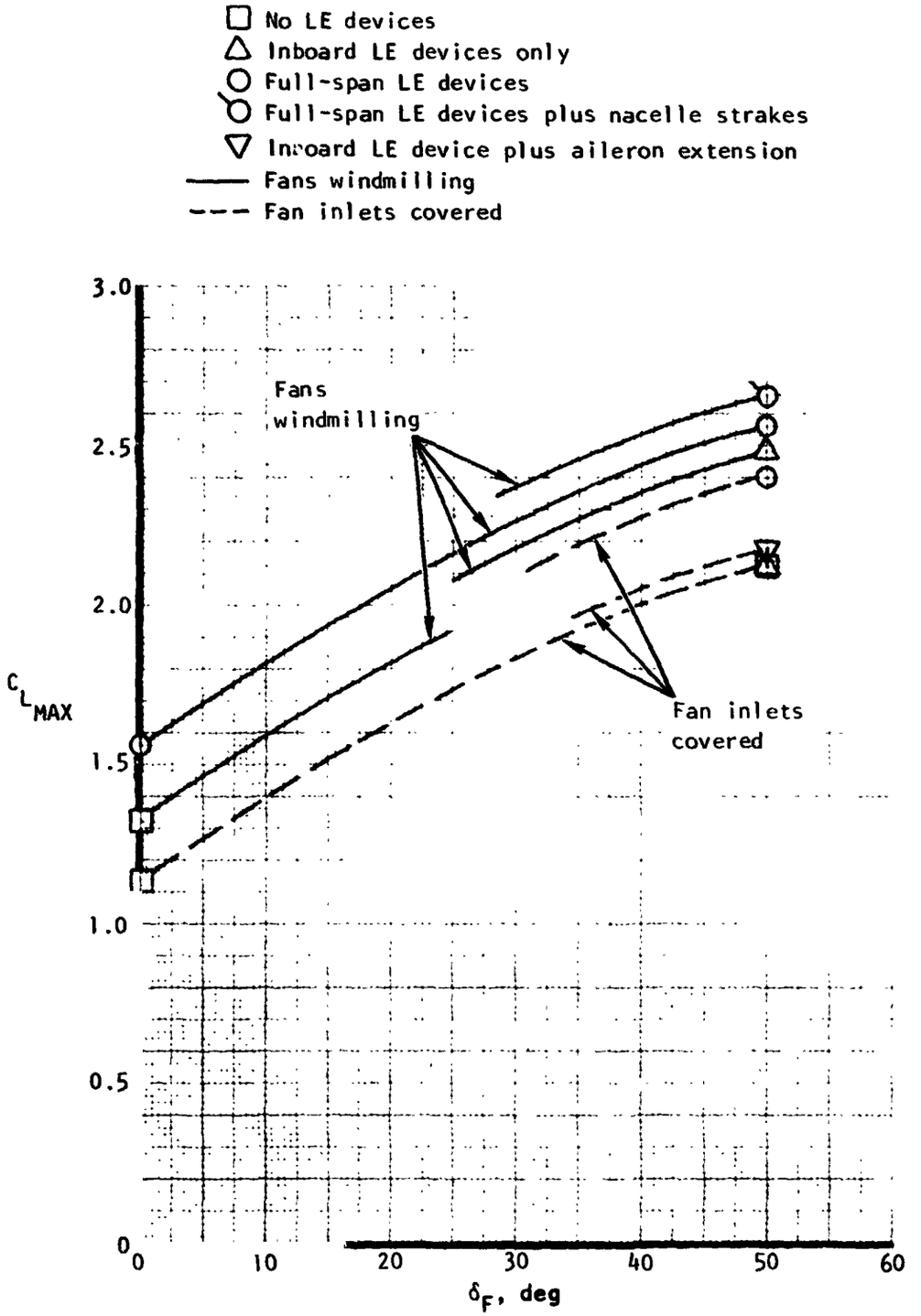

Figure 35. - Maximum lift summary. Power off, tail-off, OGE, δ_N=0°.

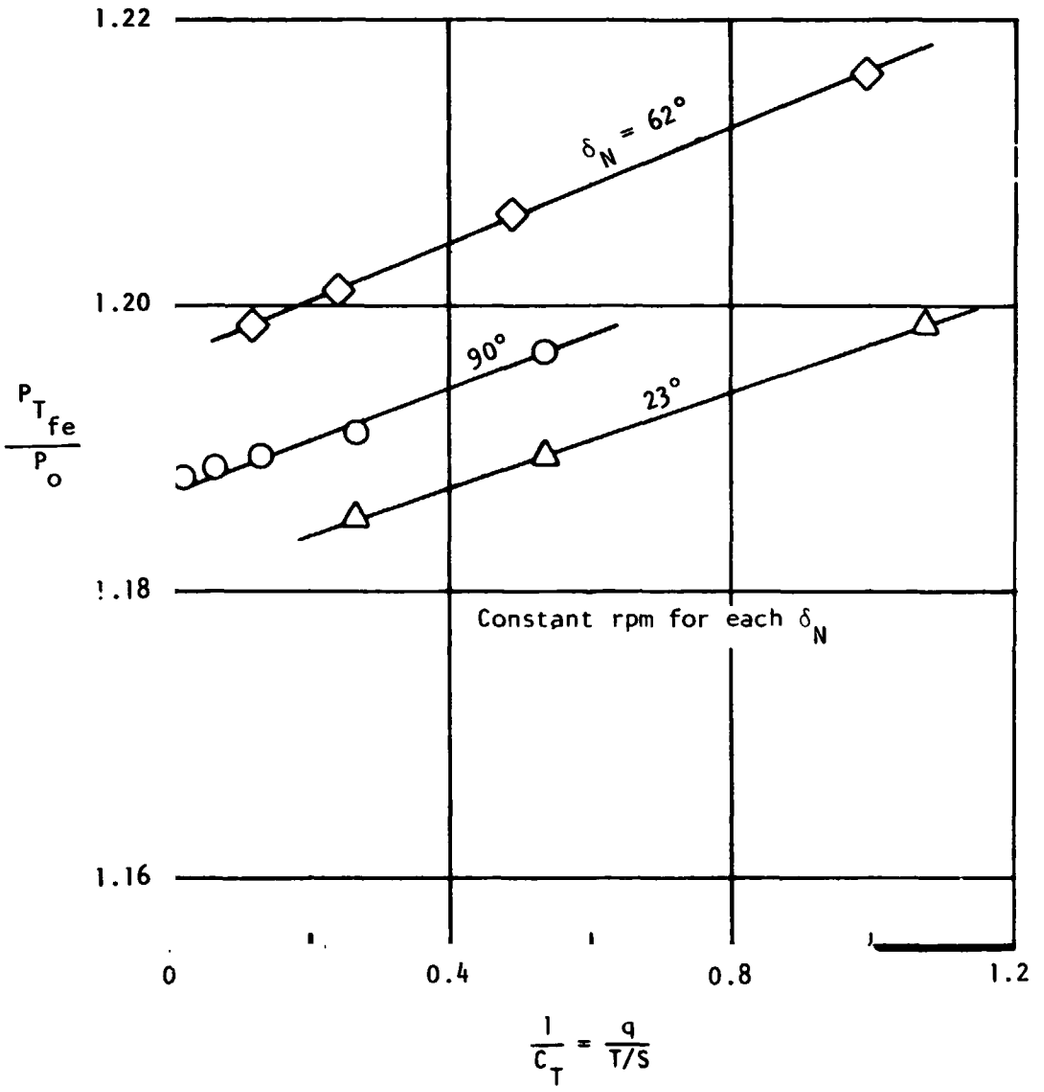

Figure 36. - Fan exit pressure ratio versus inverse of thrust coefficient.

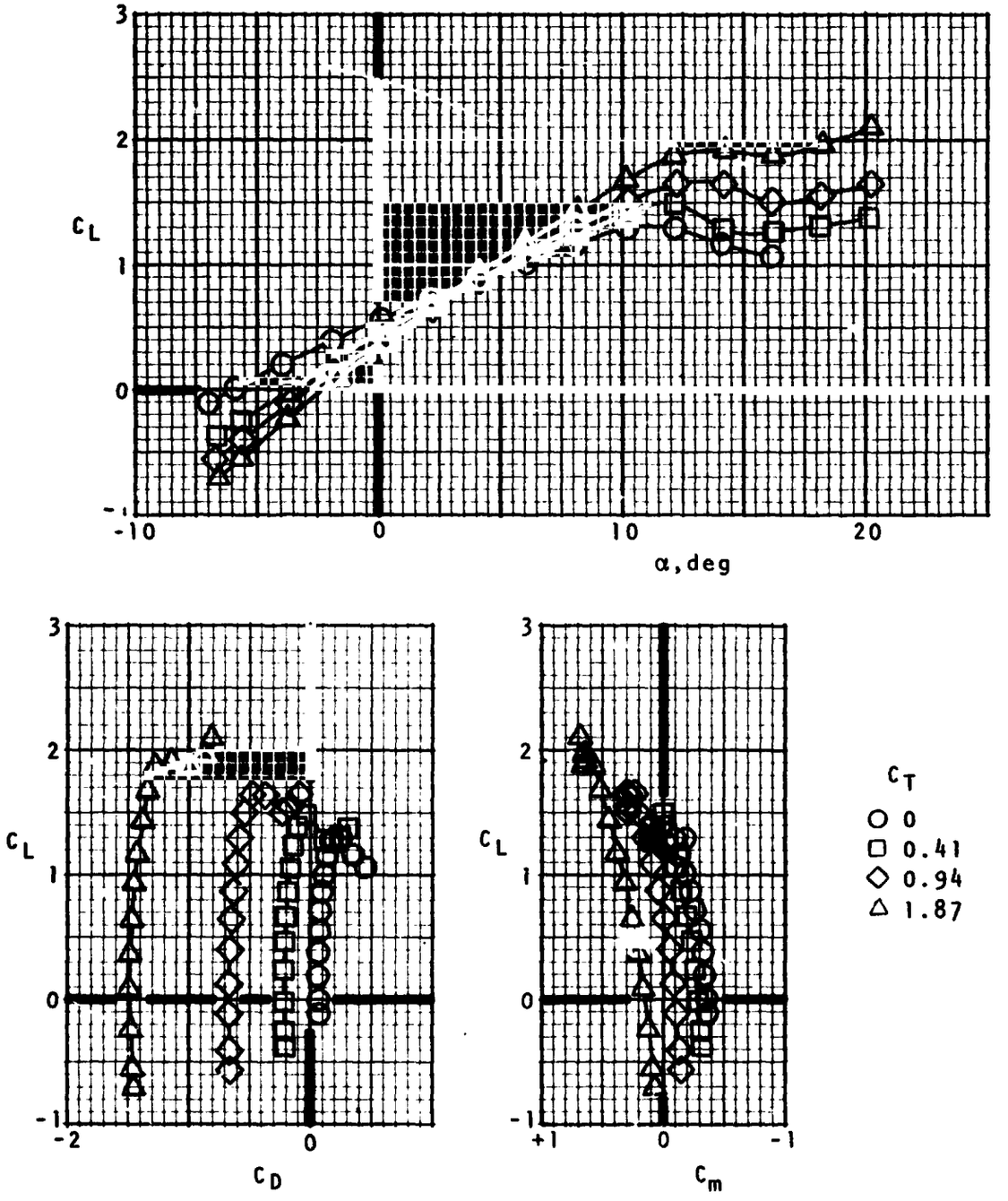

(a) Without leading edge devices.

Figure 37.- Flaps-up longitudinal forces and moments during transition out of ground effect. δ_N = 0, tail off.

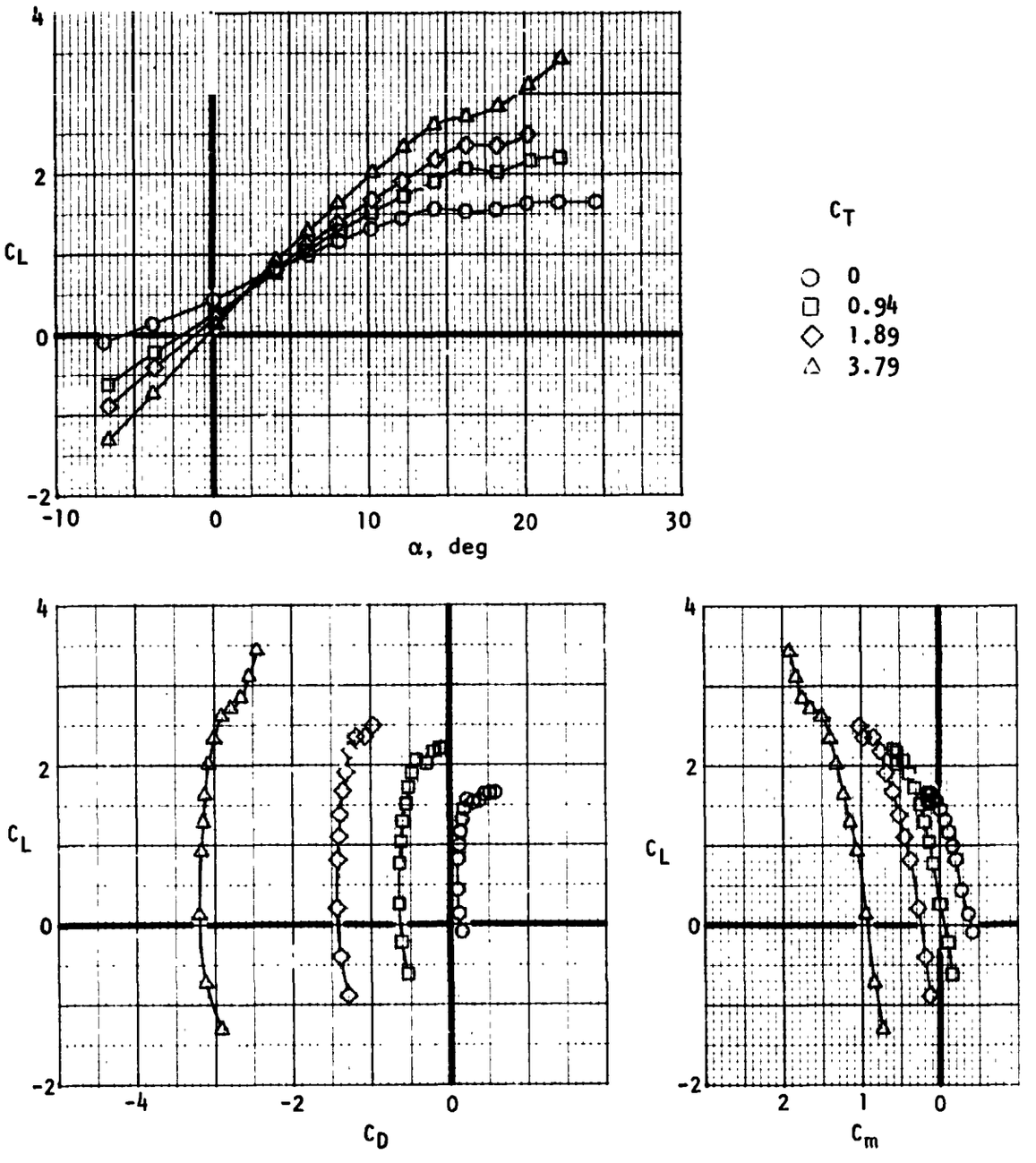

(b) With full span leading edge devices.

Figure 37.- Concluded.

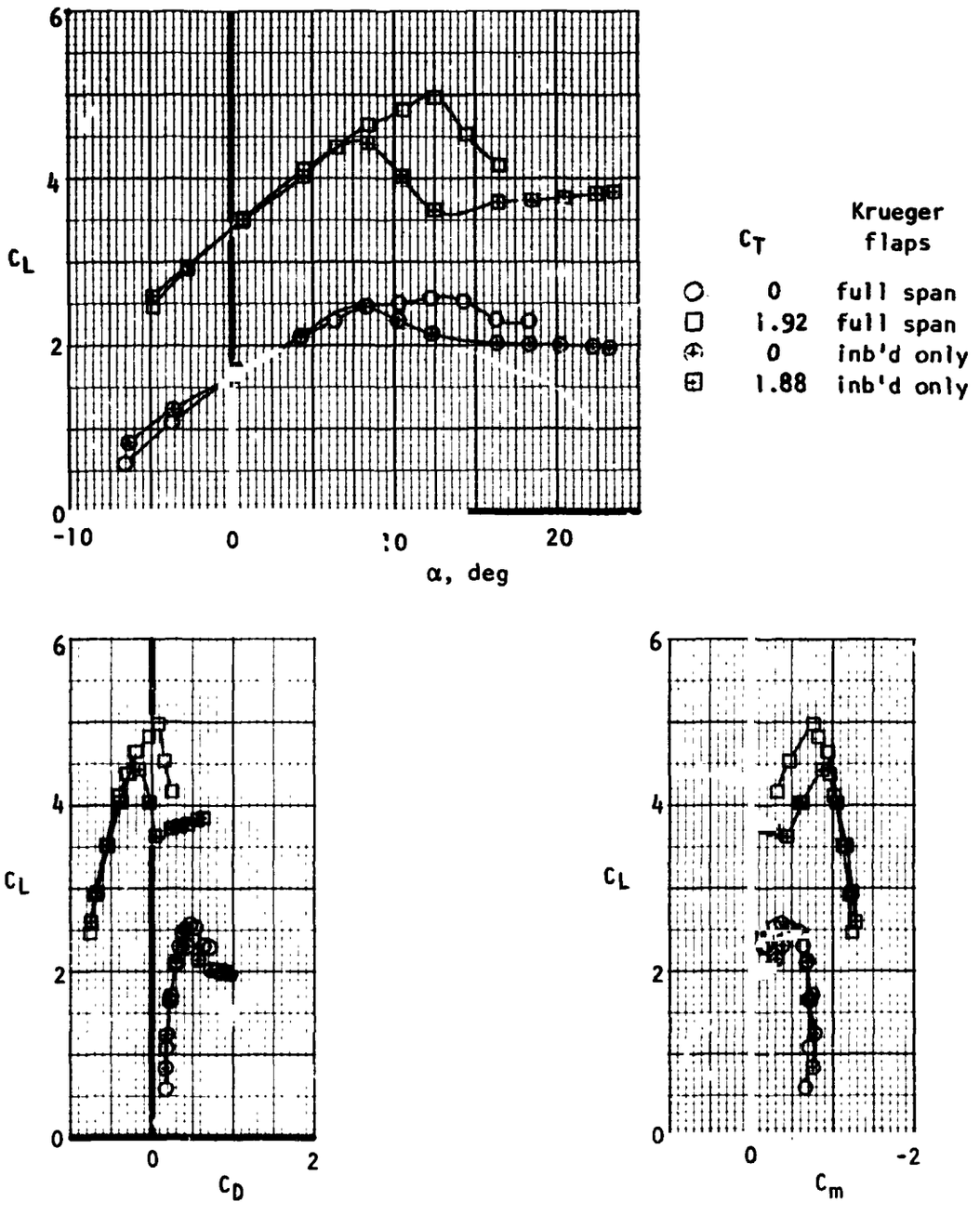

(a) Effect of leading edge devi .., tail off.

Figure 38.- Flaps-down longitudinal forces and moments during transition out of ground effect. δ_N =

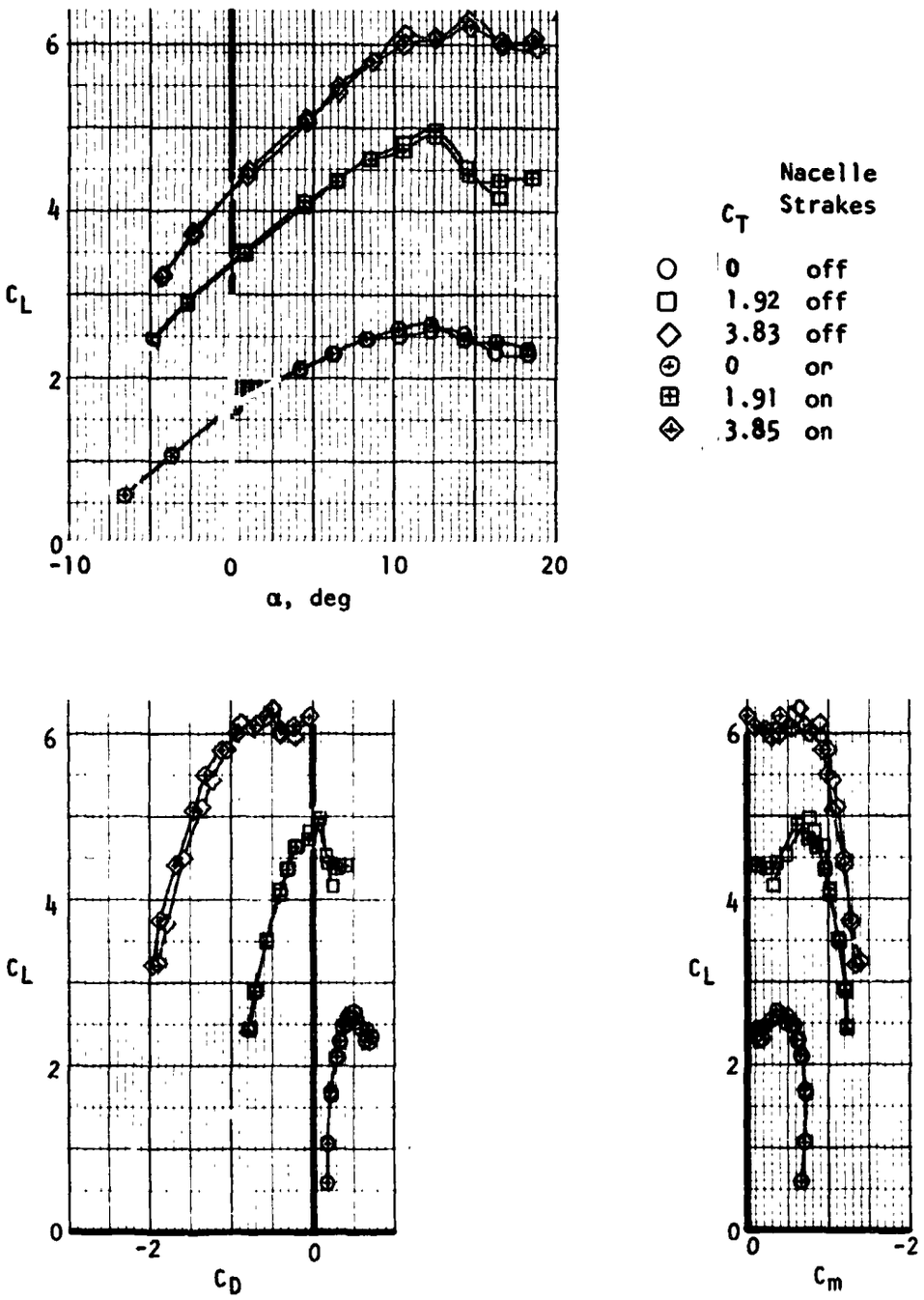

(b) Effect of nacelle strakes. Tail off, full span Krueger flap. C_L as variable.

Figure 38.- Continued.

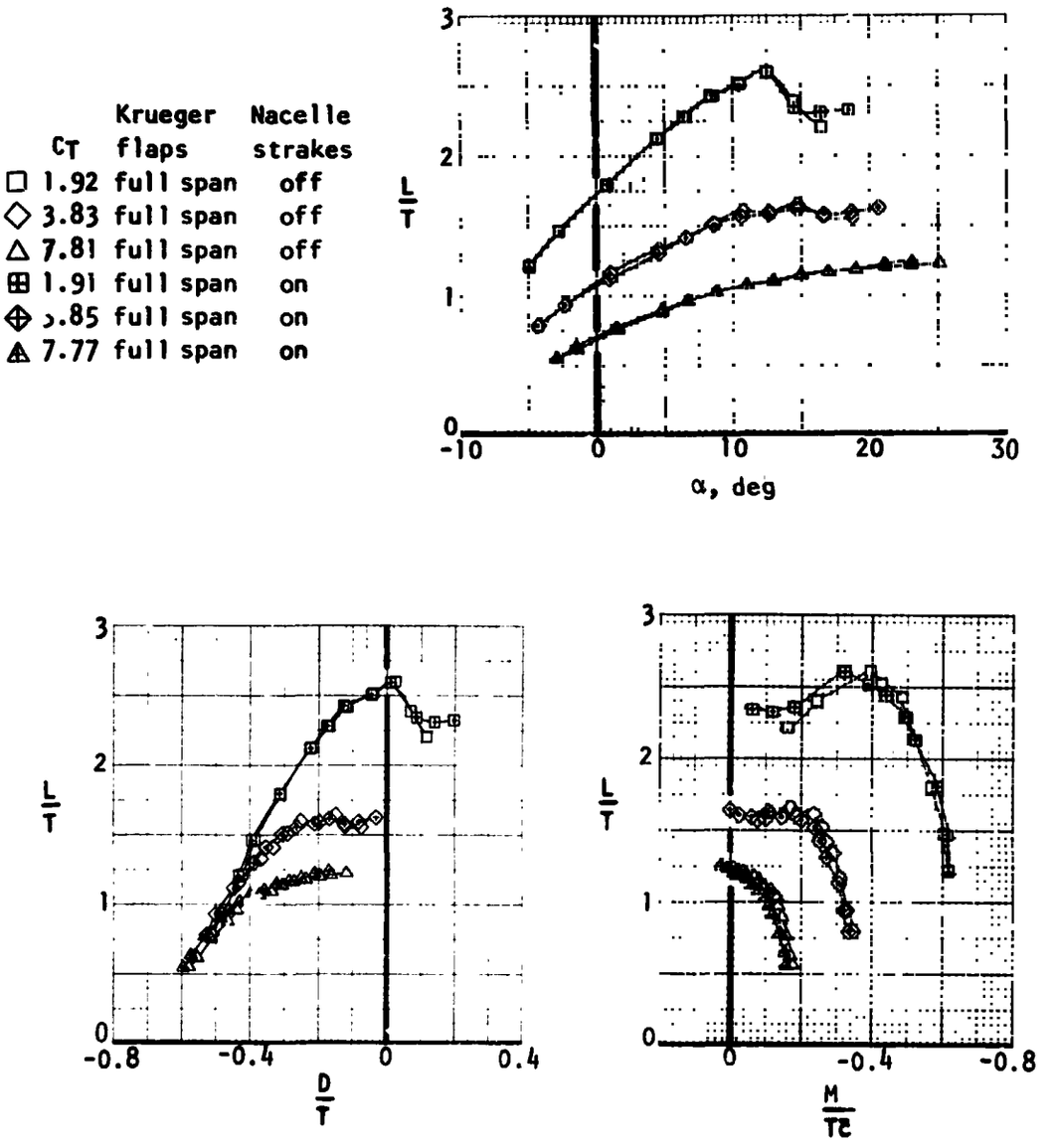

(c) Effect of nacelle strakes, tail off, L/T as variable.

Figure 38. - Continued.

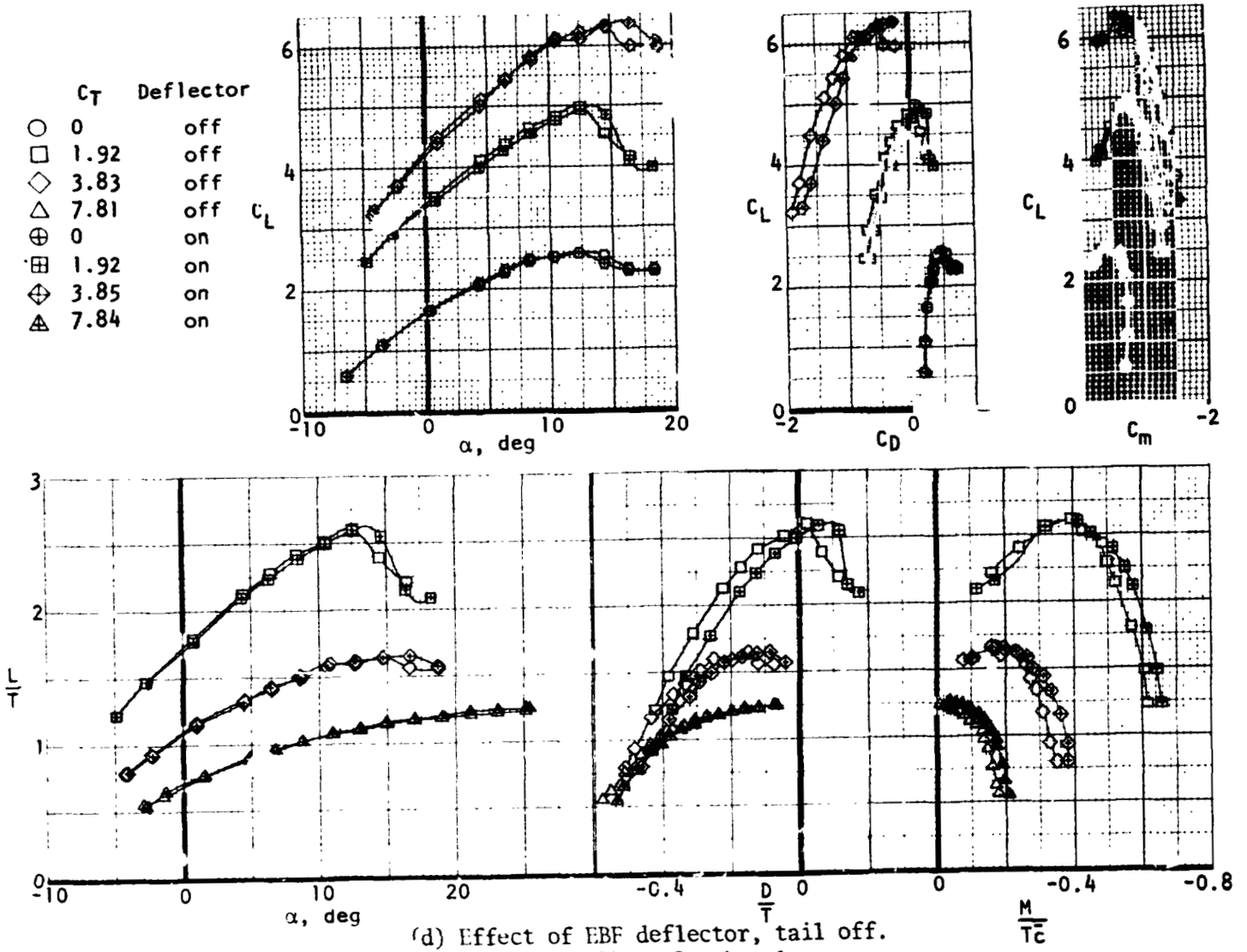

(d) Effect of EBF deflector, tail off.

Figure 38. - Continued.

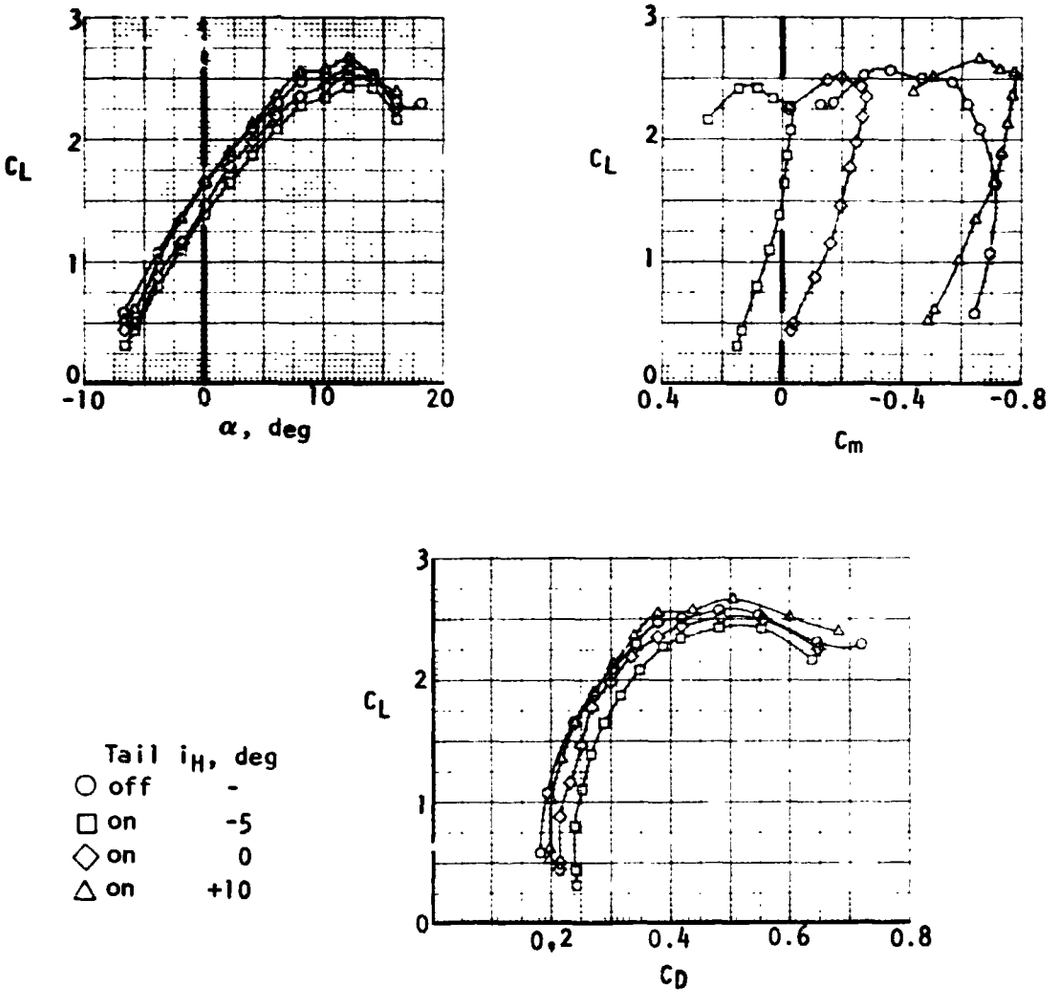

(e) Tail effectiveness at $C_T = 0$.

Figure 38.- Continued.

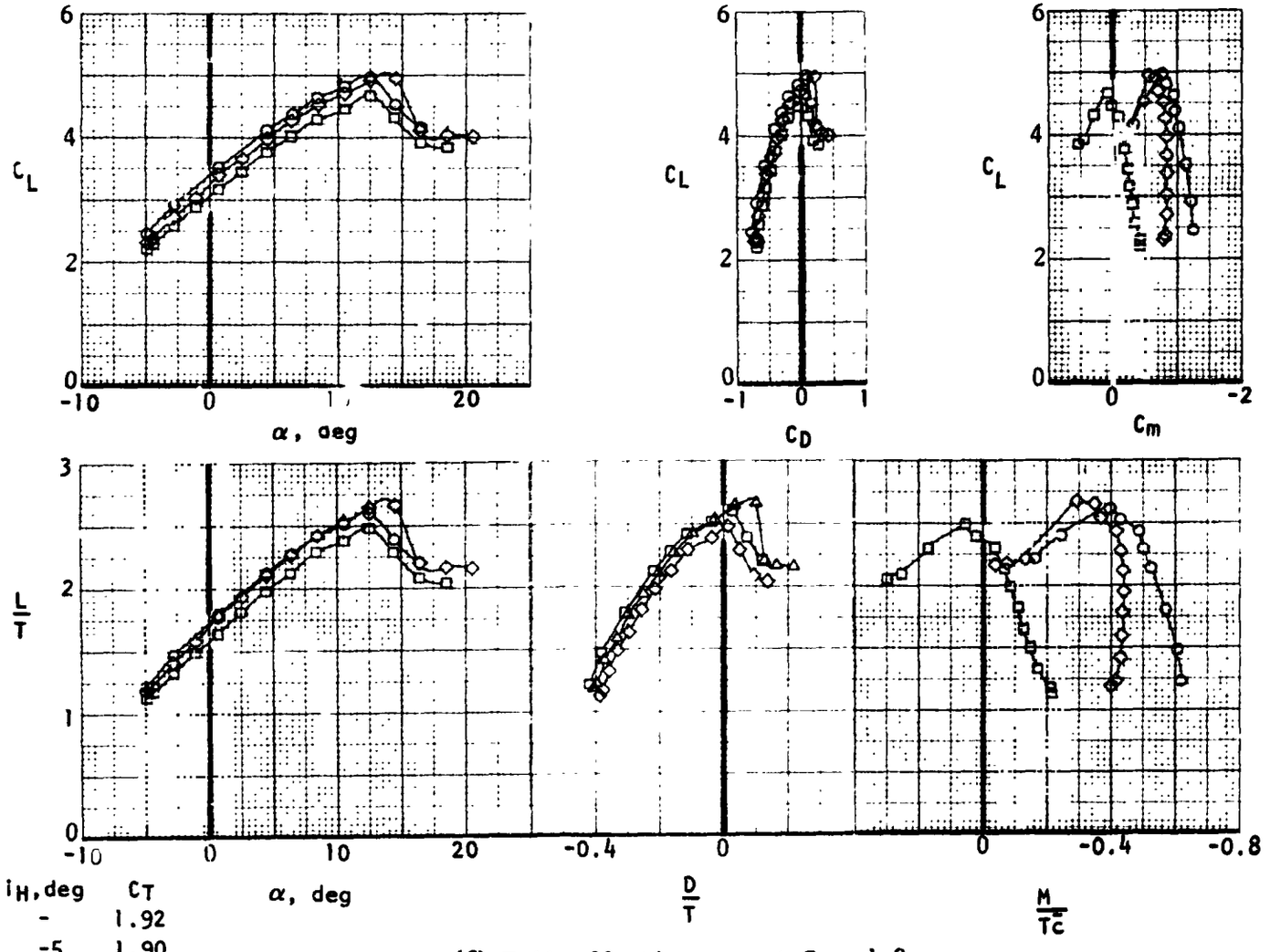

(f) Tail effectiveness at C_T = 1.9

Figure 38.- Continued.

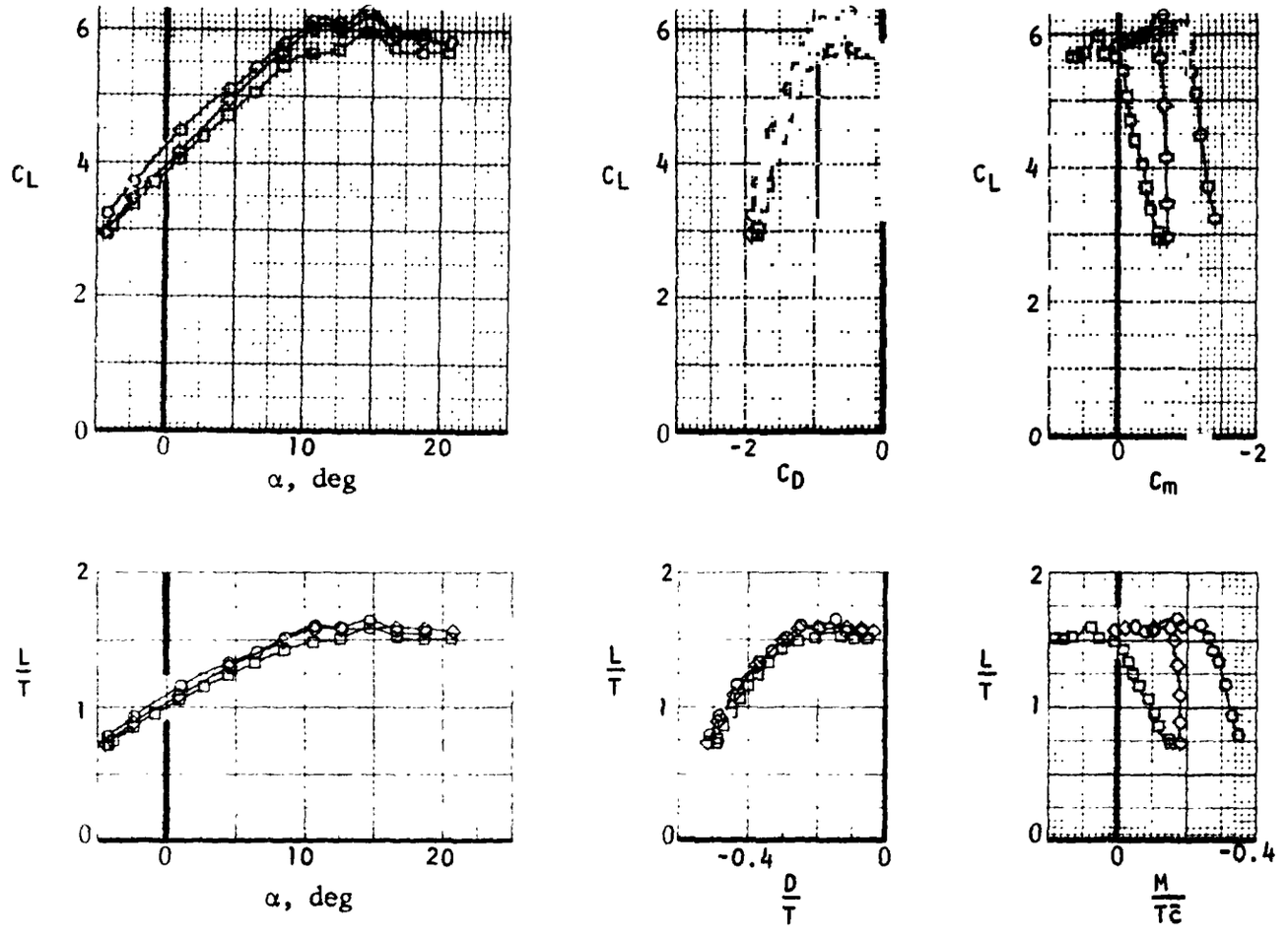

	Tail	i_H, deg	C_T
○	off	-	3.83
□	on	-5	3.80
◇	on	+10	3.77

(g) Tail effectiveness at C_T = 3.8.

Figure 38.- Continued.

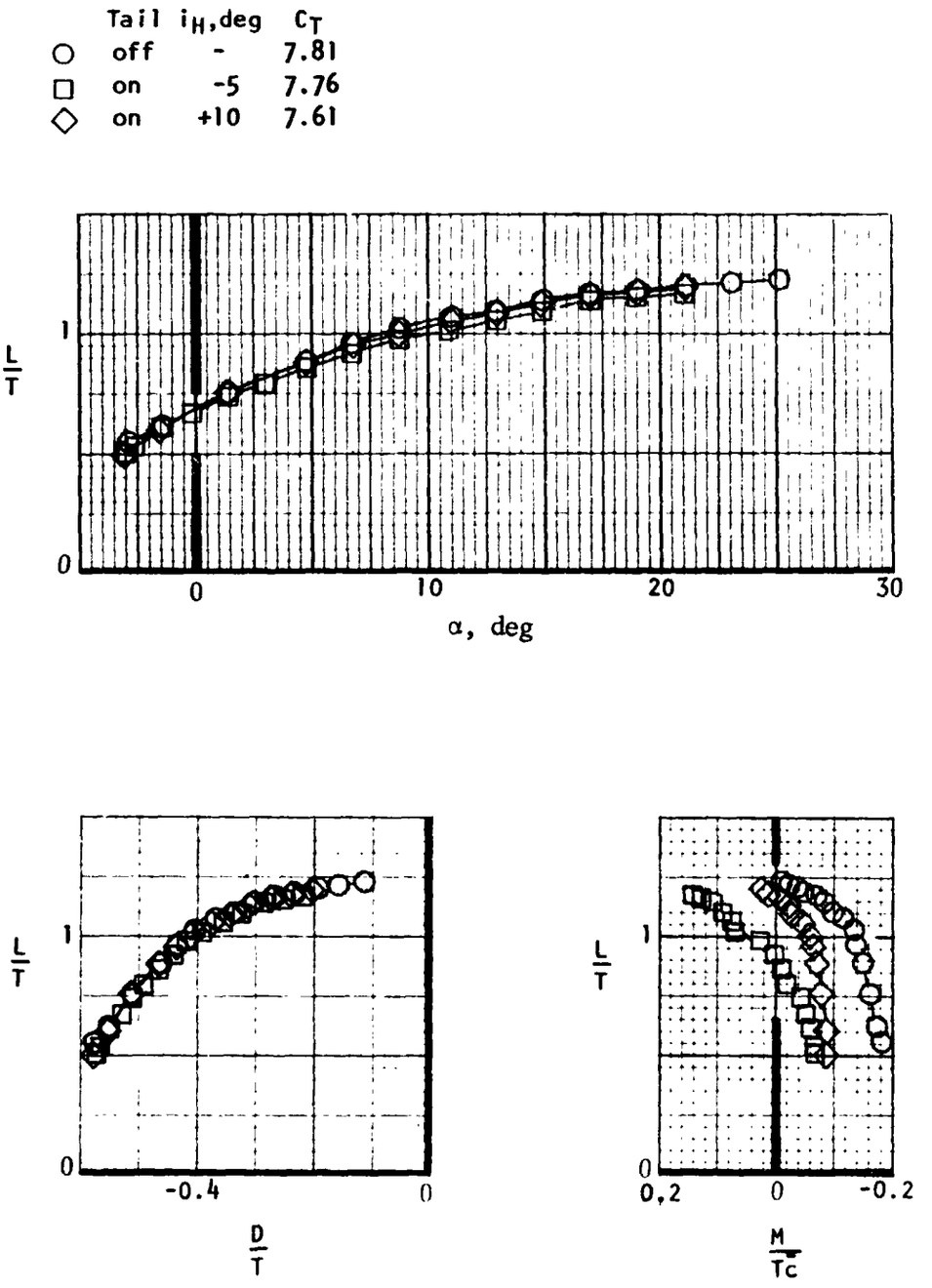

(h) Tail effectiveness at C_T = 7.7.

Figure 38.- Concluded.

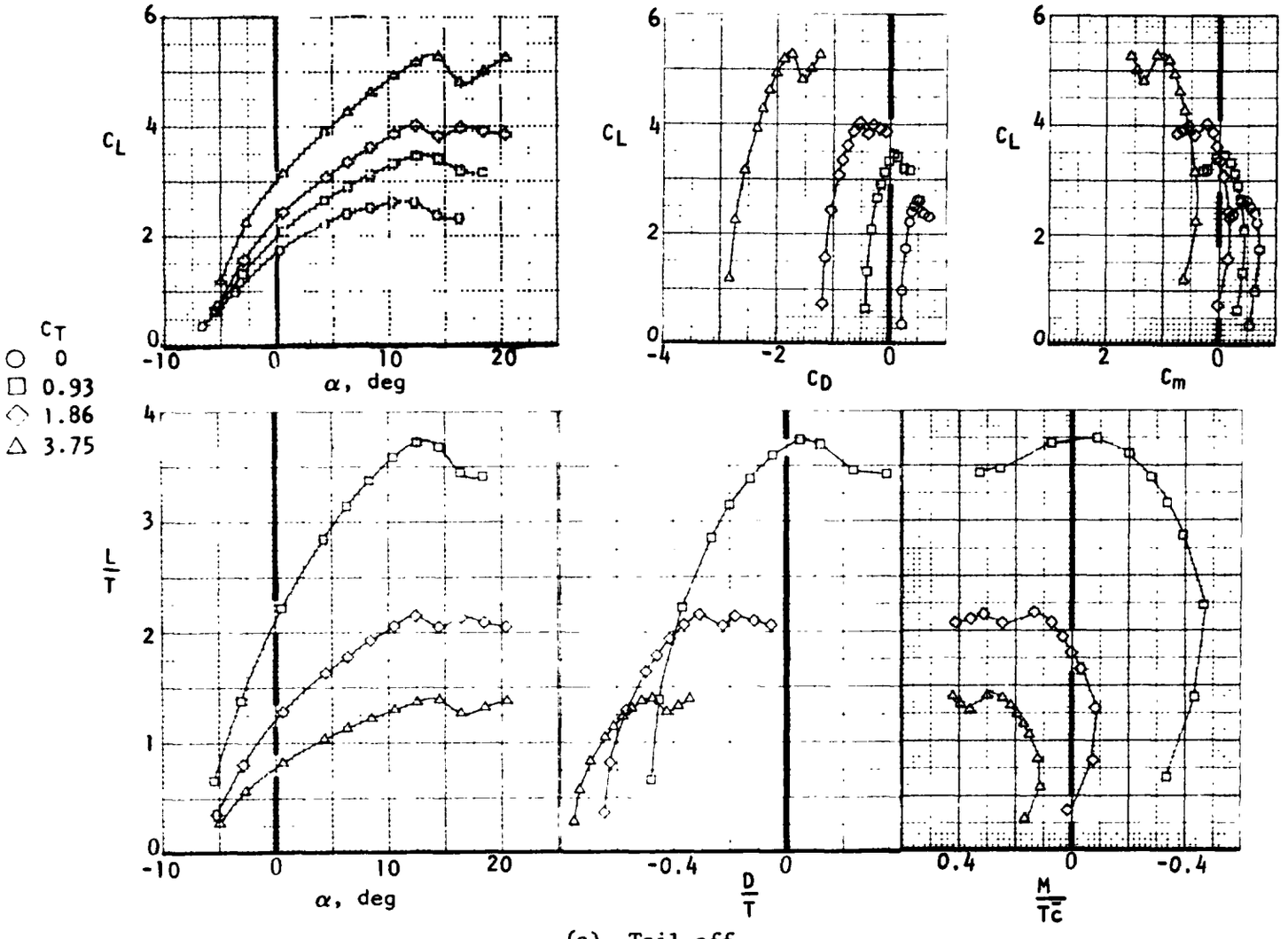

(a) Tail off.

Figure 39.- Flaps-down longitudinal forces and moments during transition out of ground effect. $\delta_N = 23°$.

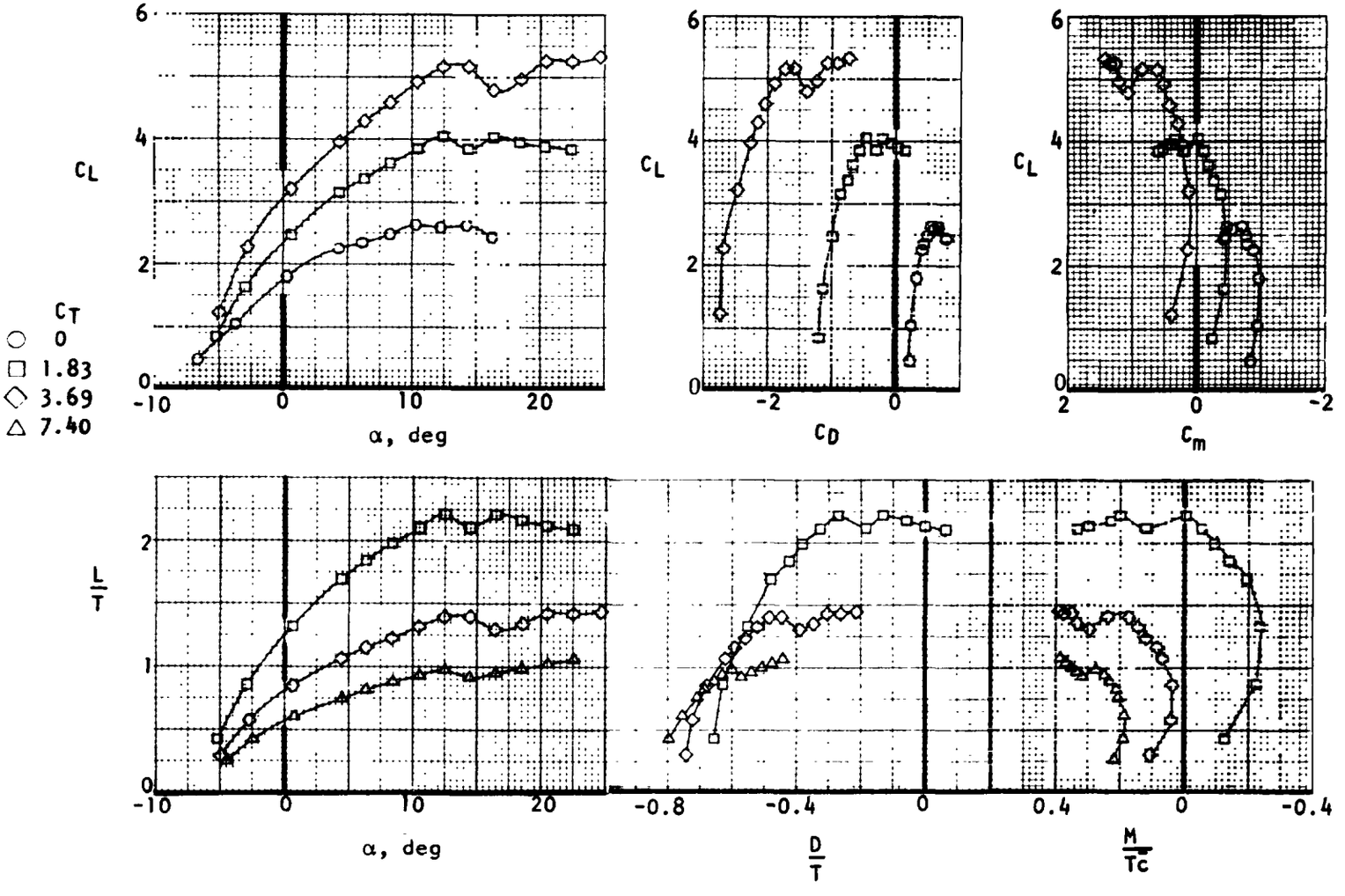

(b) Ta. on, $i_H = +20°$.

Figure 39.- Concluded.

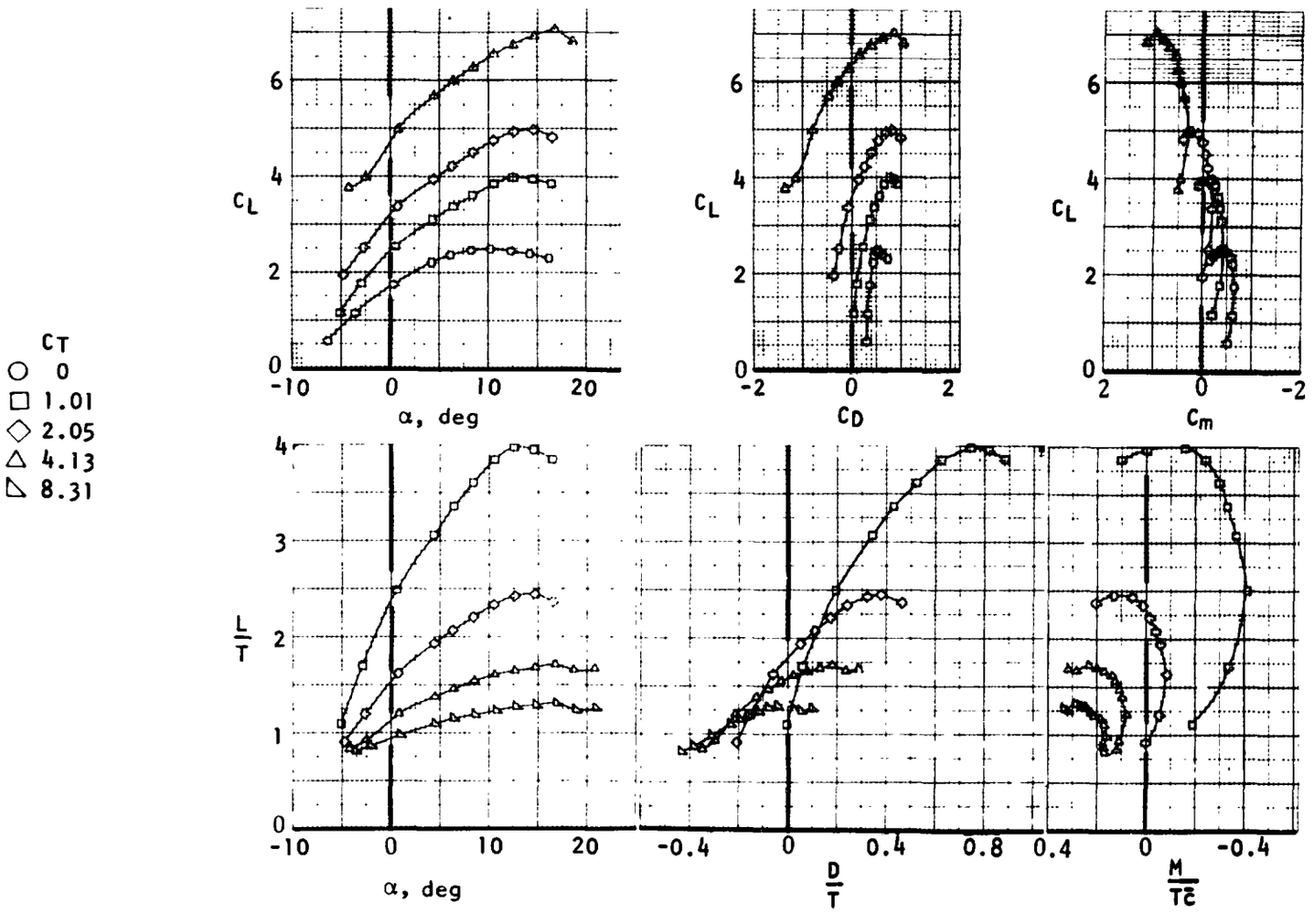

(a) Tail off.

Figure 40.- Flaps-down longitudinal forces and moments during transition out of ground effect. $\delta_N = 62°$.

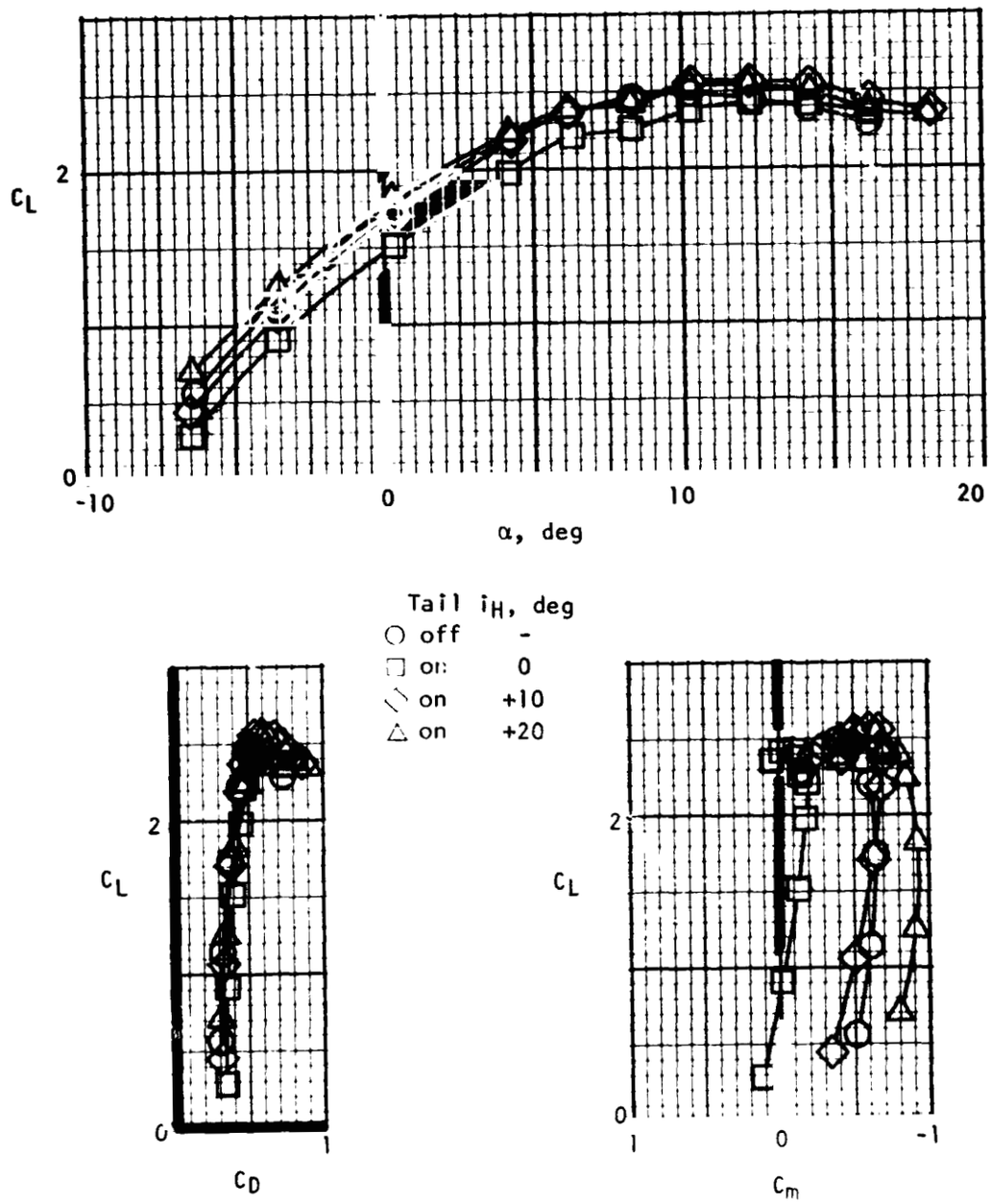

(b) Tail Effectiveness at $C_T = 0$.

Figure 40.- Continued.

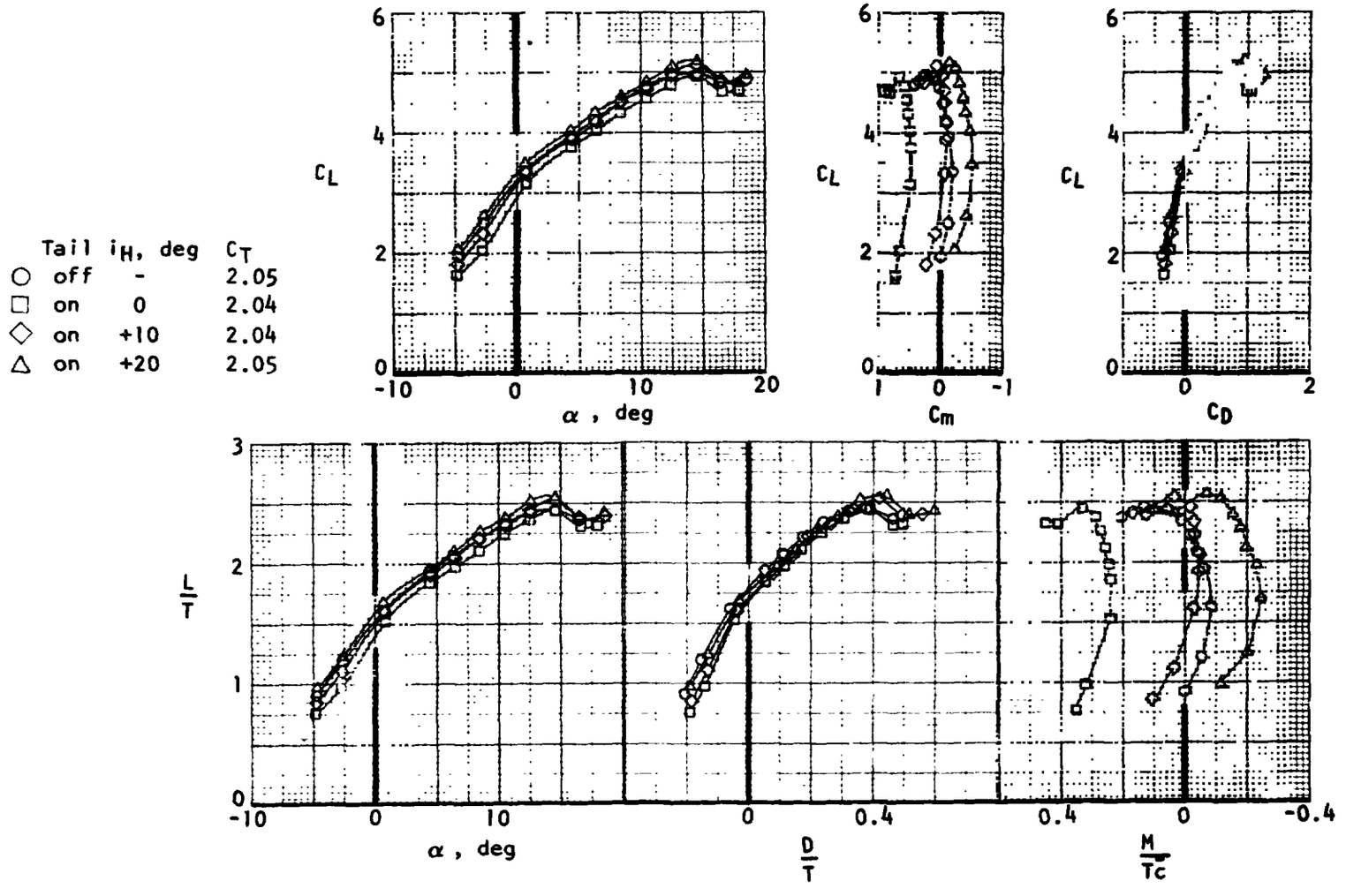

(c) Tail effectiveness at C_T = 2.0.

Figure 40.- Continued.

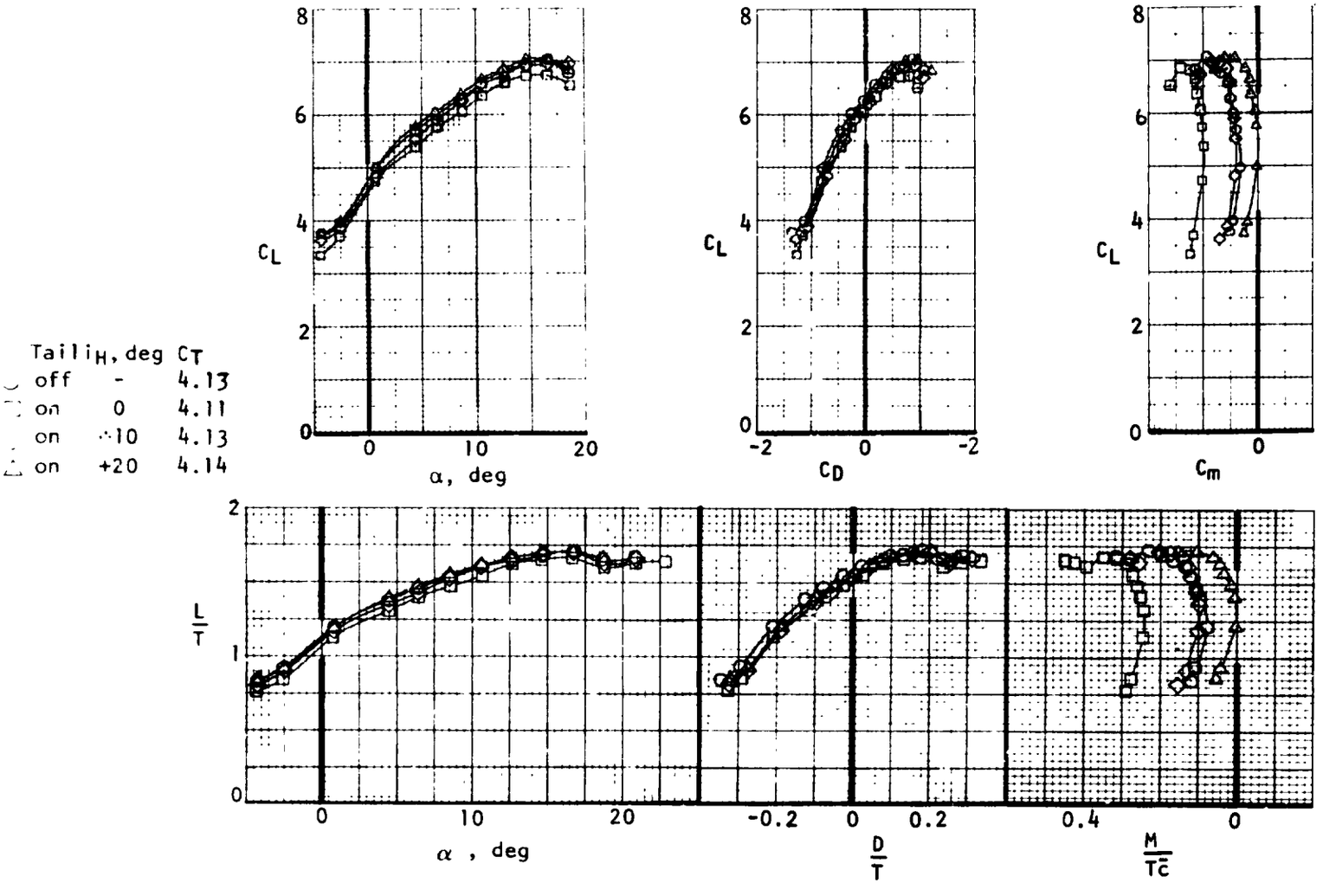

(d) Tail effectiveness at C_T = 4.1.

Figure 40.- Continued.

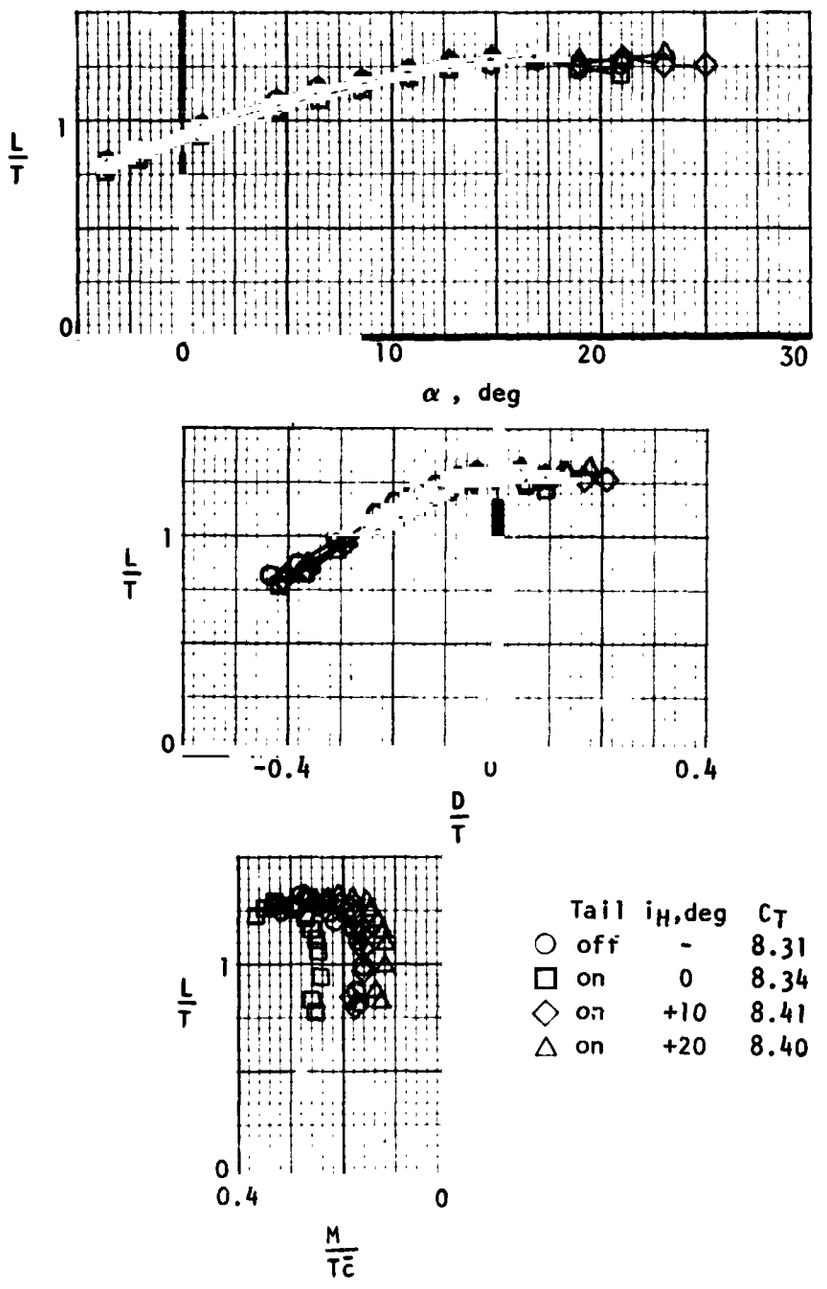

(e) Tail effectiveness at C_T = 8.4

Figure 4ι - Concluded.

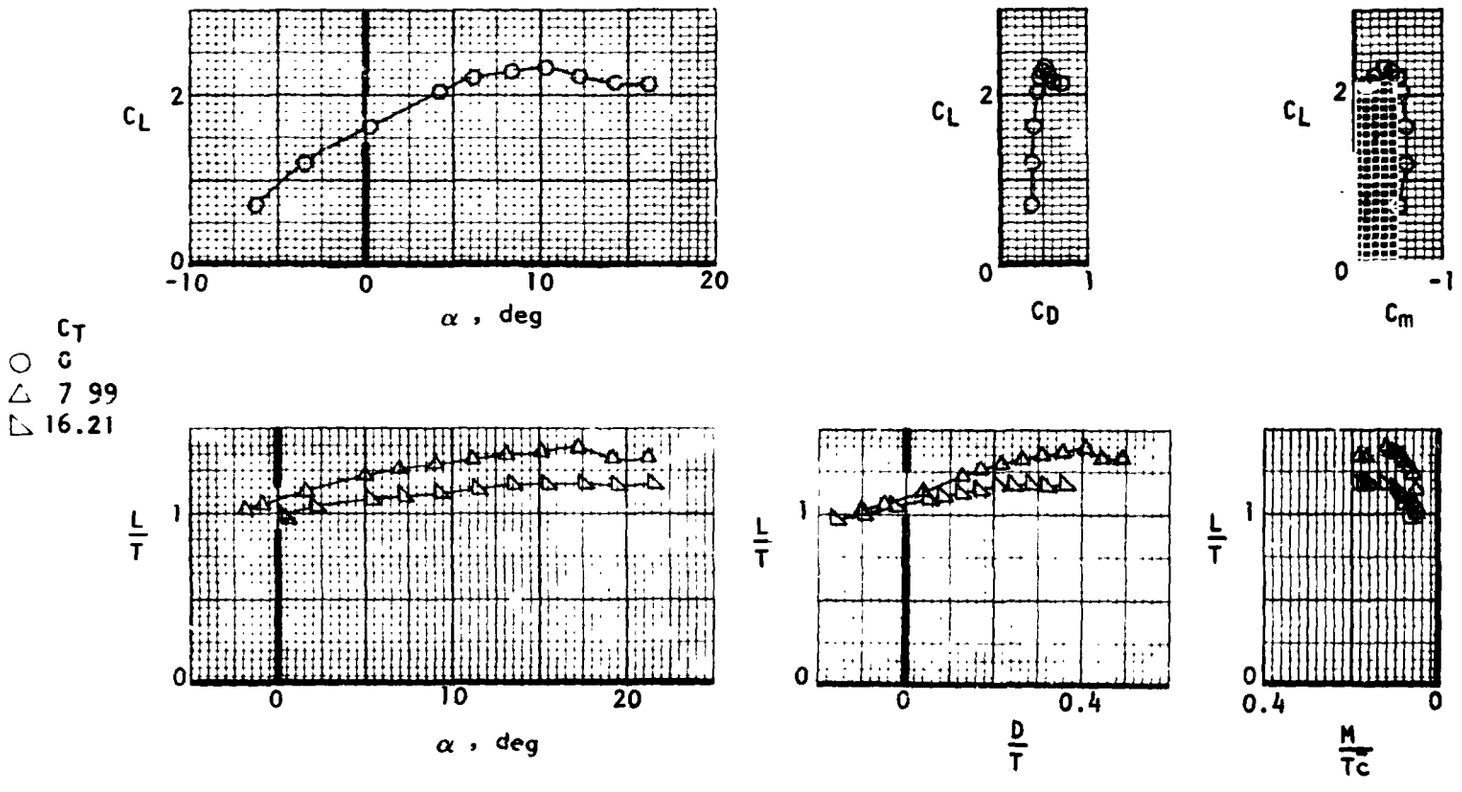

(a) Tail off.

Figure 41.- Flaps-down longitudinal forces and moments during transition out of ground effect. $\delta_N = 80°$.

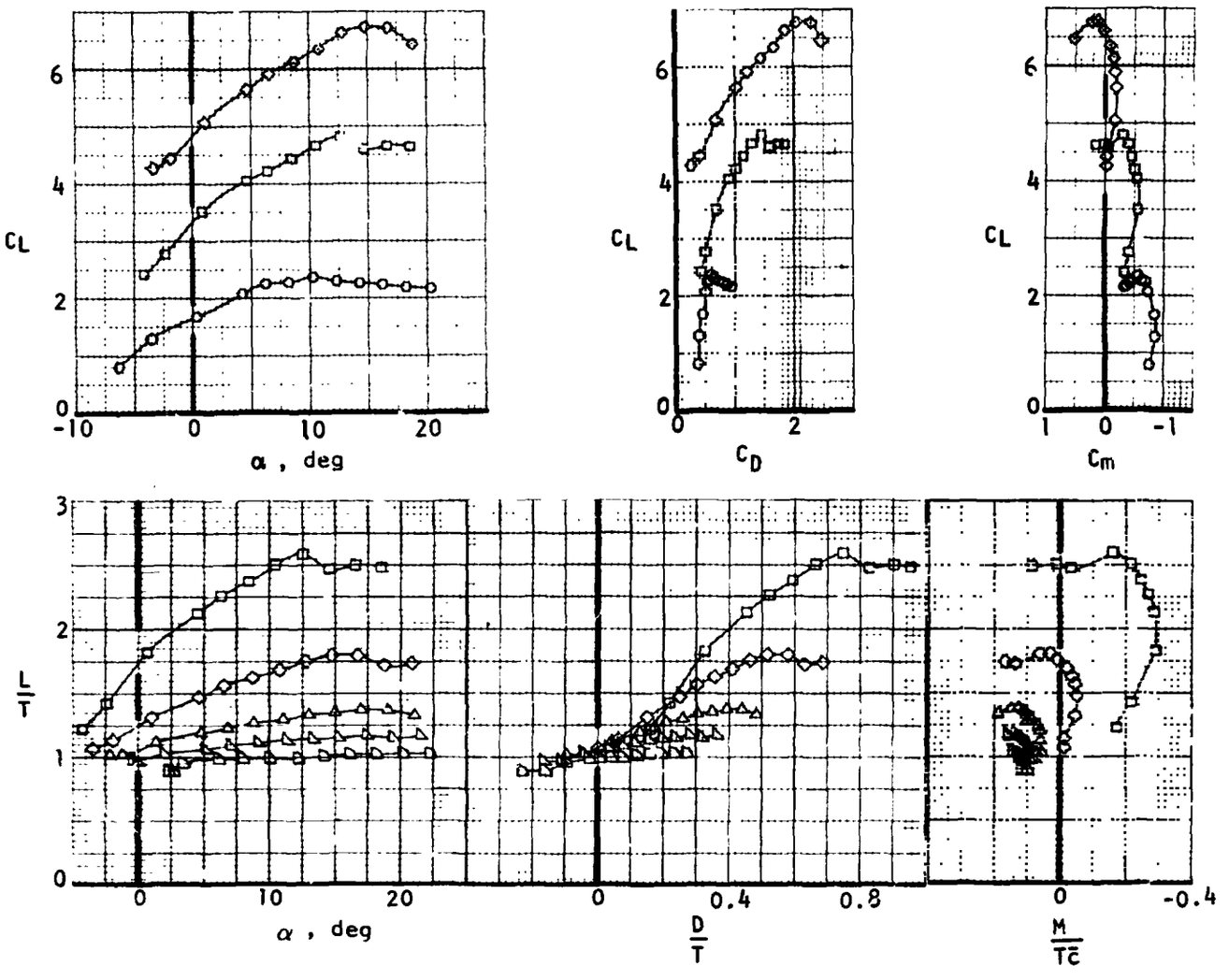

(b) Tail on, $i_H = +20°$.

Figure 41.- Concluded.

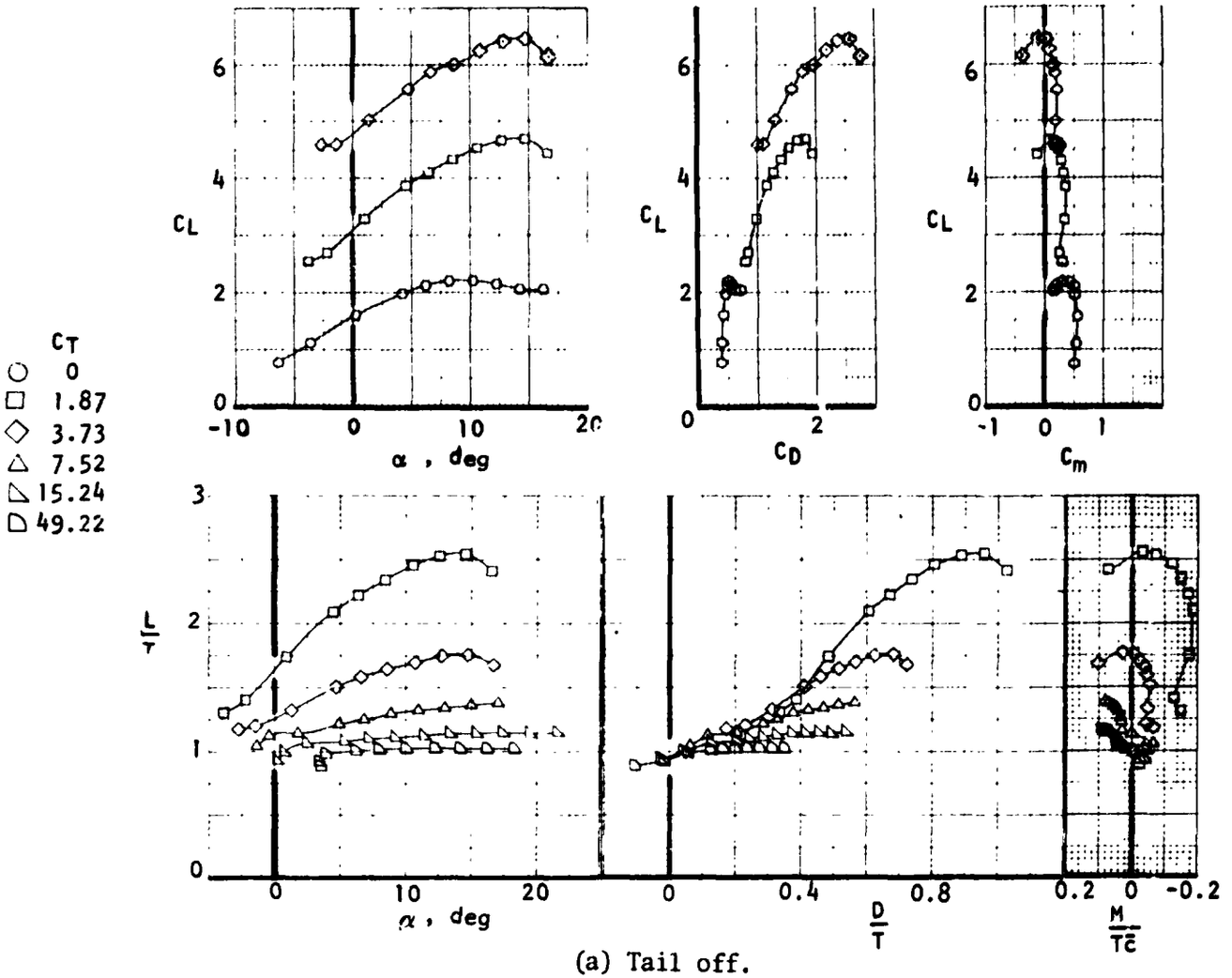

(a) Tail off.

Figure 42.- Flaps-down longitudinal forces and moments during transition out of ground effect. δ_N = 90°.

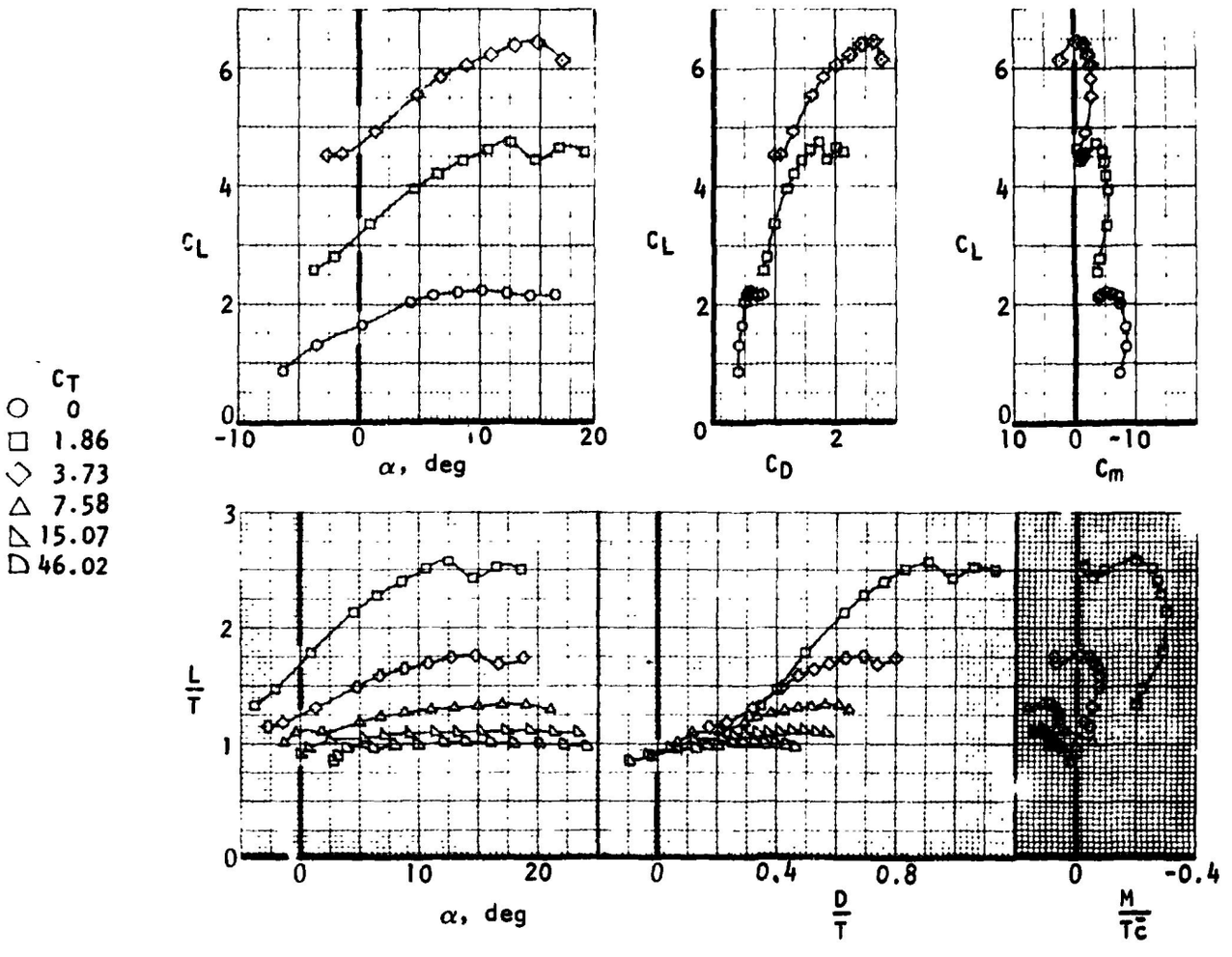

(b) Tail on, $i_H = 20°$.

Figure 42.- Continued.

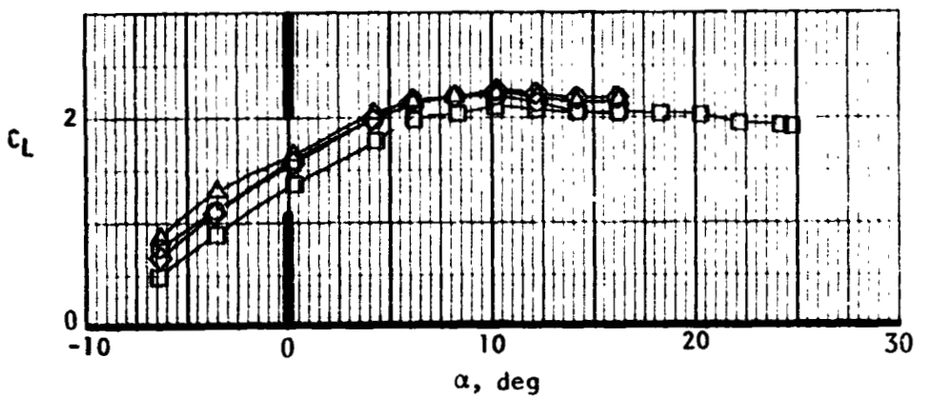

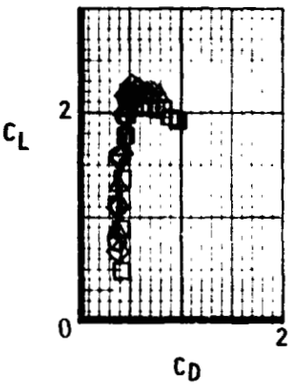

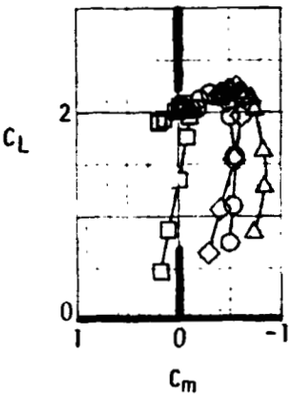

Tail	i_H, deg
○ off	-
□ on	0
◇ on	+10
△ on	+20

(c) Tail effectiveness at $C_T = 0$.

Figure 42.- Continued.

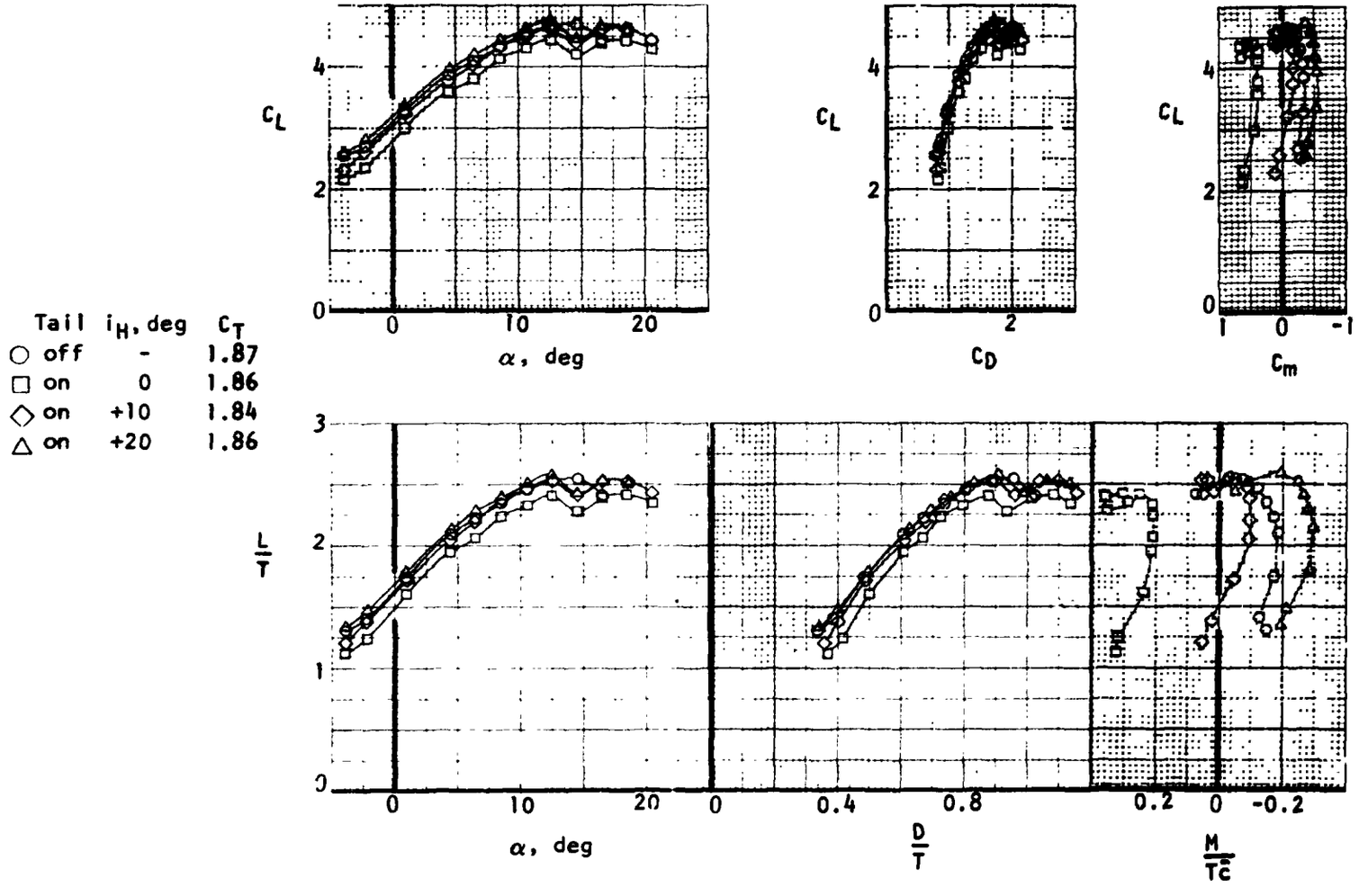

(d) Tail effectiveness at $C_T = 1.9$

Figure 42.- Continued.

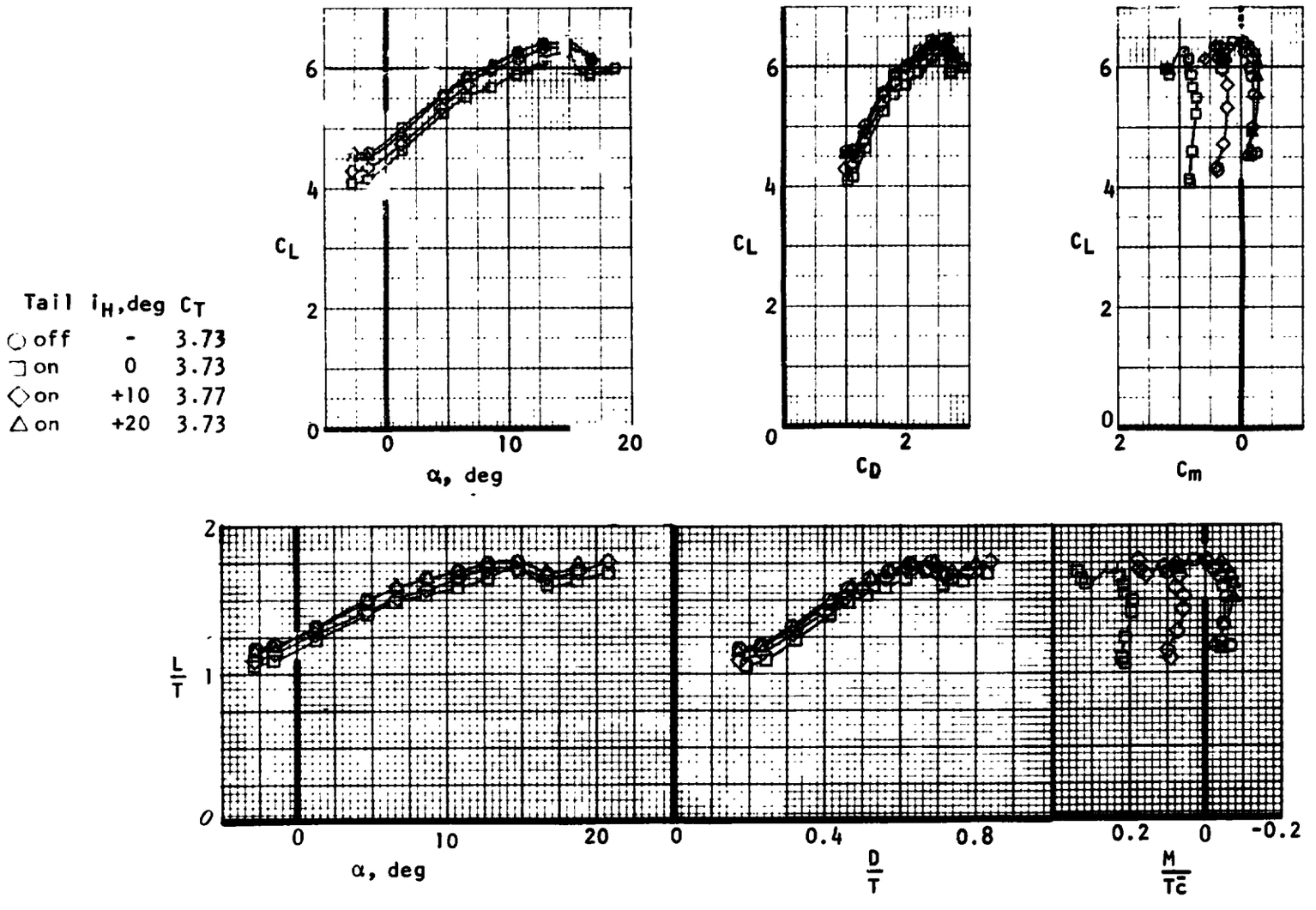

Figure 42.- Continued. (e) Tail effectiveness at C_T = 3.7.

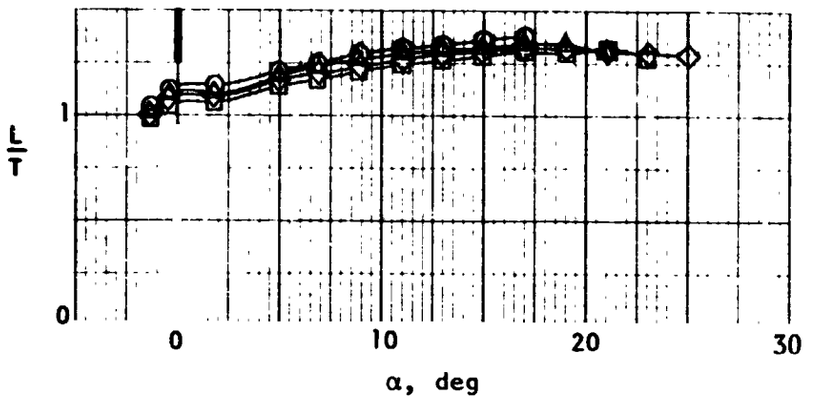

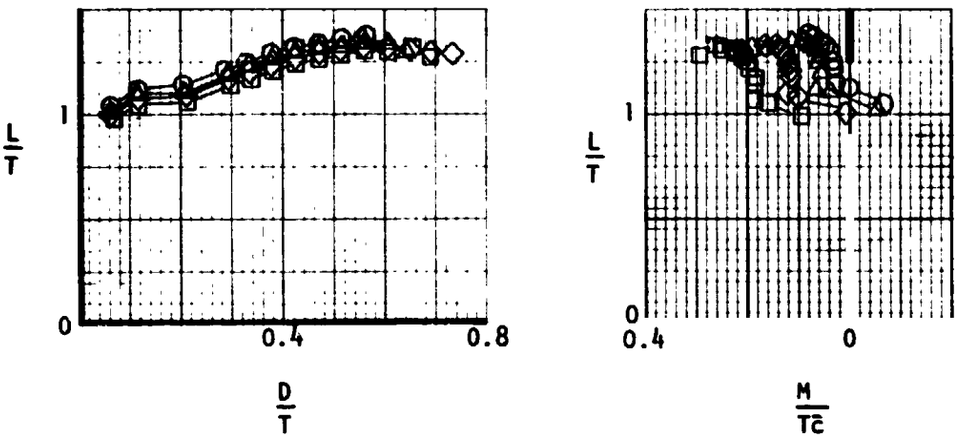

Tail	i_H, deg	C_T
○ off	-	7.52
□ on	0	7.63
◇ on	+10	7.53
△ on	+20	7.58

(f) Tail effectiveness at C_T =7.6.

Figure 42.- Concluded.

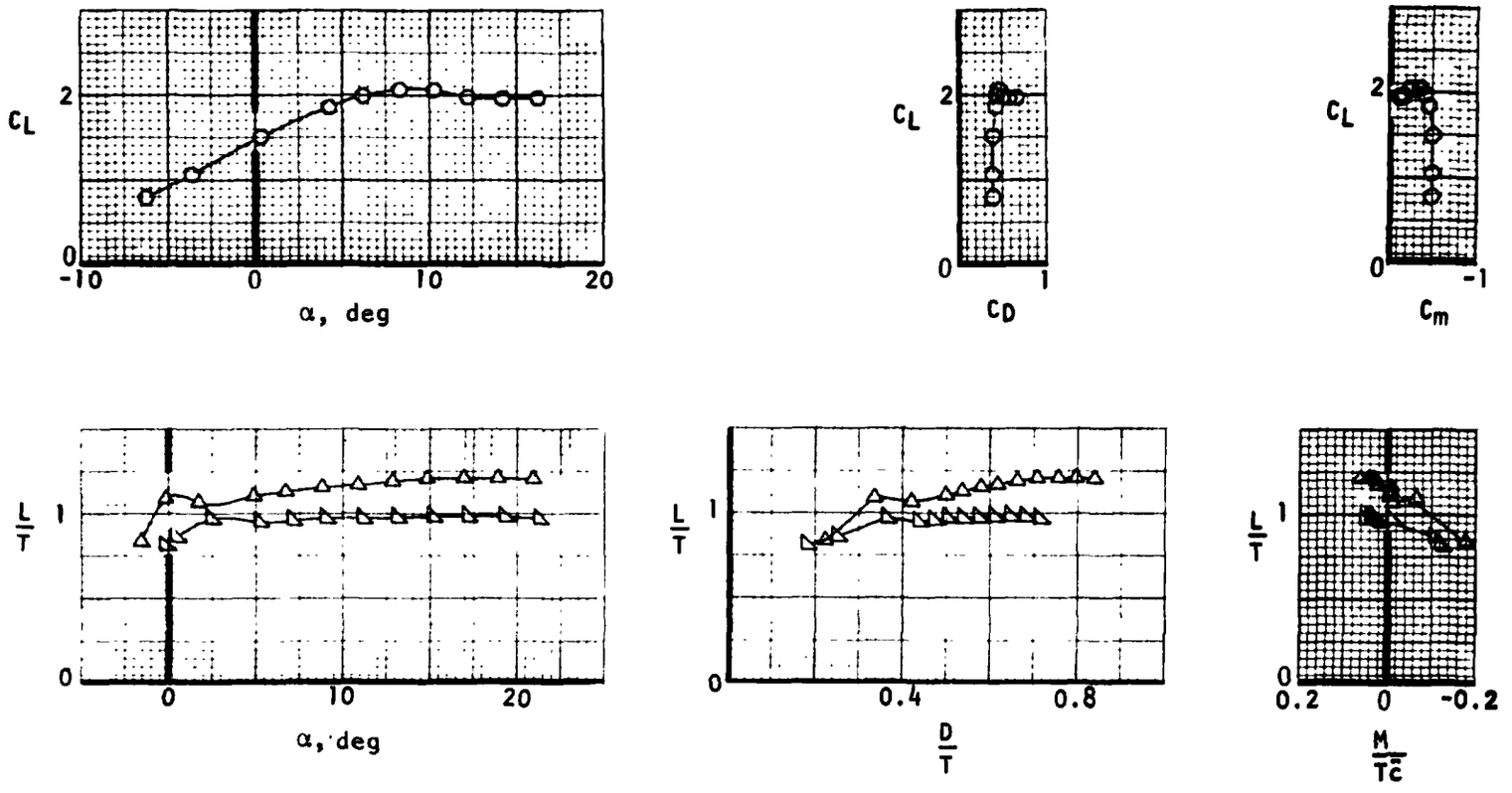

(a) Tail off.

Figure 43.- Flaps-down longitudinal forces and moments during transition out of ground effect. $\delta_N = 103°$.

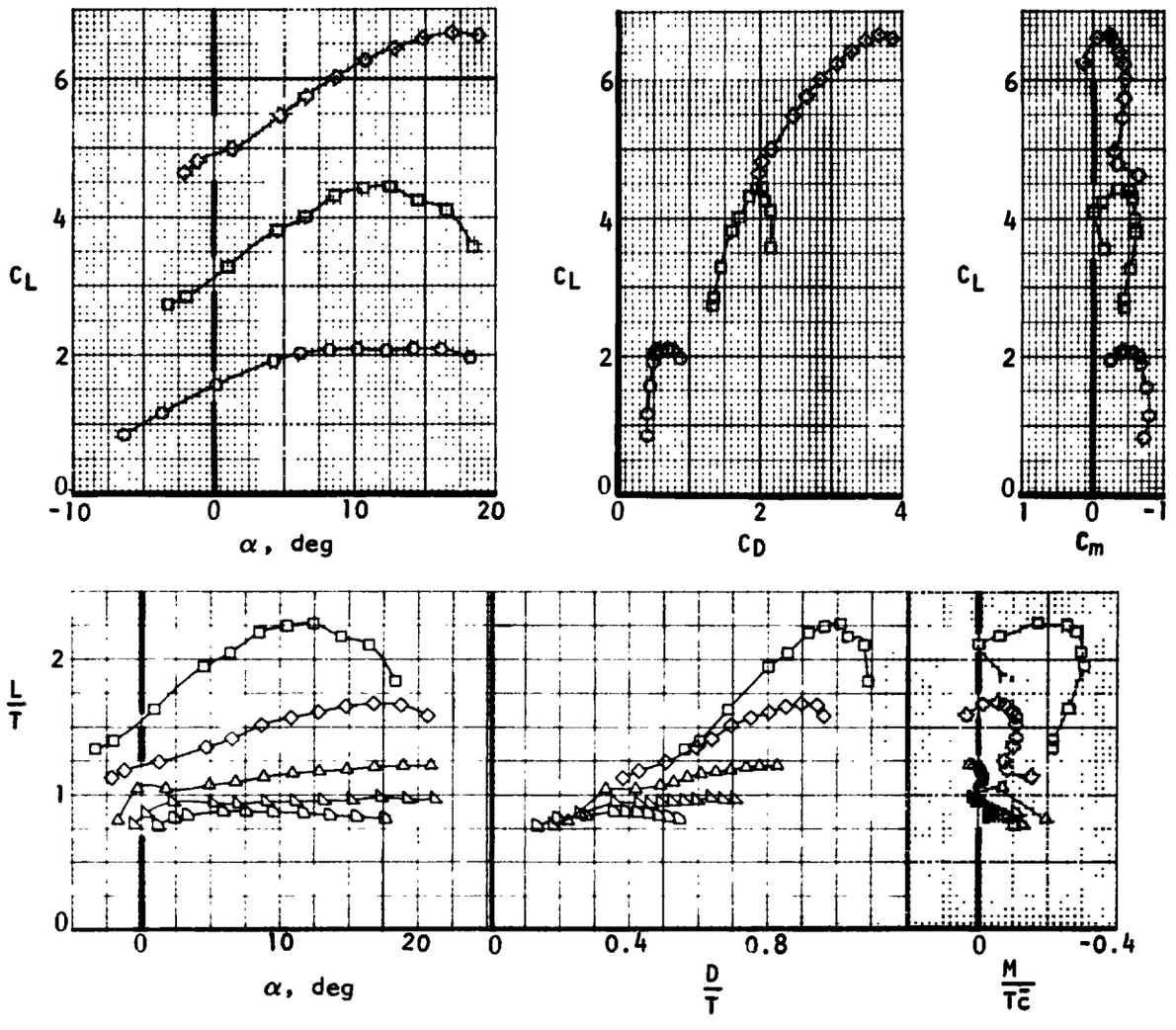

(b) Tail on, $i_H = 20°$.

Figure 43.- Concluded.

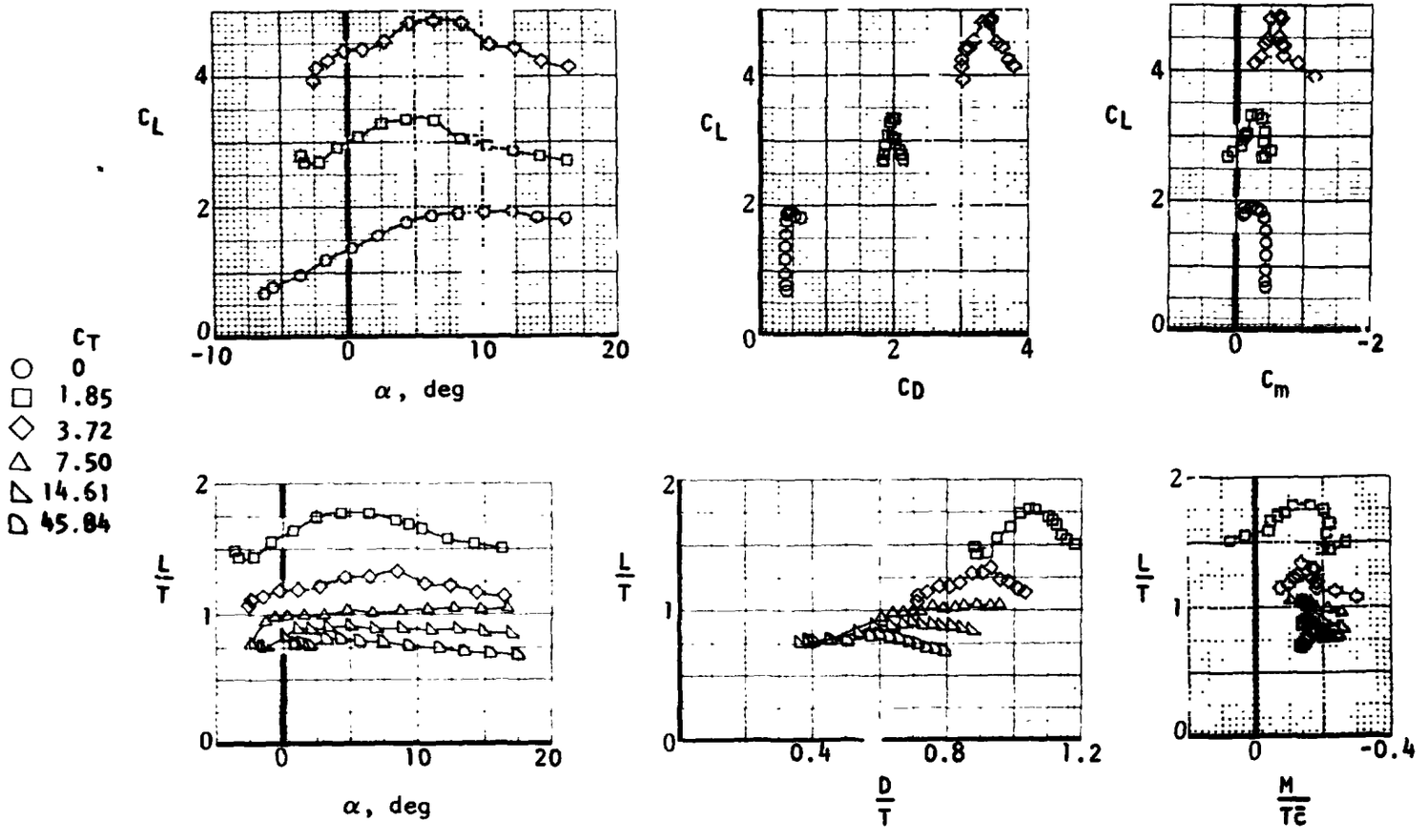

(a) Tail off.

Figure 44.- Flaps-down longitudinal forces and moments during transition out of ground effects. $\delta_N = 120°$.

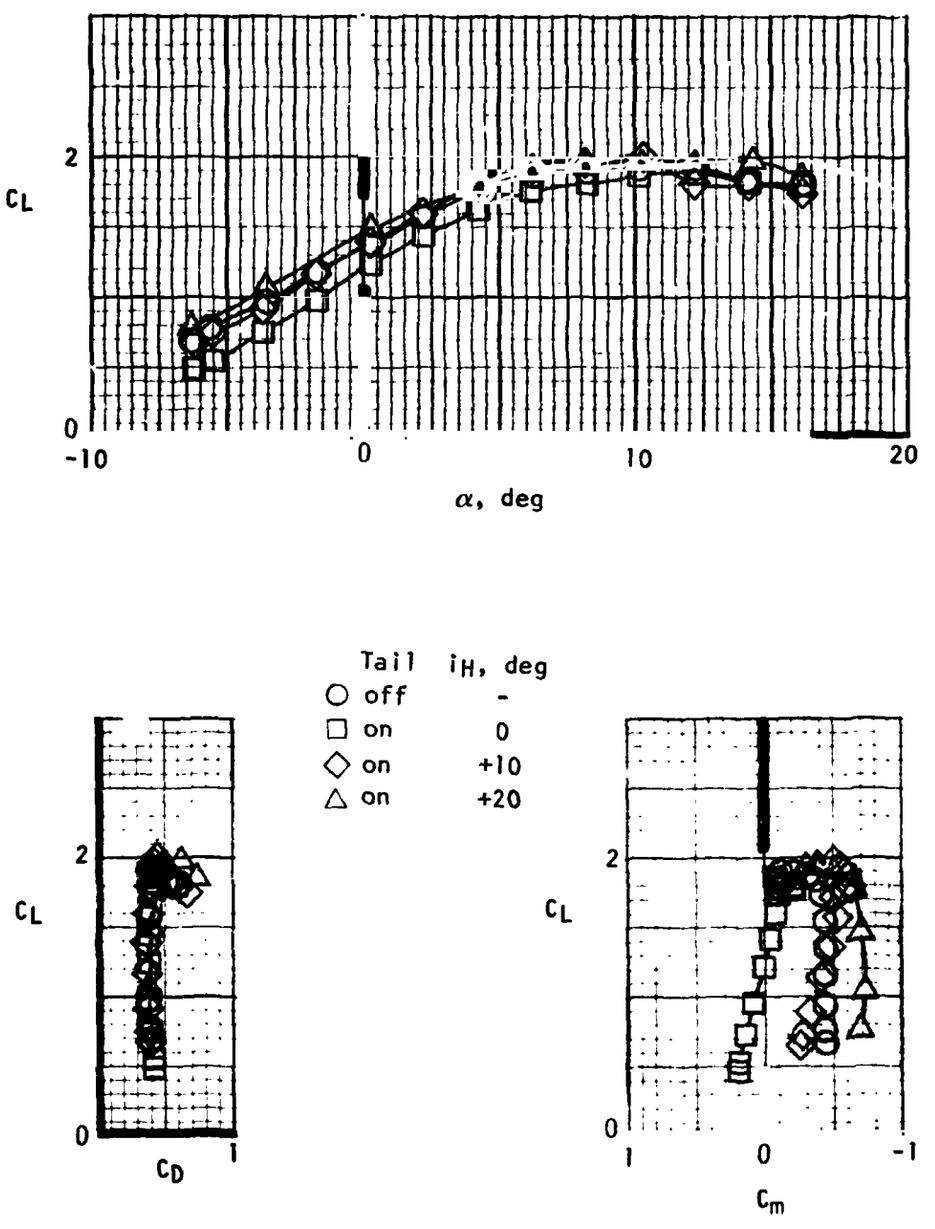

(b) Tail effectiveness at $C_T = 0$.

Figure 44.- Continued.

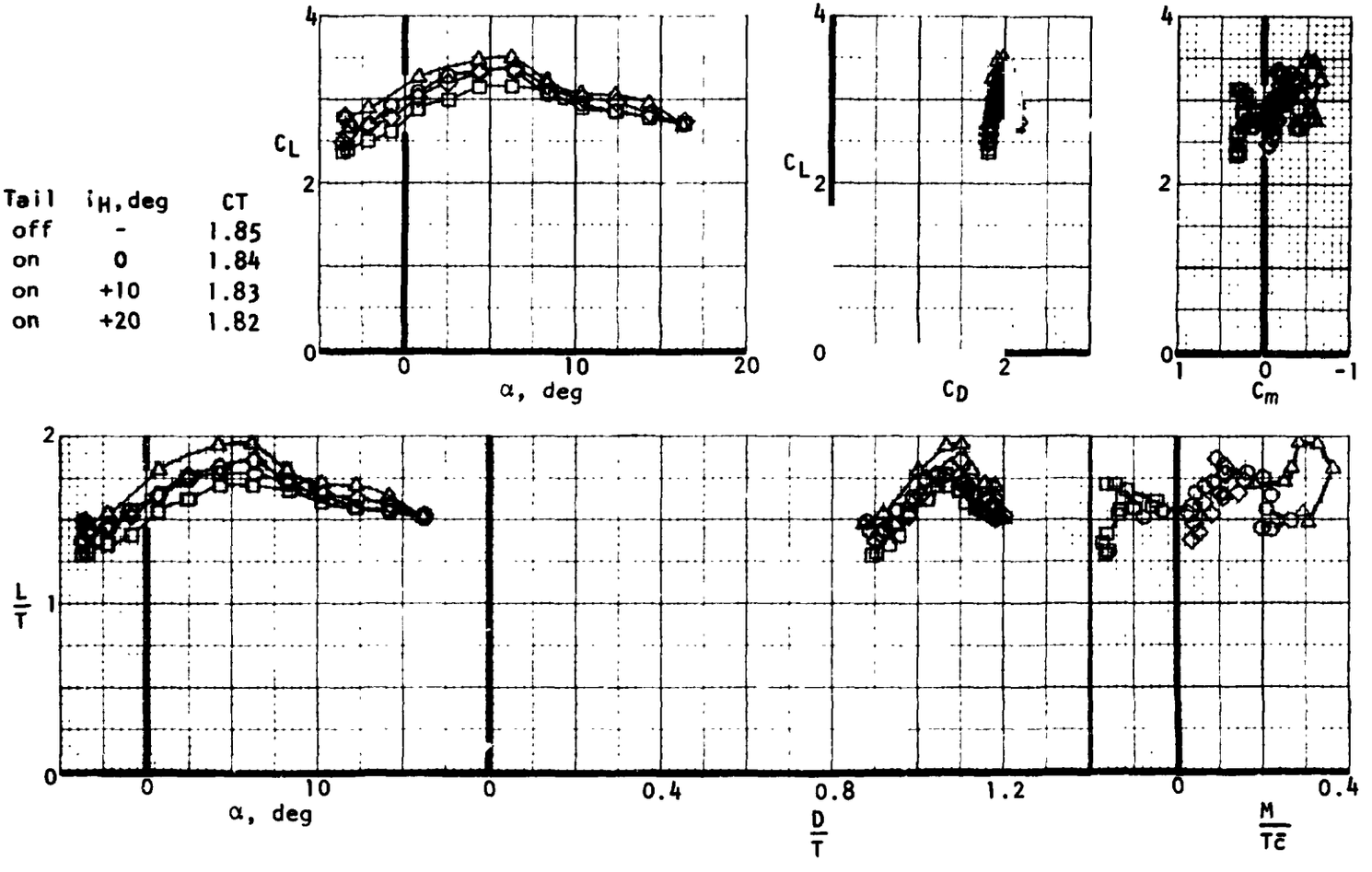

(c) Tail effectiveness at C_T = 1.8

Figure 44. - Continued

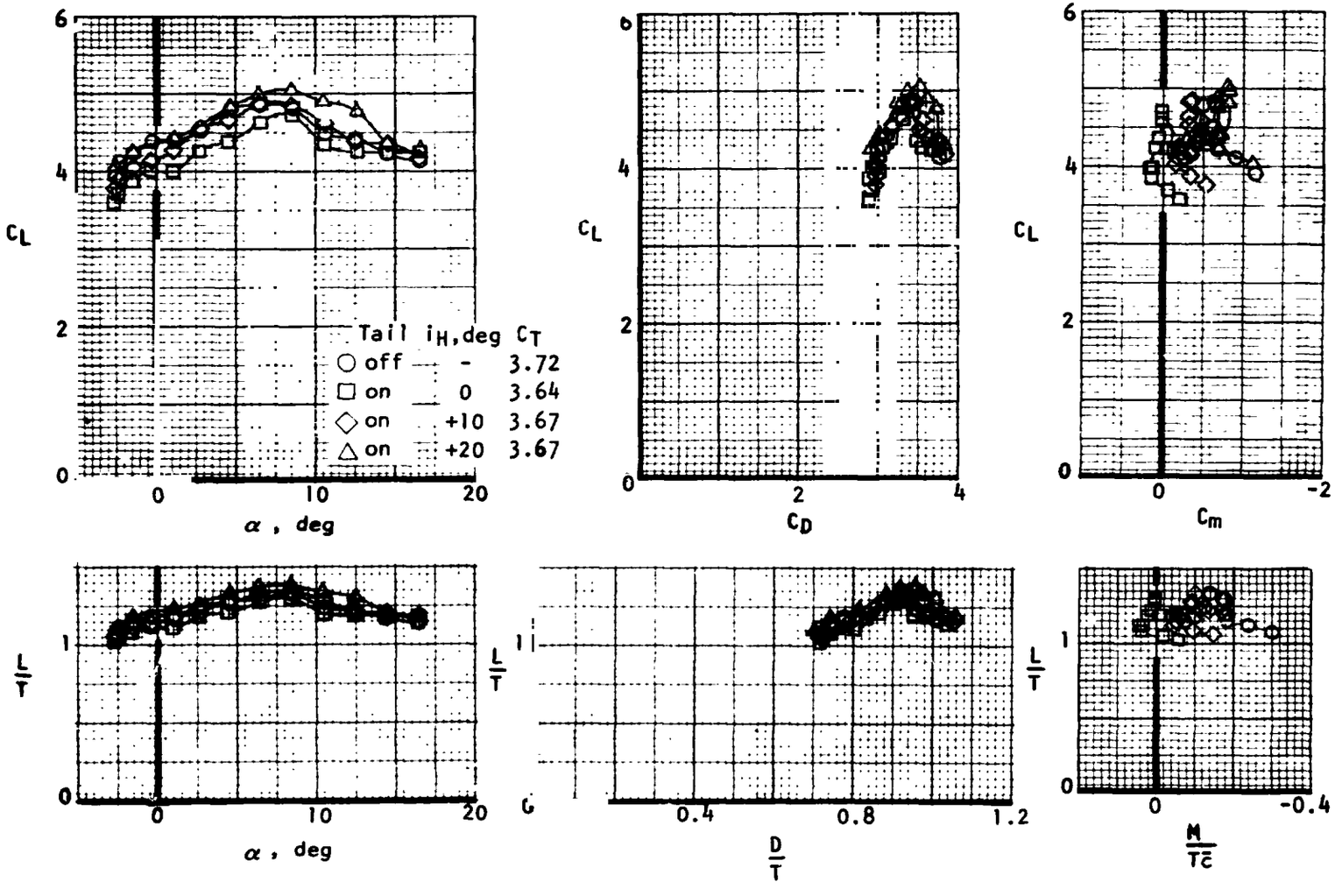

(d) Tail effectiveness at $C_T = 3.7$

Figure 44.- Continued.

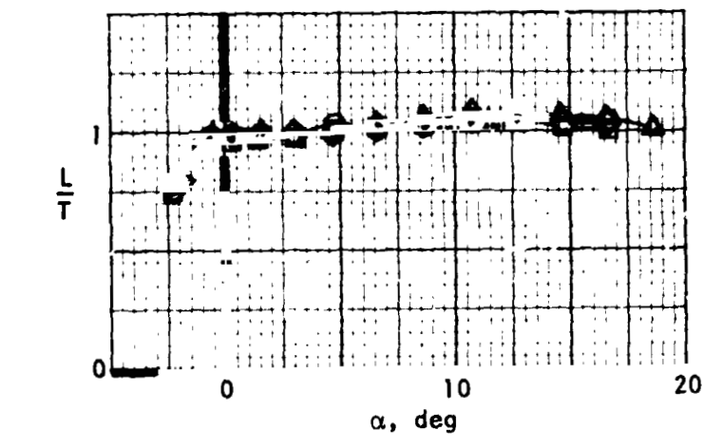

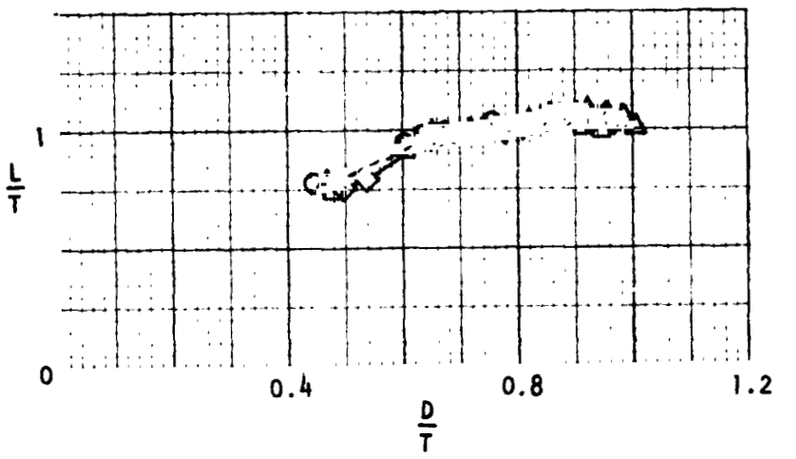

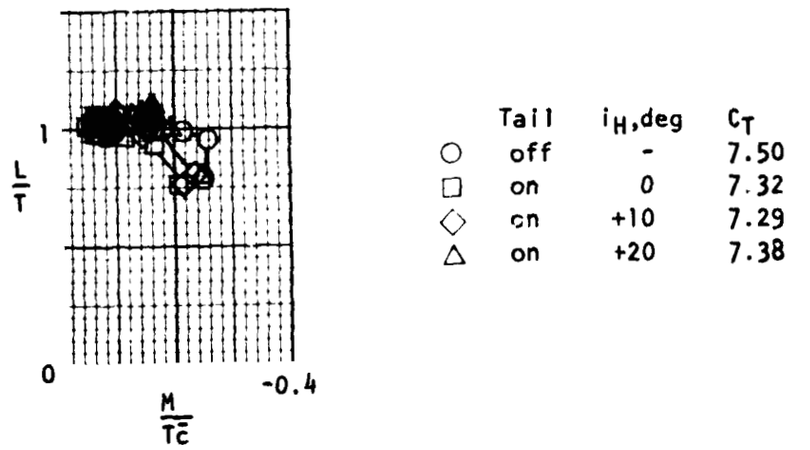

(e) Tail effectiveness at C_T = 7.4

Figure 44. - Concluded.

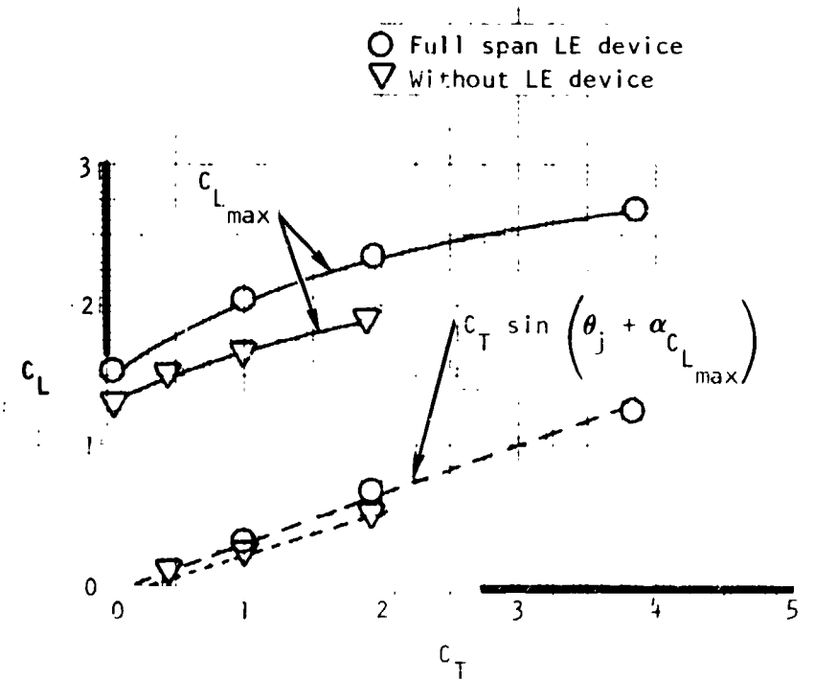

(a) Flaps up, $\delta_N = 0$.

gure 45. - Maximum lift versus power. Tail off, 0GE.

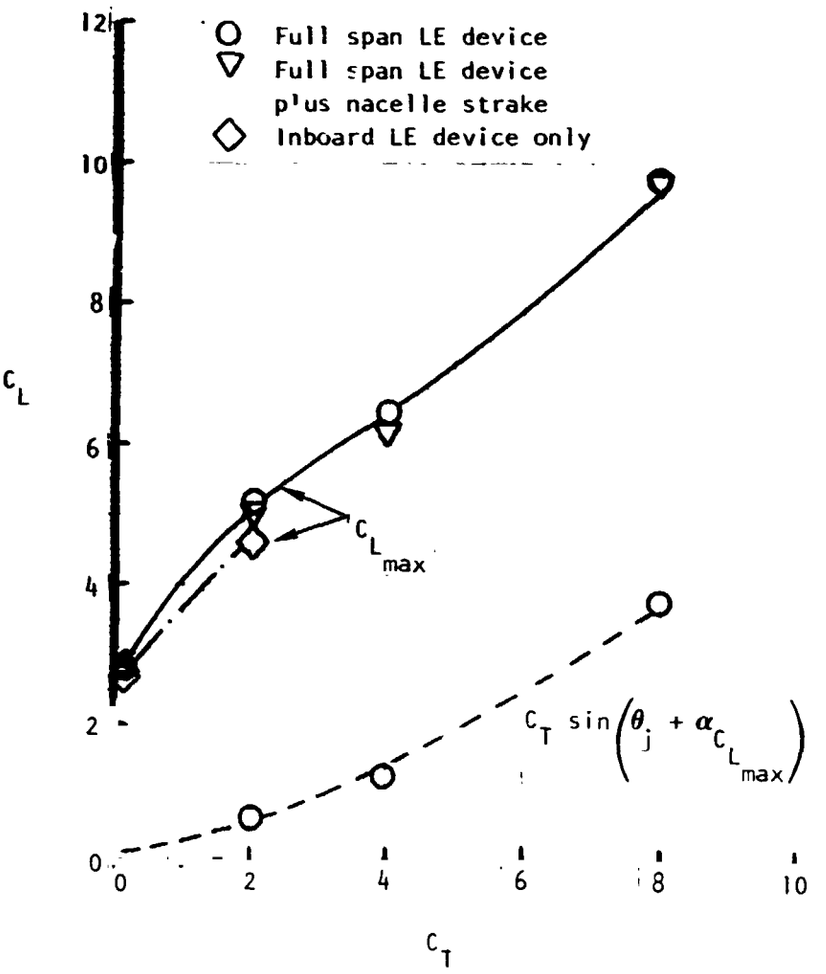

(b) Flaps down, $\delta_N = 0$.

Figure 45. - Cont

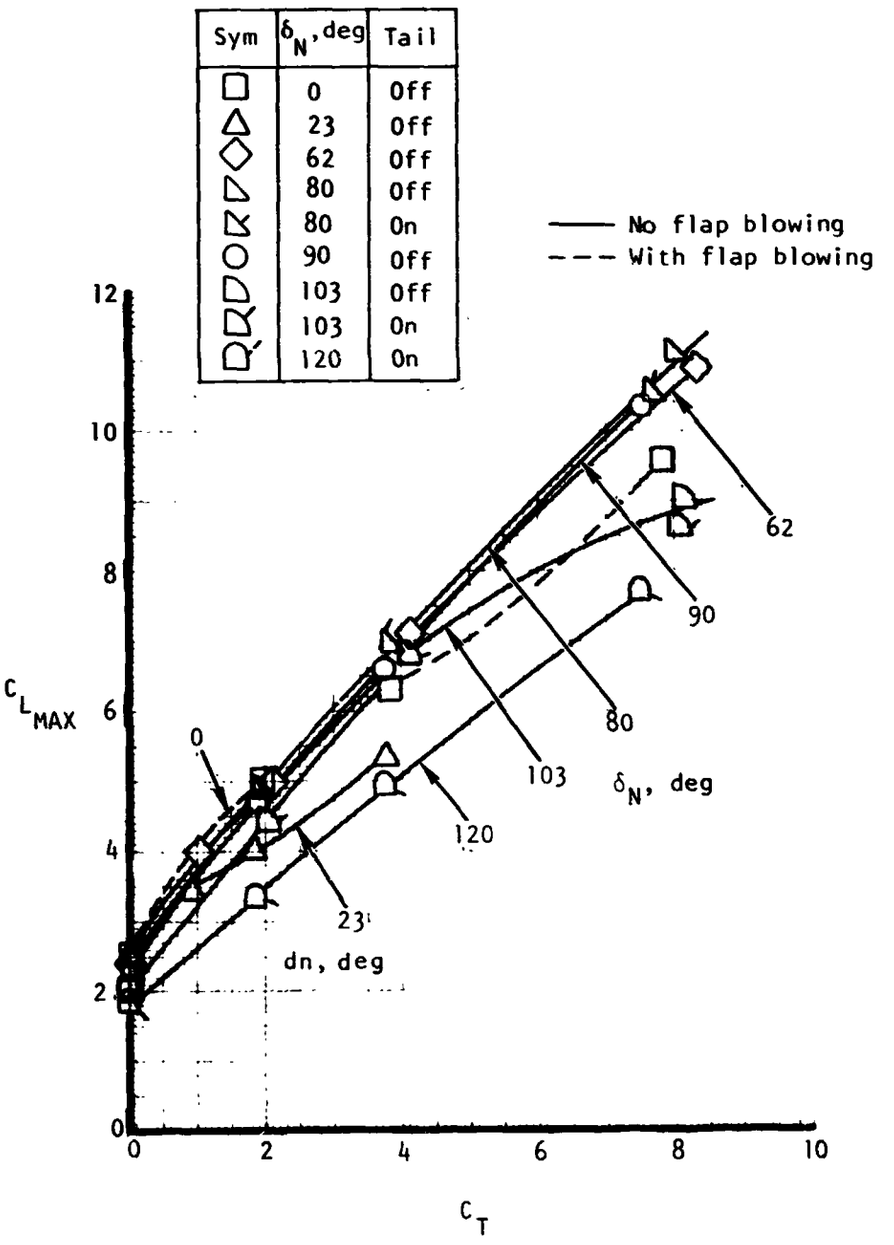

(c) Flaps down, various nozzle angles.

Figure 45. - Concluded.

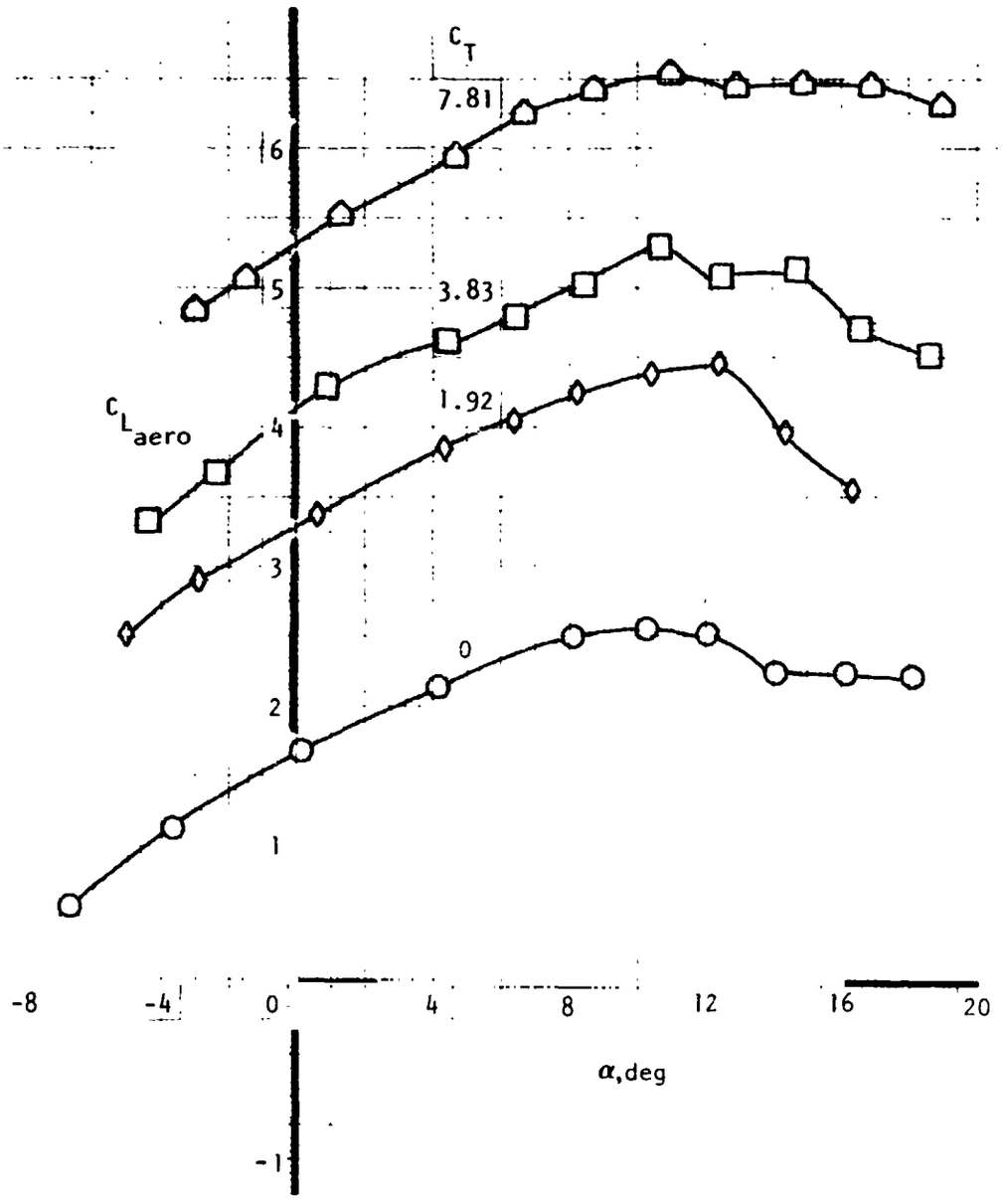

(a) $C_{L_{aero}}$ for $\delta_N = 0°$.

Figure 46. - Tail-off aerodynamic lift in coefficient form. Flaps down, OGE.

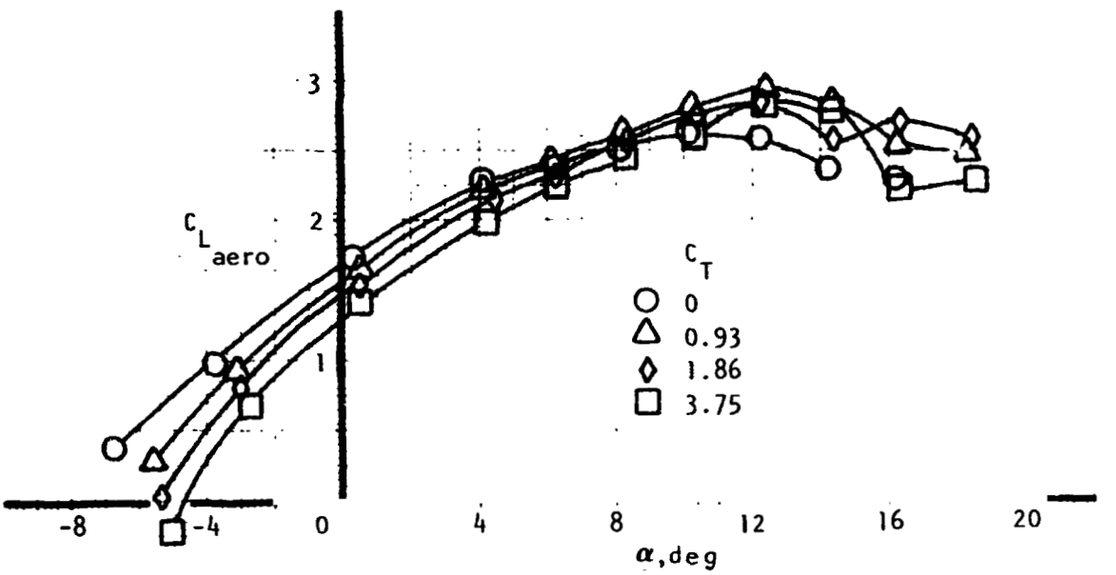

(b) C_{Laero} for $\delta_N = 23°$.

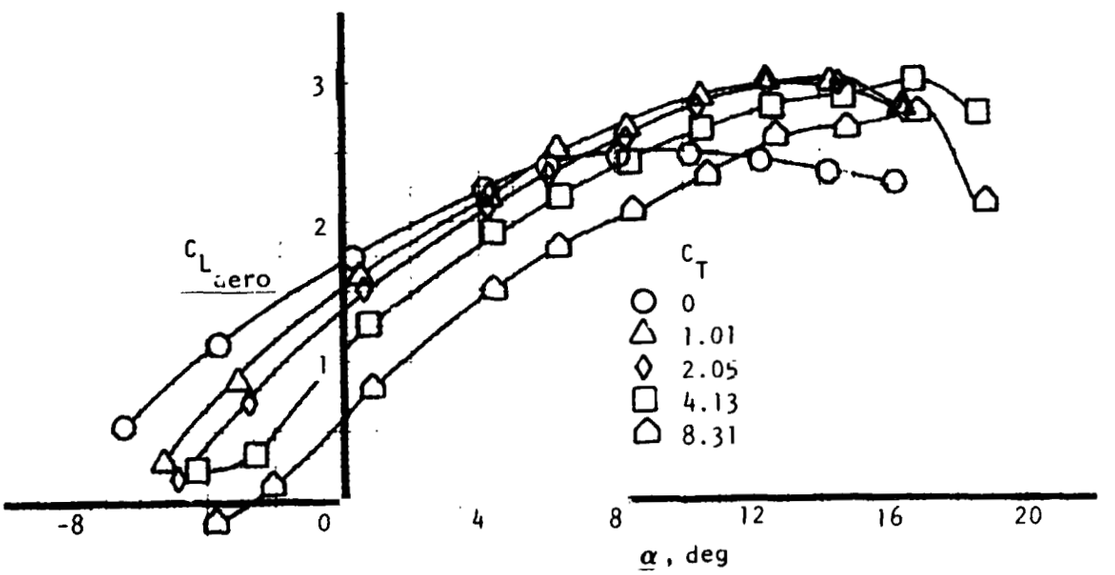

(c) C_{Laero} for $\delta_N = 62°$.

Figure 46. - Continued.

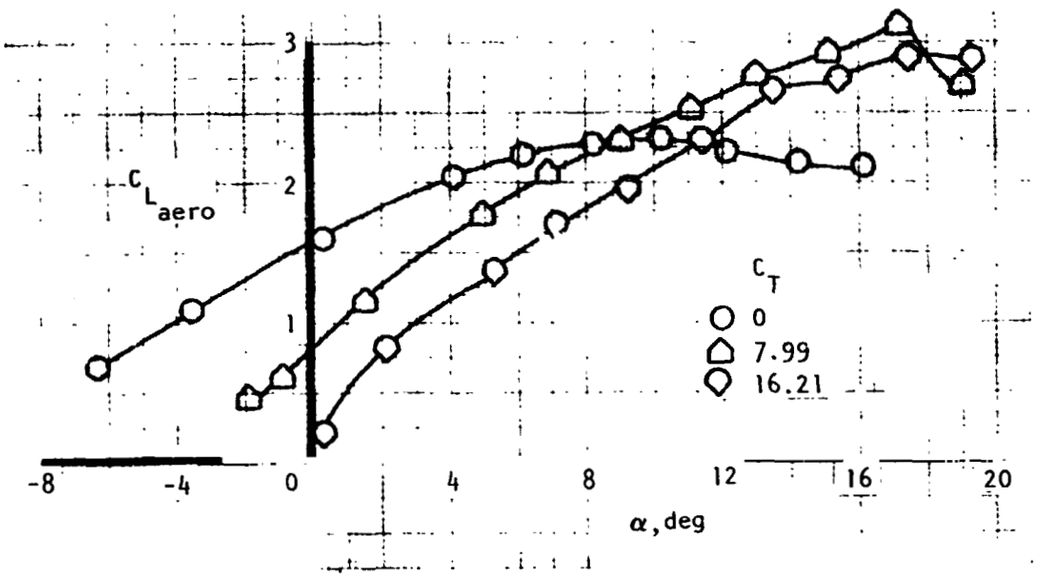

(d) C_{Laero} δ_N = 80°.

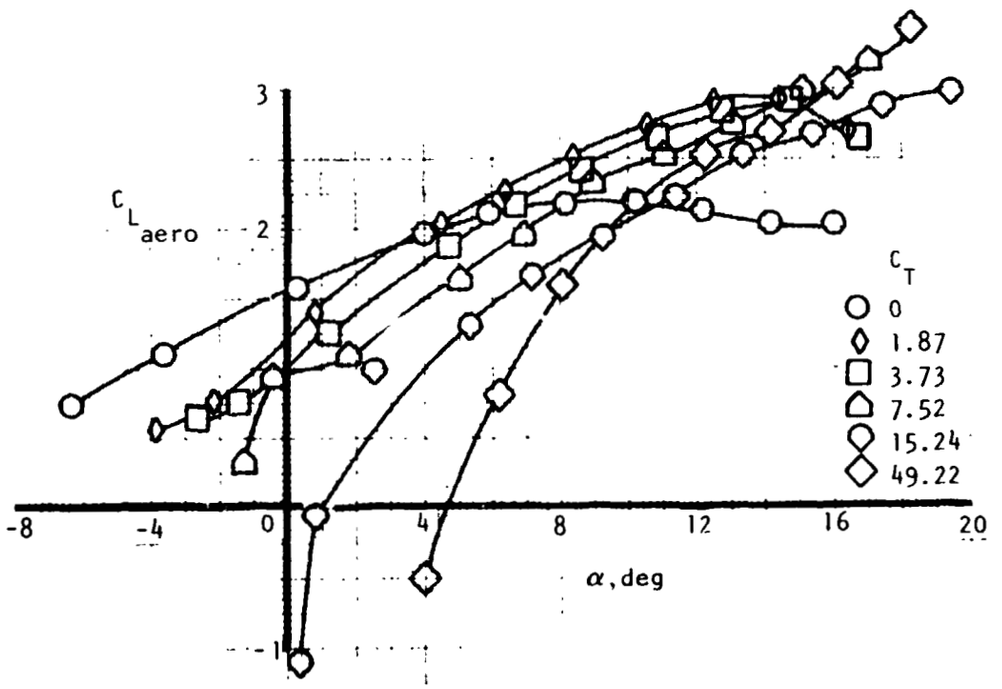

(e) C_{Laero} for δ_N = 90°

Figure 46. - Continued.

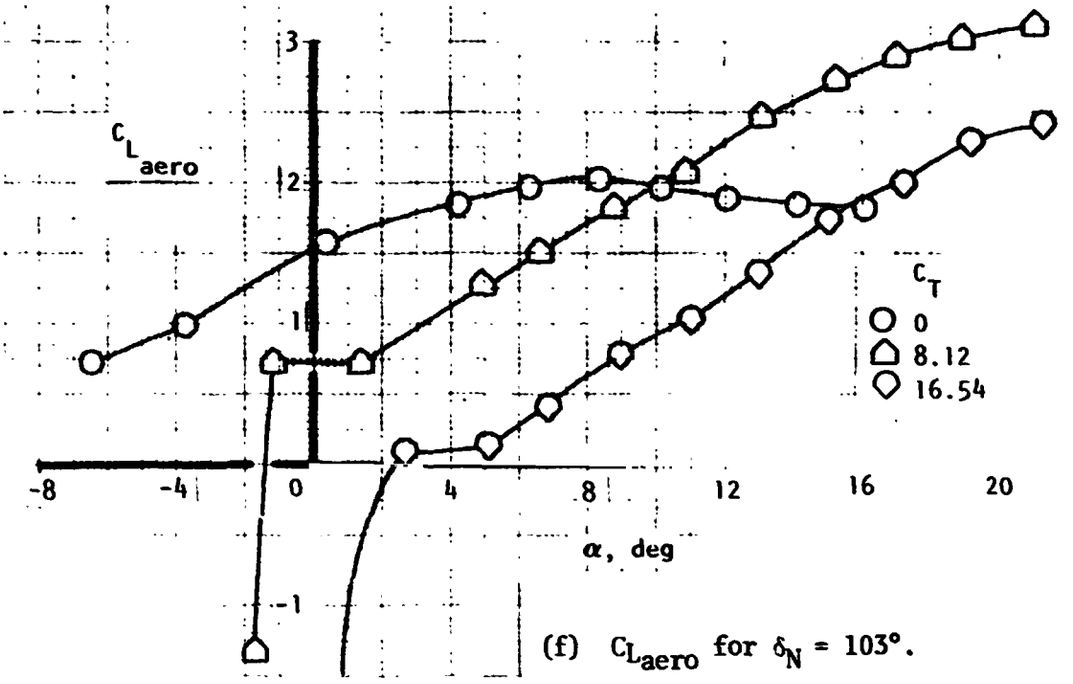

(f) $C_{L_{aero}}$ for $\delta_N = 103°$.

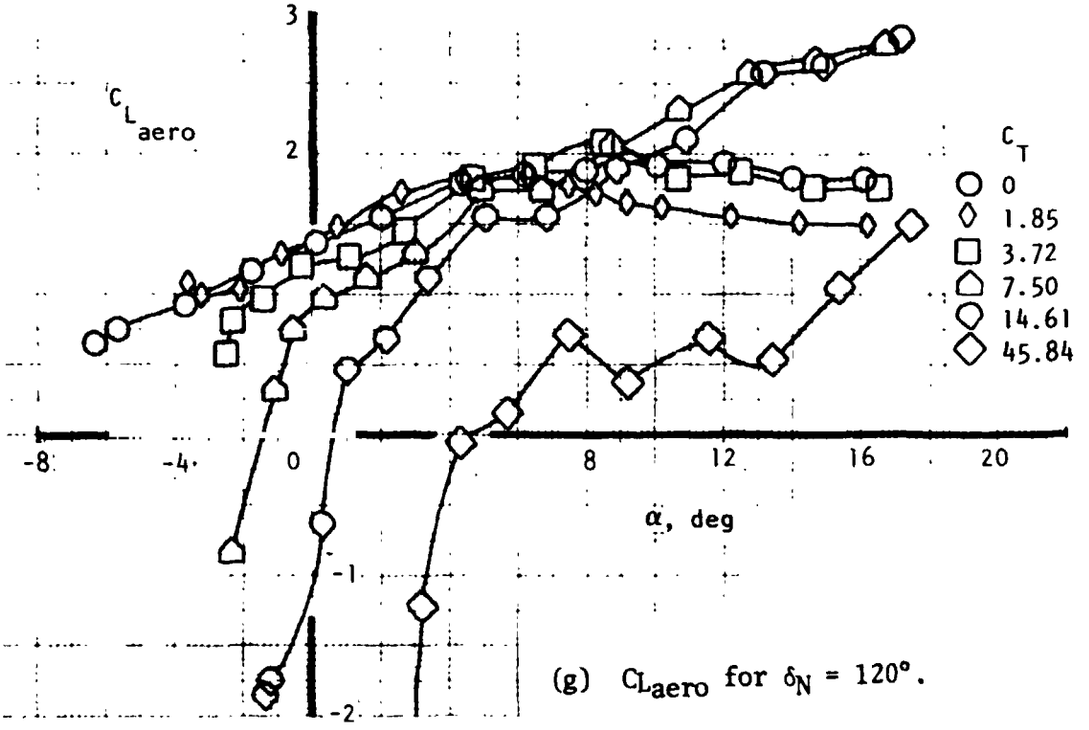

(g) $C_{L_{aero}}$ for $\delta_N = 120°$.

Figure 46. - Concluded

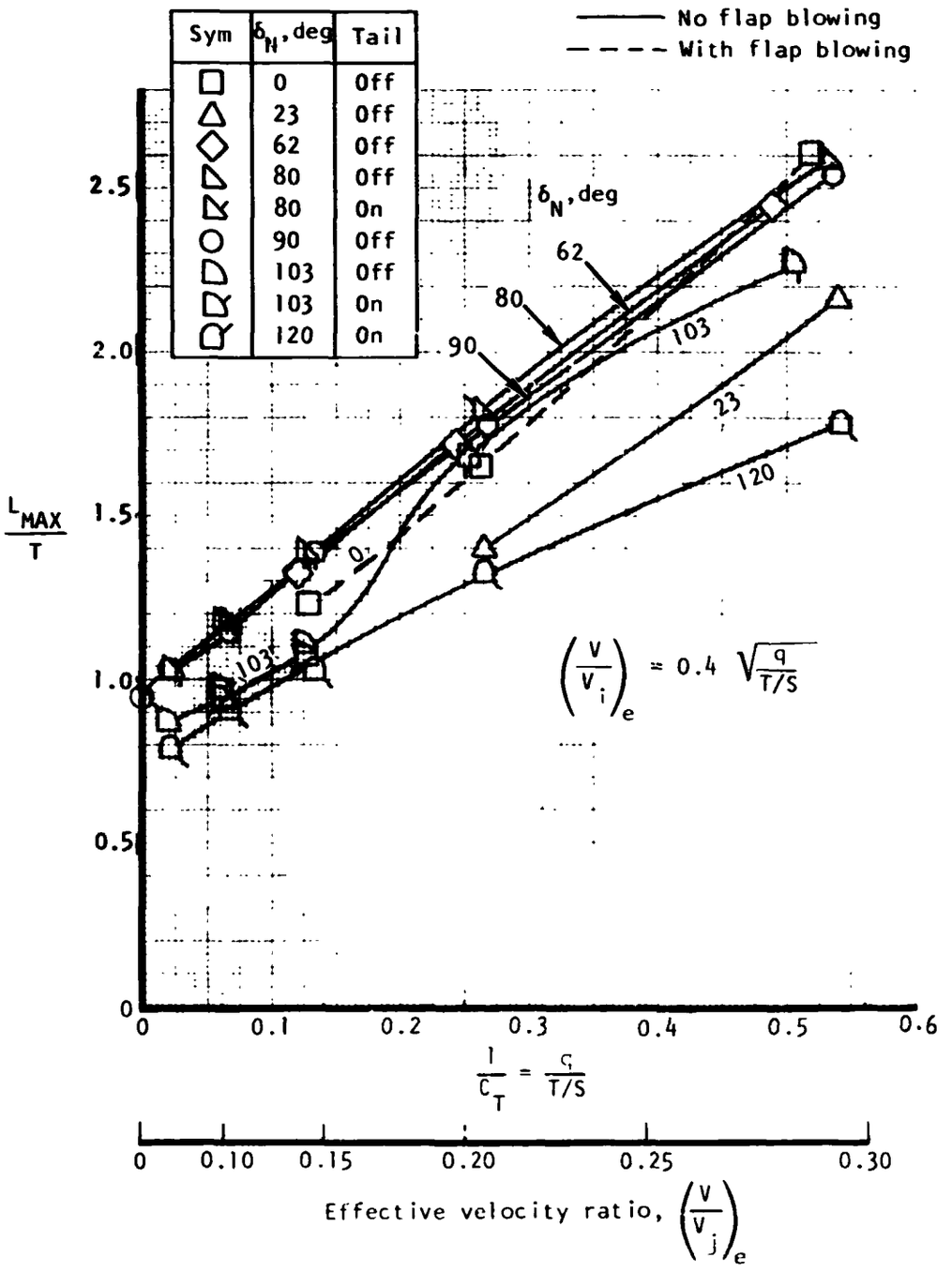

(a) **Maximum Total lift.**

Figure 47. - Tail-off lift characteristics in terms of $L/_T$, flaps down, OGE.

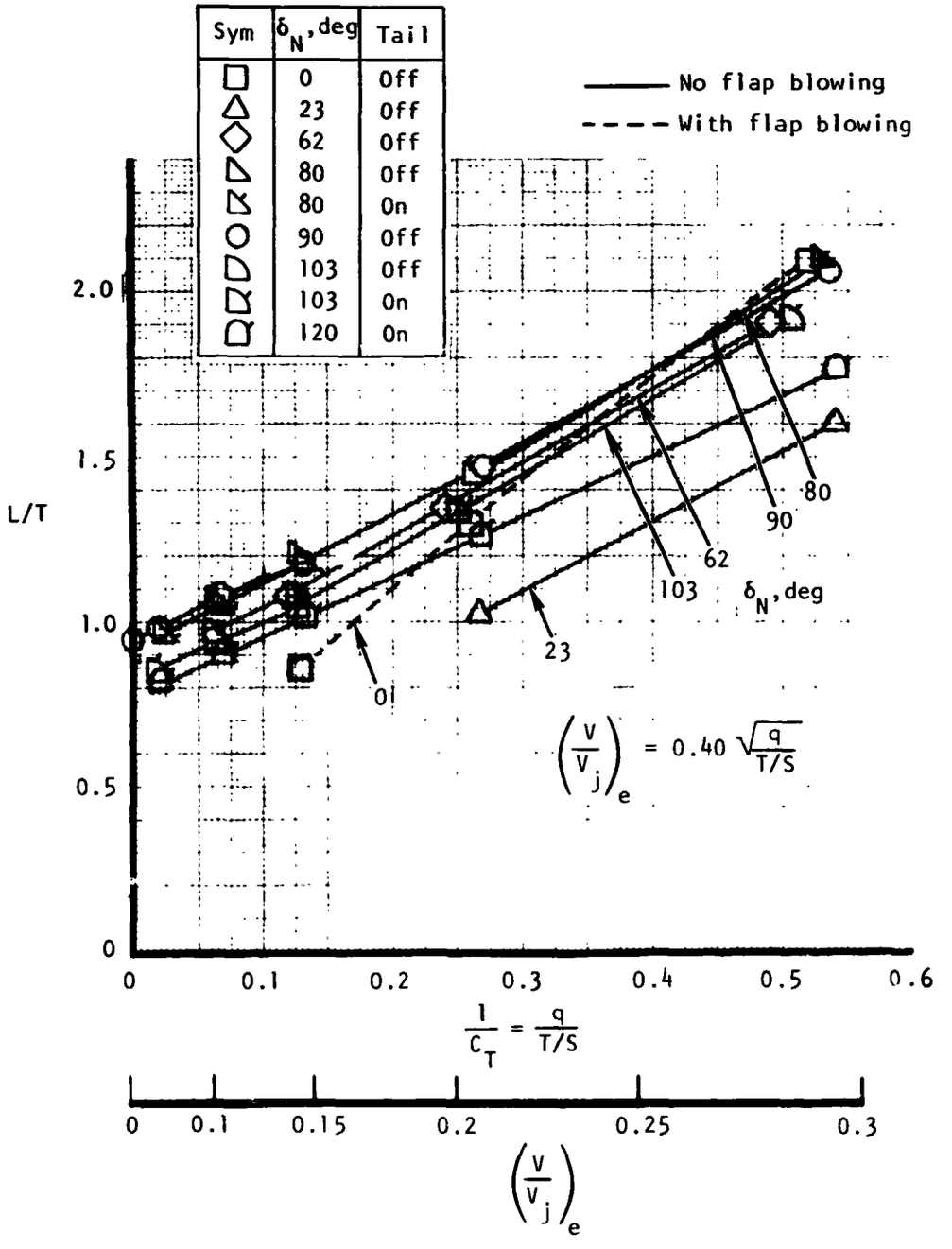

(b) Total lift at $\alpha = 4°$.

Figure 47 .-Continued.

$C_{L_{OP}}$ = Lift coeff. at zero power

θ_j = Exhaust angle with respect to FRP

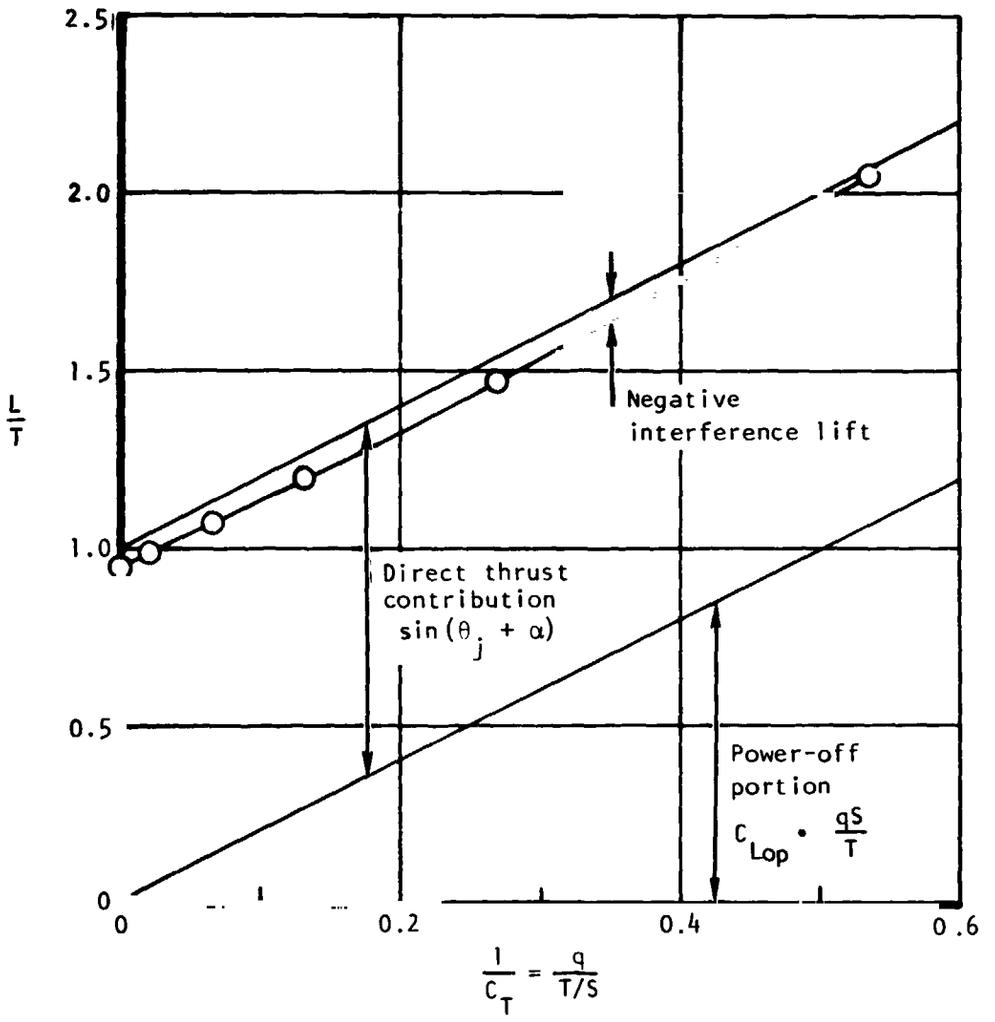

(c) Lift components for $\delta_N = 90°$, $\alpha = 4°$.

Figure 47. - Continued.

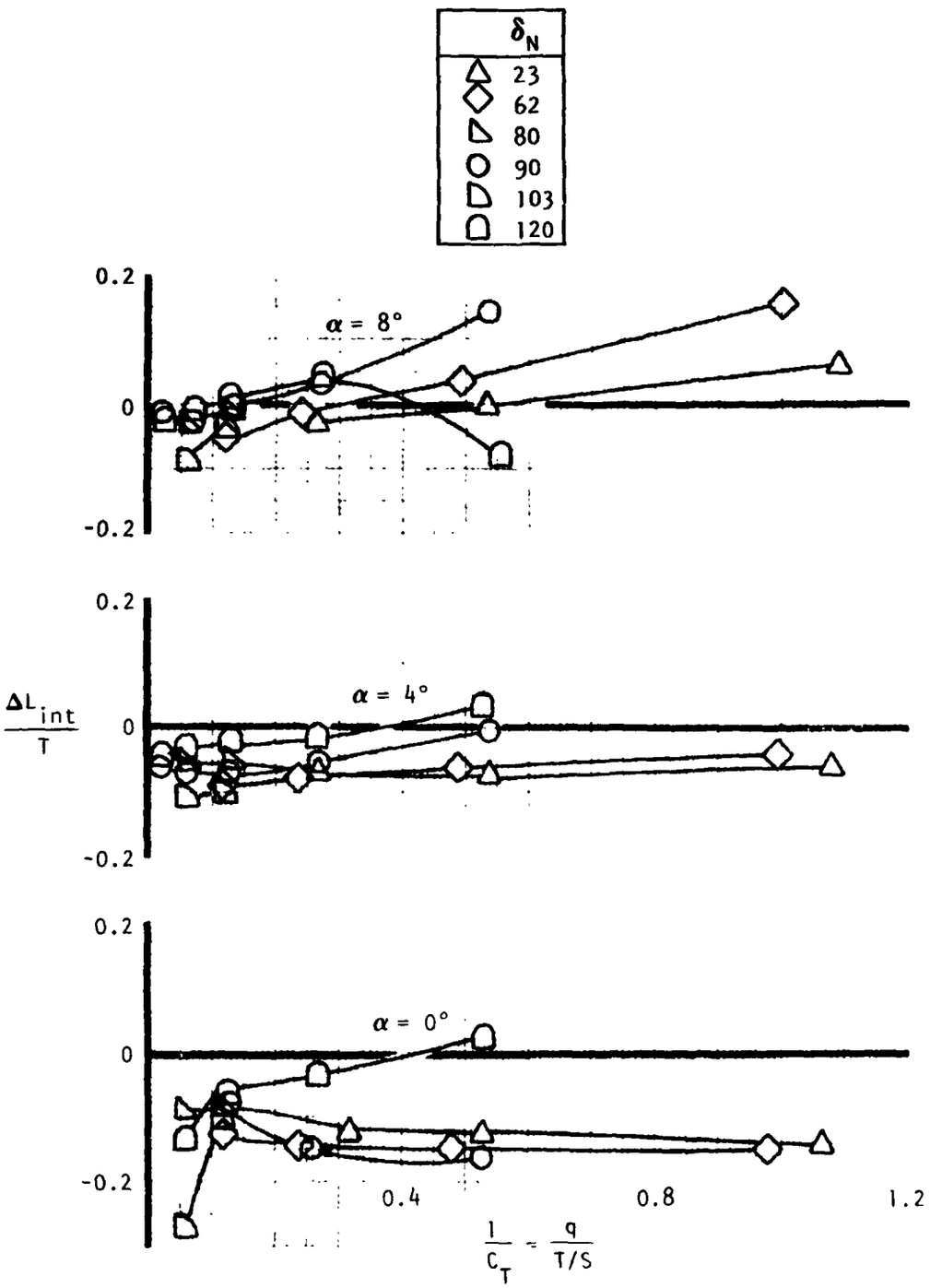

(d) Interference lift at various values of α and δ_N.

Figure 47. - Concluded.

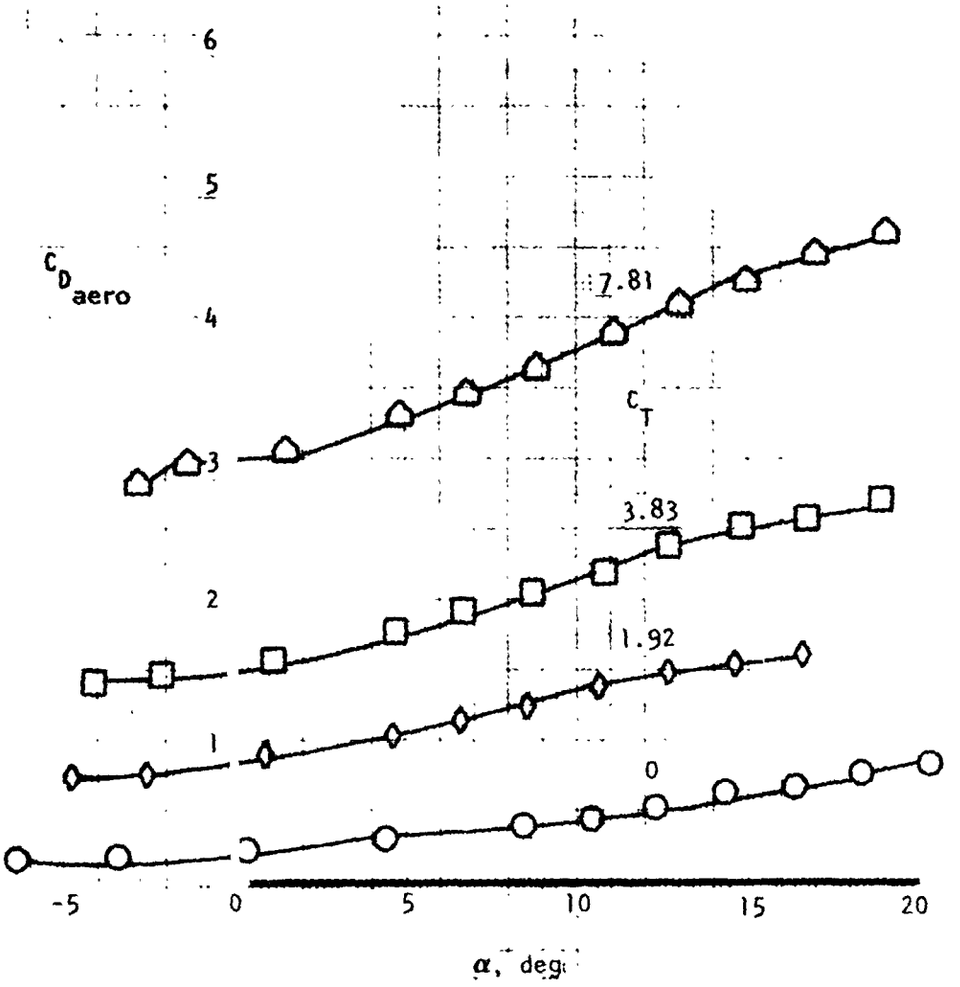

(a) $C_{D_{aero}}$ at $\delta_N = 0°$.

Figure 48. - Tail-off drag components, flaps down, transition OGE.

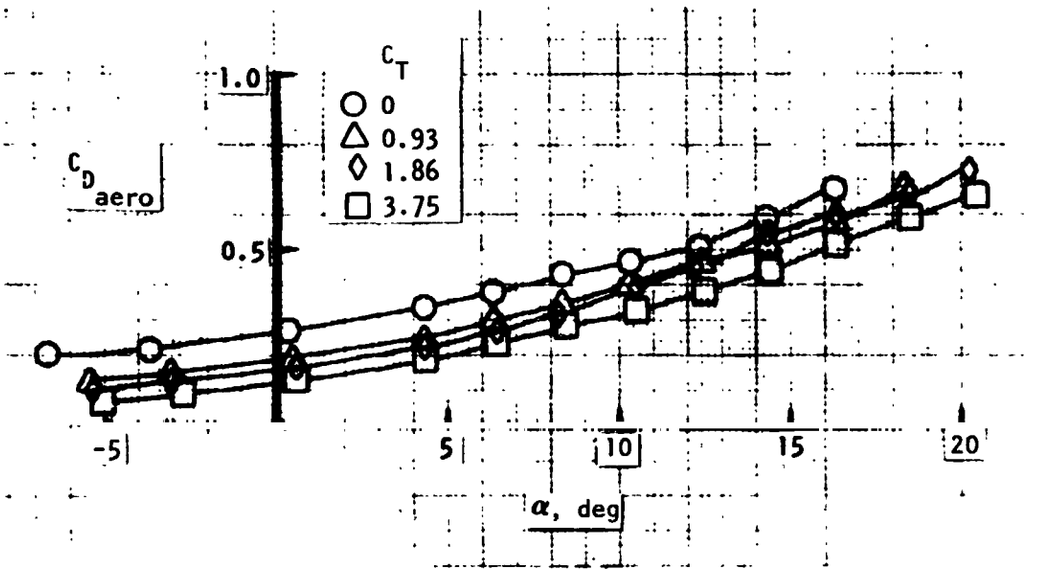

(b) $C_{D_{aero}}$ for $\delta_N = 23°$.

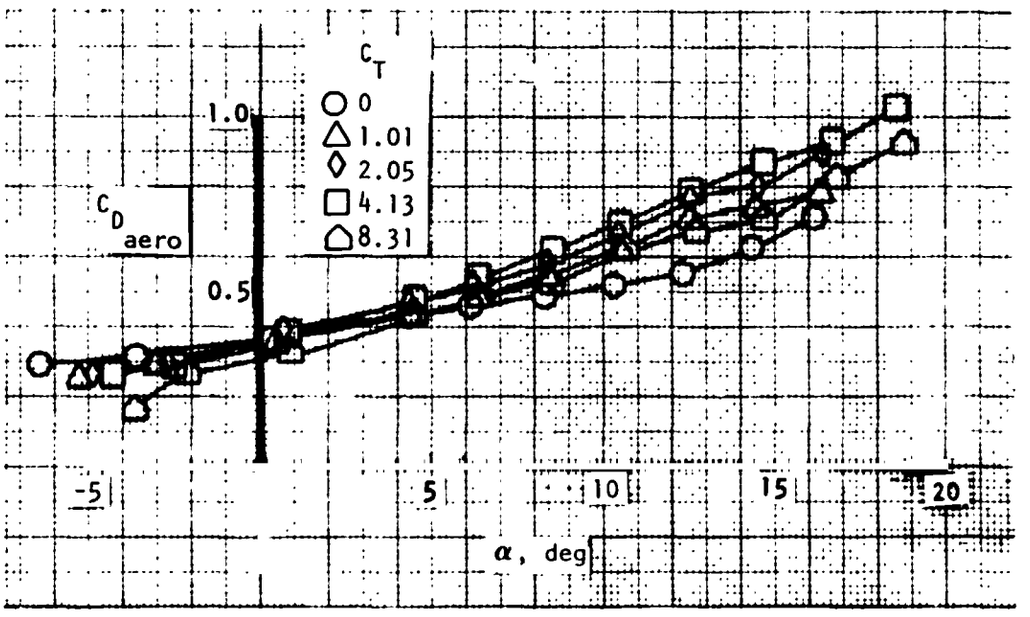

(c) $C_{D_{aero}}$ for $\delta_N = 62°$.

Figure 48. - Continued.

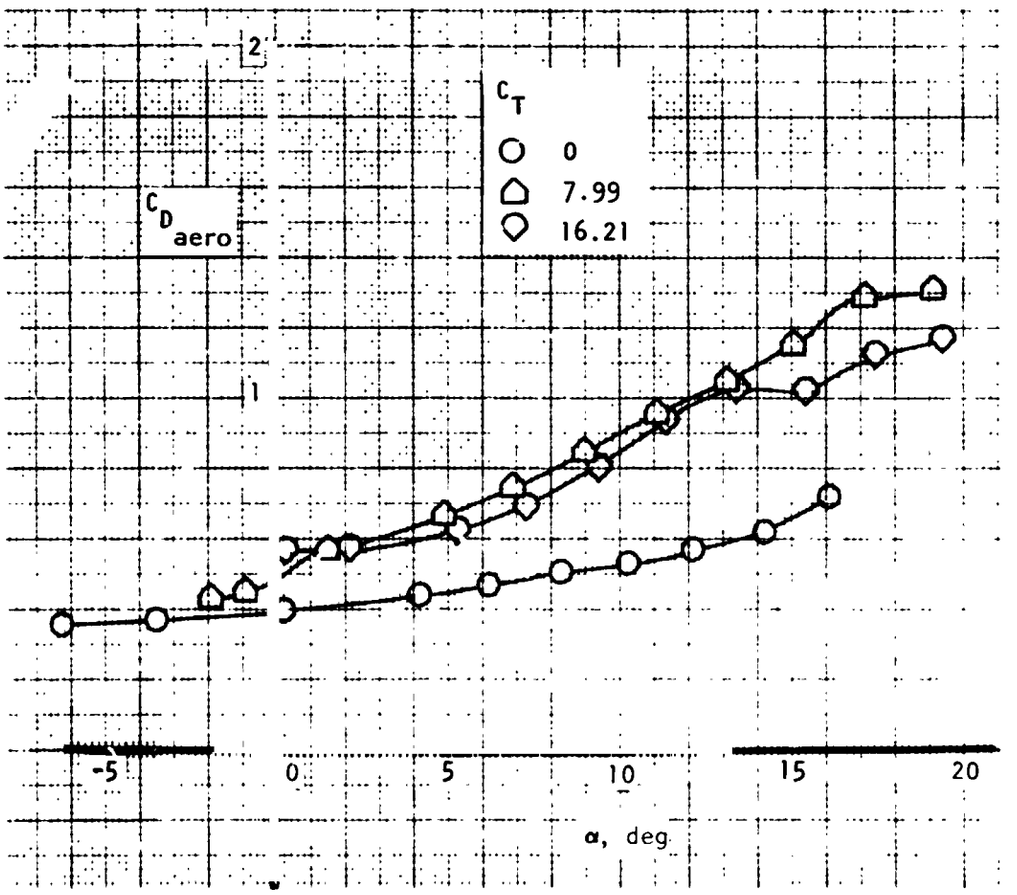

(d) $C_{D_{aero}}$ for $\delta_N = 80°$.

Figure 48.- Continued.

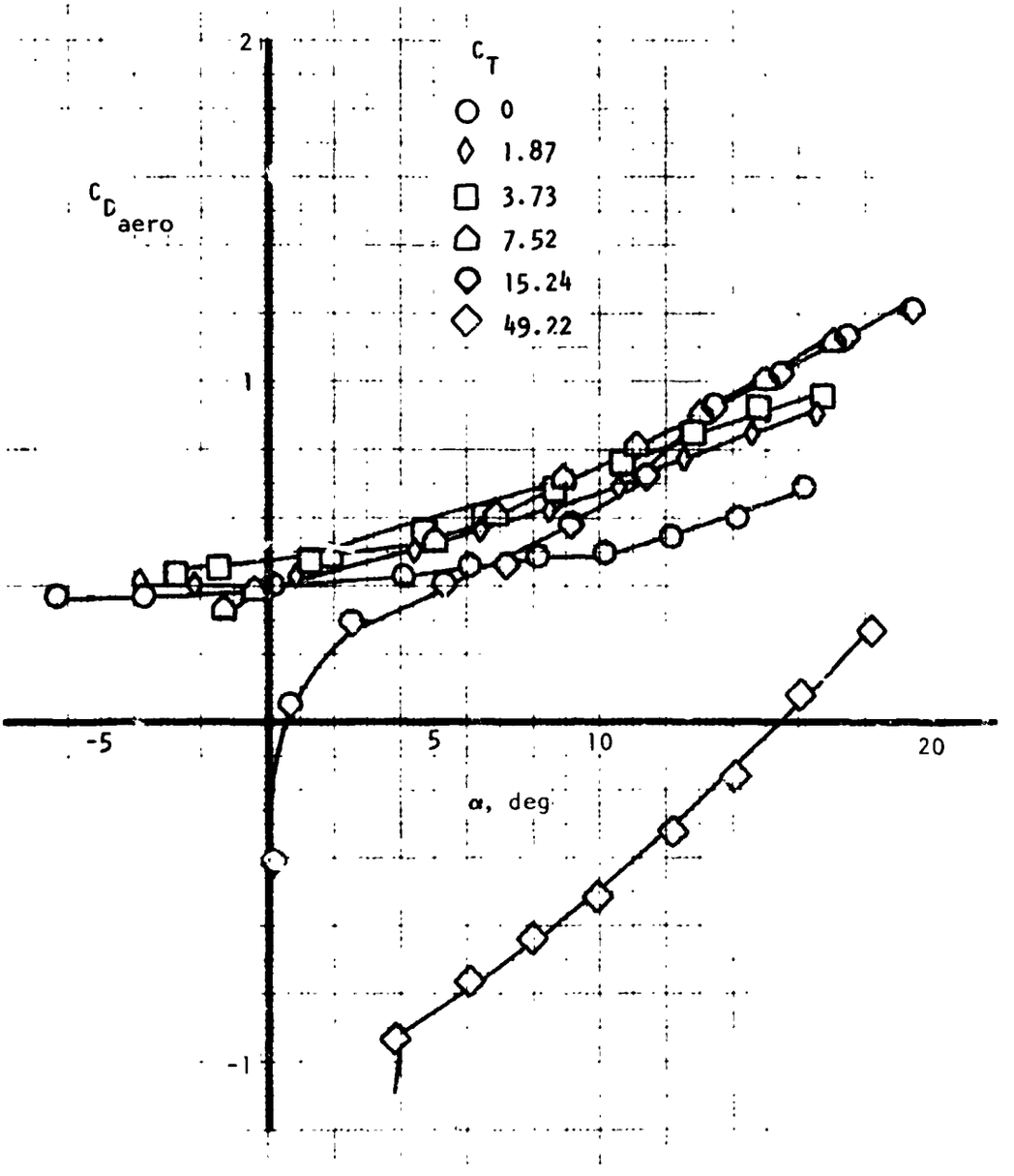

(e) C_{Daero} for $\delta_N = 90°$.

Figure 48. Continued.

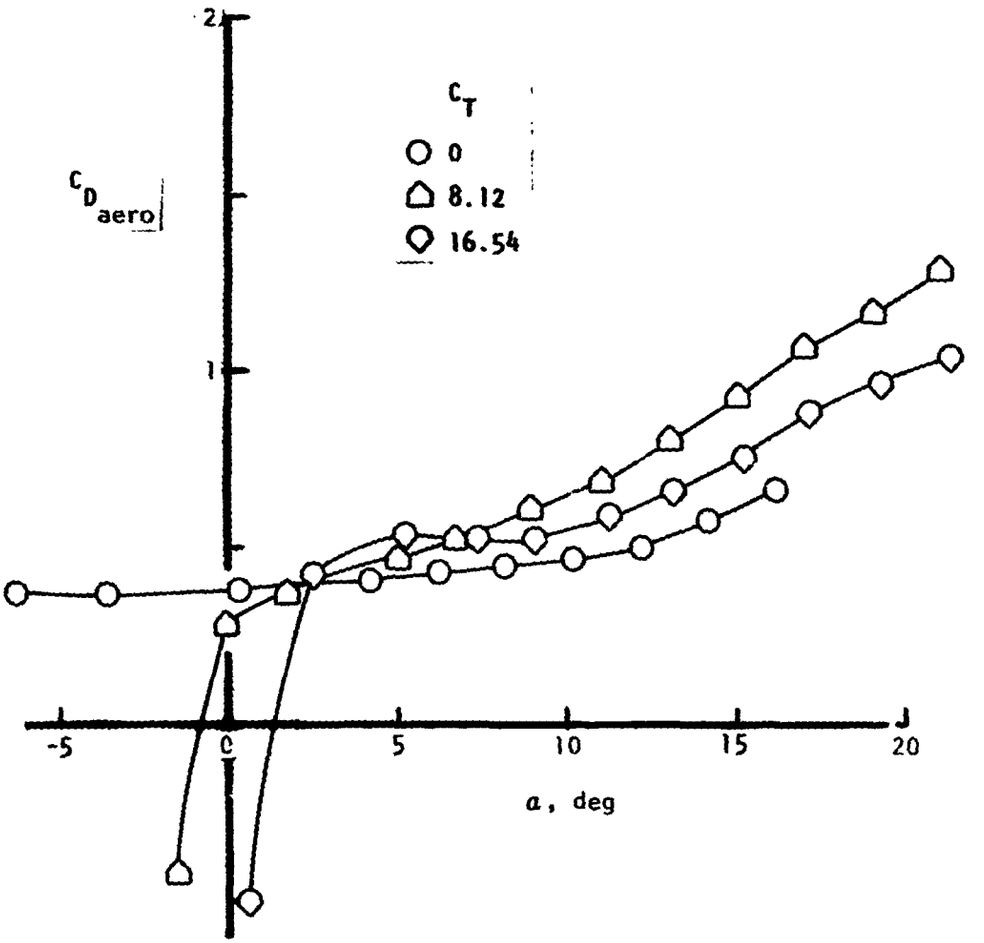

(f) $C_{D_{aero}}$ for $\delta_N = 103°$.

Figure 48. - Continued.

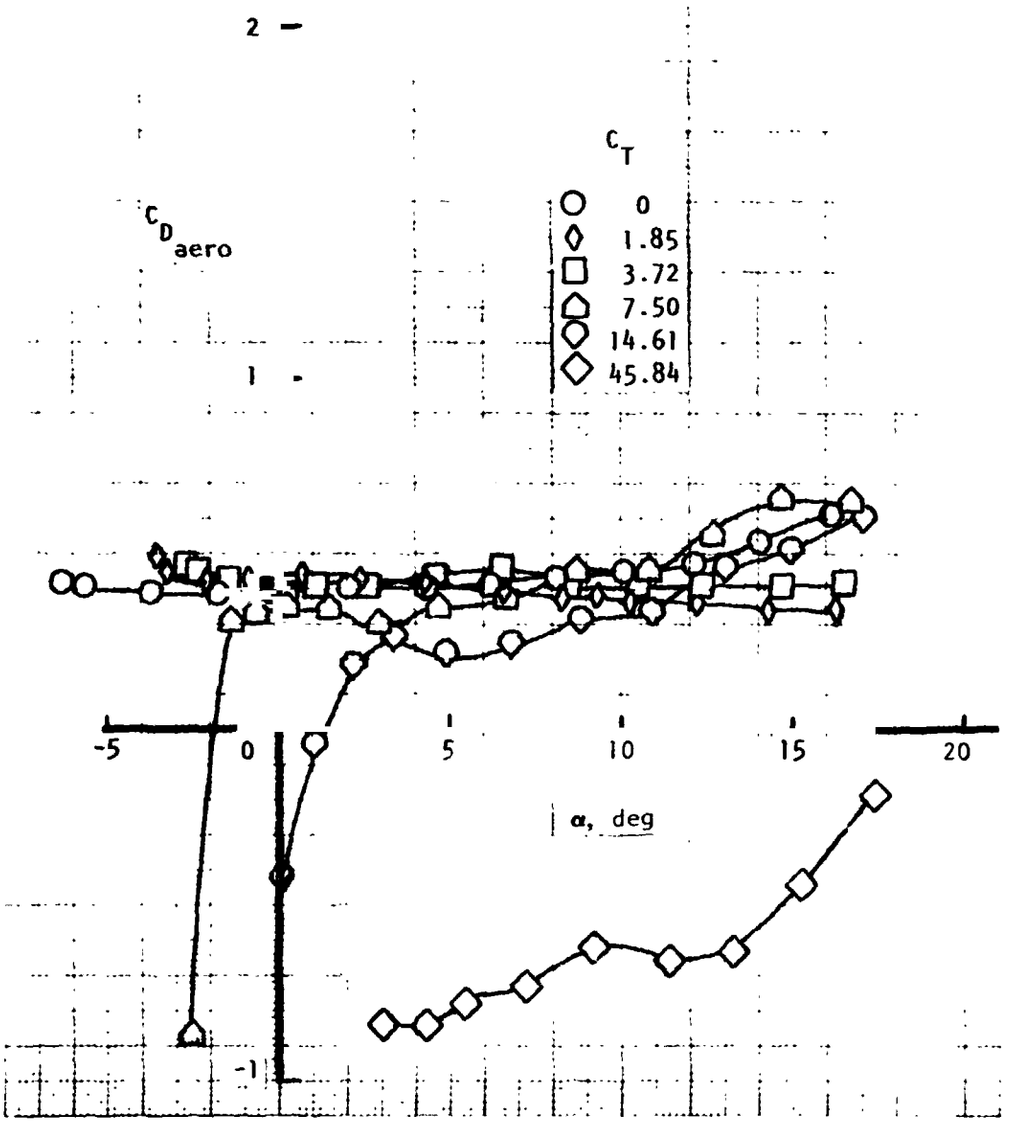

(g) $C_{D_{aero}}$ for $\delta_N = 120°$.

Figure 48. - Continued.

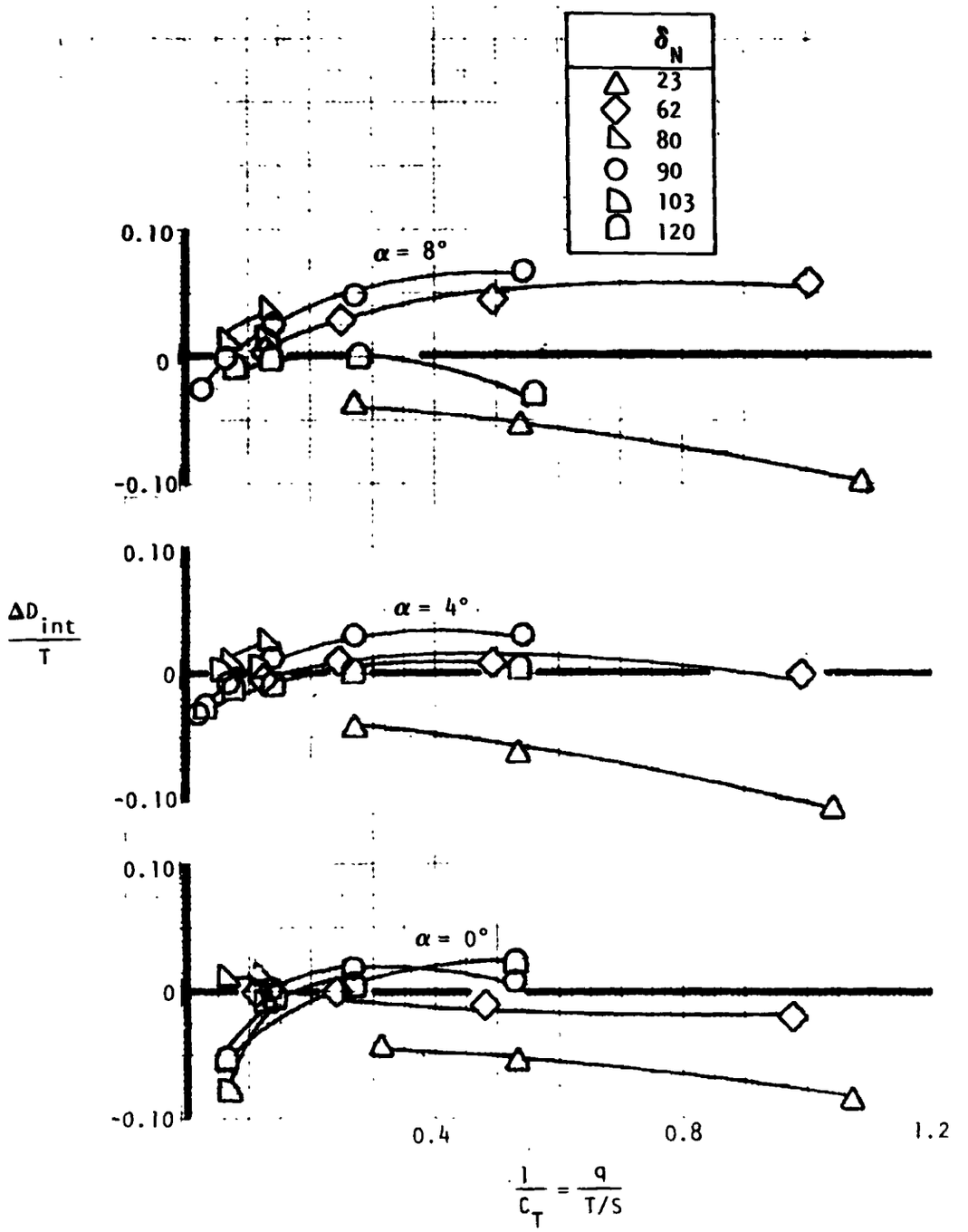

(h) Interference drag at various values of α and δ_N.

Figure 48. - Continued.

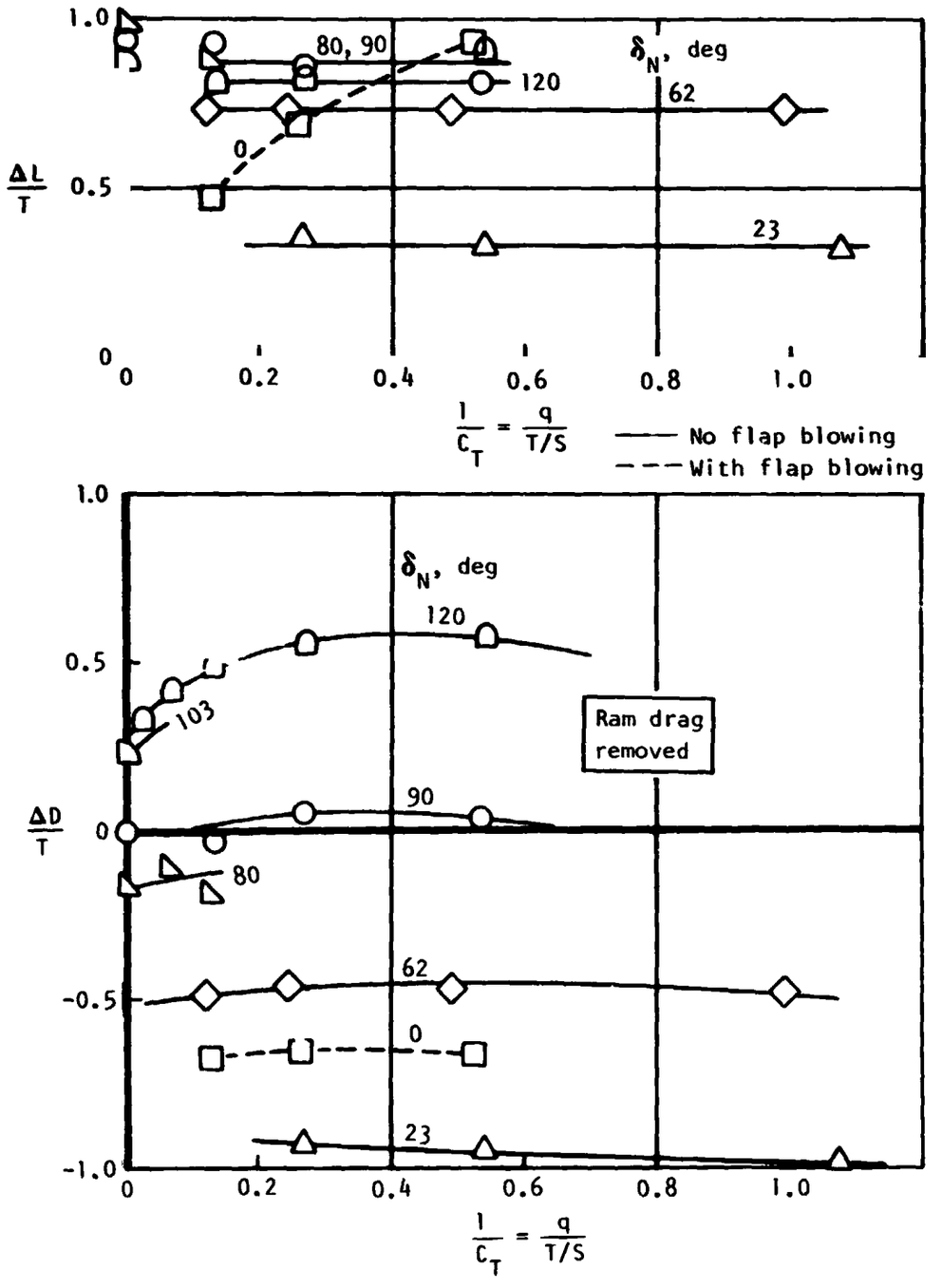

(i) Lift and drag increment due to power, $\alpha = 0$.

Figure 48. - Concluded.

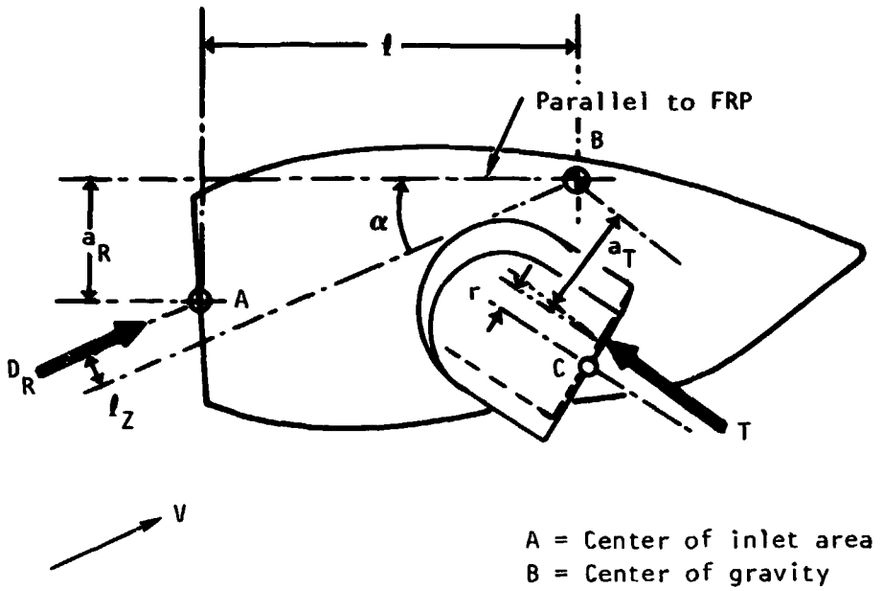

(a) Moment arms of thrust and ram drag.

Figure 49. - Analysis of pitching moments, Tail off, OGE.

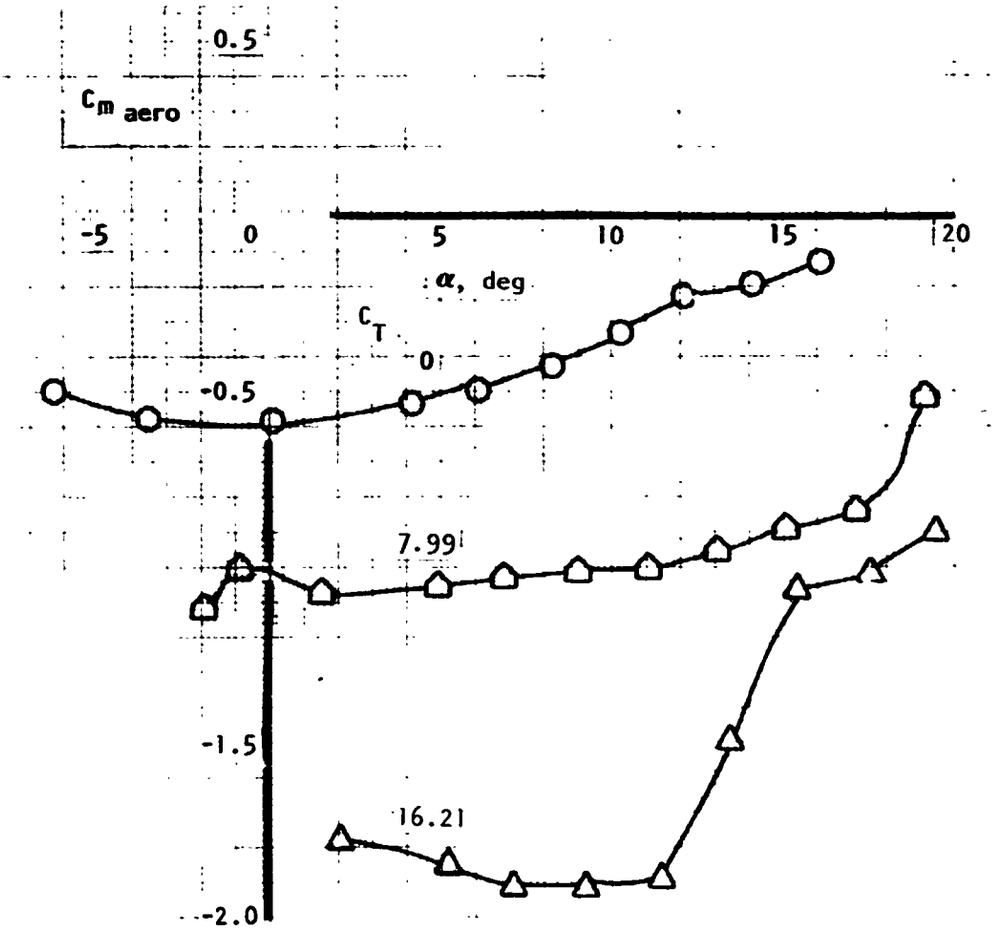

(b) Aerodynamic pitching moment in coefficient form, $\delta_N = 62°$.

Figure 49. - Continued.

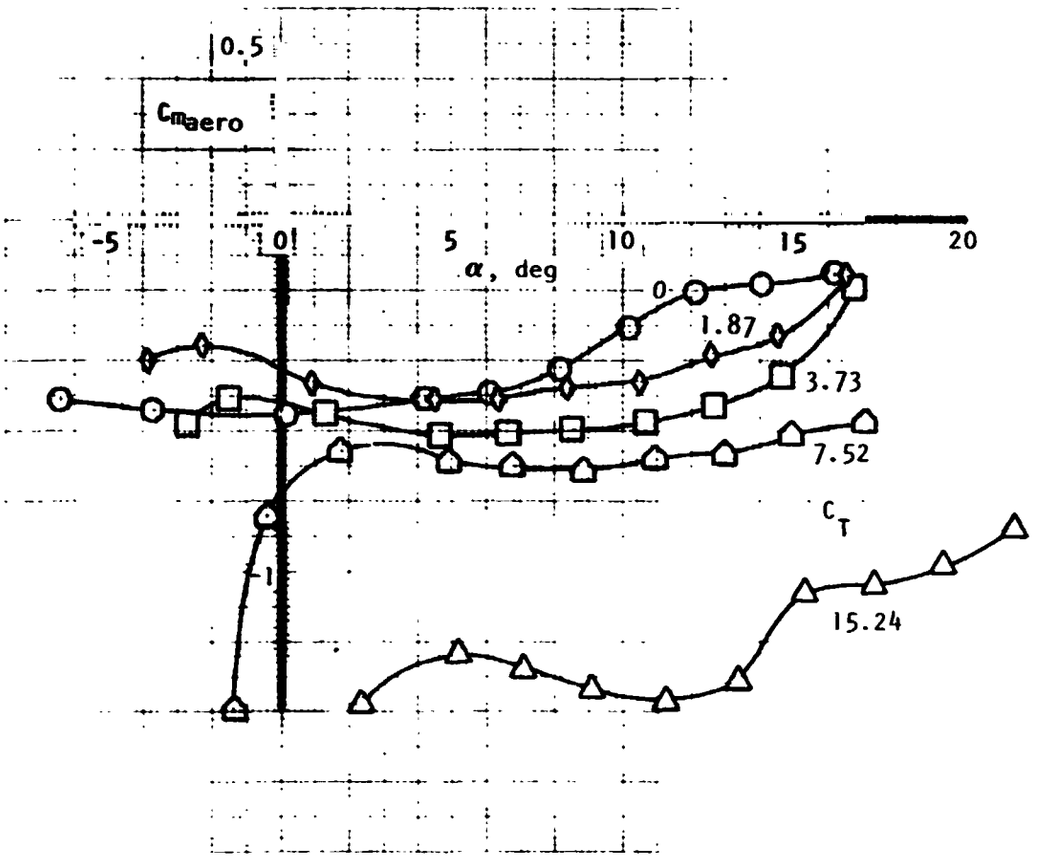

(c) Aerodynamic pitching moment in coefficient form, $\delta_N = 90°$.

Figure 49. - Continued.

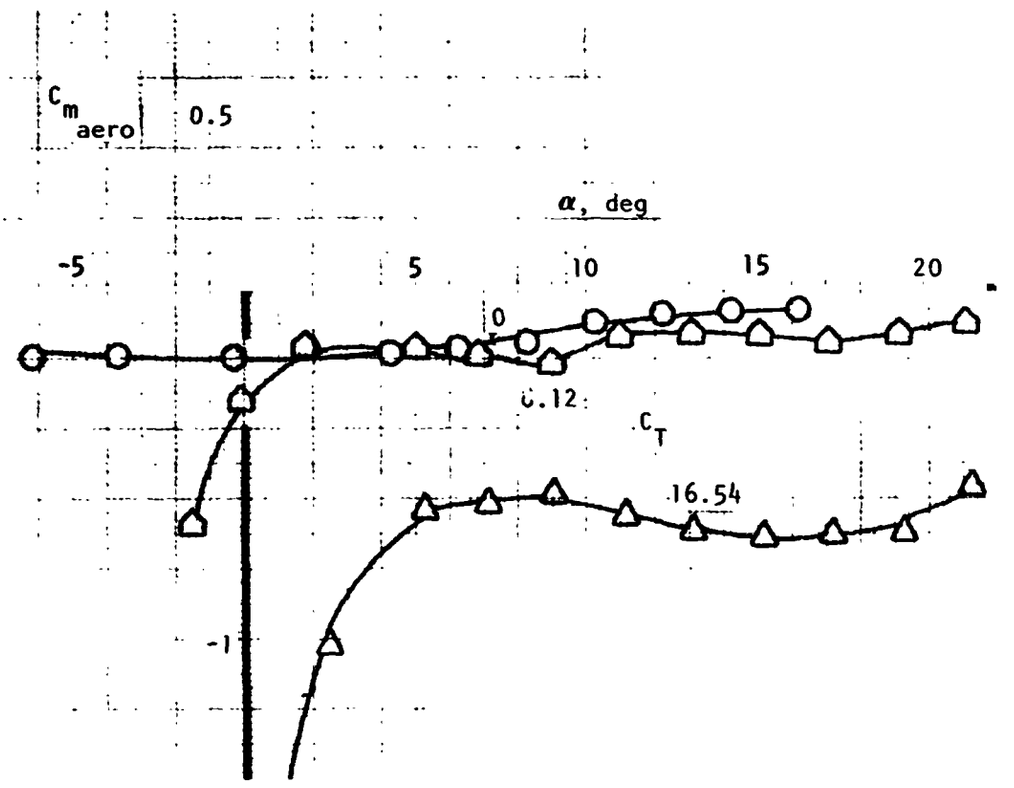

(d) Aerodynamic pitching moment in coefficient form, $\delta_N = 103°$.

Figure 49. - Continued.

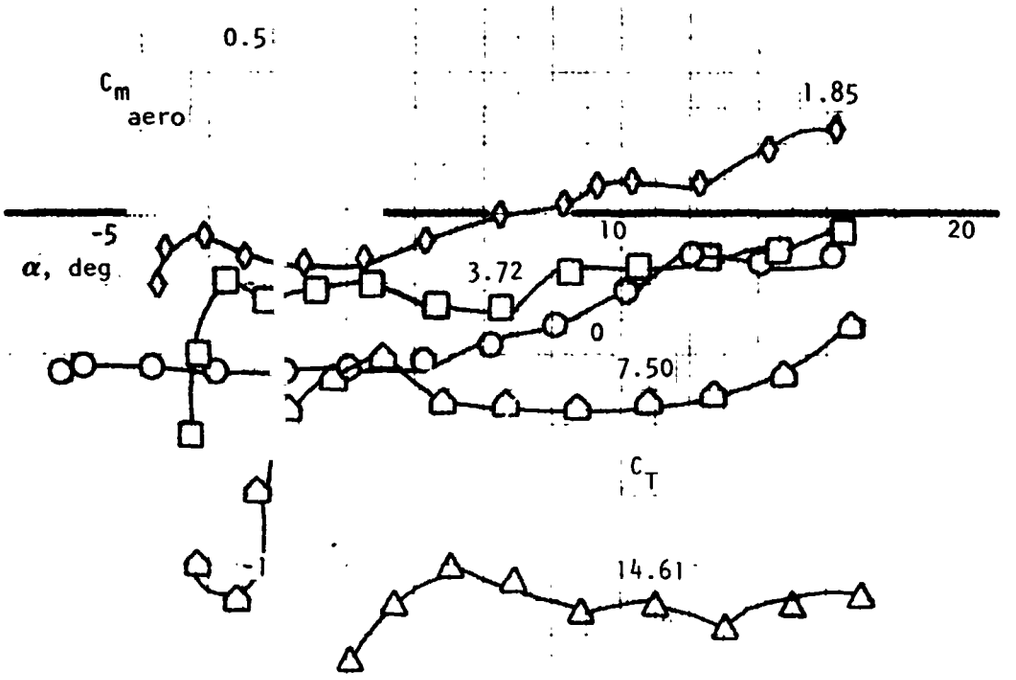

(e) Aerodynamic pitching moment in coefficient form, $\delta_N = 120°$.

Figure 49. - Continued.

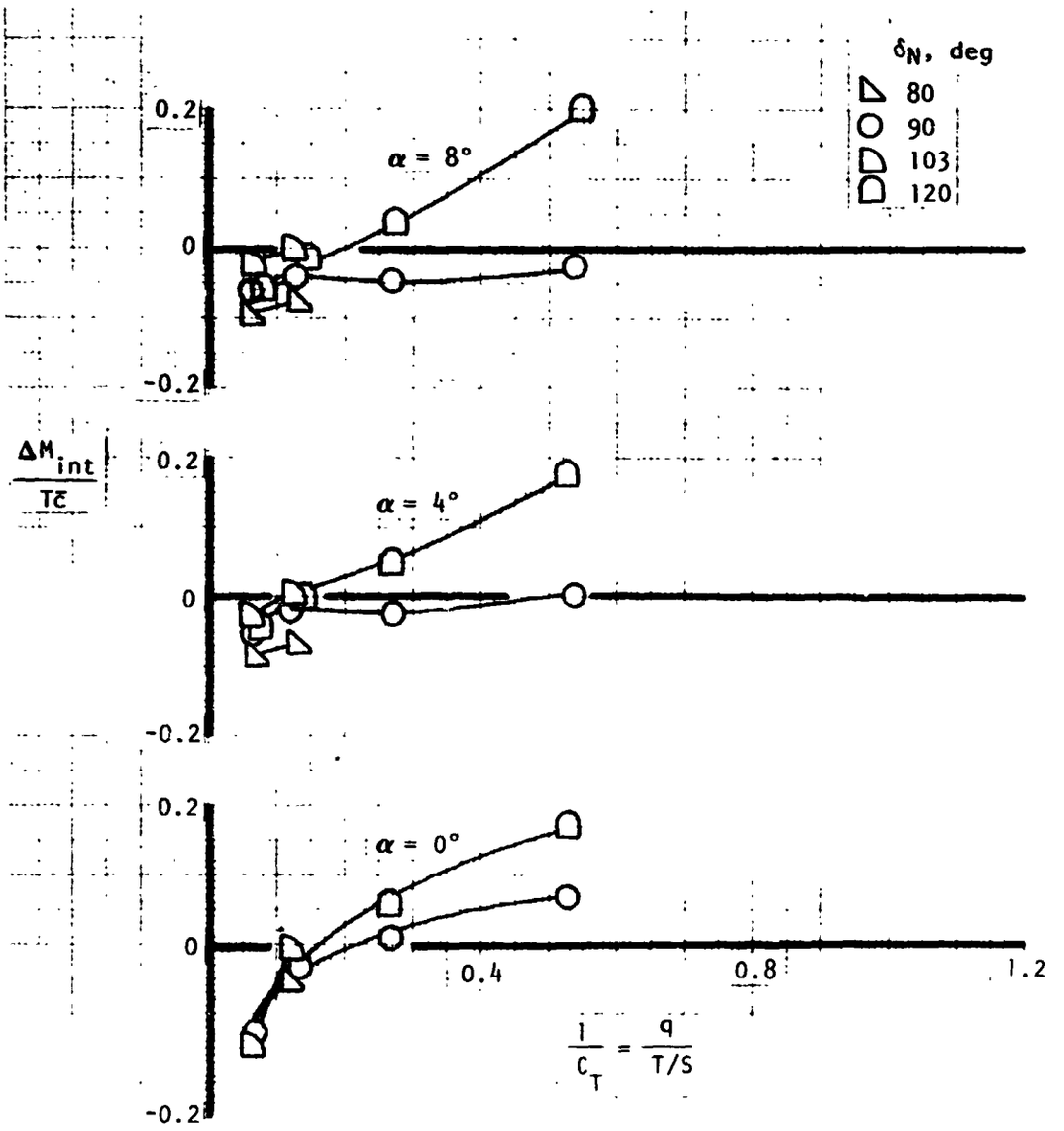

(f) Interference pitching moment in ratio form.

Figure 49.- Concluded.

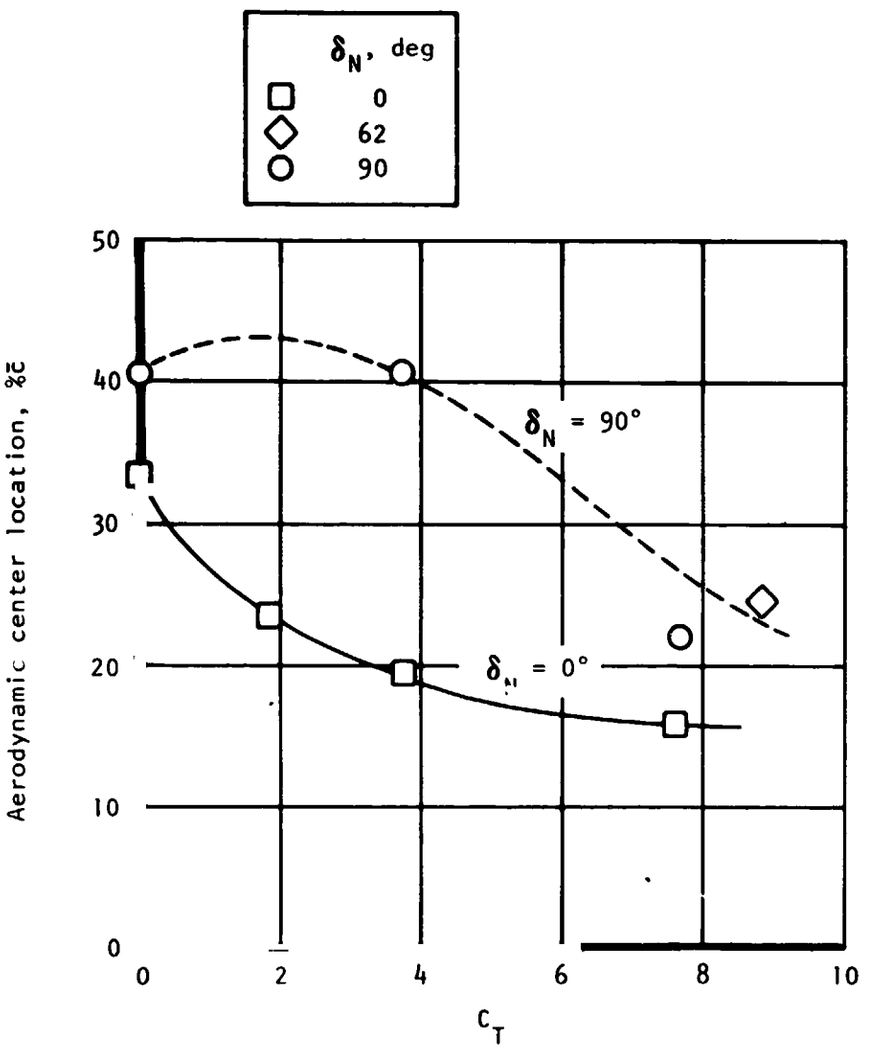

(a) Tail on.

Figure 50. - Aerodynamic center location versus thrust coefficient.

OGE, $\alpha \geq 2°$.

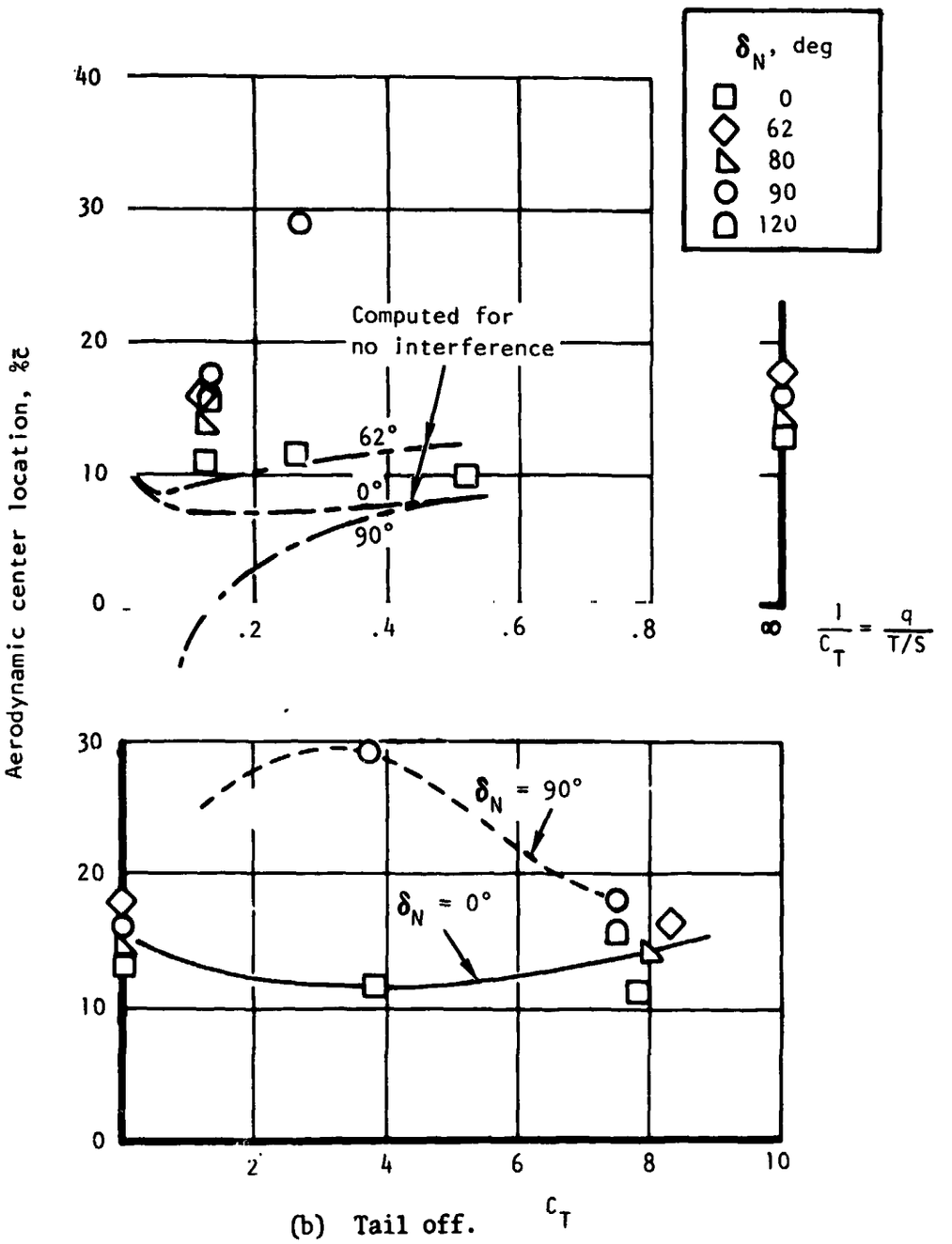

(b) Tail off.

Figure 50. Concluded.

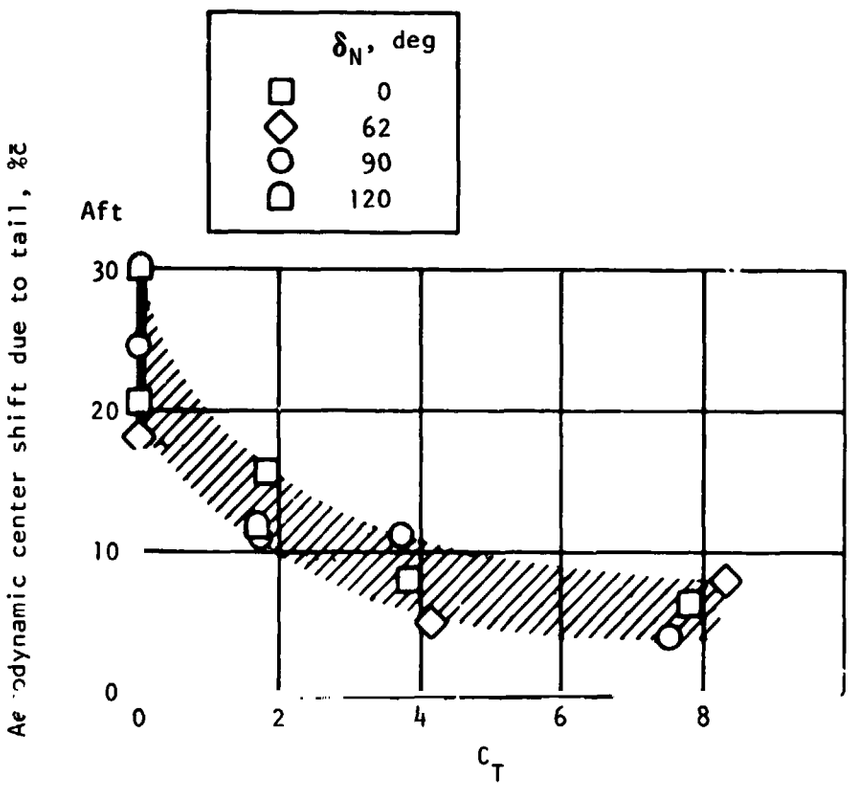

(a) A.C. shift at $\alpha \cong 2°$.

Figure 51.- Effect of horizontal tail on longitudinal stability, OGE.

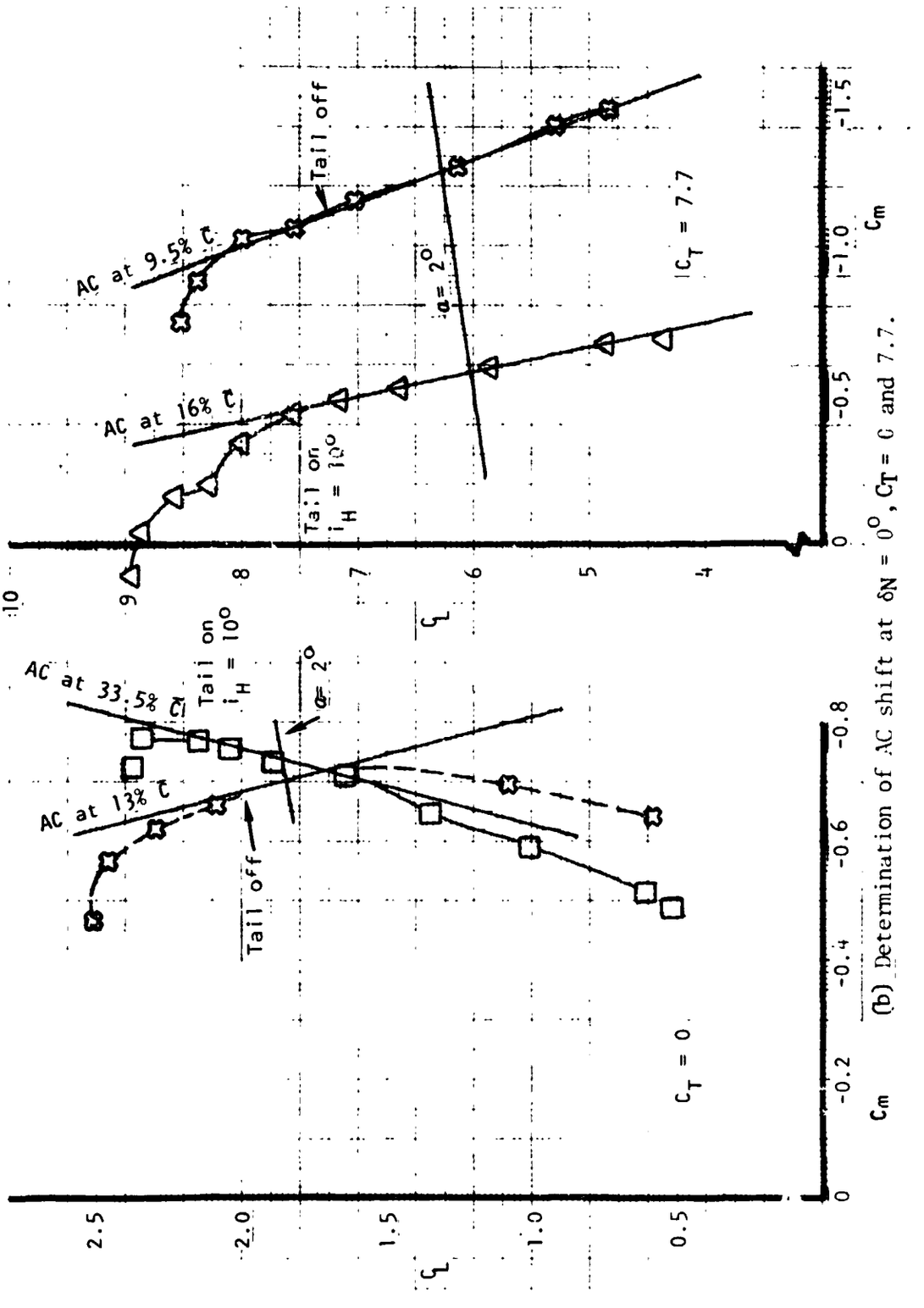

(b) Determination of AC shift at $\delta_N = 0^o$, $C_T = 0$ and 7.7.

Figure 51.- Continued.

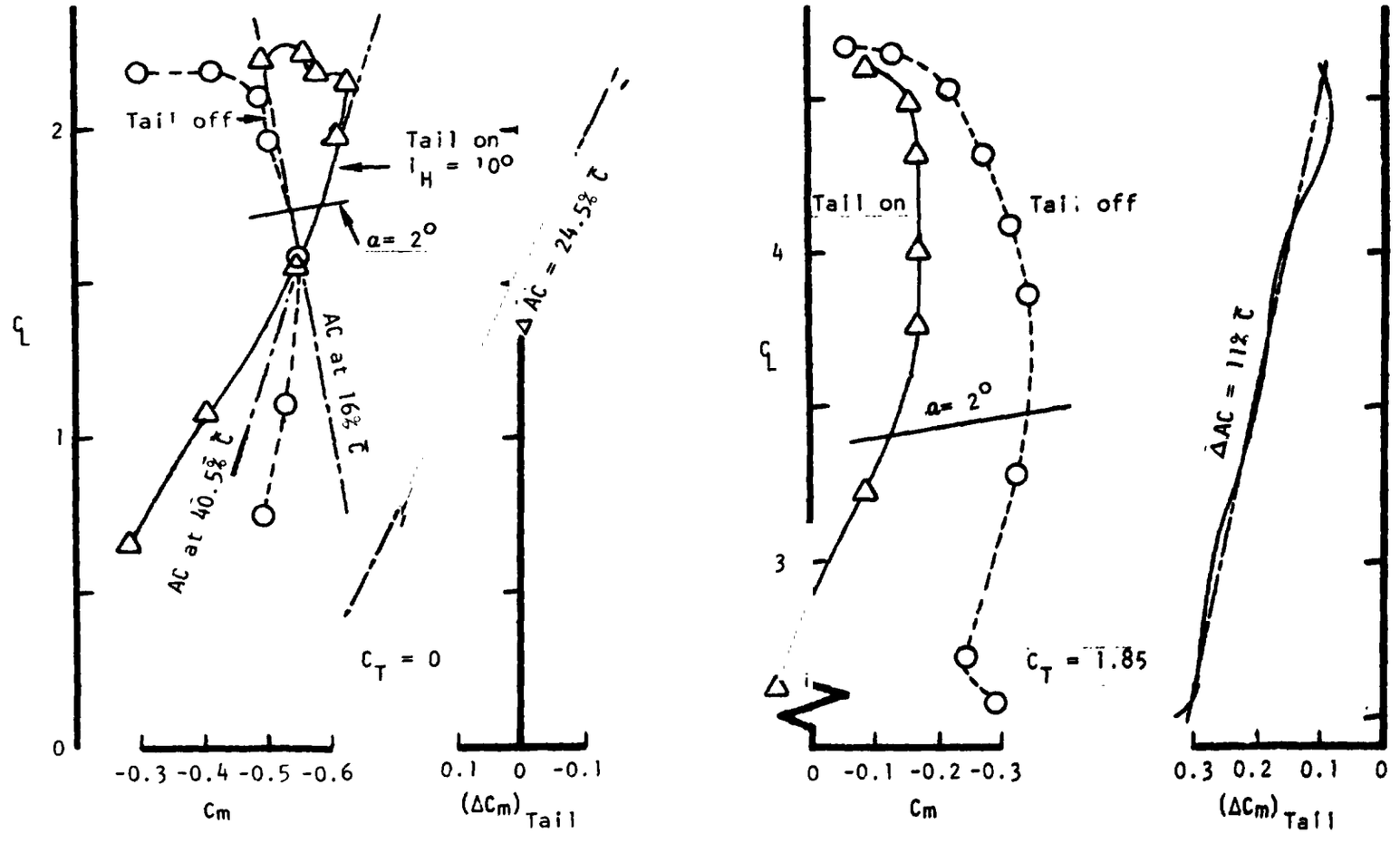

(c) Determination of AC shift at $\delta_N = 90^o$, $C_T = 0$ and 1.85.

Figure 51.- Continued.

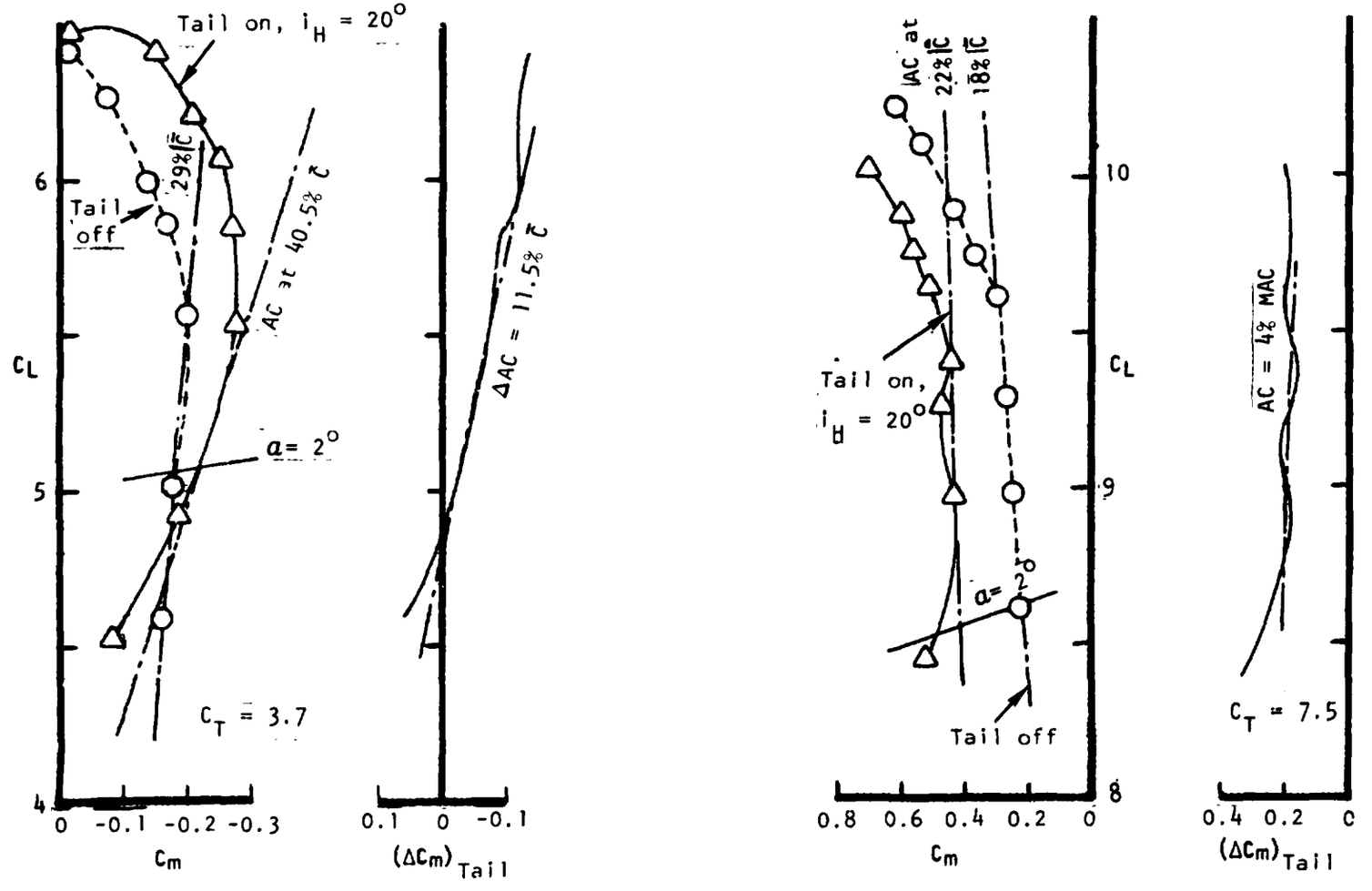

(d) Determination of AC shift at $\delta_N = 90^\circ$, C_T = 3.7 and 7.5.

Figure 51. - Concluded.

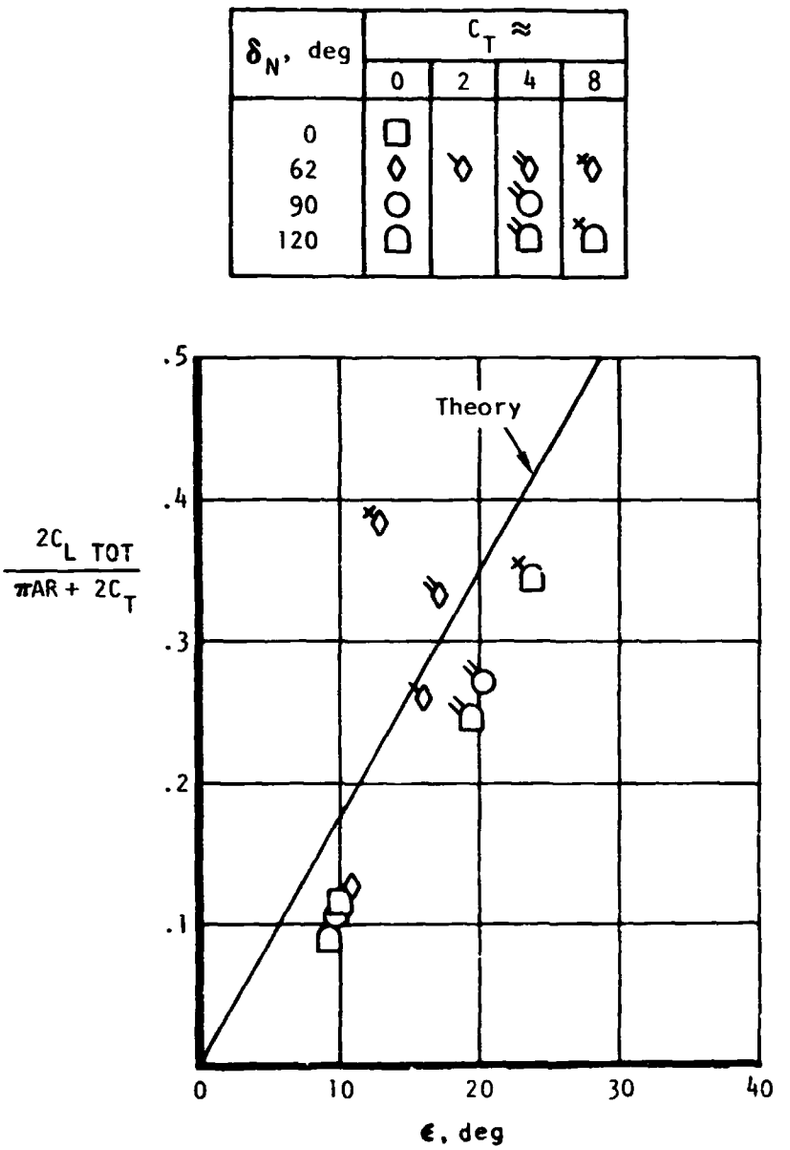

(a) Comparison with theory.

Figure 52. - Downwash correlation, OGE.

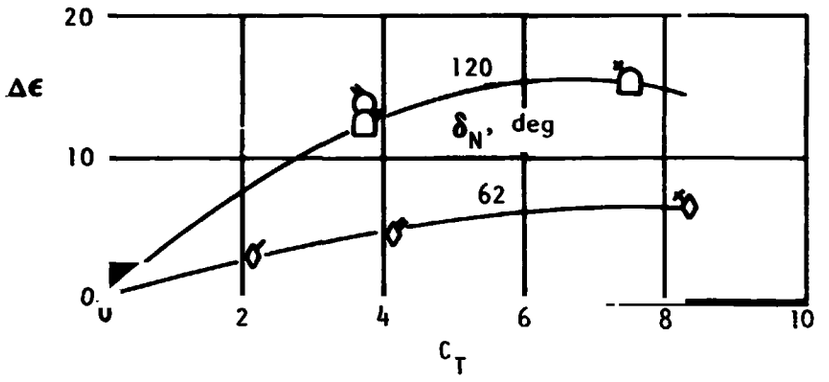

(b) Interference downwash.

δ_N, deg	$C_T \approx$ 0	2	4	8
0				
62				
90				
120				

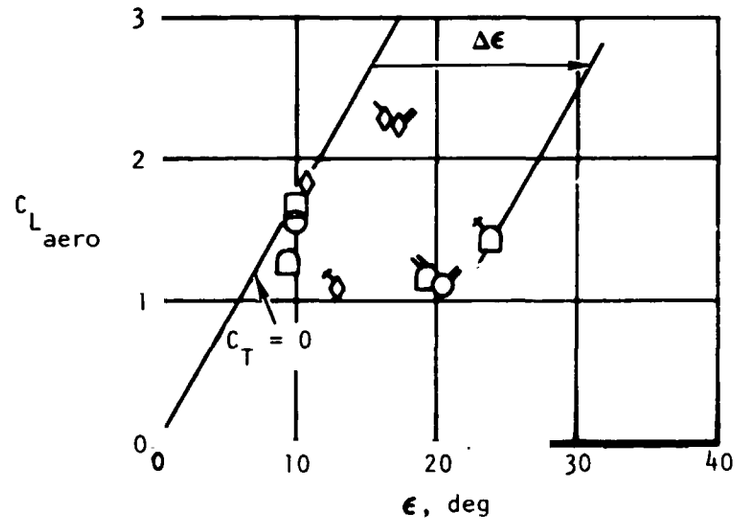

(c) Downwash versus circulation lift.

Figure 52. - Concluded.

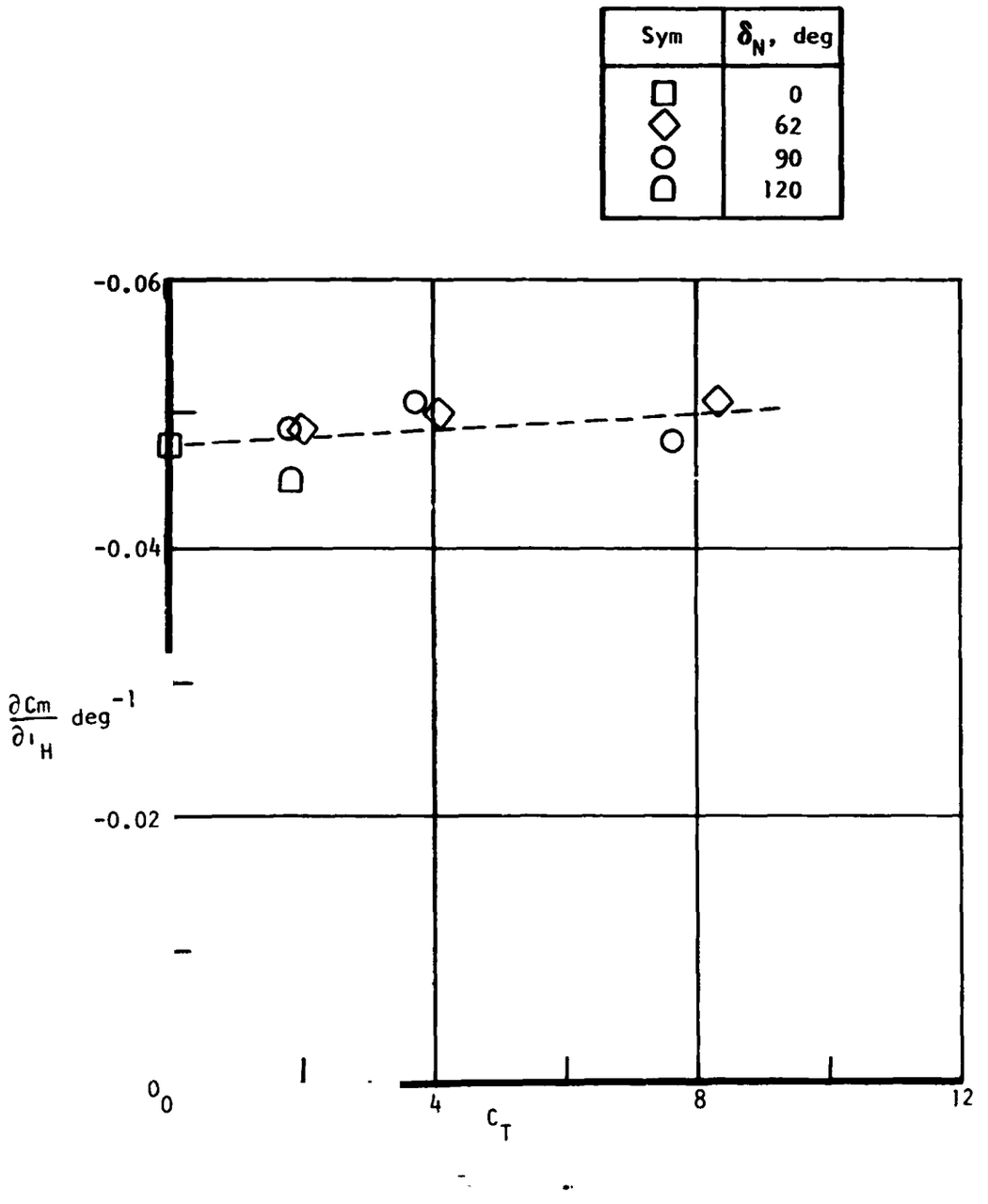

Figure 53. - Power-on tail effectiveness.

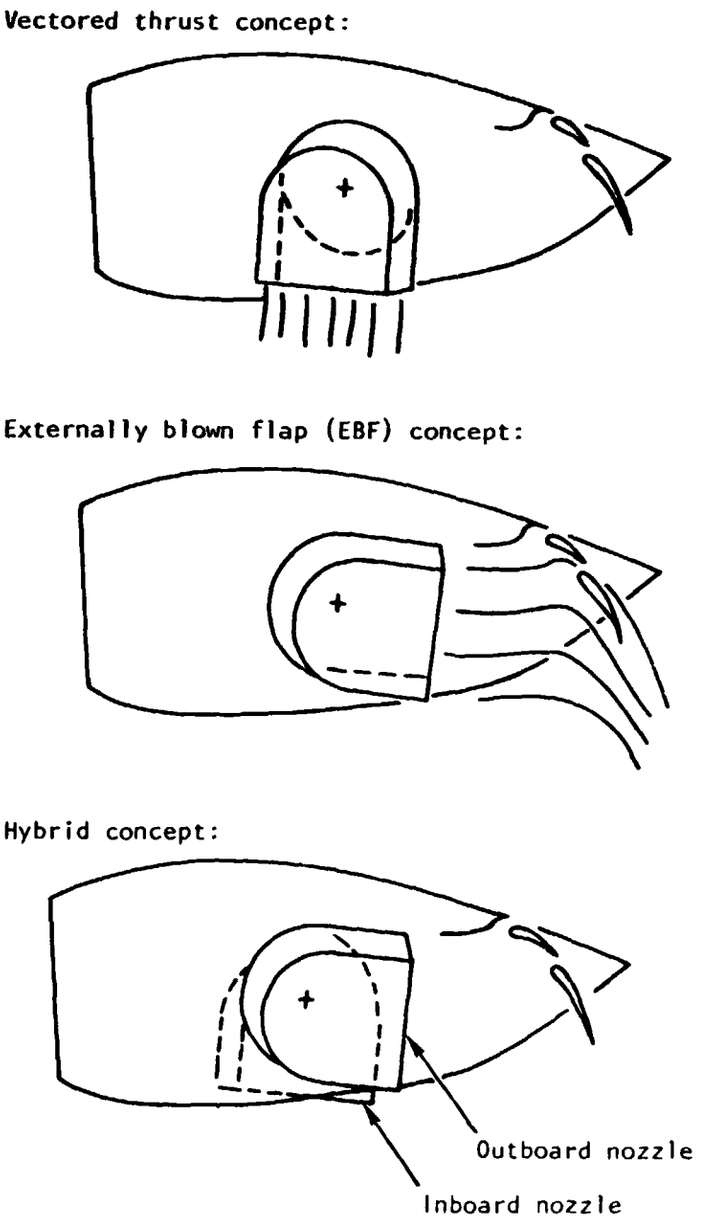

Figure 54. - Schematics of the EBF, vectored thrust, and hybrid lift/propulsion concepts.

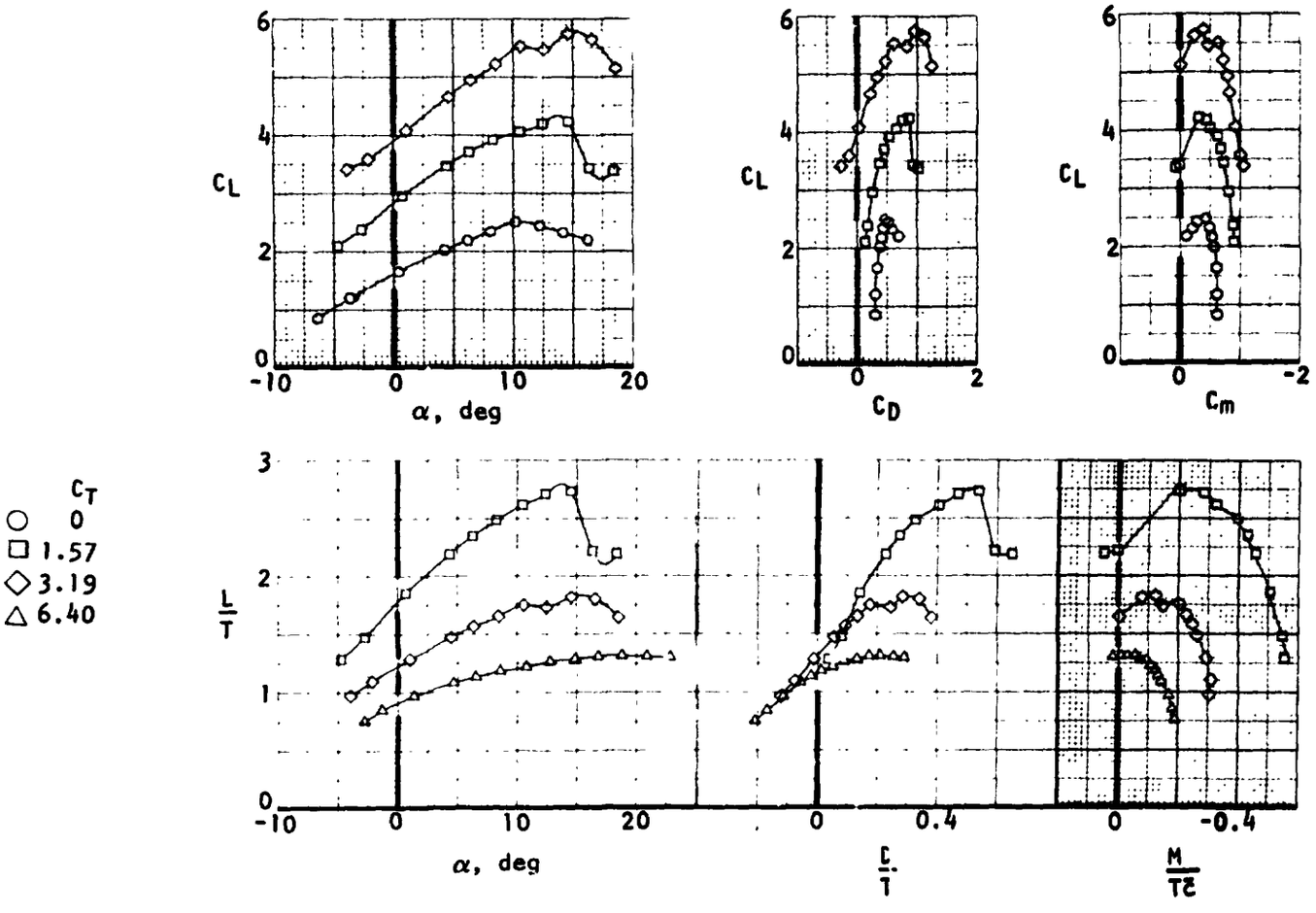

Figure 55. Flaps-down longitudinal forces and moments for nozzles deflected differentially (Hybrid). Transition out of ground effect. Tail off.

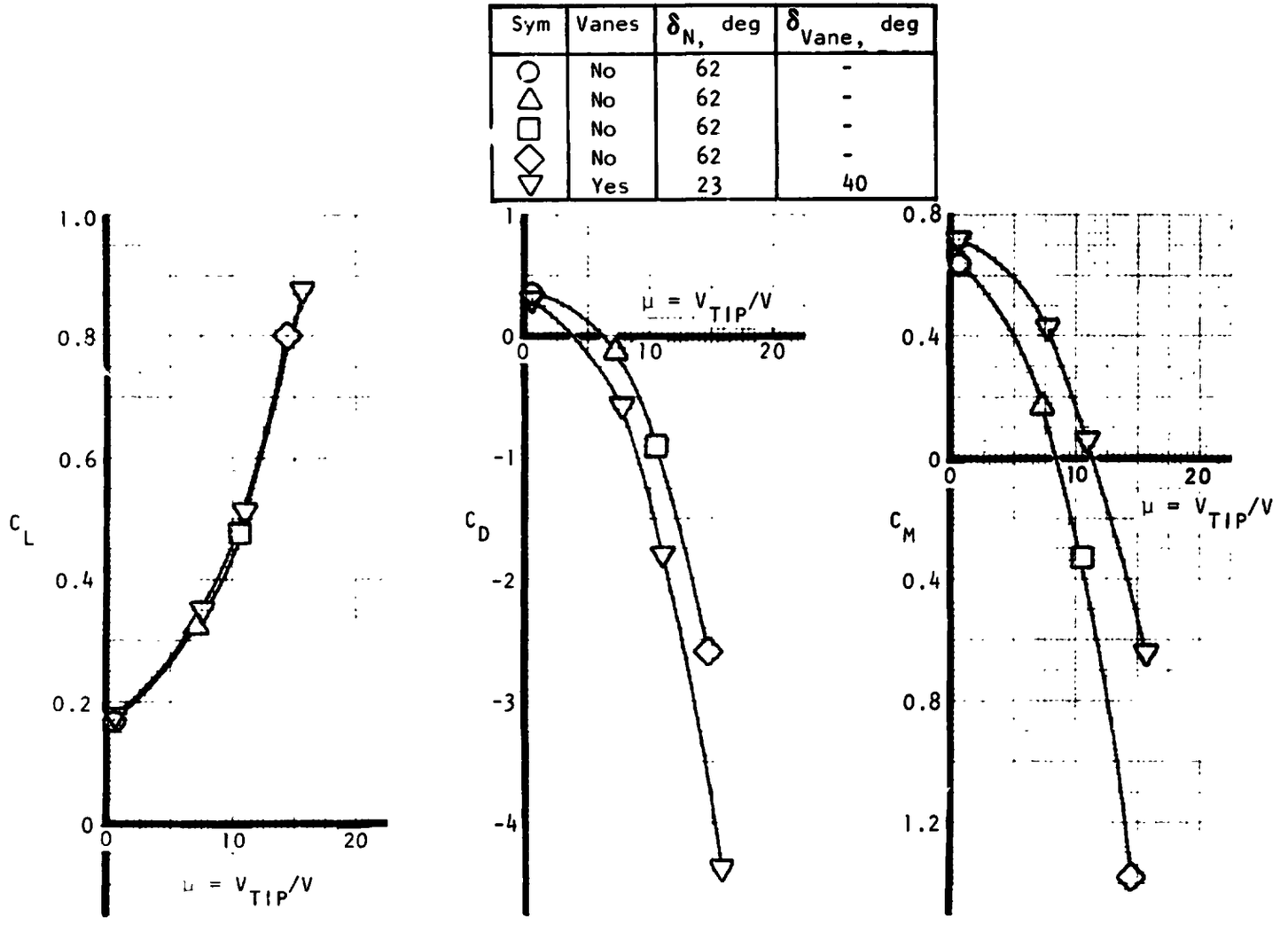

(a) Total deflection approximately 62°, α = 0.

Figure 56. - Effect of exhaust vanes on longitudinal characteristics out of ground effect. Tail off.

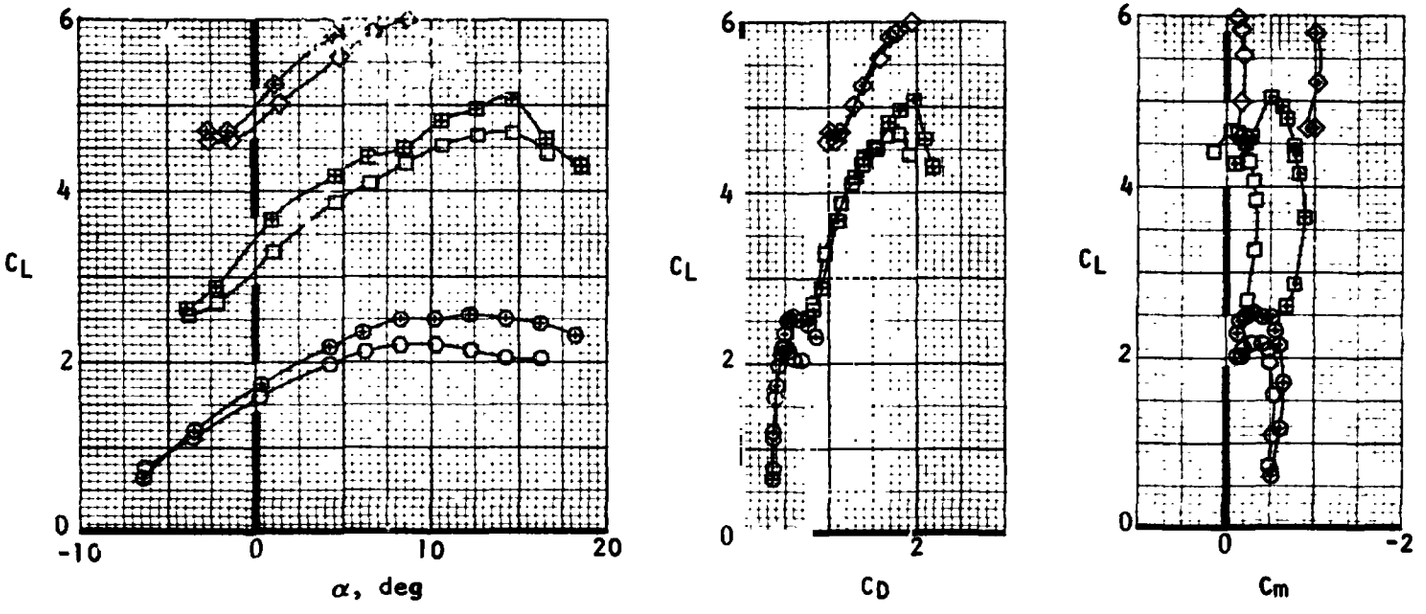

	μ	δ_N, deg	Vanes
○	0.517	90	off
□	7.22	90	off
◇	10.1	90	off
⊕	0.487	62	40
⊞	7.34	62	40
◈	10.3	62	40

(b) Total deflection approximately 90 to 100 deg.

Figure 56.- Concluded.

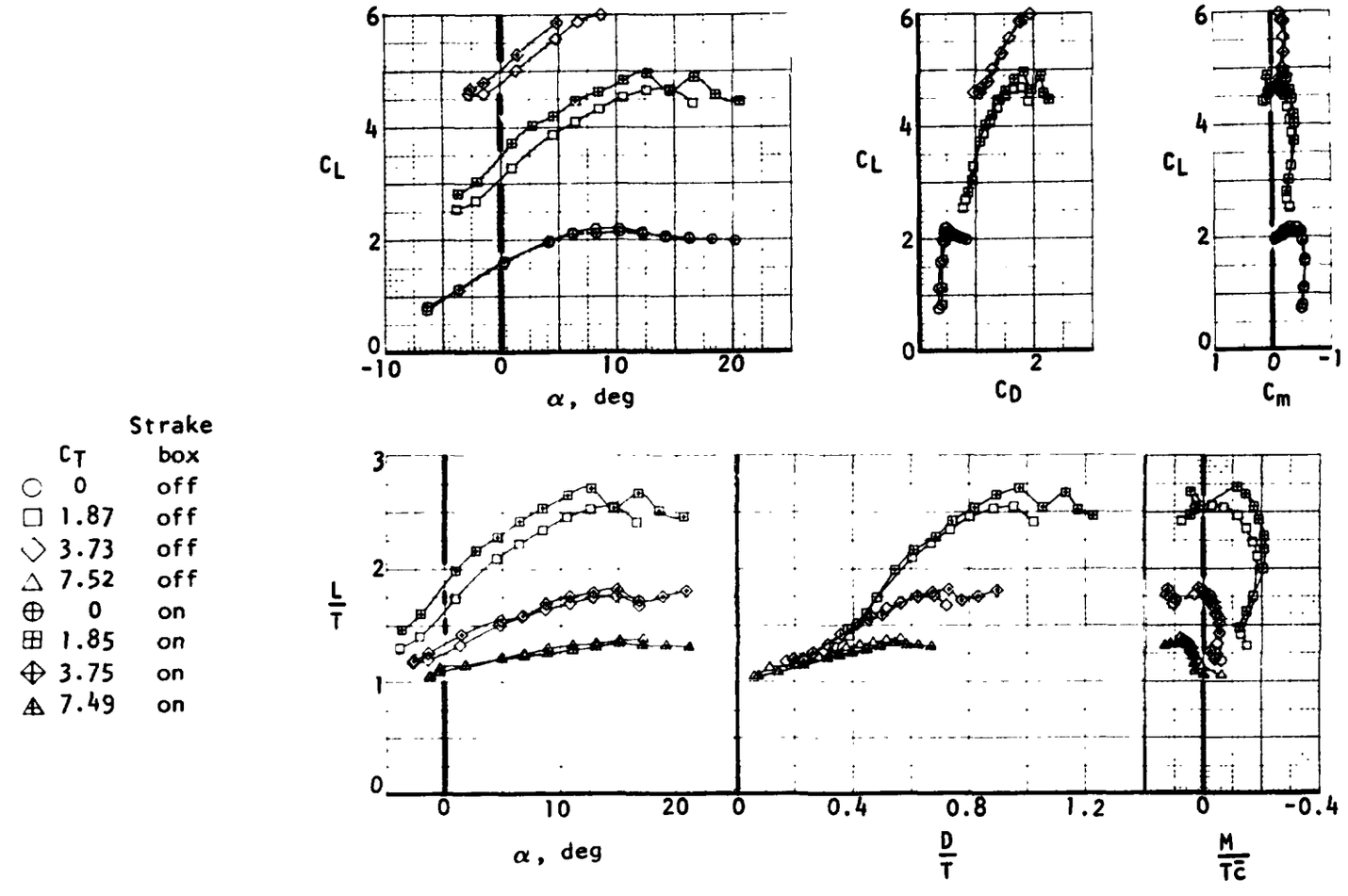

Figure 57.- Effect of strake box on longitudinal characteristics out of ground effect. Tail off. $\delta_N = 90°$.

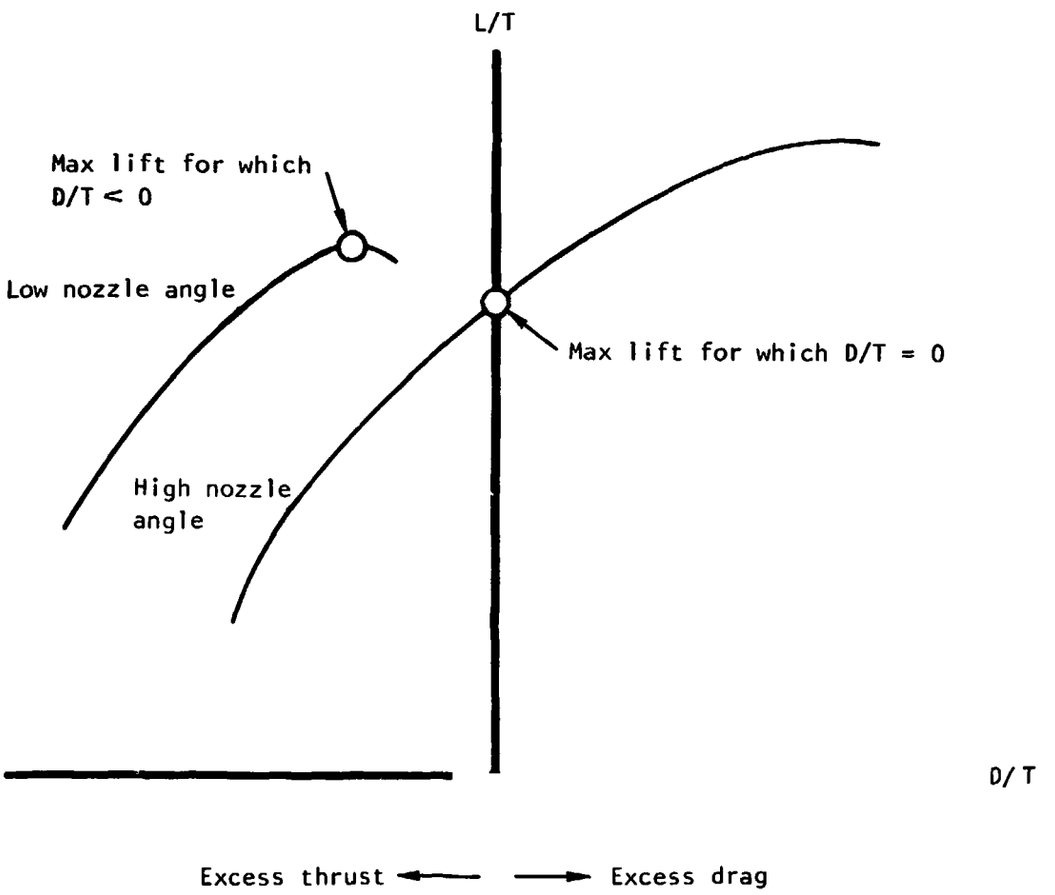

(a) Conditions for comparison.

Figure 58. - Lift comparison between vectored thrust and EBF concepts. tail off, OGE.

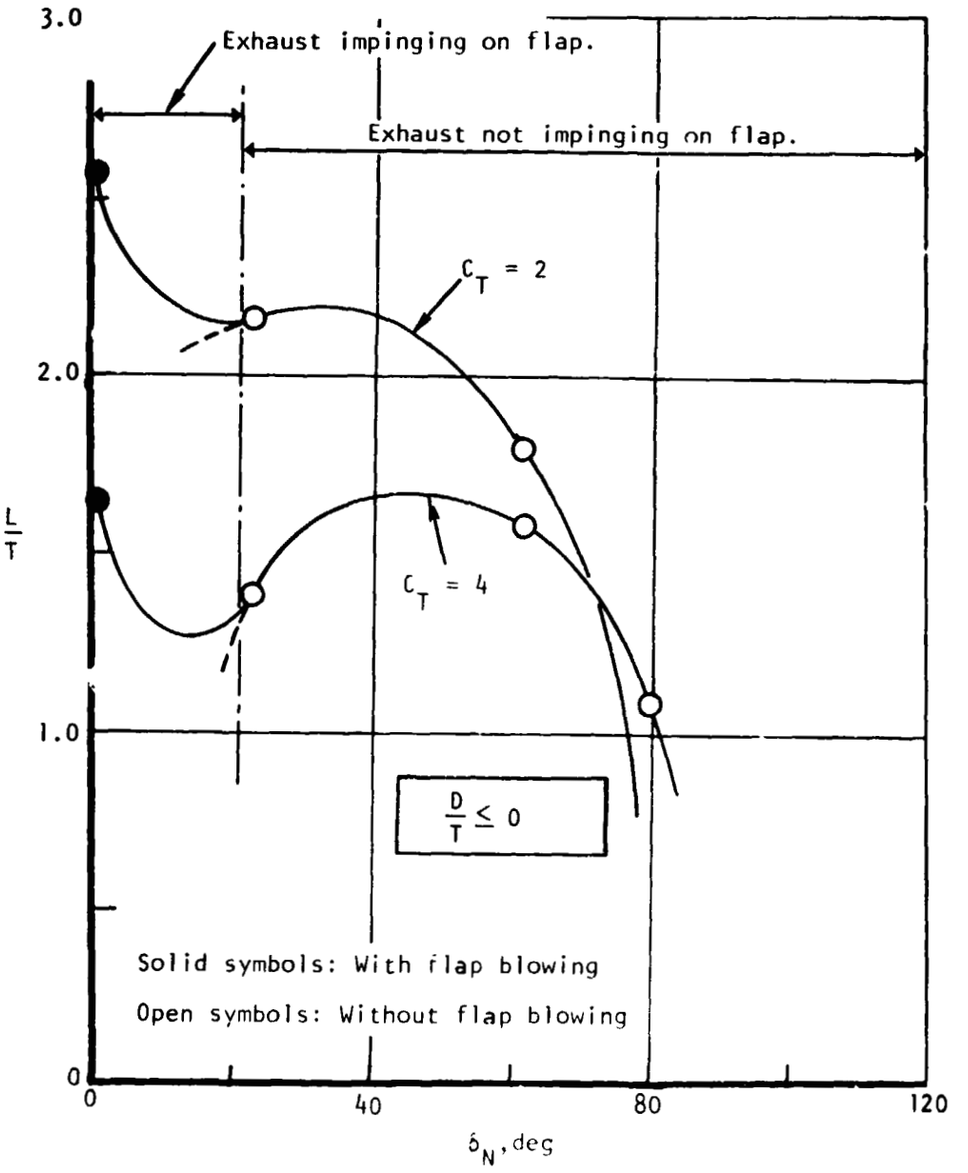

(b) Maximum lift with zero or forward acceleration.

Figure 58. Continued.

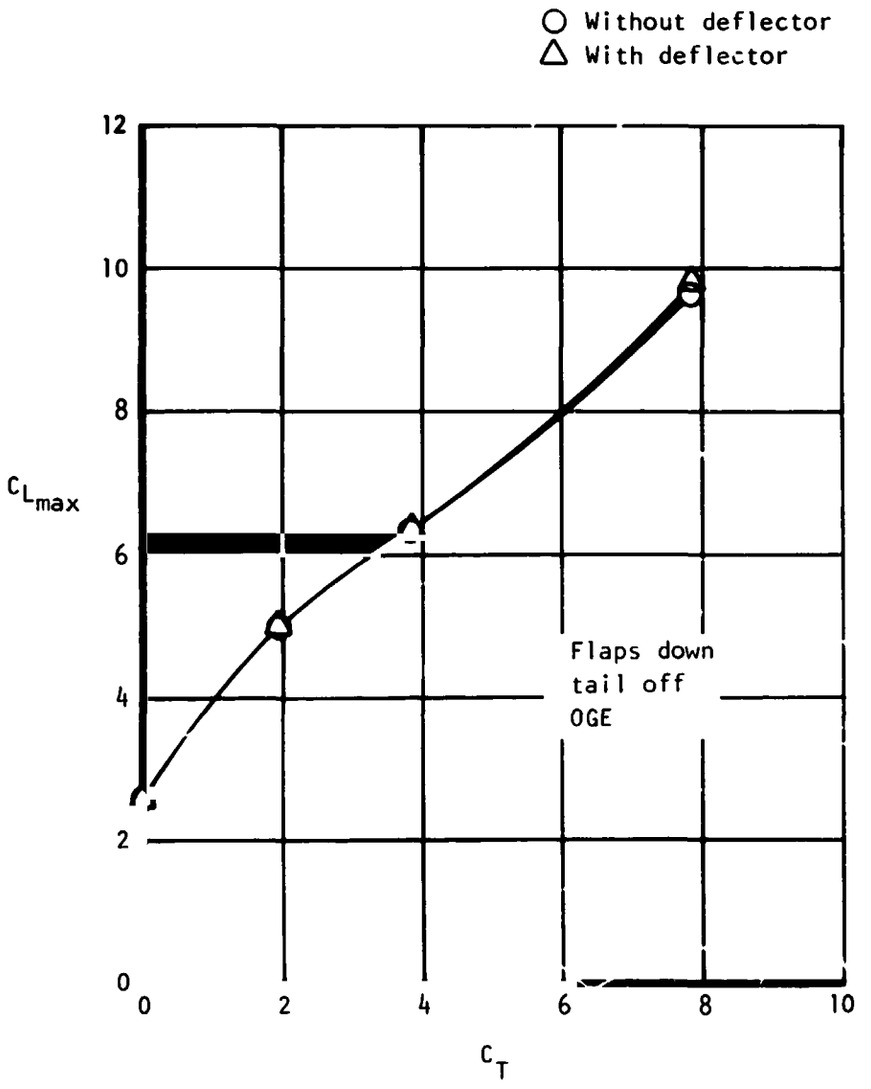

(c) Effect of EBF deflector on maximum lift.

Figure 58. - Concluded.

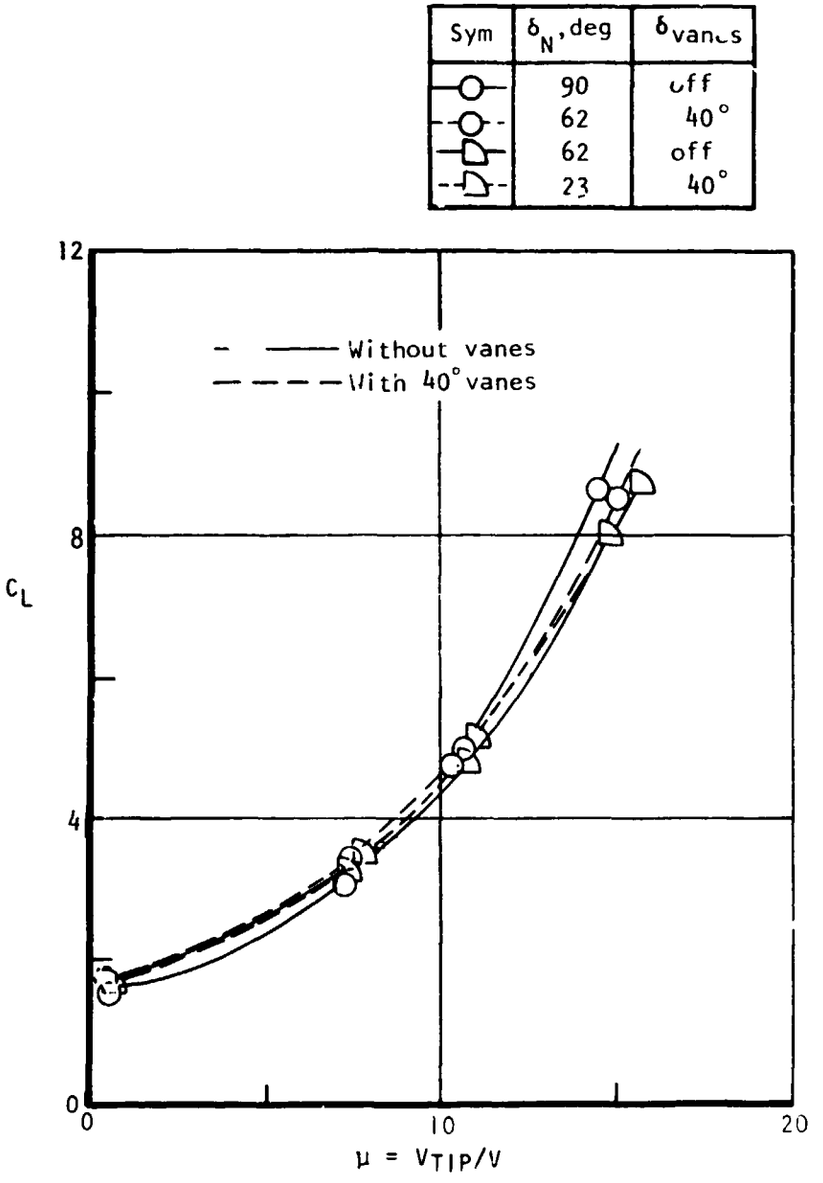

Figure 59. - Effect of exhaust vanes on lift at $\alpha = 0$. Transition OGL, tail off.

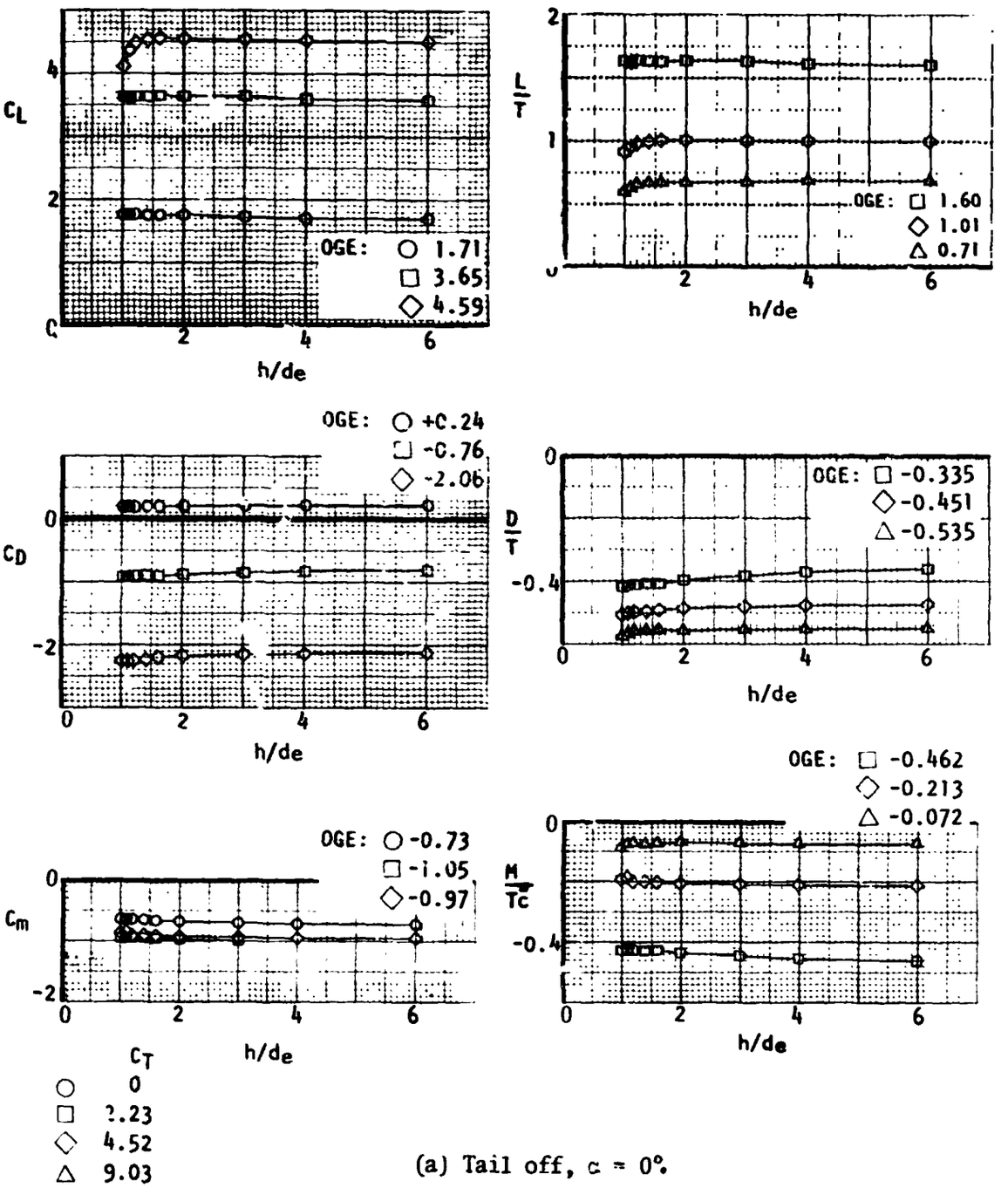

(a) Tail off, $\alpha = 0°$.

Figure 60.- Flaps-down longitudinal forces and moments during transition in ground effect. $\delta_N = 0°$.

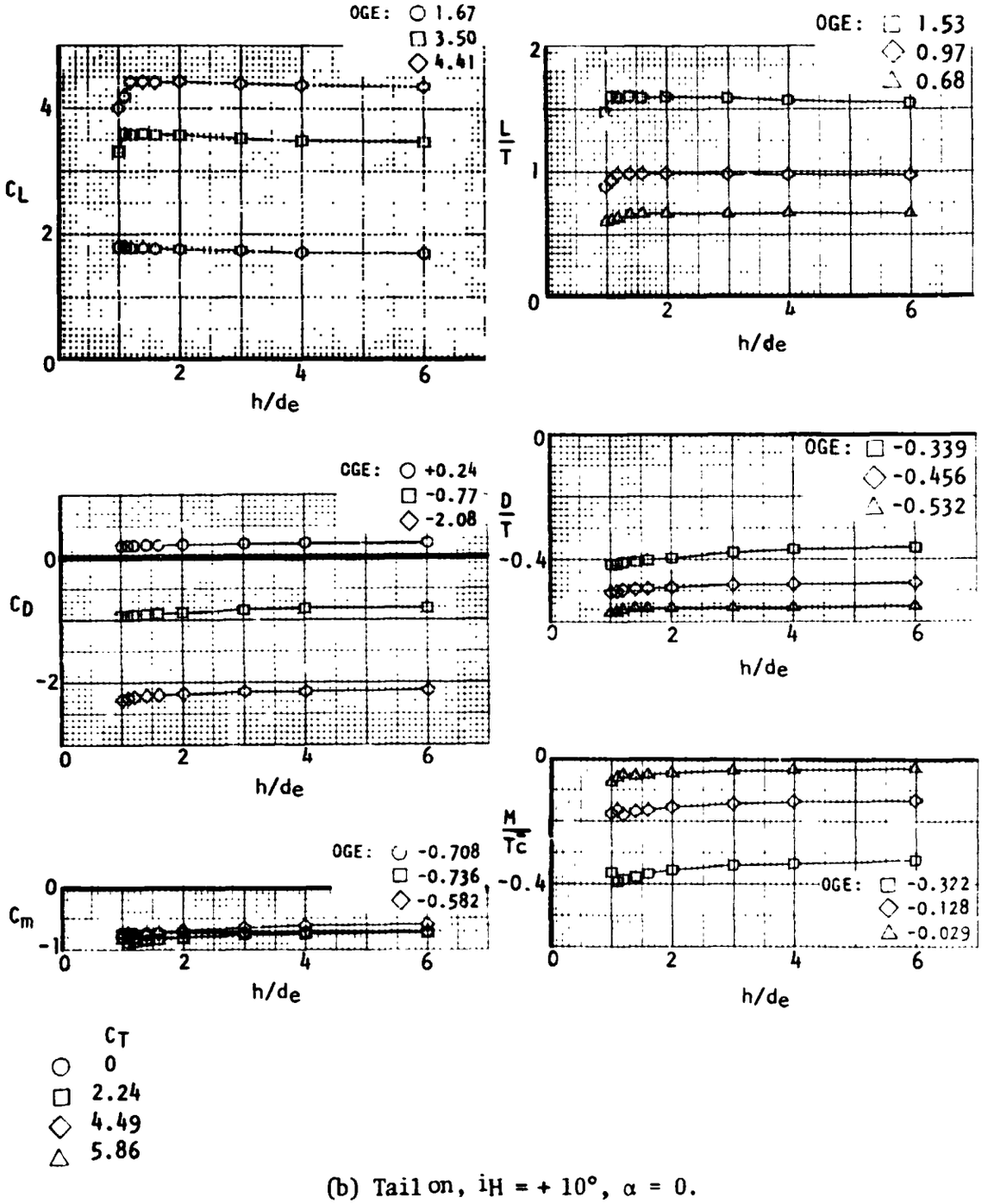

(b) Tail on, $i_H = +10°$, $\alpha = 0$.

Figure 60.- Concluded.

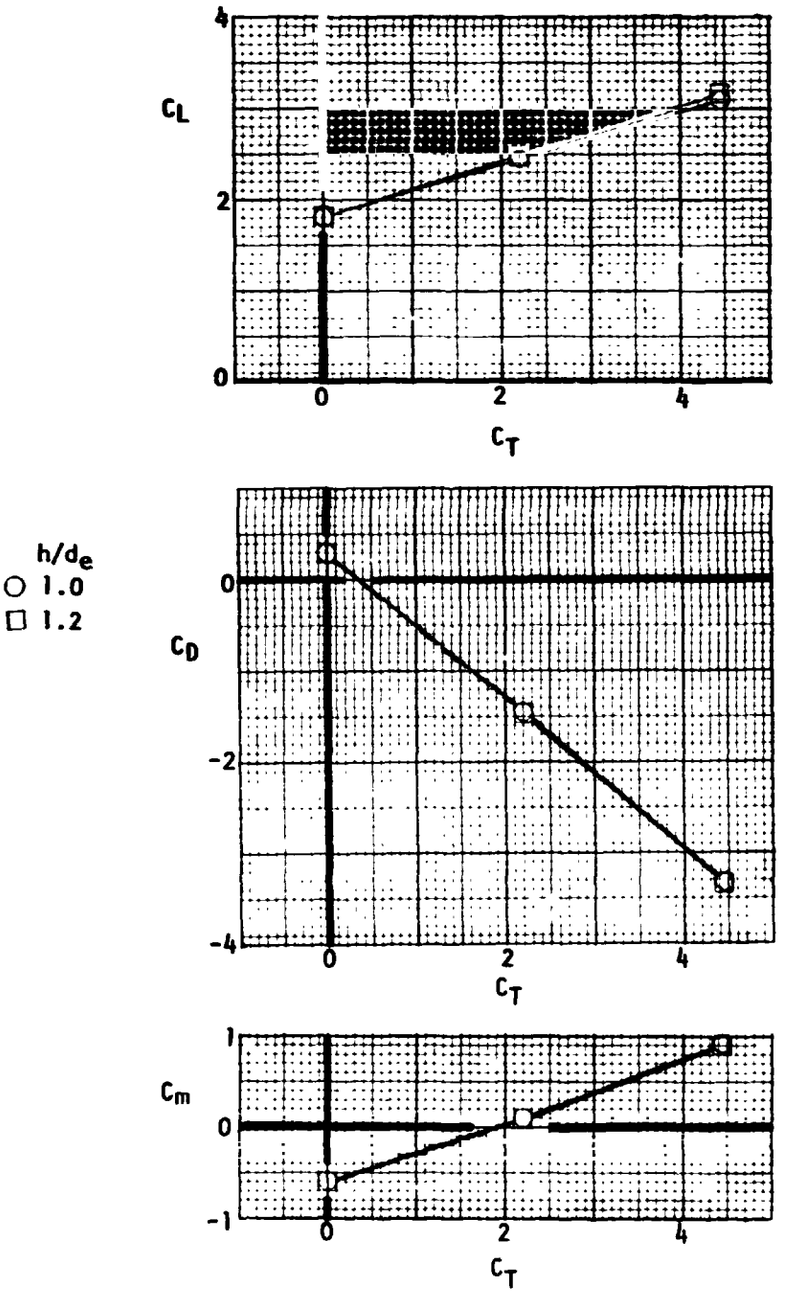

Figure 61.- Flaps-down longitudinal forces and moments during transition in ground effect. Tail off, $\alpha = 0$. $\delta_N = 23°$.

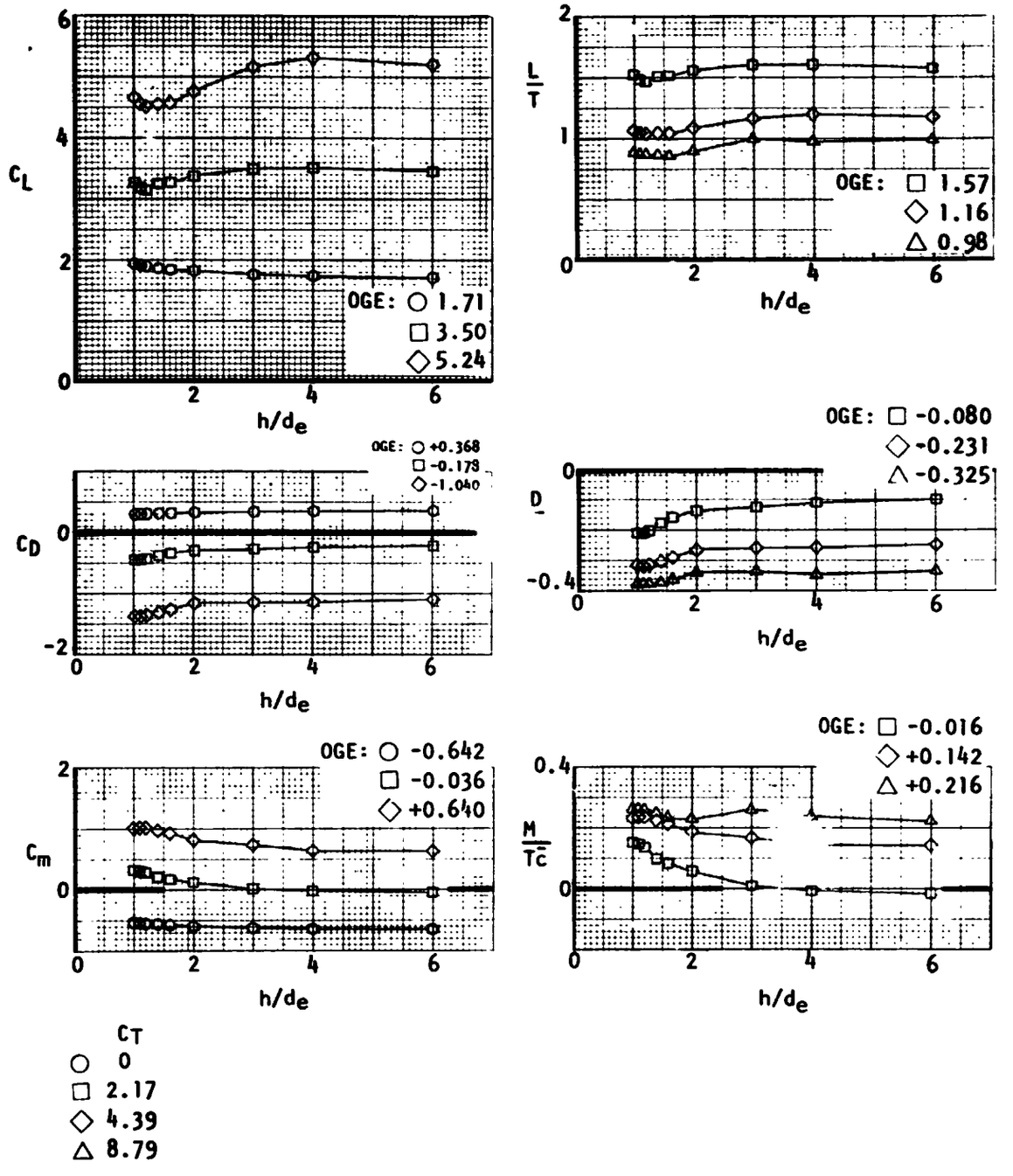

(a) Tail off, $\alpha = 0°$.

Figure 62.- Flaps-down longitudinal forces and moments during transition in ground effect. $\delta_N = 02°$.

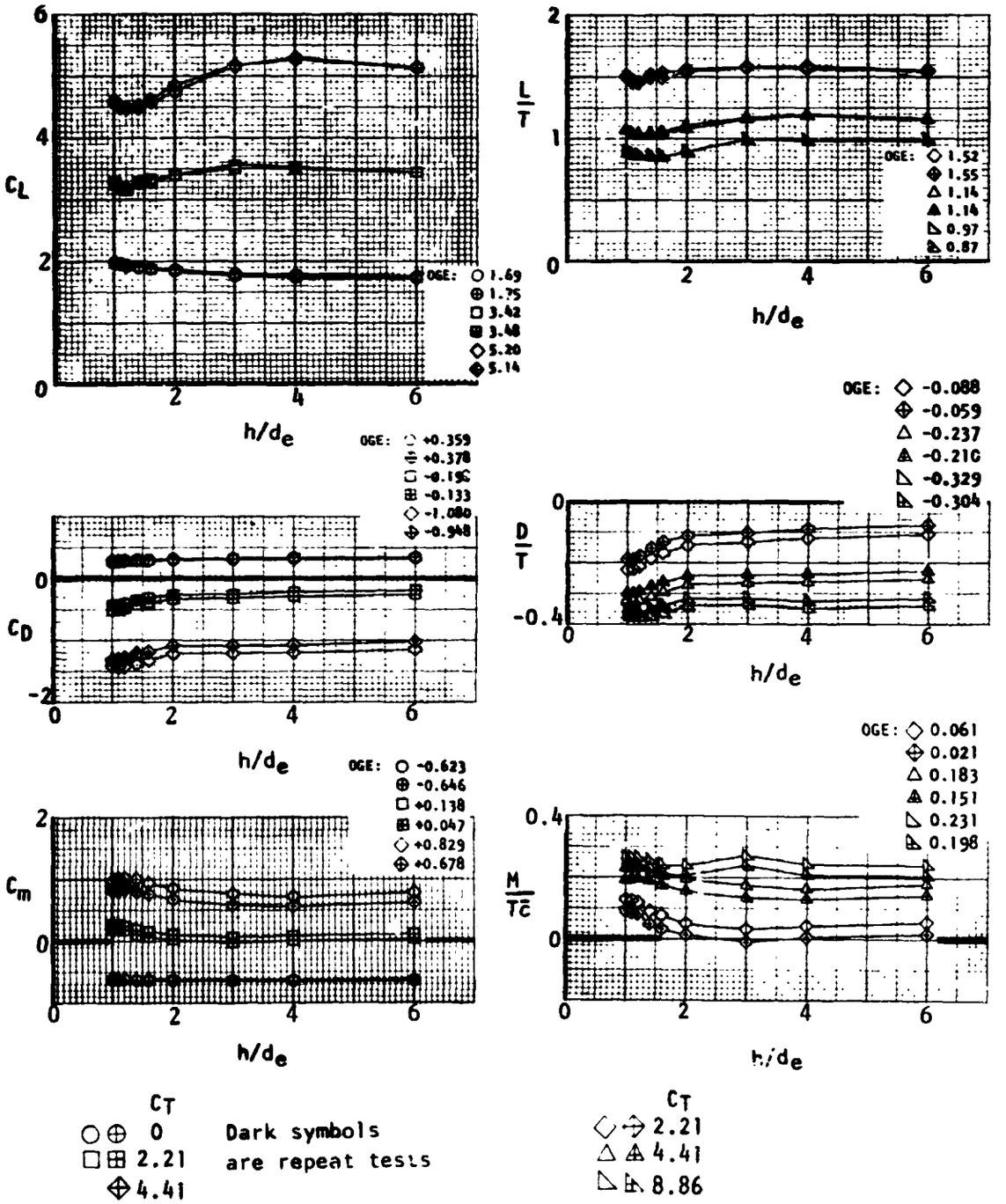

(b) Tail on, $i_H = +10°$, $\alpha = 0$.

Figure 62.- Continued.

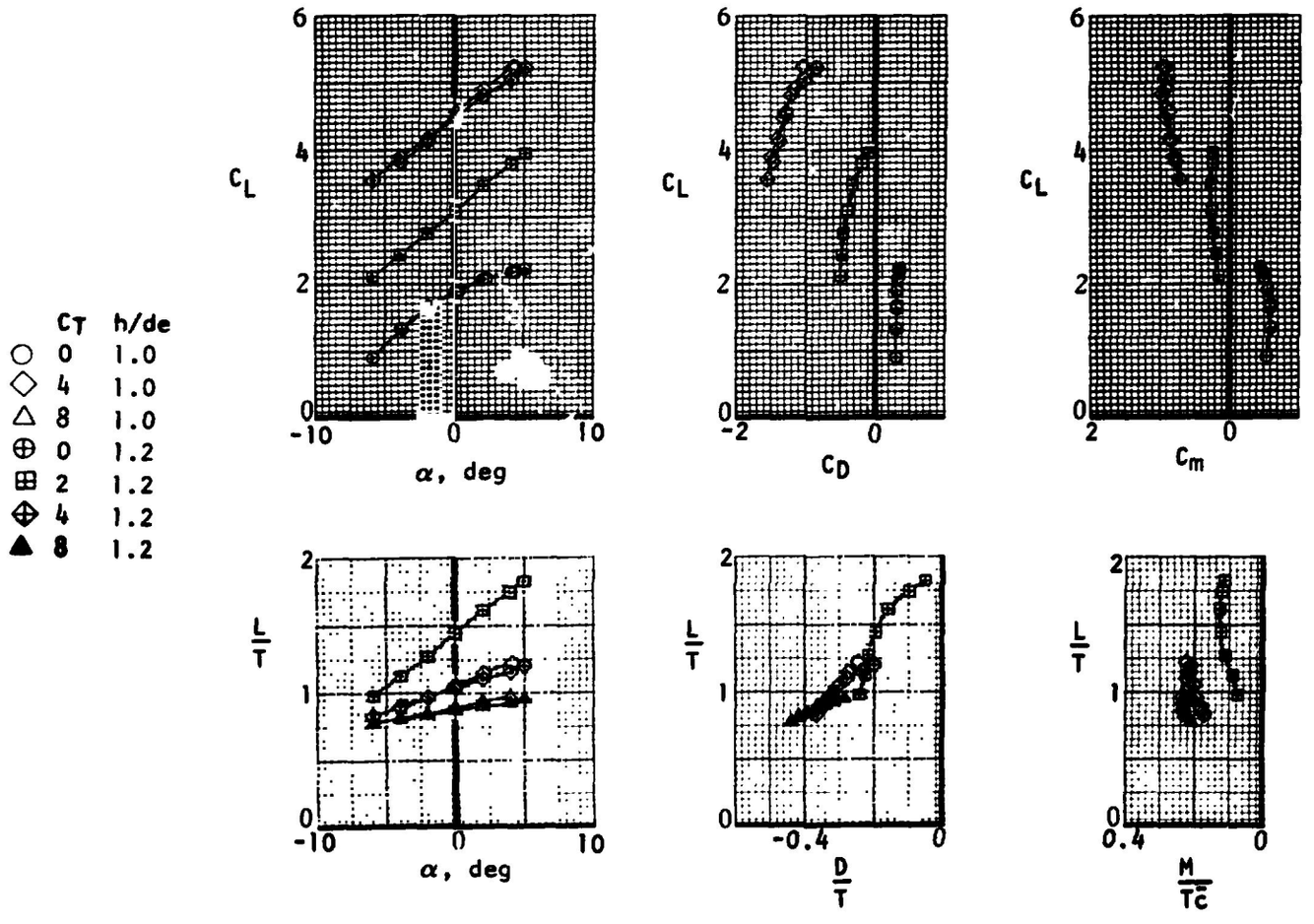

(c) Effect of angle of attack, tail off.

Figure 62.- Concluded.

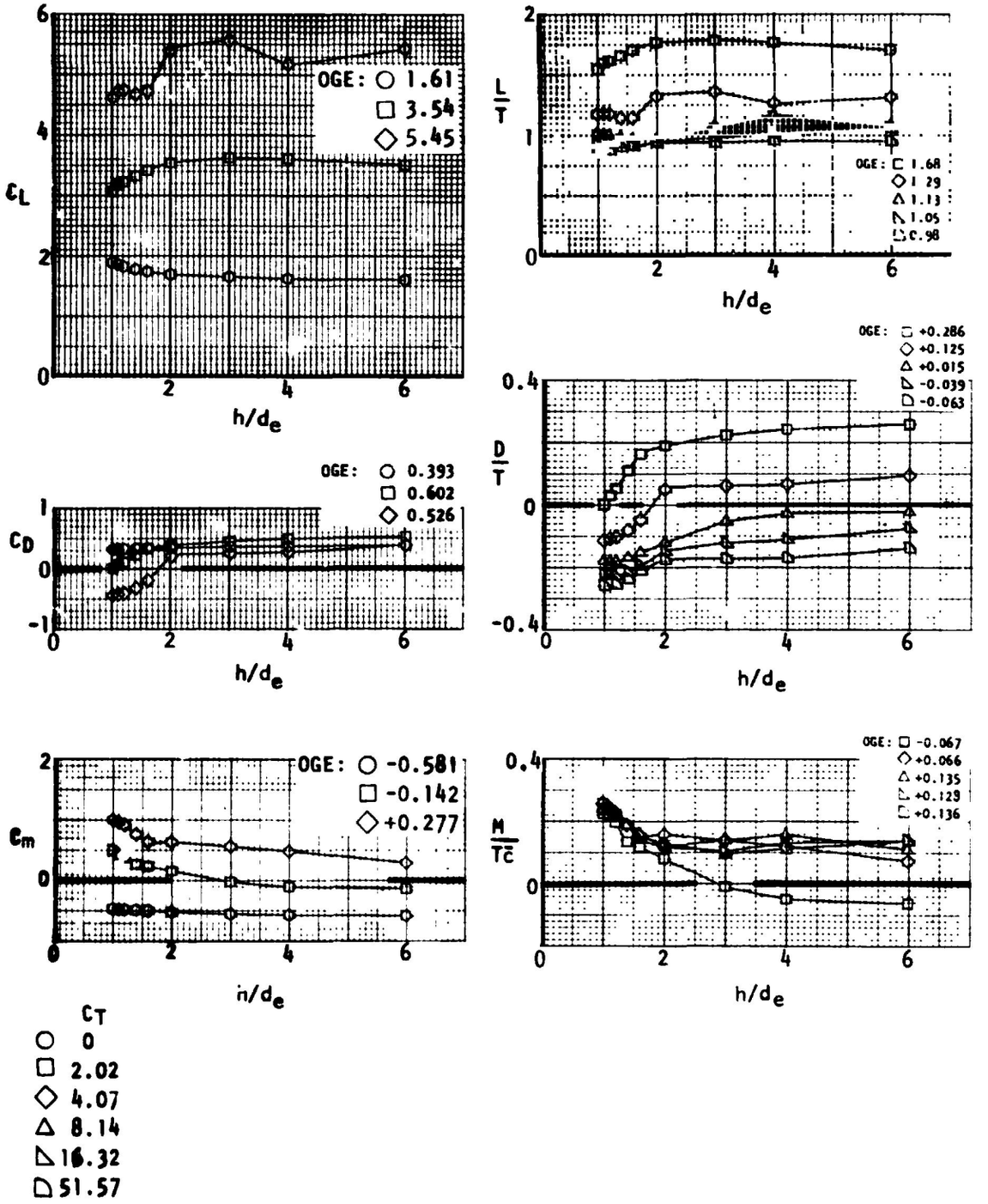

Figure 63.- Flaps-down longitudinal forces and moments during transition in ground effect. $\delta_N = 80°$, $\alpha = 0°$.

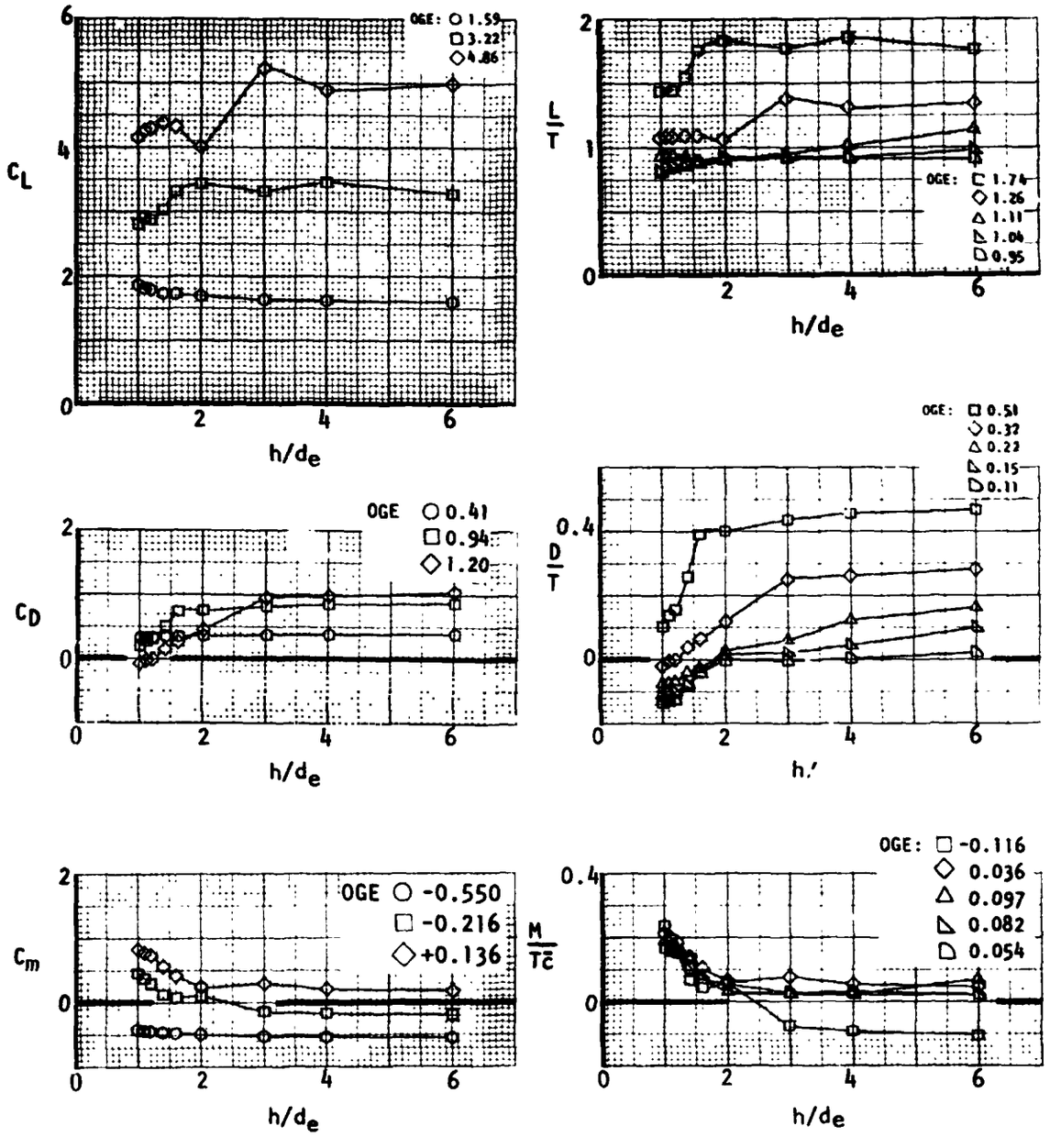

(a) Tail off, α = 0.

Figure 64.- Flaps-down longitudinal forces and moments during transition in ground effect. δ_N = 90°

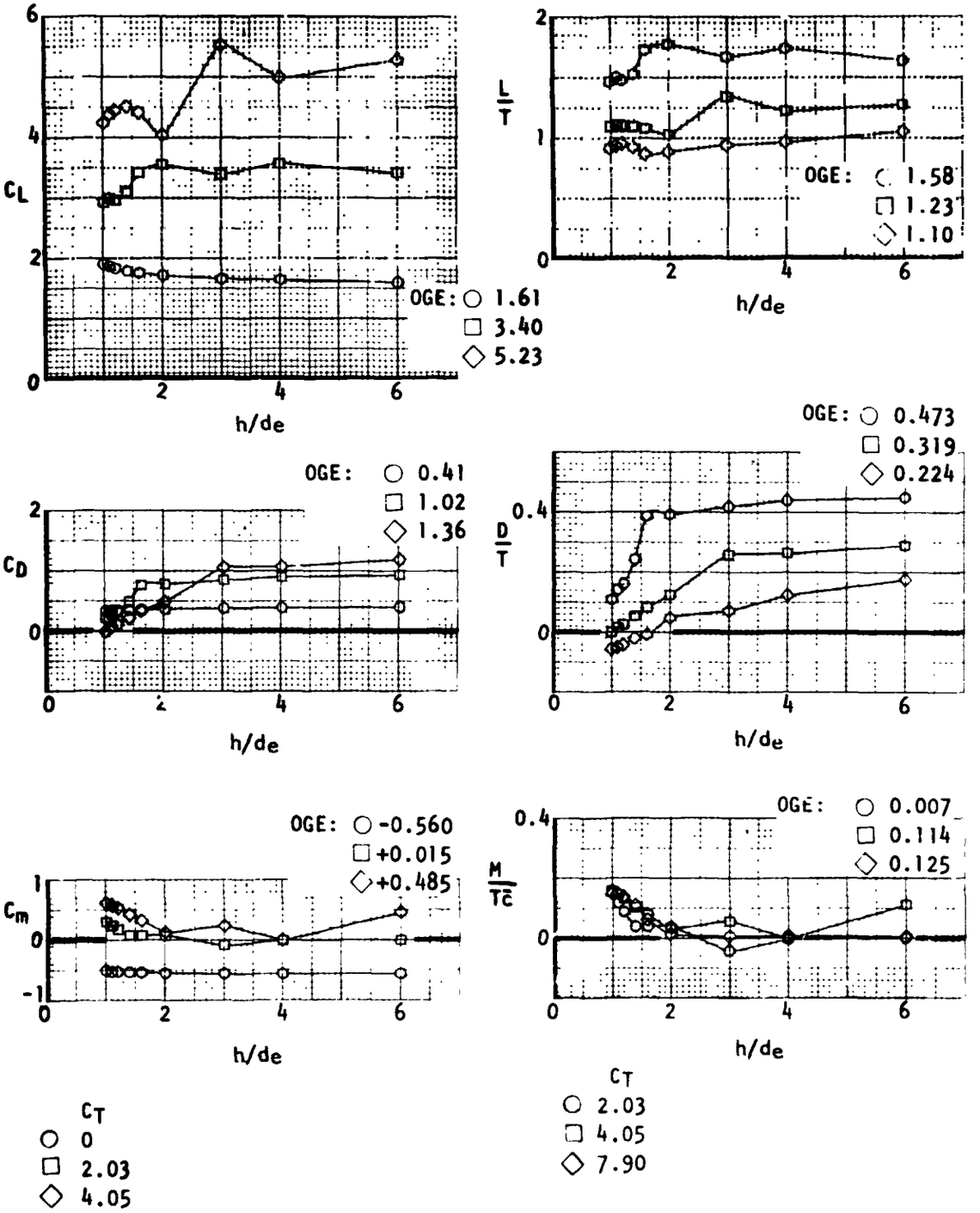

(b) Tail on, $i_H = +10°$, $\alpha = 0°$.

Figure 64.- Continued.

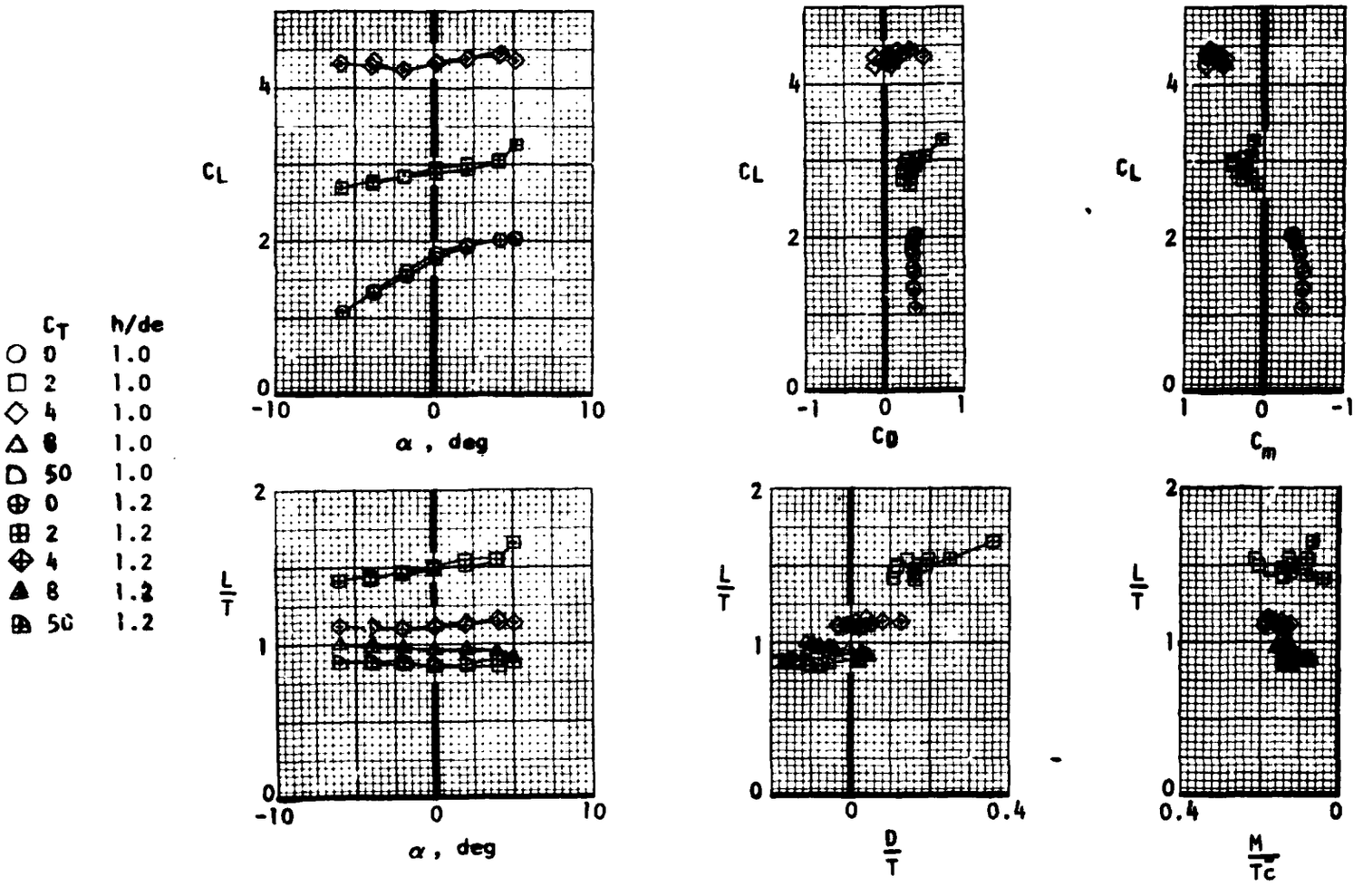

(c) Effect of angle of attack, tail off.

Figure 64.- Concluded.

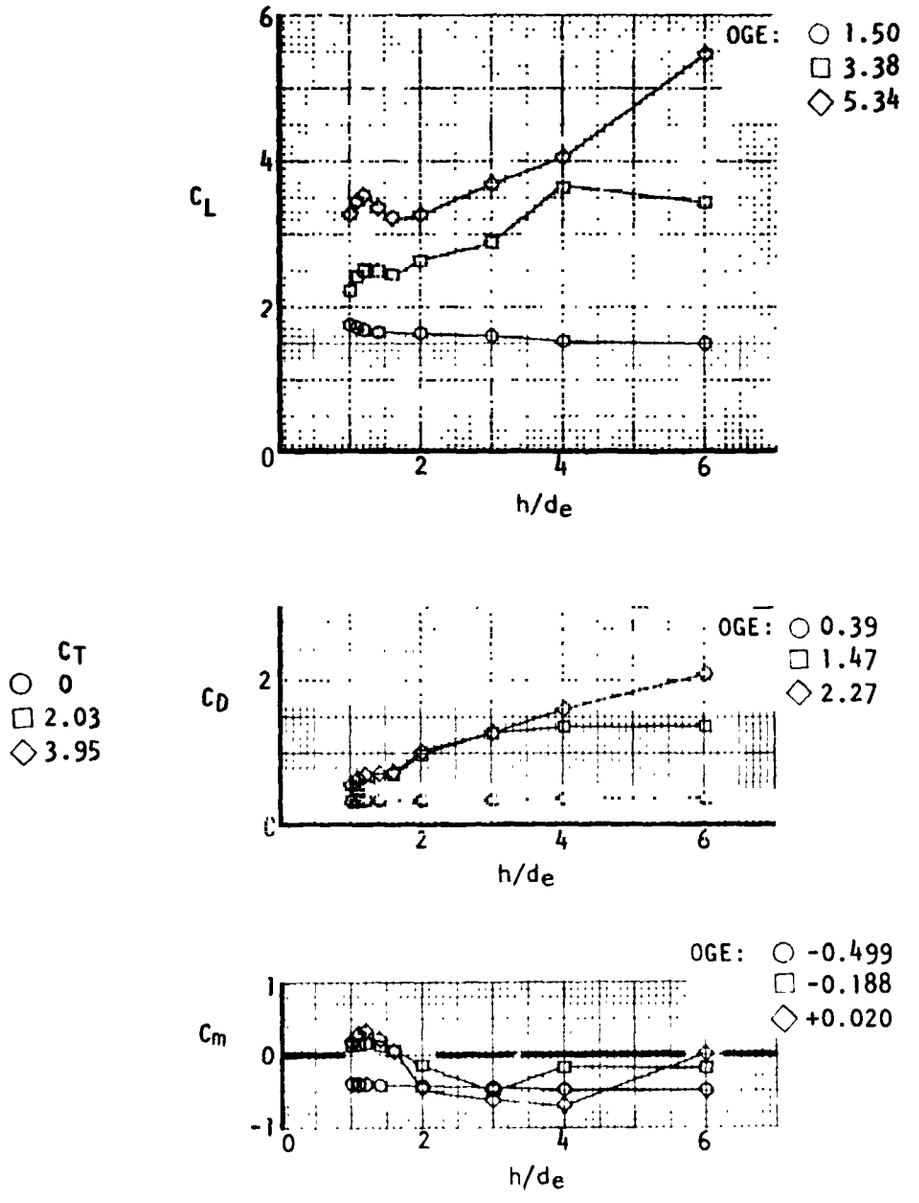

(a) Aerodynamic coefficients.

Figure 65.- Flaps-down longitudinal forces and moments during transition in ground effect. Tail off, $\alpha = 0$, $\delta_N = 103°$.

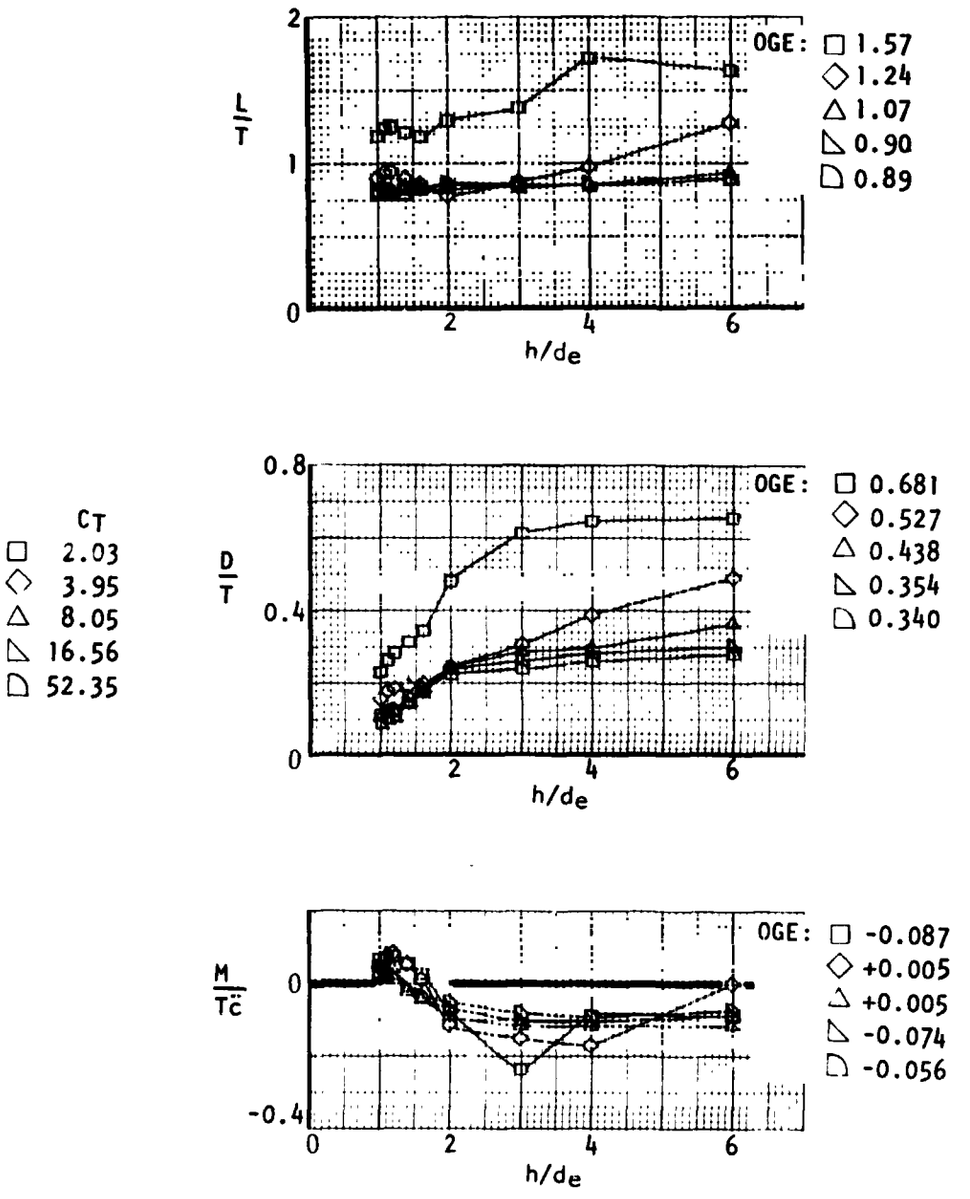

(b) Force and moment ratios.

Figure 65.- Concluded.

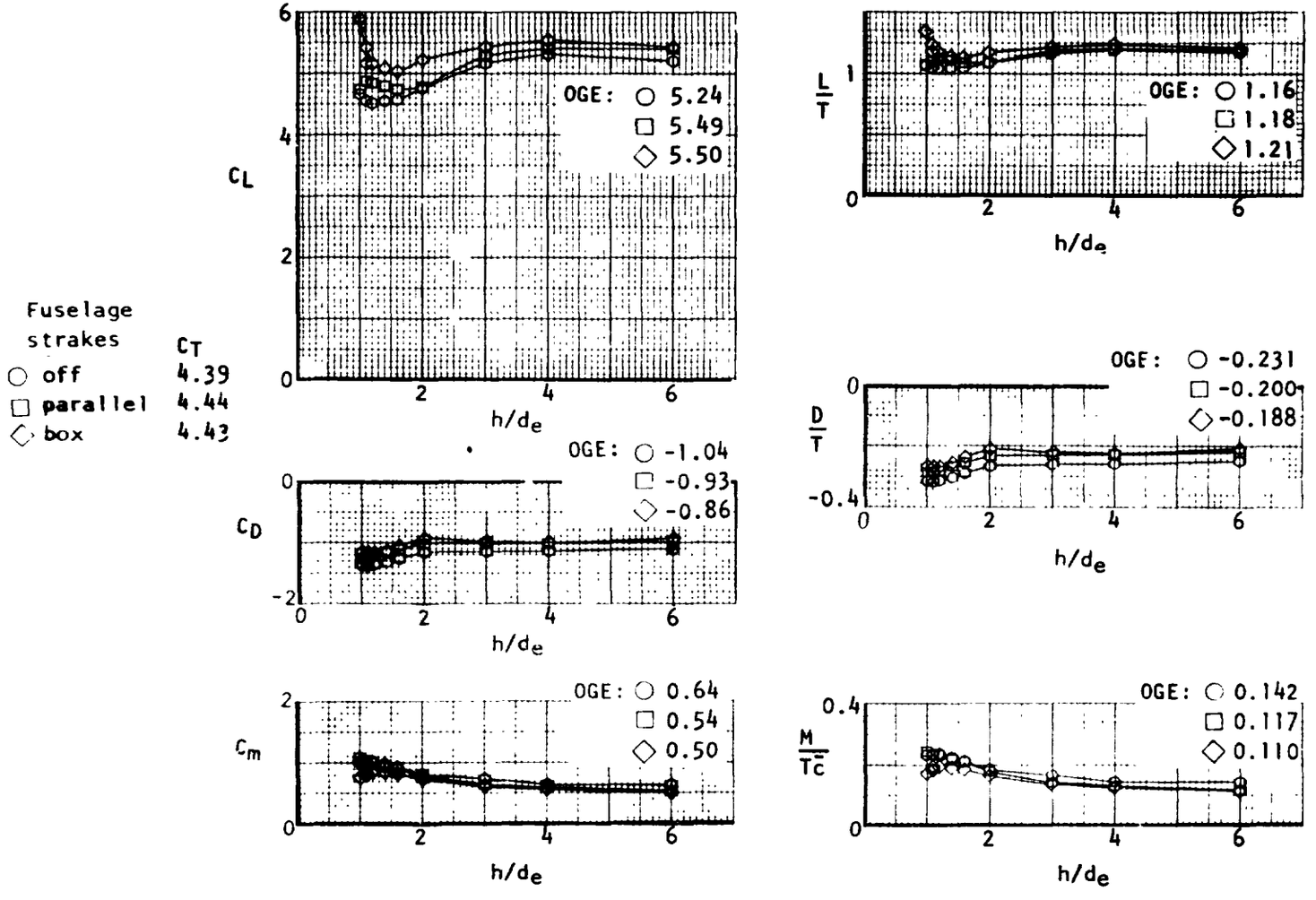

(a) Nozzle angle 62°, C_T = 4.4.

Figure 66.- Effect of fuselage strakes on longitudinal characteristics in ground effect. Tail off.

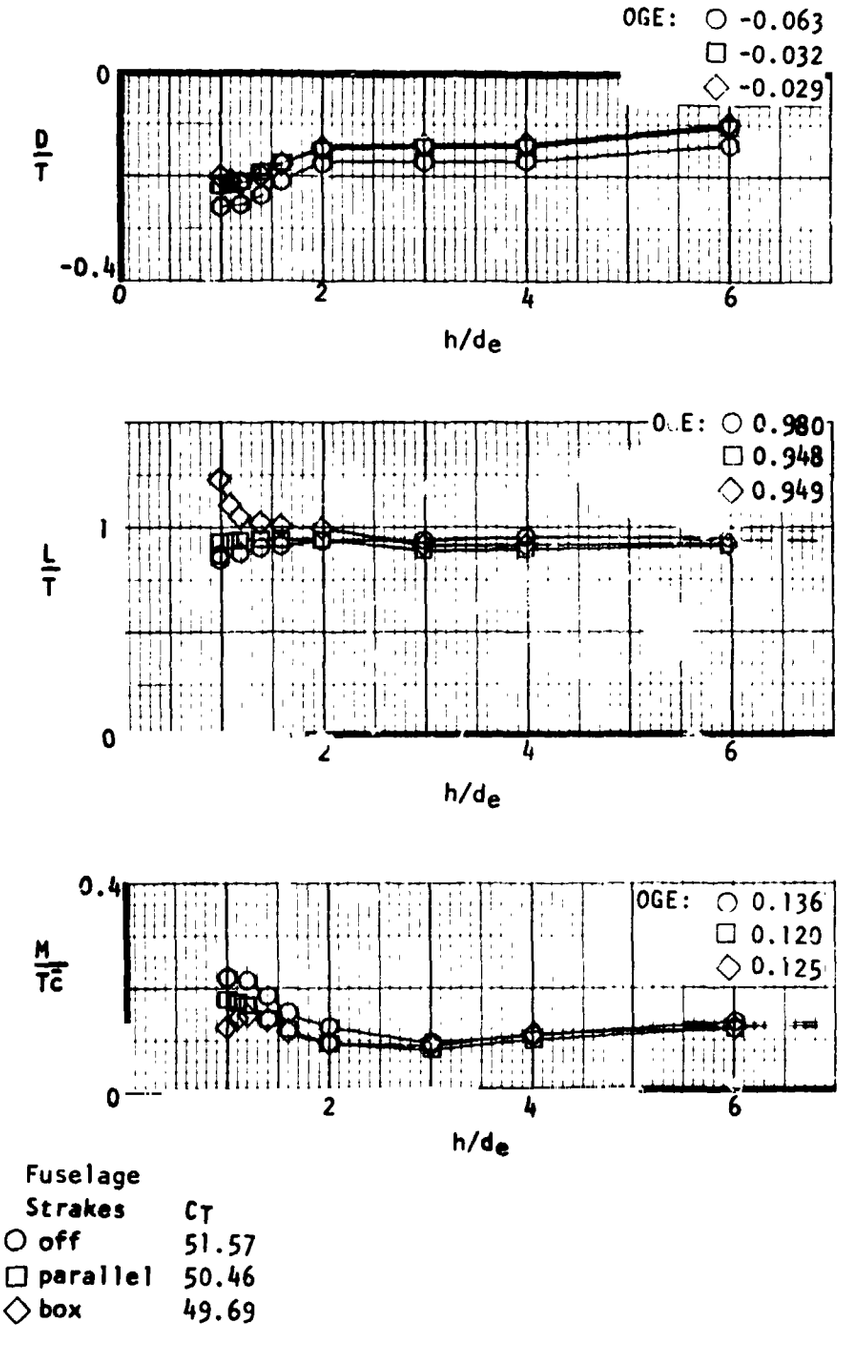

(b) Nozzle angle 80°, C_T = 50.6.

Figure 66.- Continued.

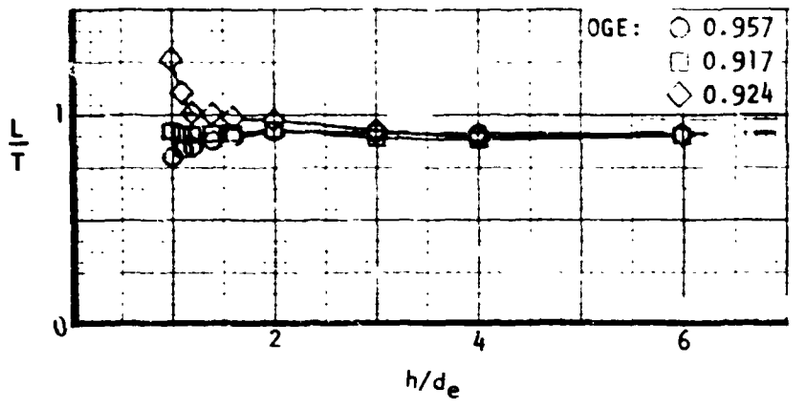

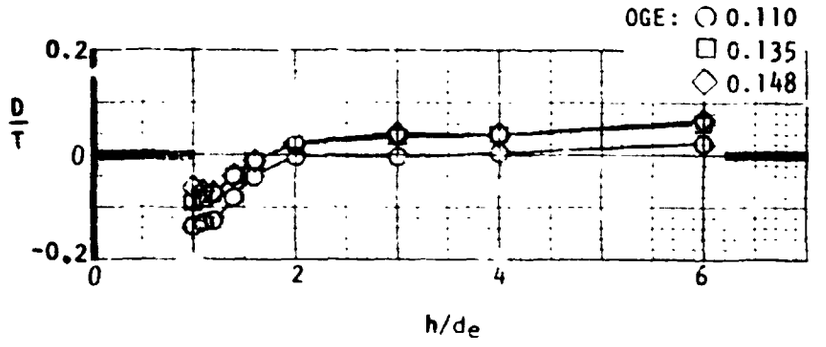

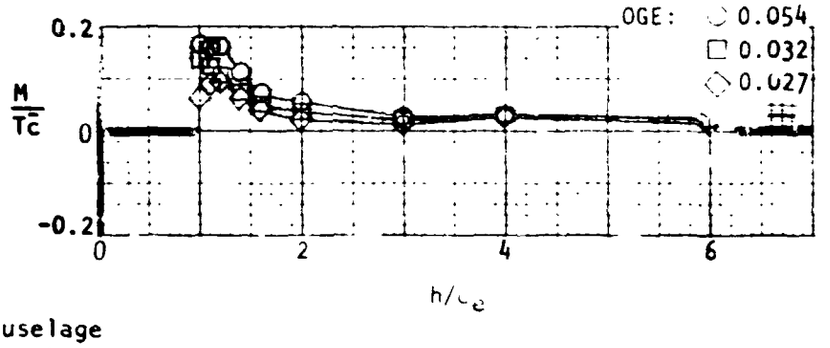

Fuselage Strakes	C_T
○ off	51.32
□ parallel	49,12
◇ box	47.83

(c) Nozzle angle 90°, C_T = 49.4.

Figure 60.- Concluded.

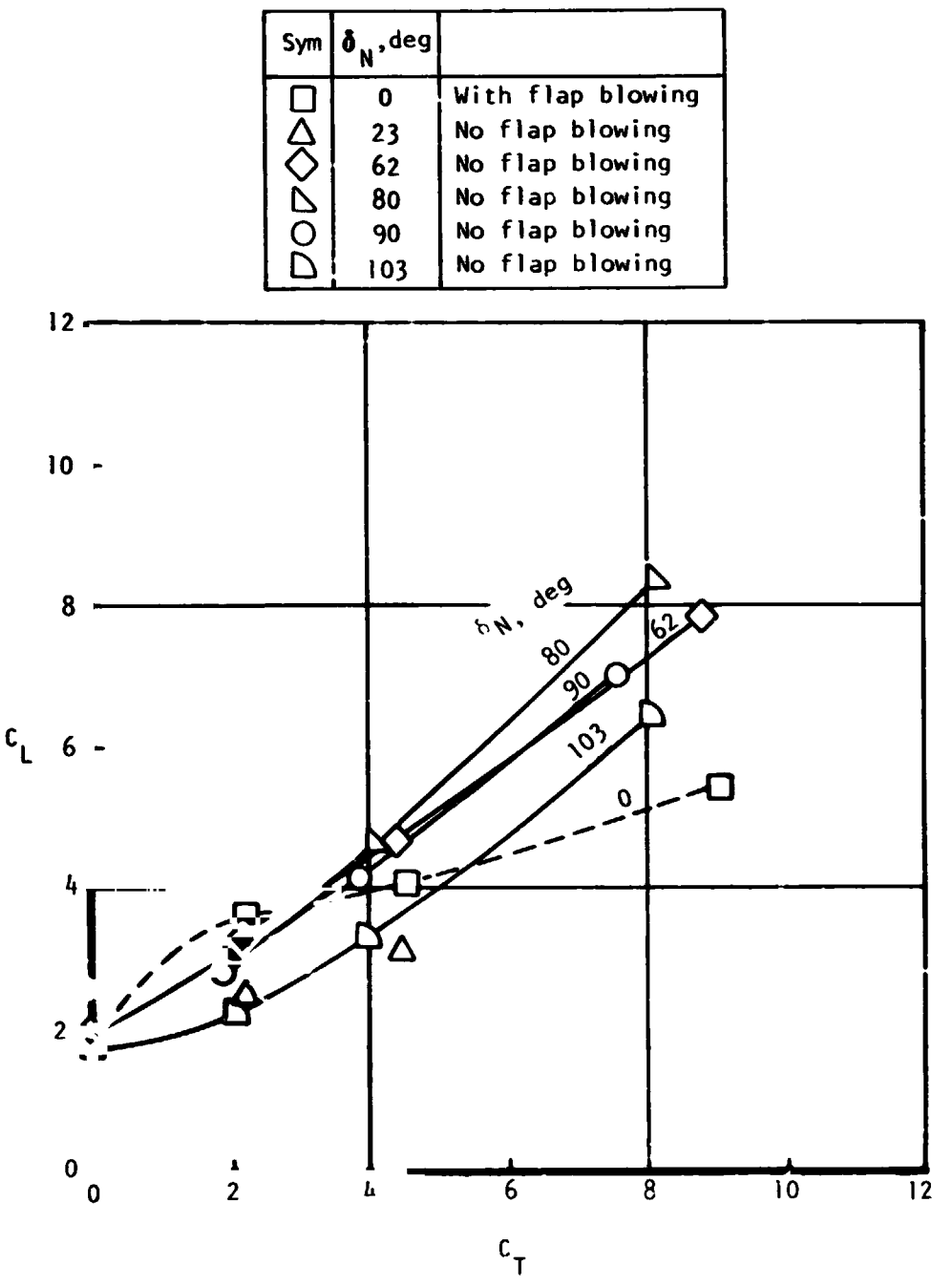

(a) C_L versus C_T, α = 0.

Figure 67. - Lift at low angle of attack. Tail off, flaps down, transition IGE (h/d_e=1.0).

Sym	δ_N, deg	
□	0	With flap blowing
△	23	No flap blowing
◇	62	No flap blowing
◺	80	No flap blowing
○	90	No flap blowing
◺	103	No flap blowing

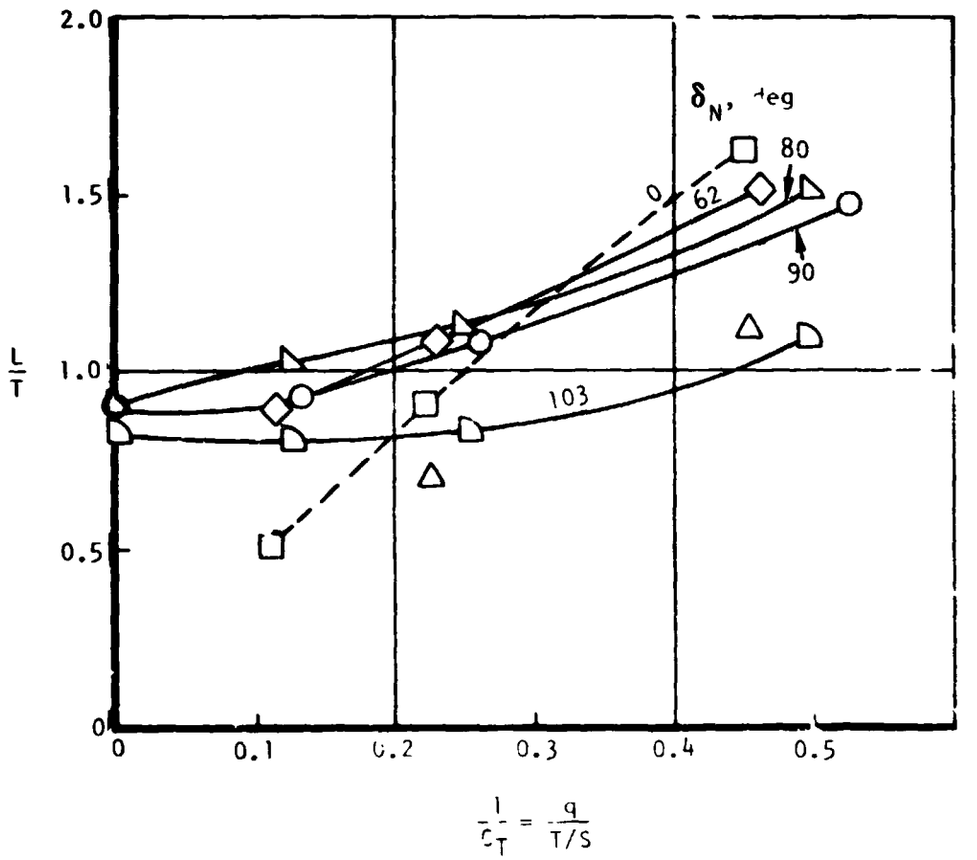

(b) L/T versus $1/C_T$, $\alpha = 0$.

Figure 67. Continued.

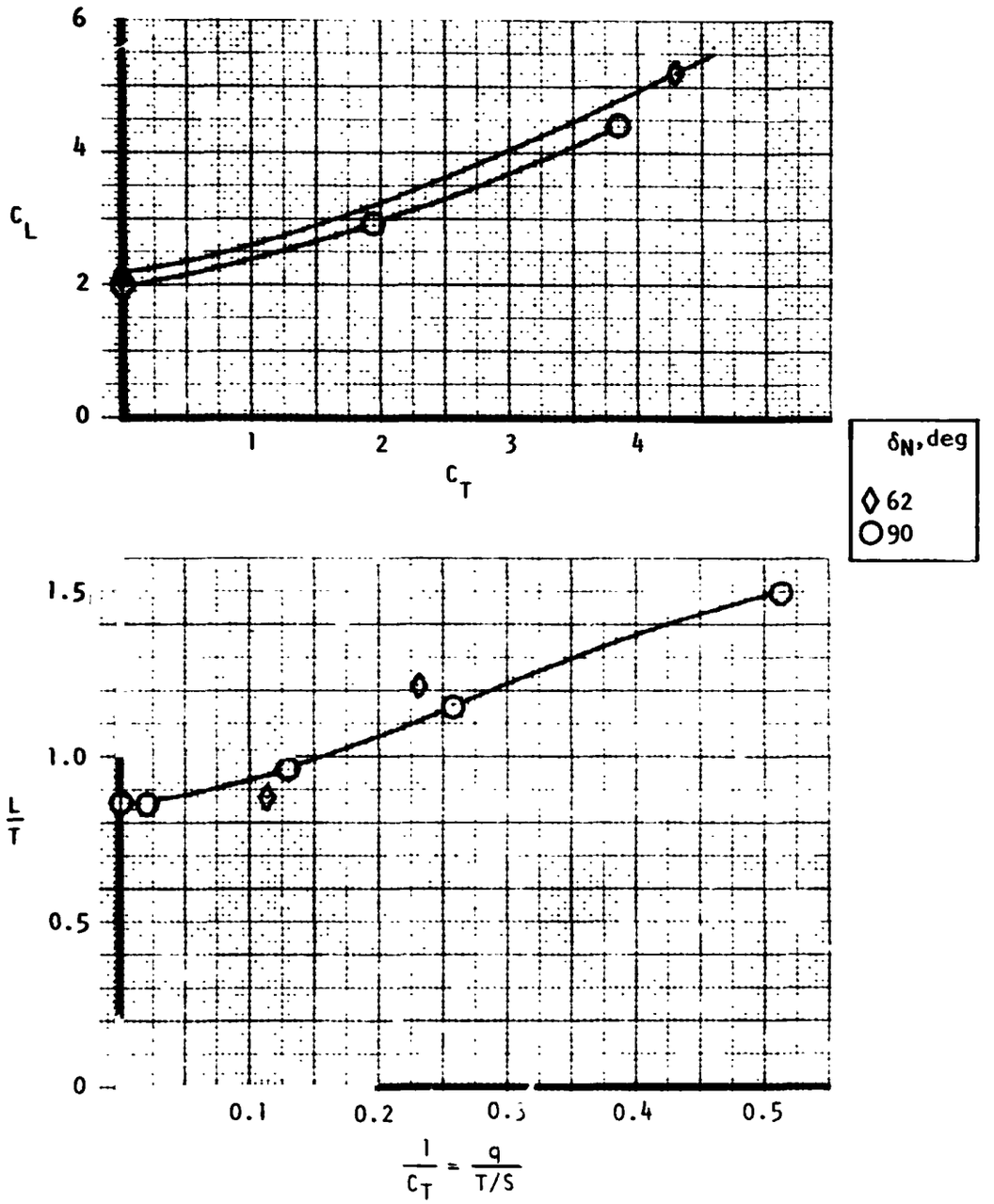

(c) Characteristics at $\alpha = 4°$.

Figure 67. - Concluded.

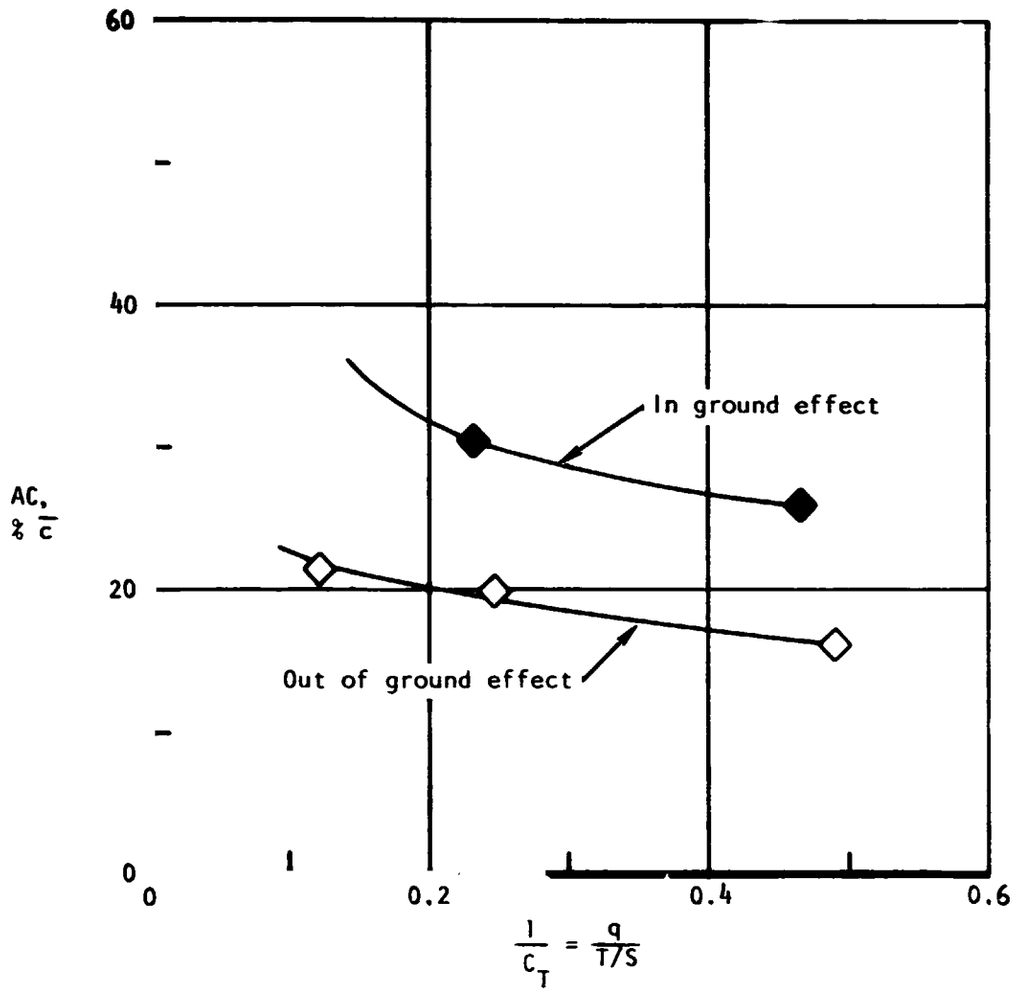

Figure 68.- Ground effect on tail-off aerodynamic center location with power, $\delta_N = 62°$, $\alpha = 2°$.

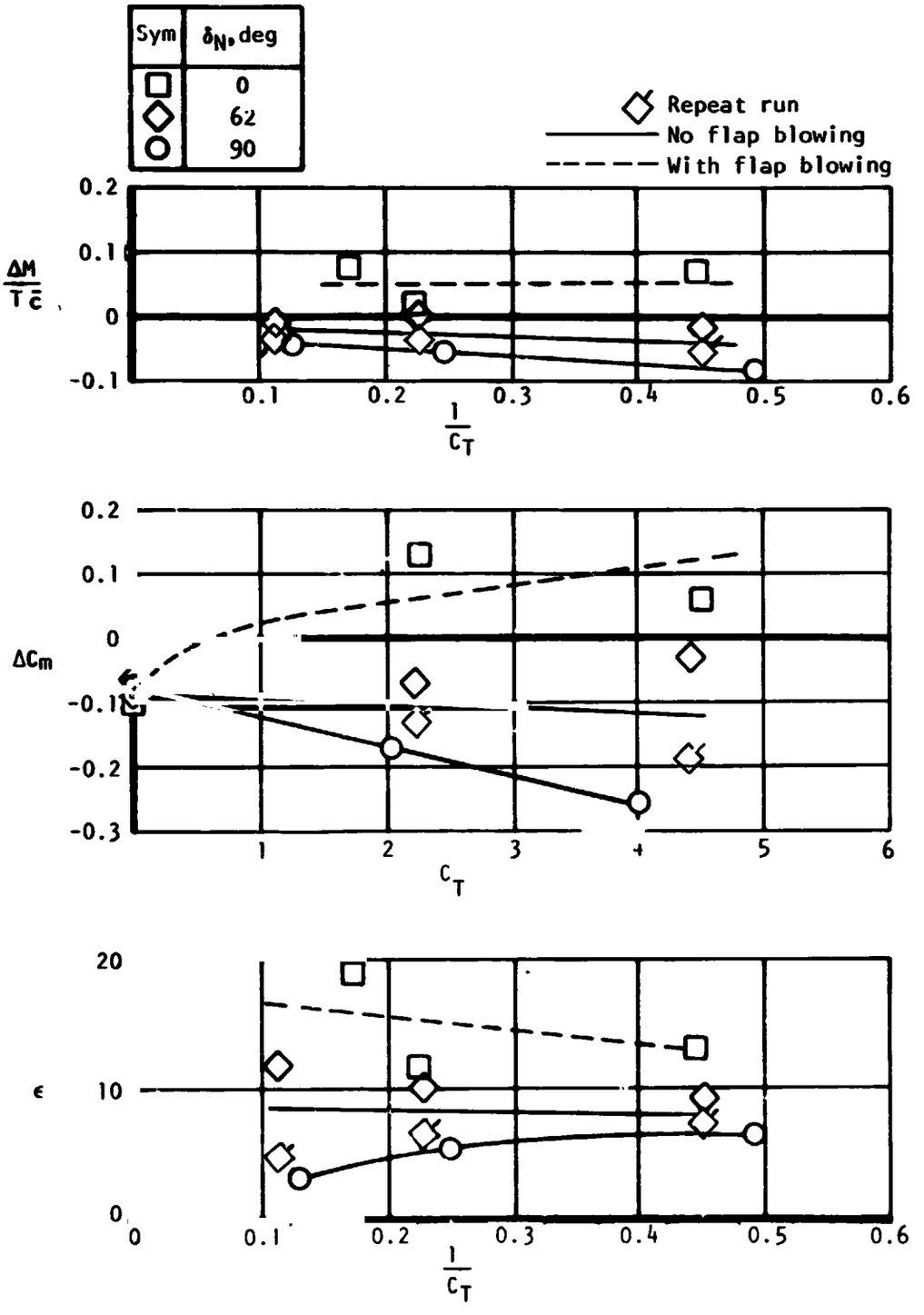

Figure 69. - Downwash correlation in ground effect. $h/d_e=1.0, \alpha=0$.

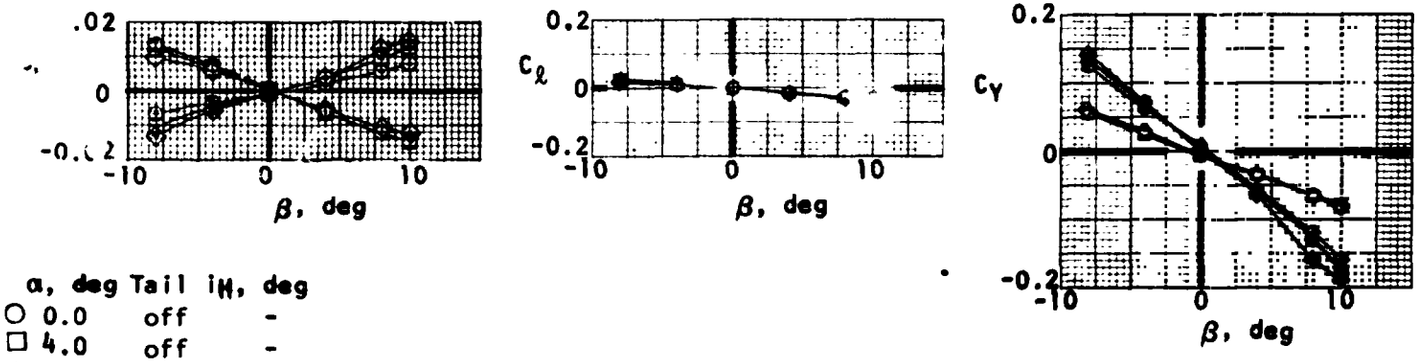

α, deg	Tail	i_H, deg
○ 0.0	off	-
□ 4.0	off	-
◇ 8.1	off	-
⊖ 0.1	on	0
⊞ 4.0	on	0
⊕ 8.1	on	0

(a) Flaps up.

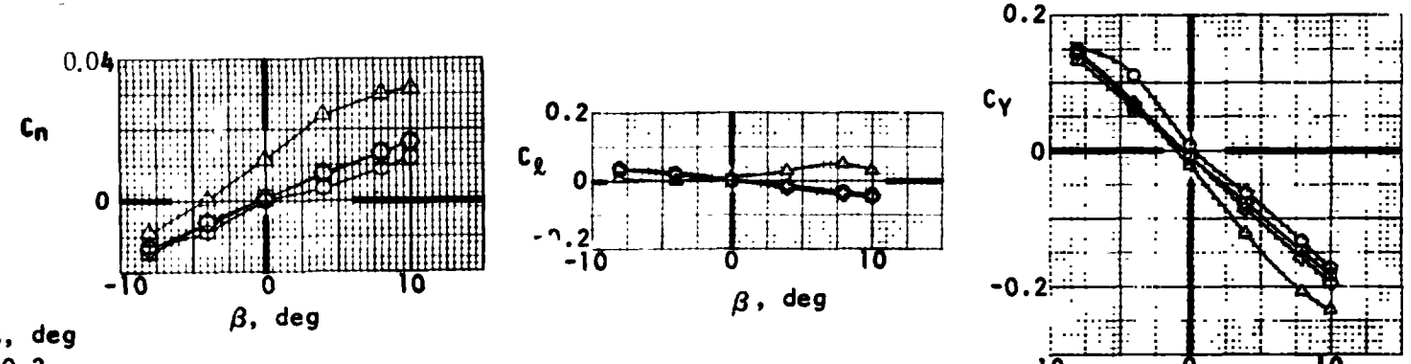

α, deg
○ 0.2
□ 4.2
◇ 8.2
△ 12.2

(b) Flaps down. Tail on, $i_H = 0°$

Figure 70.- Lateral-directional power-off forces and moments out of ground effect. $\delta_N = 0°$

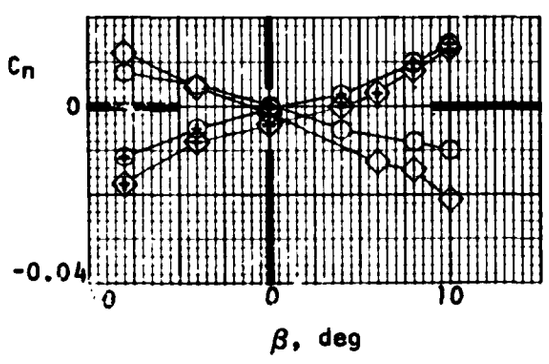

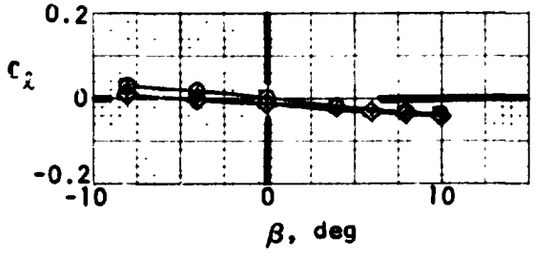

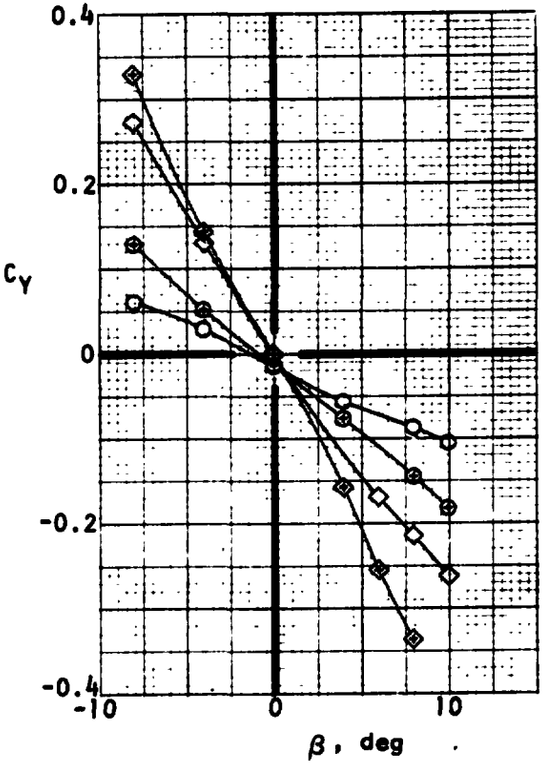

	C_T	Tail	i_H, deg
○	0	off	-
◇	3.83	off	-
⊕	0	on	0
◈	3.81	on	0

(a) Nozzle angle 0°, tail on and off.

Figure 71.- Lateral-directional forces and moments during transition out of ground effect. Flaps down, $\alpha = 0^\circ$.

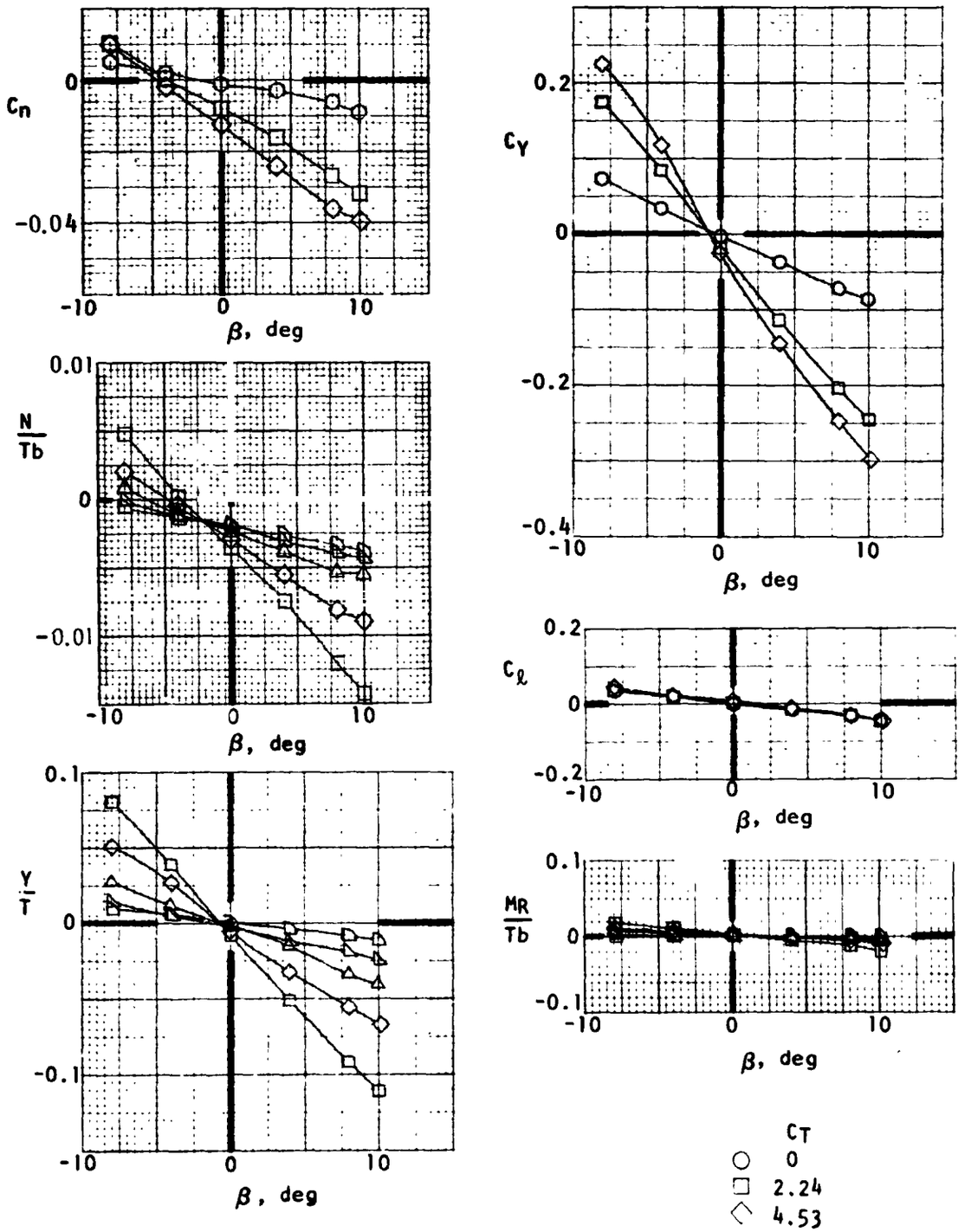

(b) Nozzle angle 62°, tail off.

Figure 71.- Continued.

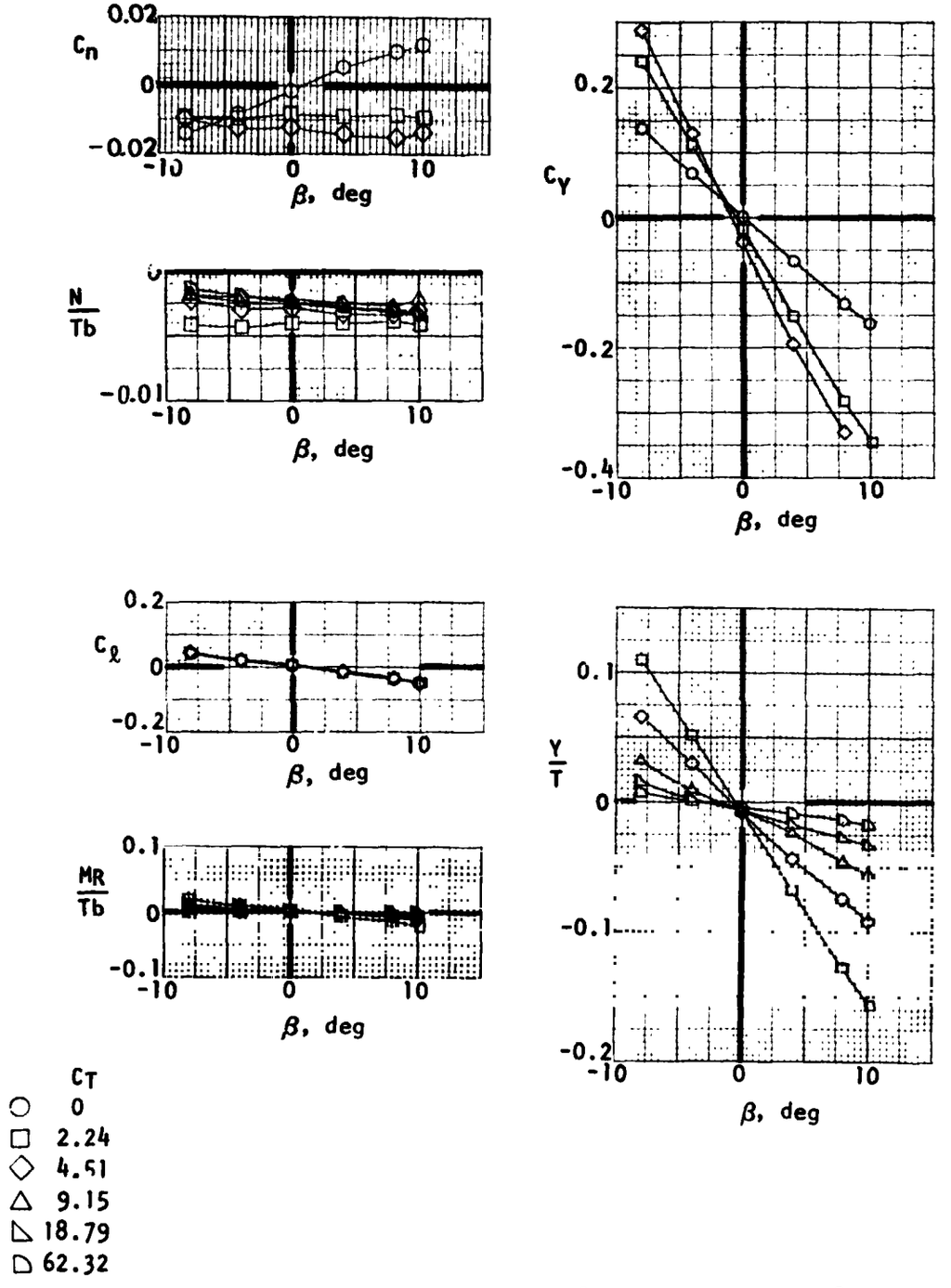

(c) Nozzle angle 62°, Tail on, i_H = 10°.

Figure 71.- Continued.

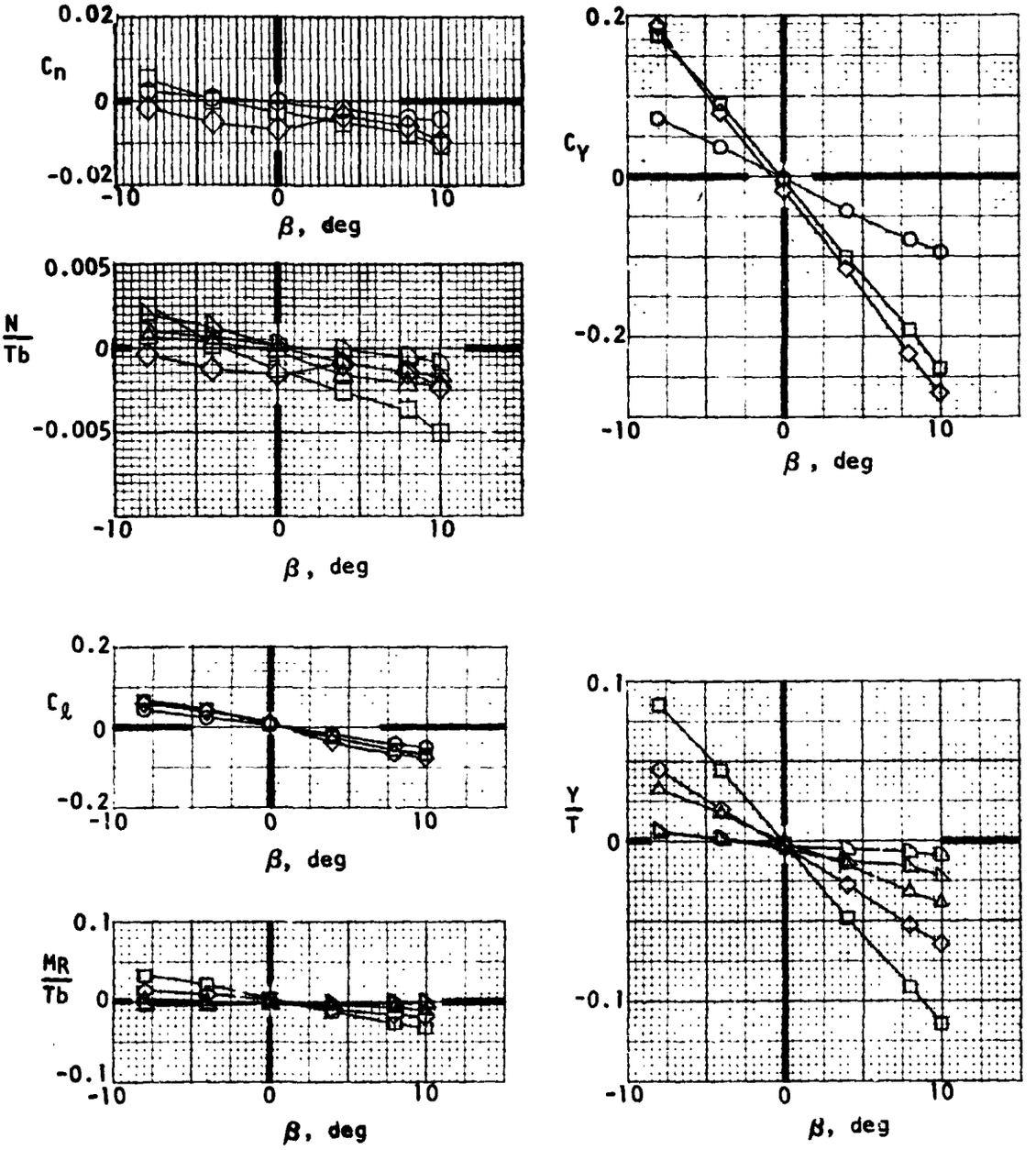

(d) Nozzle angle 90°, tail off.

Figure 71.- Continued.

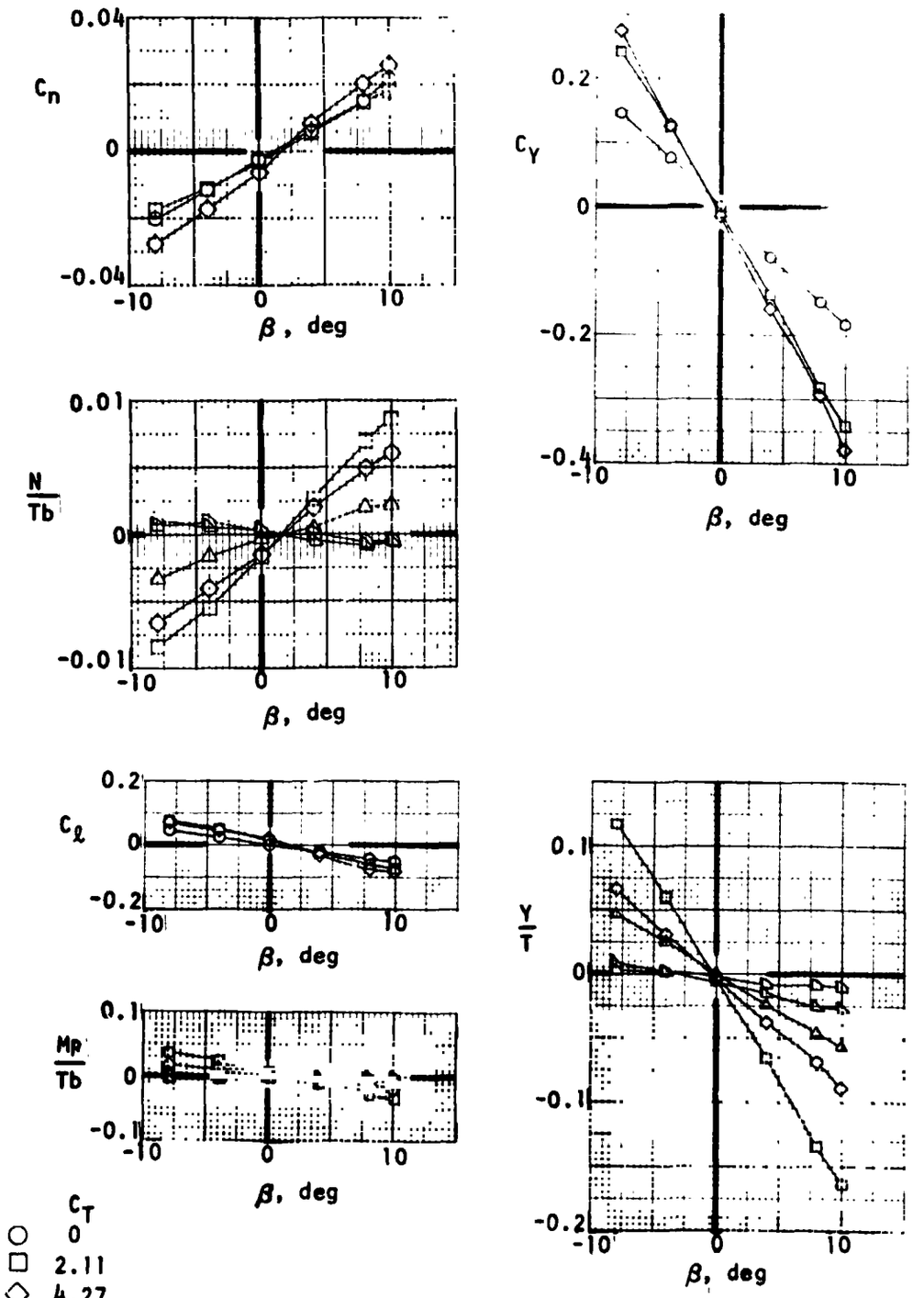

(e) Nozzle angle 90°, Tail on, $i_H = 20^\circ$.

Figure 71.- Continued.

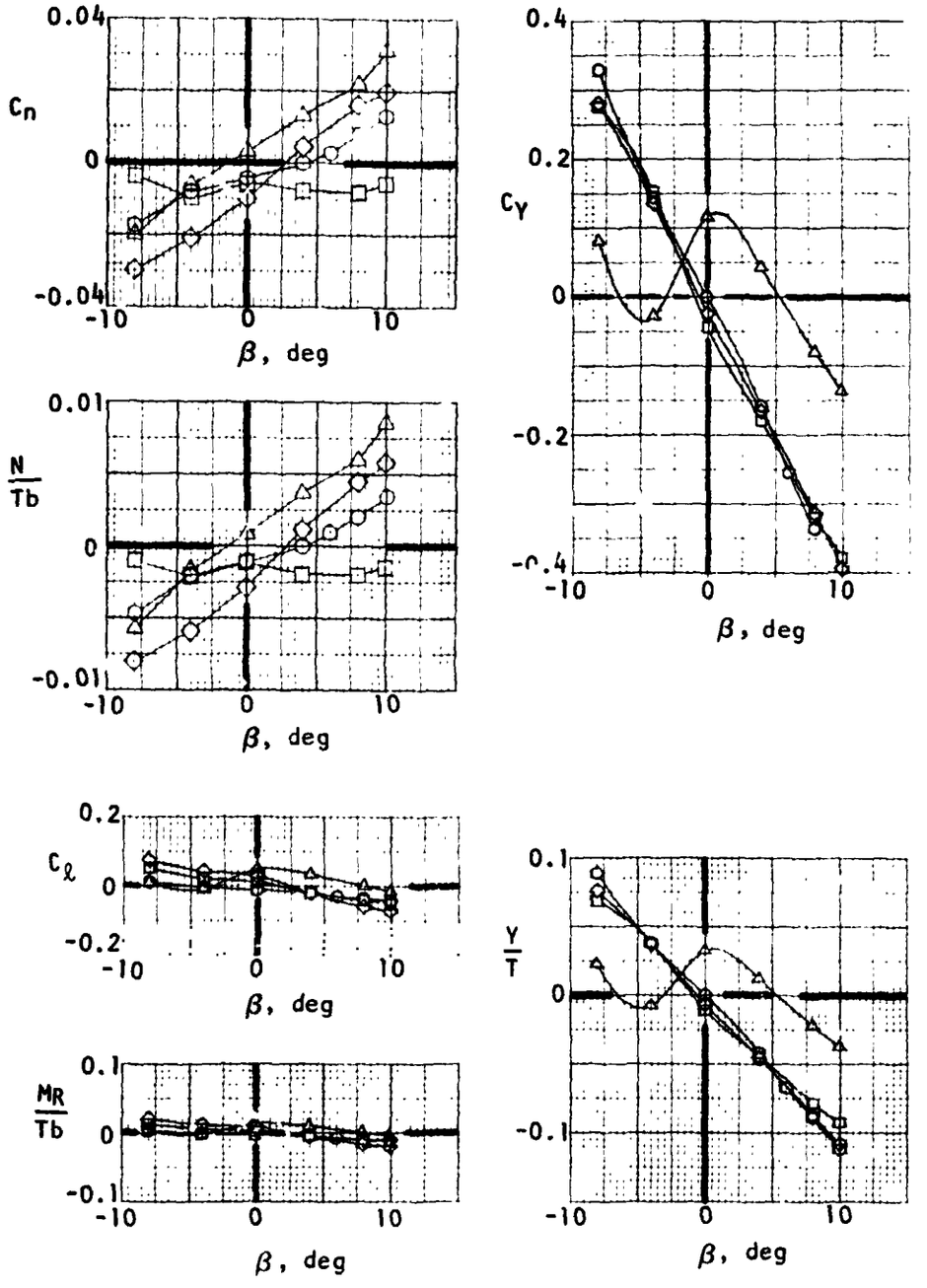

	δ_N, deg	i_H, deg
○	0	0
□	62	20
◇	90	20
△	120	20

(f) Effect of nozzle angle at C_T = 4.01. Tail on.

Figure 71.- Concluded.

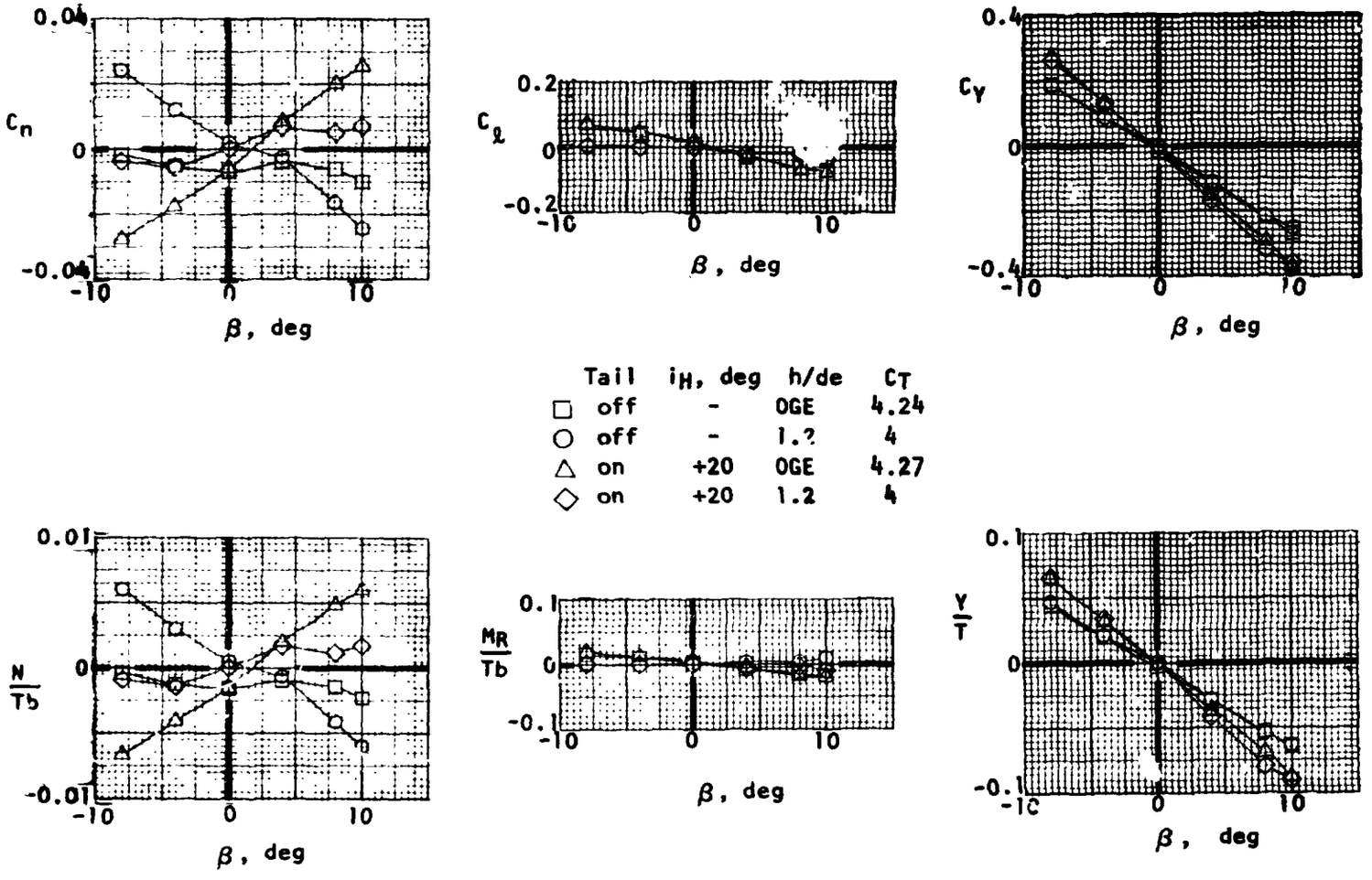

Figure 72.- Ground effect on lateral-directional forces and moments during transition. Flaps down, Nozzle angle 90°. $\alpha = 0$. $C_T = 4.01$

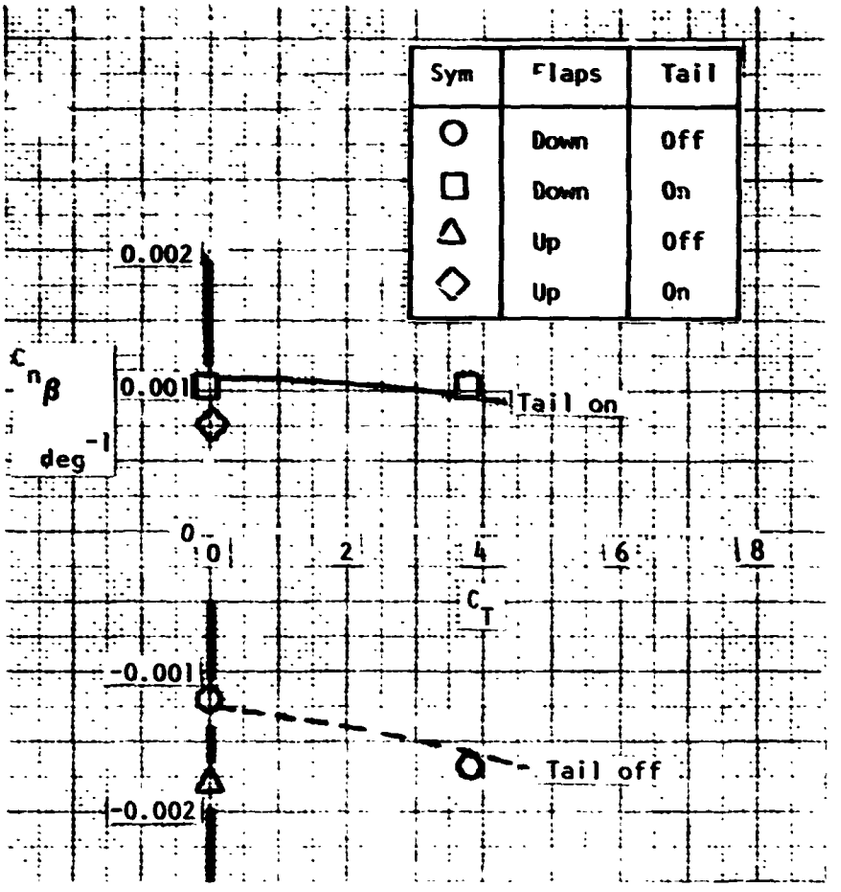

Figure 73. - Power effect on directional stability at $\delta_N = 0$. OGE, $\alpha = 0$, $\beta = 0$

13

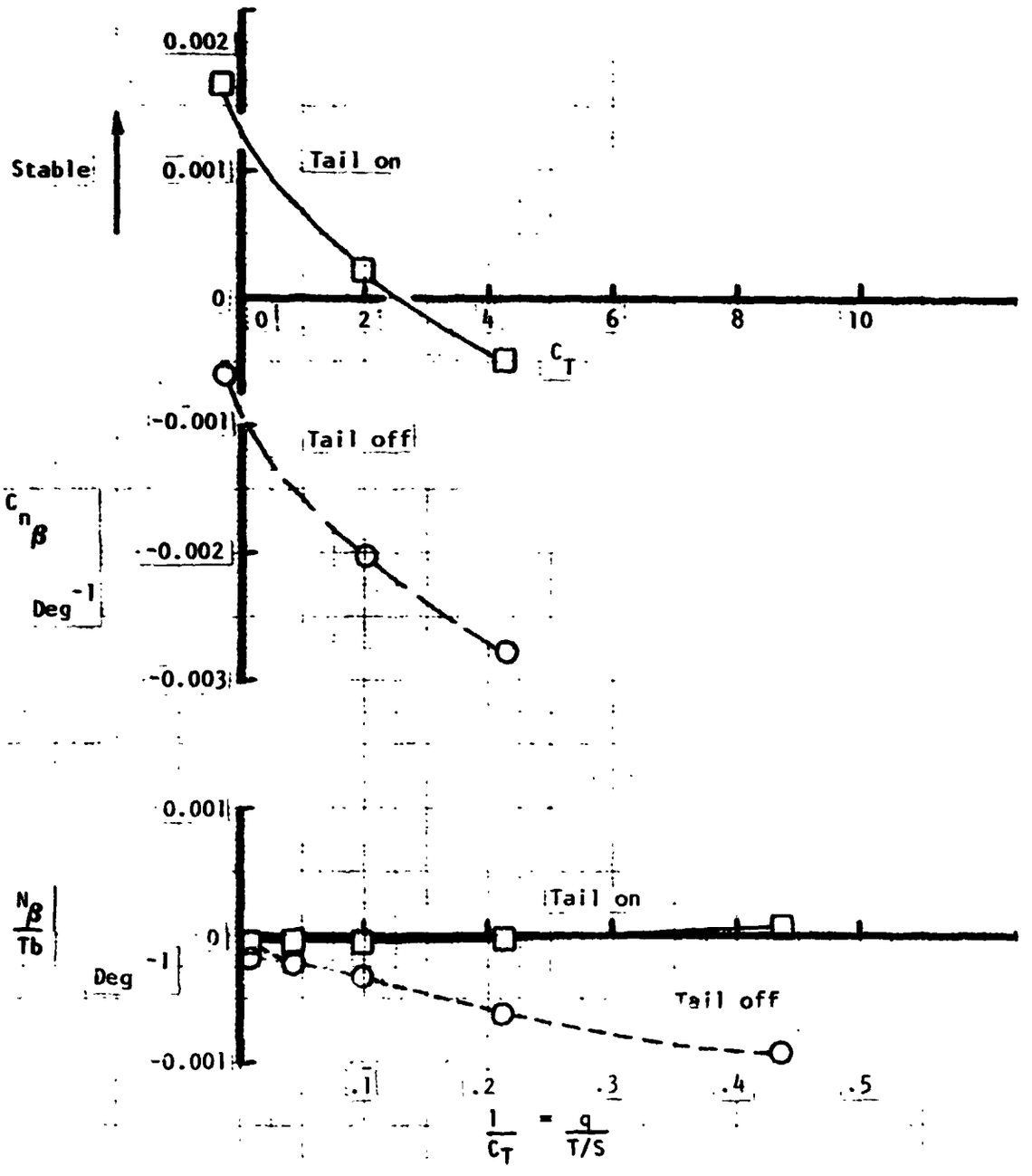

(a) $\delta_N = 62°$.

Figure 74. - Power effect on directional stability, flaps down, OGE, $\alpha = 0$, $\beta = 0$.

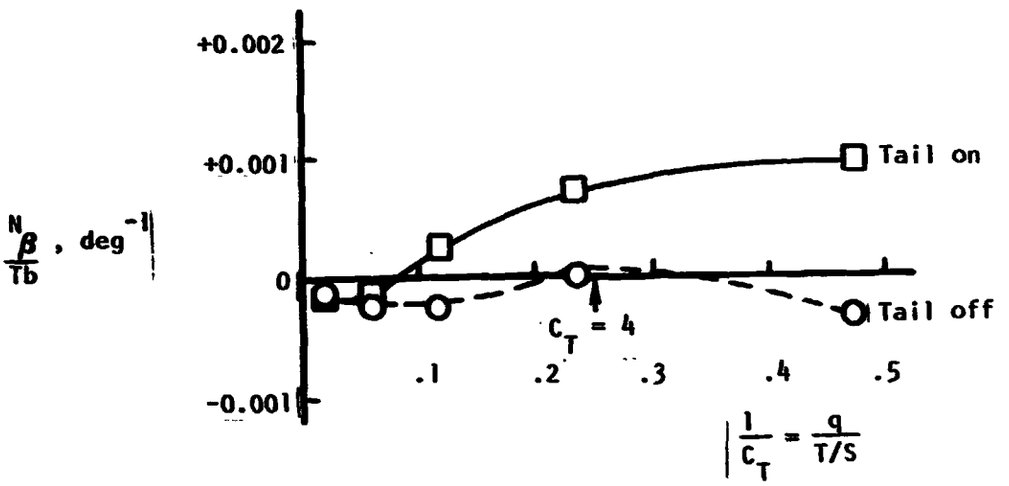

(b) $N_\beta/(Tb)$ versus $1/C_T$ for δ_N = 90°.

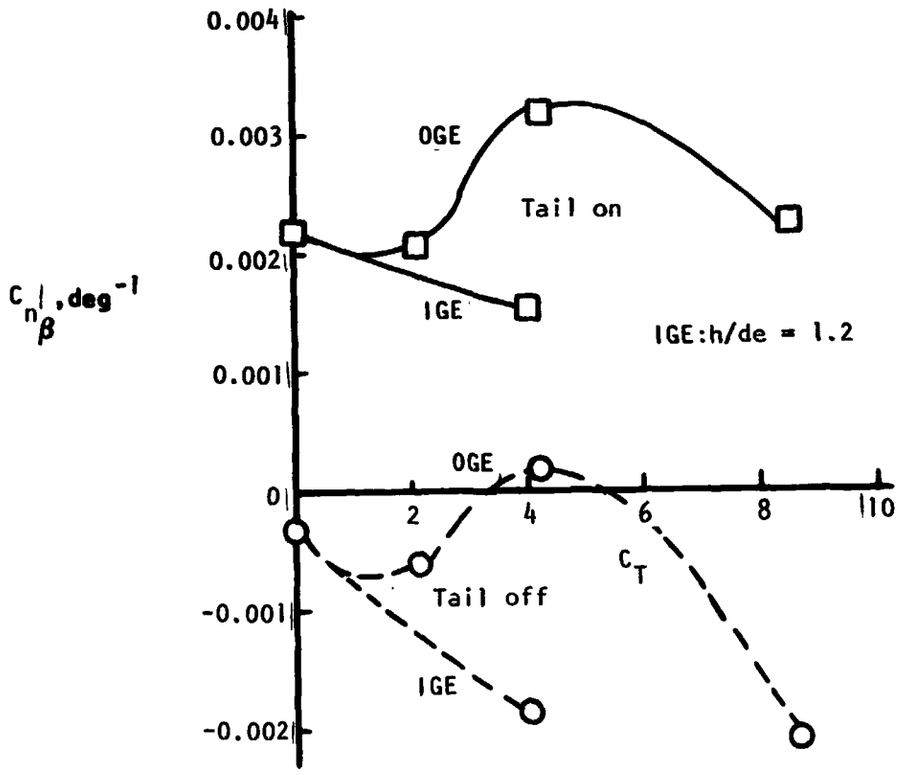

(c) C_{n_β} versus C_T for δ_N = 90°.

Figure 74. - Continued.

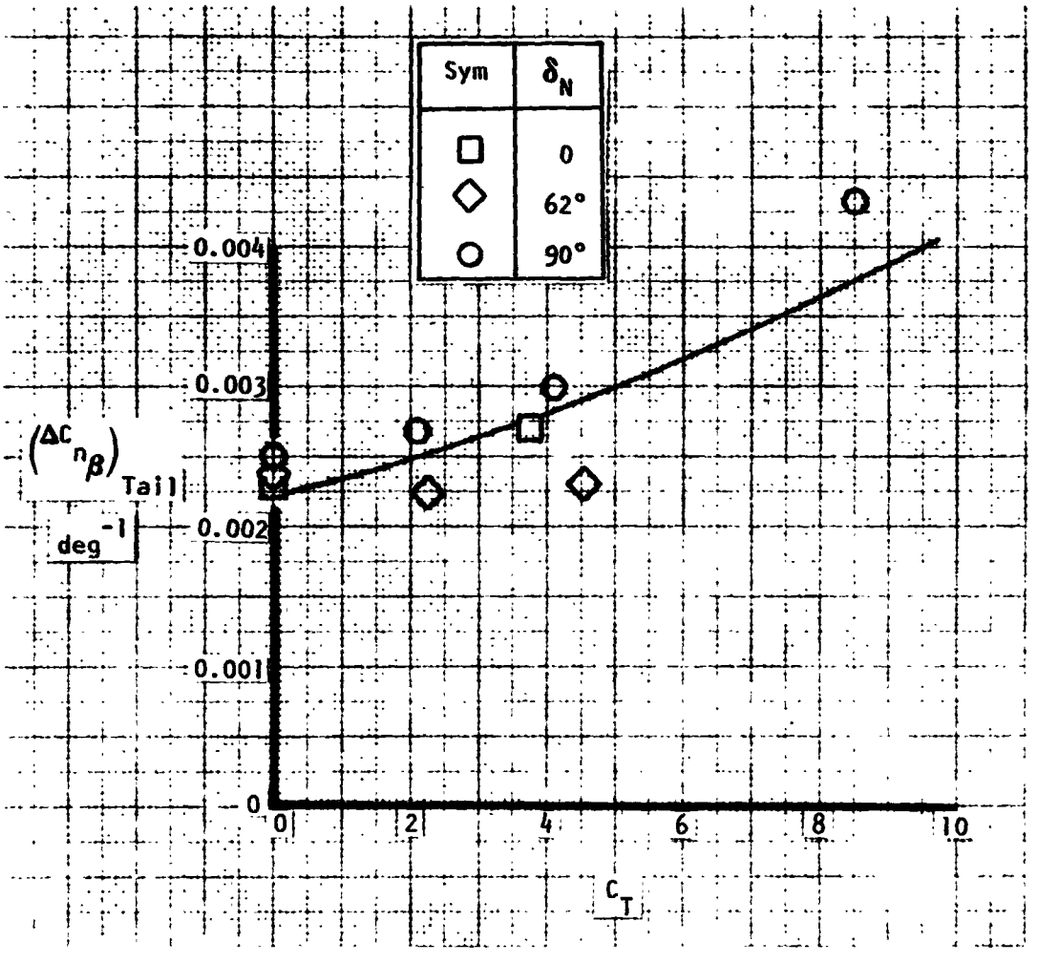

(d) Effect of power on vertail tail effectiveness.

Figure 74. - Concluded.

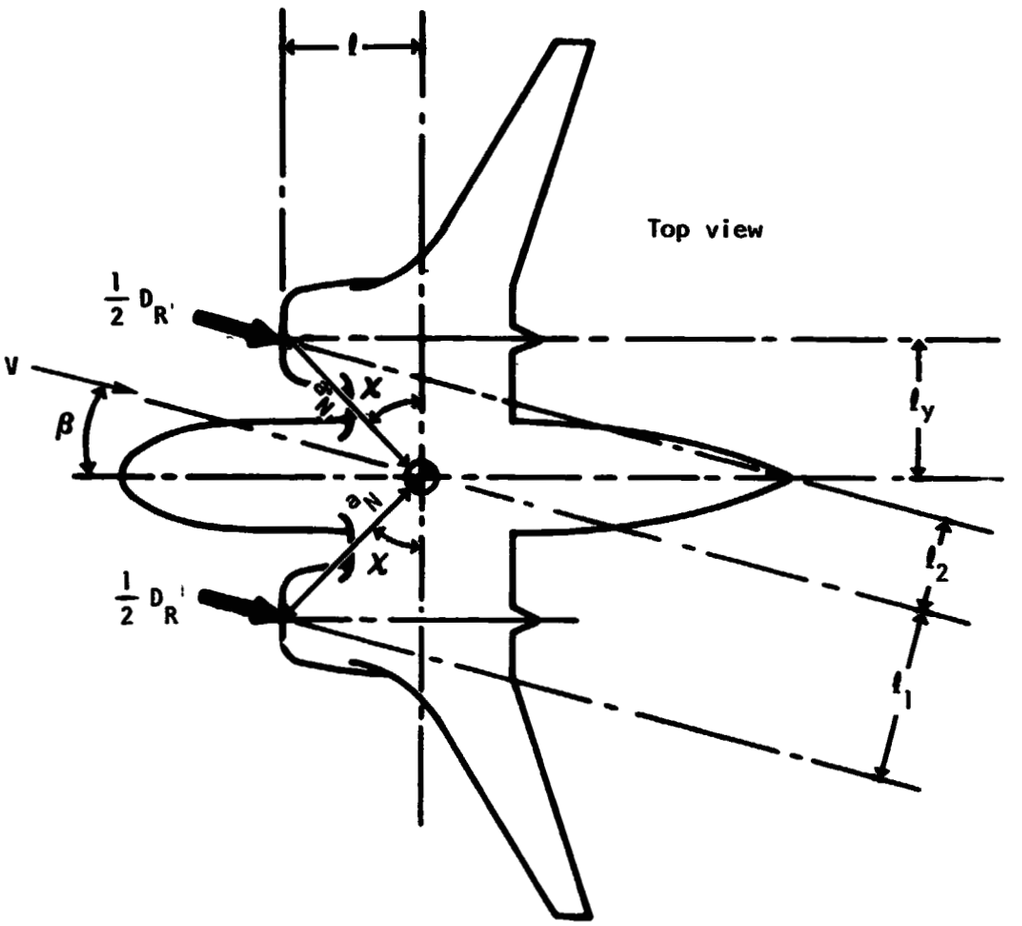

(a) Description of moment arms and angles.

Figure 75. - Computation of lateral-directional derivatives. Flaps down, tail off, transition OGE, α=0.

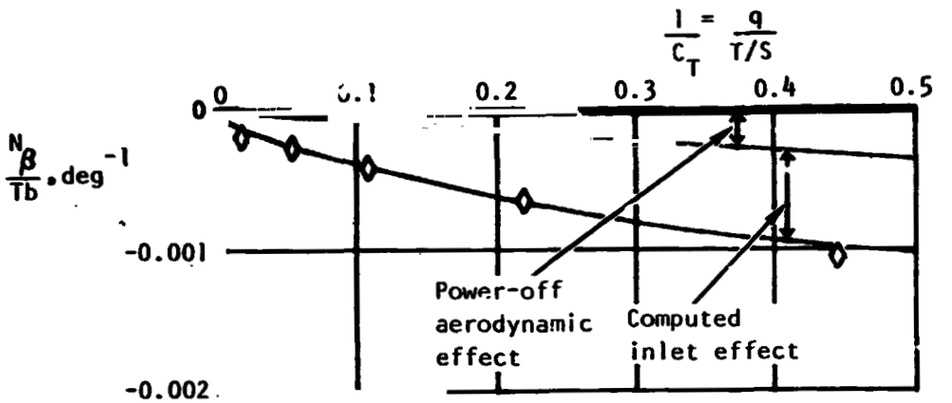

(b) Yawing moment derivatives for $\delta_N = 62°$.

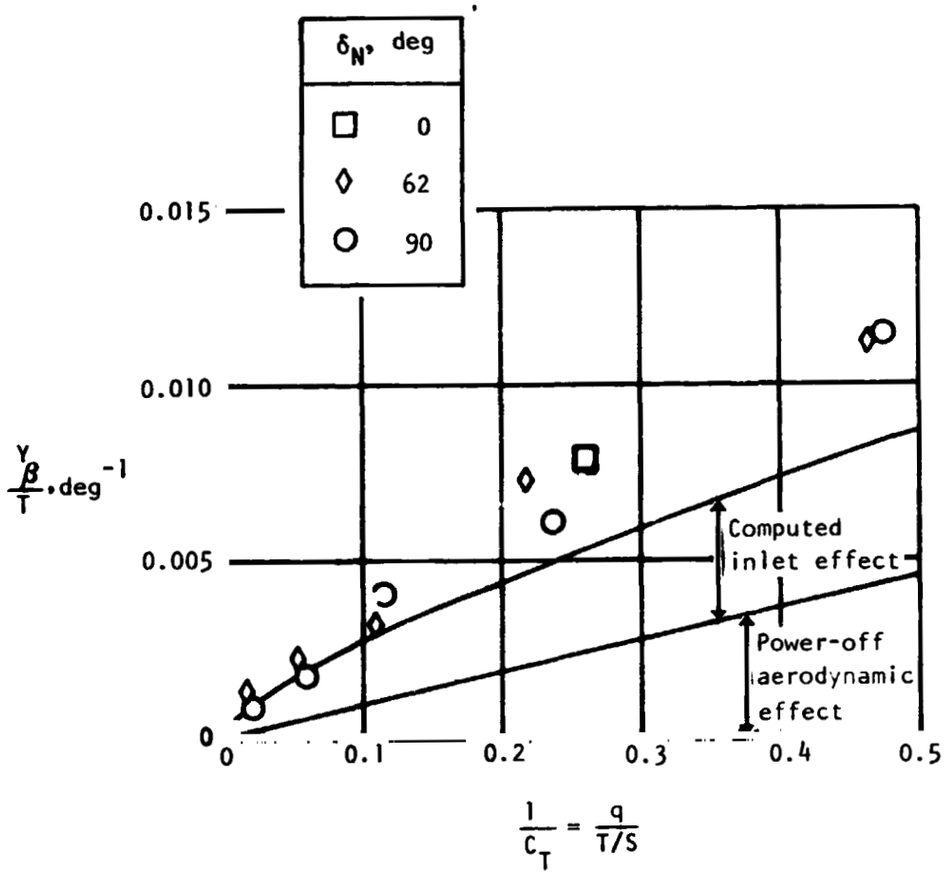

(c) Side force derivatives.

Figure 75. - Continued.

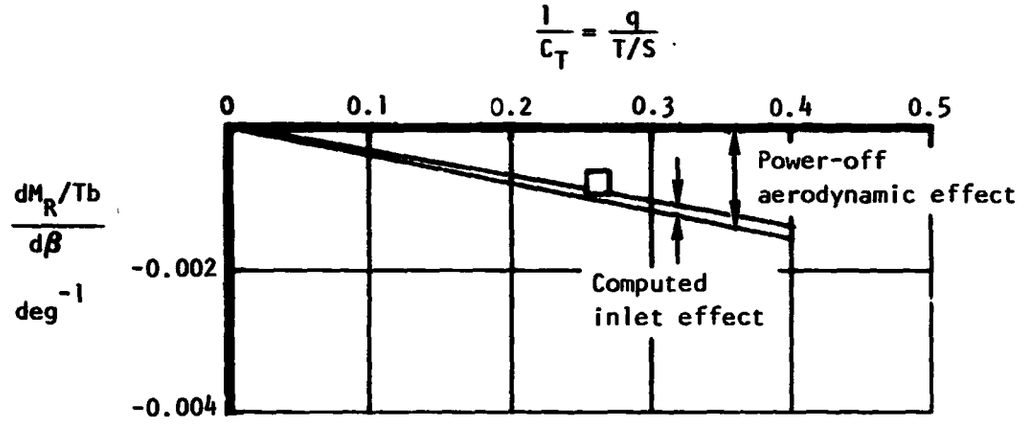

(d) Rolling moment derivative for $\delta_N = 0°$.

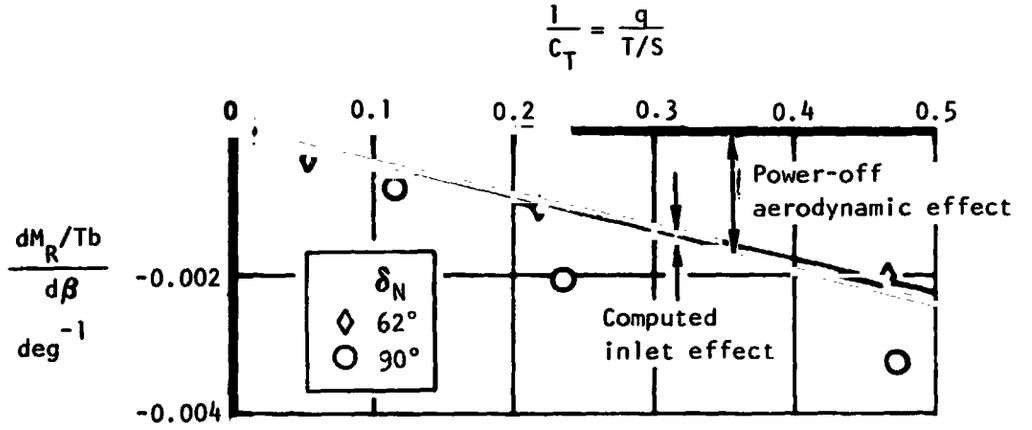

(e) Rolling moment derivative for $\delta_N = 62°$ and $90°$.

Figure 75. - Concluded.